

# **Development of Ni-based Superalloy Metal Matrix Composites, Featuring High Creep Resistance**

Von der Fakultät für Maschinenbau, Elektro- und Energiesysteme  
der Brandenburgischen Technischen Universität Cottbus–Senftenberg  
zur Erlangung des akademischen Grades eines  
Doktors der Ingenieurwissenschaften

genehmigte Dissertation

vorgelegt von

Georges Lemos

geboren am 07. August 1979 in Telemaco Borba, Brasilien

Vorsitzende: Prof. Dr.-Ing. habil. Sabine Weiß

Gutachter: Prof. Dr.-Ing. habil. Florian Pyczak

Gutachter: Prof. Dr.-Ing. Ulrich Tetzlaff

Gutachter: Prof. Dr.-Ing. Pedro Dolabella Portella

Tag der mündlichen Prüfung: 4. August 2020



## Acknowledgements

I wish to manifest my gratitude to the National Council for Scientific and Technological Development (CNPq, Brazil), the German Academic Exchange Service (DAAD) and the Technische Hochschule Ingolstadt (THI, Germany), for the funding granted. Without the financial support from these institutions, this work would never be possible. Likewise, I am grateful to the Brandenburgische Technische Universität Cottbus-Senftenberg (BTU) for accommodating me in the graduate program and providing exceptional guidance in every step during the doctorate process.

I am also thankful for the warm reception at THI, as well as for the sponsorship of my work at international conferences by the AWARE program (Applied NetWork on Automotive Research and Education), supported by the government of Bavaria and the DAAD (Germany), in cooperation with Brazilian universities.

I wish to express my deep gratitude to my supervisors, Prof. Dr.-Ing. habil. Florian Pyczak (BTU) and Prof. Dr.-Ing. Ulrich Tetzlaff (THI), in addition to my tutor Prof. Dr.-Ing. Marcio Celso Fredel (UFSC), who provided outstanding support during all stages of this work. The engagement, knowledge and opportunities offered by them created the right set of circumstances not just for the doctoral work development, but also for my personal growth.

I would like to express a sincere appreciation to my committee chair, Prof. Dr.-Ing. habil. Sabine Weiß, and the committee expert Prof. Dr.-Ing. Pedro Dolabella Portella. Their contributions to evaluate my work were vital to conclude the assignment and to assure the right focus on future publications derived from the results obtained.

I express my warm thanks to Prof. Dr.-Ing. Harald Göllinger and Ms. Karin Ebenbeck for their support with the renovation and tailoring of the creep equipment utilized in this work. I am equally thankful to Dr. Jonathan Paul, for supporting the first set of compression creep tests at the Helmholtz-Zentrum Geesthacht (HZG).

My sincere thanks also goes to the Material Analysis laboratory staff at THI, Mr. Christian Biber, Dipl.-Ing. Eva-Maria Fiegler, Mr. Markus Bauch and M.Eng. Sabine Pöllmann, for their prompt and helpful support. I am grateful to the invaluable contributions from my colleagues and friends Adriano Pereira and Guilherme Volpato, as well as to my fellow labmates Albin Gottwalt, Benedikt Ernst, Janina Schmidt and Simon Keim.

Last but not the least, I would like to thank my family, with special mention to my wife Karin Scheschowitsch, who also went through a personal journey during her PhD and still gave unconditional support during mine.



## Abstract

The increasing demand for competitive, whilst also environment-friendly airplane travel, compels the design of highly efficient engines in the aeronautical field. A potential for improvement of traditional polycrystalline Ni-based superalloys, aiming higher creep resistance, was investigated. The approach adopted the concept of metal matrix composites (MMCs) to incorporate a rigid discontinuous phase, in the form of particles, to a  $\gamma'$ -strengthened Ni-based superalloy. In order to make the concept feasible, different microstructures resulting from diverse manufacturing techniques were investigated. By using distinct mixing and sintering methods, powders of Inconel X-750 and TiC were combined to form composites containing 15 vol.% of reinforcing particles. Powders were prepared with low and high energy milling processes, and formed by uniaxial pressure sintering and spark plasma sintering methods. Non-reinforced variants and composites had microstructures thoroughly examined at their initial state and after long isothermal aging treatments. Selected variants were further submitted to tensile and compression creep tests at temperatures between 700 and 800 °C, in the stress range of 200 to 500 MPa.

A comprehensive analysis was conducted using techniques such as EBSD, XRD Rietveld refinement, EDS and TEM to evaluate the development of  $\gamma'$ ,  $\eta$  and TiC phases, determining the achievable microstructures with each fabrication method and establishing their evolution after aging treatments over times up to 1000 h. Likewise, creep properties were analyzed by obtaining parameters such as creep exponents, threshold stresses and activation energies. A creep life estimation was conducted with the use of a Monkman-Grant relationship and a Larson-Miller parametrization. Lastly, the potential for a reduction in creep strain rates in a working turbine blade, considering the density of investigated materials as a parameter, was evaluated.

All produced composites presented power law creep, with dislocations surpassing  $\gamma'$  particles by climb. The variant produced by high energy ball milling and spark plasma sintering exhibited the highest creep rates, resulting from intense diffusion through grain boundaries. It also presented  $\eta$  phase after long isothermal aging, which affects negatively the creep resistance. Contrastingly, in the variant produced by low mixing combined with pressure sintering the lowest creep rates were observed. It was proposed that reinforcing TiC particles effectively acted as a load bearing phase, counterbalancing the adverse effects of the intergranular diffusion in the refined microstructure. Furthermore, a higher microstructural stability was observed in this variant, resulting from limited interaction between TiC particles and the matrix during fabrication.

Keywords: superalloys, MMC, creep resistance, TiC, isothermal aging.



## Zusammenfassung

Die zunehmende Nachfrage nach wettbewerbsfähigen und zugleich umweltfreundlicheren Flugzeugen erfordern die Entwicklung hocheffizienter Triebwerke. Deswegen wurde das Verbesserungspotential für herkömmliche polykristalline Ni-Superlegierungen untersucht, mit dem Ziel einer höheren Kriechbeständigkeit. Der verwendete Ansatz verfolgt das Konzept von Metallmatrix-Verbundwerkstoffen (MMCs), mit dem Einbringen einer starren diskontinuierlichen Phase in Form von TiC-Partikeln in eine  $\gamma'$ -verstärkte Ni-Superlegierung. Um die Umsetzbarkeit dieses Konzepts zu prüfen, wurden verschiedenen Fertigungstechniken eingesetzt, wodurch sich unterschiedliche Mikrostrukturen ergaben. Unter Verwendung mehrerer Misch- und Sinterverfahren wurden Pulver aus Inconel X-750 und 15 Vol.-% TiC kombiniert. Diese gemischten Pulver wurden mit Niedrig- und Hochenergie-Mahlprozessen hergestellt und durch einachsiges Drucksintern und Spark Plasma-Sintern weiterverarbeitet. Bei unverstärkten Varianten und den Verbundwerkstoffen wurden die Mikrostrukturen im Anfangszustand und nach langen isothermen Alterungsbehandlungen untersucht. Ausgewählte Varianten wurden Zug- und Druckkriechversuchen bei Temperaturen zwischen 700 und 800 °C im Spannungsbereich von 200 bis 500 MPa unterzogen.

Umfassende Mikrostrukturanalysen wurde unter Verwendung von Techniken wie EBSD, XRD-Rietveld-Verfeinerung, EDS und TEM durchgeführt. Deren Fokus lag auf der Entwicklung von  $\gamma'$ -,  $\eta$ - und TiC-Phasen, der Bestimmung der Ausgangszustände unterschiedlicher Herstellungsmethoden und der Untersuchung deren Alterungsverhalten über Zeiträume bis zu 1000 h. Ebenso wurden Kriecheigenschaften analysiert, indem Parameter wie Kriechexponenten, Schwellenspannungen und Aktivierungsenergien ermittelt wurden. Eine Abschätzung der Kriechlebensdauer wurde unter Verwendung der Monkman-Grant-Beziehung und einer Larson-Miller-Parametrisierung durchgeführt. Zuletzt wurde das Potenzial für eine Verringerung der Kriechdehnungsraten als Laufschaufel in der Turbine unter Berücksichtigung der Dichte der untersuchten Materialien als Parameter bewertet.

Die hergestellten Verbundwerkstoffe zeigten ein Kriechverhalten nach dem Potenzgesetz, wobei Klettern von Versetzungen über  $\gamma'$ -Partikel als Hauptkriechmechanismus identifiziert werden konnte. Die Variante, die durch Hochenergie-Kugelmahlen und Spark Plasma-Sintern hergestellt wurde, zeigte die höchsten Kriechraten, die sich aus intensiver Diffusion entlang die Korngrenzen ergaben. Des Weiteren zeigte diese, nach langer isothermer Alterung, das Auftreten der  $\eta$ -Phase, was sich negativ auf die Kriechbeständigkeit auswirkte. Im Gegensatz dazu wurden die niedrigsten Kriechraten in der Variante beobachtet, die durch Niedrigenergie-Mahlprozesse in Kombination mit Drucksintern hergestellt wurde. Außerdem wurde festgestellt, dass verstärkende TiC-Partikel effektiv als lasttragende Phase wirken und die nachteiligen Auswirkungen der intergranularen Diffusion in der verfeinerten Mikrostruktur ausgleichen. Darüber hinaus wurde in isothermen Auslagerungsversuchen dieser Variante eine höhere Gefügestabilität als in dem

Material beobachtet, dass durch Hochenergie-Kugelmahlen und Spark Plasma-Sintern hergestellt wurde. Dieser Unterschied kann auf eine begrenzte Wechselwirkung zwischen TiC-Partikeln und der Matrix während der Herstellung zurückgeführt werden.

Schlüsselwörter: Superlegierungen, MMC, Kriechbeständigkeit, TiC, isotherme Alterung.



## Table of contents

<b>1. INTRODUCTION .....</b>	<b>1</b>
1.1 Scope of the work .....	2
<b>2. LITERATURE REVIEW .....</b>	<b>3</b>
2.1 Gas turbines for airspace applications.....	3
2.1.1 Forces acting on a turbine blade .....	4
2.2 Nickel-based Superalloys .....	6
2.2.1 Lattice misfit between matrix and intermetallics.....	8
2.3 Inconel X-750 .....	9
2.3.1 Role of elements .....	11
2.3.2 Role of the grain size .....	12
2.3.3 Typical phases.....	13
2.3.4 Fabrication methods.....	14
2.4 Metal Matrix Composites (MMCs).....	15
2.4.1 Influence of Size and Volume of Particles .....	18
2.5 Creep in Ni-based superalloys .....	20
2.5.1 Diffusional Creep .....	21
2.5.2 Power Law Creep .....	22
2.5.3 Power Law Breakdown .....	24
2.5.4 Negative Creep in Tension.....	25
2.5.6 Creep of Inconel X-750 .....	26
2.5.7 Creep of Particle Reinforced MMCs .....	29
<b>3. MATERIALS AND METHODS .....</b>	<b>34</b>
3.1 Reference materials .....	34
3.2 Composites produced .....	36
3.3 Microstructure Analysis .....	38
3.4 Mechanical Analysis .....	40
3.4.1 Creep tests .....	40
3.4.2 Hardness and Elastic Modulus Measurements .....	42

<b>4. RESULTS .....</b>	<b>43</b>
4.1 Initial state characterization .....	43
4.1.1 Inconel X-750 hot-rolled (reference material) .....	43
4.1.2 Inconel X-750 (high energy milling + spark plasma sintering).....	47
4.1.3 X-750/TiC 15 vol.% (low energy mixing + pressure sintering).....	50
4.1.4 X-750/TiC 15 vol.% (high energy milling + spark plasma sintering).....	54
4.1.5 Distribution of grain and primary $\gamma'$ size .....	58
4.1.6 Phases identification and quantification with XRD .....	60
4.1.7 Elastic modulus estimation with nanoindentation .....	63
4.2 Development over long isothermal aging .....	65
4.3 Tensile creep results .....	72
4.3.1 Microstructure after rupture.....	72
4.3.2 Creep-rupture curves and determination of parameters .....	74
4.4 Compression creep results .....	81
4.4.1 Microstructure after test.....	81
4.4.2 Creep curves and determination of parameters .....	86
4.4.3 Estimation of load transfer in the composites .....	94
<b>5. DISCUSSION.....</b>	<b>96</b>
5.1 Initial and overaged microstructures.....	96
5.2 Creep fracture and microstructure.....	104
5.3 Creep parameters .....	107
5.4 Creep mechanisms.....	111
5.5 Estimation of life under creep .....	115
5.6 Functional effect of density reduction.....	116
<b>6. CONCLUSIONS .....</b>	<b>118</b>
<b>7. REFERENCES .....</b>	<b>120</b>

## 1. Introduction

Propulsive efficiency is a main concern in the design of airplane engines. To achieve lower fuel consumption, the project of a gas turbine must consider possible improvements in alloys for the fabrication of blades and discs. Over the past few decades, Ni-based superalloys were widely studied, resulting in advanced poly and mono crystalline variants that today are broadly employed in the industry [1,2]. Yet, further improvements are called for, aiming for the development of more environment-friendly airplane engines [3].

The strength enhancement of metallic alloys by the inclusion of a hard ceramic phase, resulting in metal matrix composites (MMCs), is a developing trend in technological-prominent industries. These materials offer a compromise between favorable and adverse characteristics of each component class, often generating a material that possess superior properties when compared to the non-reinforced varieties [4–8]. Regarding turbine blades, particularly, one of the most important attributes of a suitable material must be a high creep resistance [9–12].

A distinguished attribute of MMCs is the capability to transfer load from the metallic matrix to the ceramic reinforcement [6,13–16]. The characteristic is particularly of interest in materials submitted to creep, where the load partitioning relieves the stress sustained by the matrix. Another feature of some MMCs is a potential for density reduction, in relation to non-reinforced alloys. When considering the centripetal force acting on a section of a rotating turbine blade, the material density is directly related to the effective stress on this section. Accordingly, the creep rate in this case will also be directly proportional to the stress, elevated to the power of a stress exponent during certain creep regimes. Therefore, the ideal MMC candidate should be able to improve the creep resistance by both a reinforcement load bearing mechanism and by reducing the material density [10,11,17–19].

To address the subject, a  $\gamma'$  strengthened Ni-based superalloy reinforced by TiC particles was proposed. By combining a refractory alloy, with distinguished creep resistance, and a highly compatible ceramic phase that presents lower density, it was possible to introduce a new MMC concept. The approach associates three different strengthening mechanisms, aiming to increase the creep life at high temperatures. The first one concerns the mobility restriction of dislocations, handed by the presence of a high amount of coherent  $\gamma'$  precipitates. A second mechanism enables a load transfer from the  $\gamma$  matrix to TiC particles during strain by the Eshelby inclusion model [13,14,20–24]. Lastly, a third strategy involves a stress relief deriving from the material density reduction, on a rotating turbine blade.

Different fabrication methods might greatly influence the microstructure and creep properties of composites. The powder routes are among the most used to produce MMCs, for their practical handling of different materials mixtures. Distinct mixing and milling processes can

also be used to prepare the powders prior to the sintering process, as a measure to further improve the size and dispersion of particle reinforcements [25,26]. To establish the optimal manufacturing method, variations in both milling and sintering processes need to be experimented with.

The microstructure ability to endure long exposure to high temperatures while retaining its most valuable characteristics, is a critical aspect in materials for turbine blades. Likewise, creep parameters that support the premise of a high creep resistance, are decisive in the selection of the most adequate composite for the application. Both aspects must be thoroughly addressed, in order to devise an MMC that meets the strict requirements of the aerospace industry.

## 1.1 Scope of the work

The research offers a contribution on MMCs for use in turbine elements, namely Ni-based superalloys reinforced by TiC particles. As main goal, the investigation targets the development of a composite with elevated microstructural stability and high creep resistance, aiming application in turbine blades.

Additionally, the work seeks to expand the knowledge on the interactions between the metallic matrix and the reinforcing phase after fabrication by different methods, as well as after long exposure to high temperatures. It is also investigated which creep mechanisms act on the produced materials, and how the characteristics resulting from different manufacturing routes affect the creep resistance of the proposed composites.

## 2. Literature Review

In order to delineate the conditions of operation of a turbine blade, the involved creep mechanisms in the envisaged circumstances, the current Ni-based superalloys alternatives and the behavior of metal matrix composites regarding creep resistance, these subjects have been reviewed.

### 2.1 Gas turbines for airspace applications

Aircraft engines (Figure 1) are designed to achieve the best thrust/weight relation possible, attained using high-aspect ratio blades in the compressor, in addition to improvements in the pressure ratio and temperature of firing, to boost the work output. Till certain limits, the higher the pressure ratio, the higher the firing temperature, thus increasing the turbine thermal efficiency. However, a high reliability is also a prerequisite in aircraft engines. To achieve an optimal balance between performance and dependability, the turbine elements must be able to endure several thousands of hours in service without presenting faults or signals of material weakening [10,11,19,27,28].

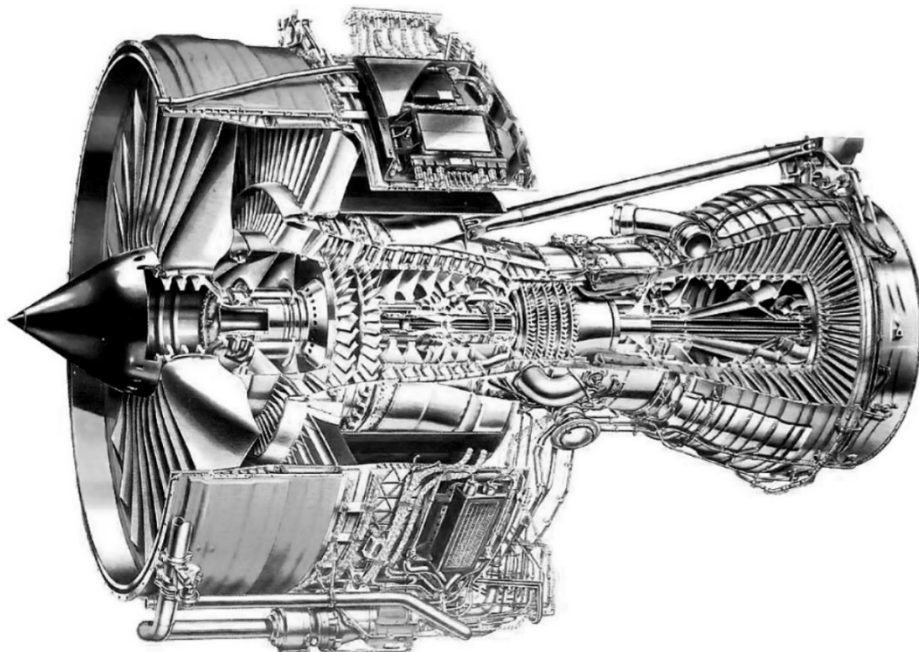


Figure 1 – Example of a Rolls-Royce Trent 800 turbine, used in the Boeing 777. Image from Rolls-Royce Holding plc [28].

Some of the adversities faced by turbine components, such as blades, are high temperatures, corrosive environments and high stresses. In highly optimized aircraft engines, the materials are frequently the bottleneck of performance. In the turbines, the combustor liner and the blades are the most critical components. Regarding moving parts, the blades are subject to creep, corrosion, fatigue and thermal strains. They frequently fail through creep and corrosion, having thermal fatigue as a tertiary cause of faults [11,12,27].

From the 1960 decade the average turbine firing temperature went from 760 °C to over 1400 °C. While the use of cooling systems helped significantly to increase these values over the last few decades, the advances in metallurgy also contributed greatly, by proposing new heat-resistant alloys. Accordingly, the average blade metal temperature went from 700 °C to over 900 °C, with the introduction of single crystal superalloys in the market [27,29,30].

Fracture in turbine blades is highly associated with creep. To predict it through elongation and reduction in area, is often a hard task. Ductility is erratic in superalloys, with failure frequently occurring with just a small deformation, especially at operating temperatures. That leads to a fracture that possess more brittle than ductile characteristics, such as intergranular crack propagation and very small section reduction. As a result, frequently the development of surface notches is initiated by corrosion and erosion processes, culminating with a rapid crack propagation. The occurrence of such defects can be mitigated with the use of coatings [27].

The design of gas turbines includes long stress-to-rupture tests on blades, often conducted for 10.000 hours. These results must be extrapolated to hundreds of hours, using parametrization methods such as Larson-Miller plots. During these long tests, the blades experience creep, sustaining elongation along their major axis. Generally, no more than 1 to 2 percent of creep elongation is tolerated in a turbine blade, to avoid closing the tight tip clearances [9,30].

To minimize the severity of creep in turbine blades, new processes and Ni-based superalloys were developed. These were devised to alter or reduce grain boundaries, which are prone to diffusion, and consequently promote creep. Directional solidification (DS), used in large scale since early 1990s, allowed to obtain elongated grains, oriented parallel to the major axis of the blade. To further improve the creep resistance, the single crystal variants were developed soon after using special investment casting furnaces that possess a "grain selector" at the wax mold base, usually in the form of a pig-tail-shaped spiral. This setup allows to a single grain to enter the casting cavity, forming a monocrystalline material [2,27].

### 2.1.1 Forces acting on a turbine blade

While a turbine blade is subjected to a complex state of stresses during operation, the centripetal force acting along the major axis is the main cause for the creep deformation [31]. In

this scenario, the material density that composes the turbine blade is directly proportional to the effective stress in a cross section of the blade ( $\rho \propto \sigma$ ).

As an example, a large civil turbofan engine develops a power of roughly 50 MW, with each row of blades producing enough to power a small town. The blades rotate at an angular speed ( $\omega$ ) of more than 10 thousand revolutions per minute, with their tip spinning at more than 1200 km/h. The force acting on the blade root can be calculated with the equation 1:

$$F = \int_{r_{root}}^{r_{tip}} \rho A \omega^2 r \, dr = \frac{\rho A \omega^2}{2} (r_{tip}^2 - r_{root}^2) \quad (1)$$

where  $r_{tip}$  and  $r_{root}$  are the radial positions of the tip and root,  $A$  is the cross-sectional area and  $\rho$  is the material density [2]. So, for the example of a blade with a hypothetical constant cross-section of  $0.0012 \text{ m}^2$  and tip length  $r_{tip} = 1.2 \text{ m}$ , mounted over a disc with  $r_{root} = 0.4 \text{ m}$ , assuming  $\omega = 523.3 \text{ rad/s}$  (5000 rpm) and  $\rho = 7778 \text{ kg/m}^3$ ,  $F$  can be calculated as follows:

$$F = \int_{r_{root}}^{r_{tip}} 7778 \times 0.0012 \times 523.3^2 r \, dr = 1277970 \times (1.2^2 - 0.4^2) = 1635.8 \text{ kN/blade}$$

Assuming a root cross-sectional area  $A_{root} = 0.008 \text{ m}^2$ , the stress in the example will be:

$$\sigma = \frac{F}{A} = \frac{1638.8 \times 10^3}{0.008} = 204.5 \text{ MPa/blade}$$

It is imperative to consider that the blades bear stress for long periods of time at high temperatures, thus the material must be able to withstand creep, which can occur at stresses significantly lower than the alloy yield resistance [2]. It is also important to take into account that the creep rate is often dependent on an exponential relation of the stress acting on section of the blade material (as further discussed in chapter 2.5). This relationship can be taken advantage of, for instance with a reduction of the blade material density, thus consequently also reducing the centripetal force and the resulting creep rates by an exponential factor [32].

## 2.2 Nickel-based Superalloys

Nickel-Chromium and Nickel-Iron-Chromium alloys, generally referred just as Nickel-based superalloys, had their development initiated in the 1940 decade. These alloys presented the ability to retain creep-rupture and high strength at a high temperature, relative to their melting points. Presenting a face centered cubic (fcc) matrix that permitted significant alloying, it was possible to make them corrosion resistant and generate new precipitates, to further improve their strength [1,2,33,34].

With the production using casting processes in the 1950's, the directional solidification in the 1970's and single crystal in the 1980's, the modern processes enabled the development of new superalloys and further increased their creep resistance (Figure 2). Since then, Ni-based superalloys became a regular choice for use in power and transportation industries, being mainly employed in gas turbines components [2].

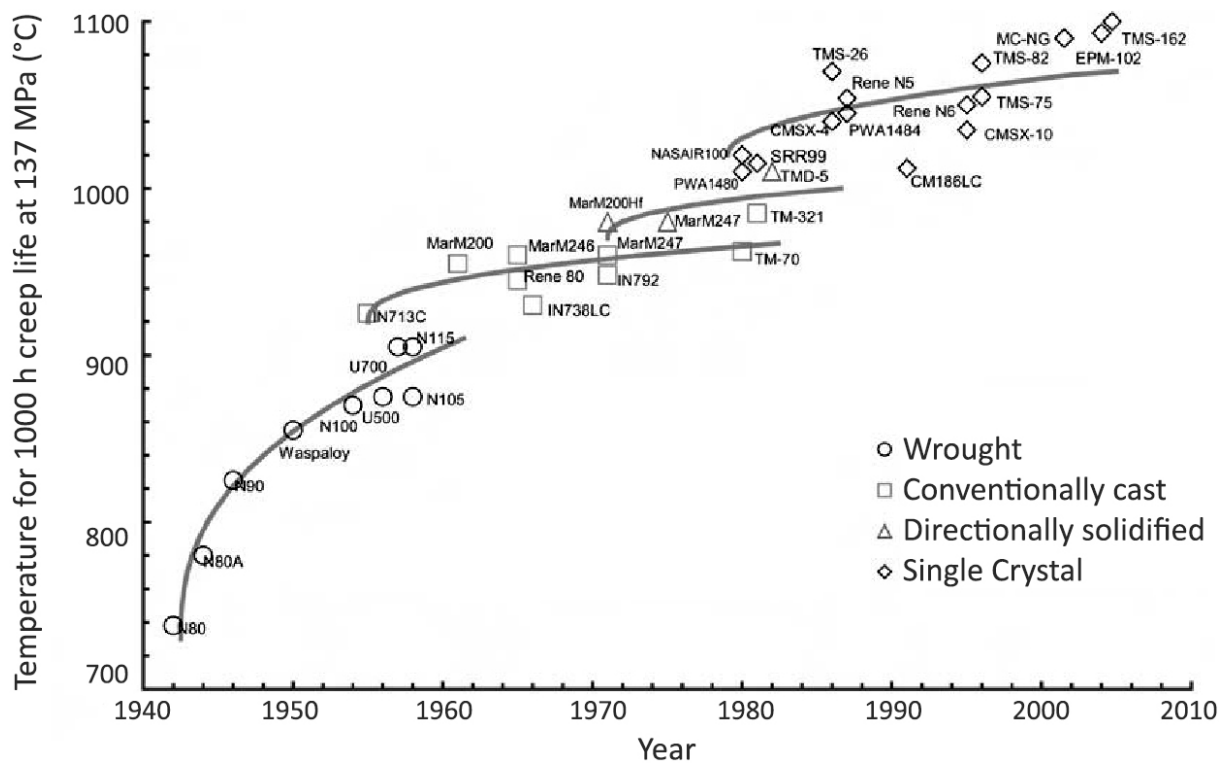


Figure 2 - Development timeline of superalloys, regarding creep resistance and production processes. Adapted from Reed, R. C. (2006).

The development of vacuum induction casting technology in the 1950's made possible to achieve higher control over the resulting microstructure, enhancing creep resistance. In addition to the equiaxed-crystal structure produced through conventional casting (Figure 3a), it also



became possible to obtain columnar grains by directional solidification (Figure 3b), which brought further improvement to turbine blades. More recently, the complete elimination of grain boundaries became possible by the production of single-crystal variants (Figure 3c), which also excluded the need for elements as boron and carbon to be added for grain-boundary strengthening. Beyond creep resistance enhancement, this also resulted in less segregation and eutectic products formed during casting, bringing improvement to fatigue life [2].

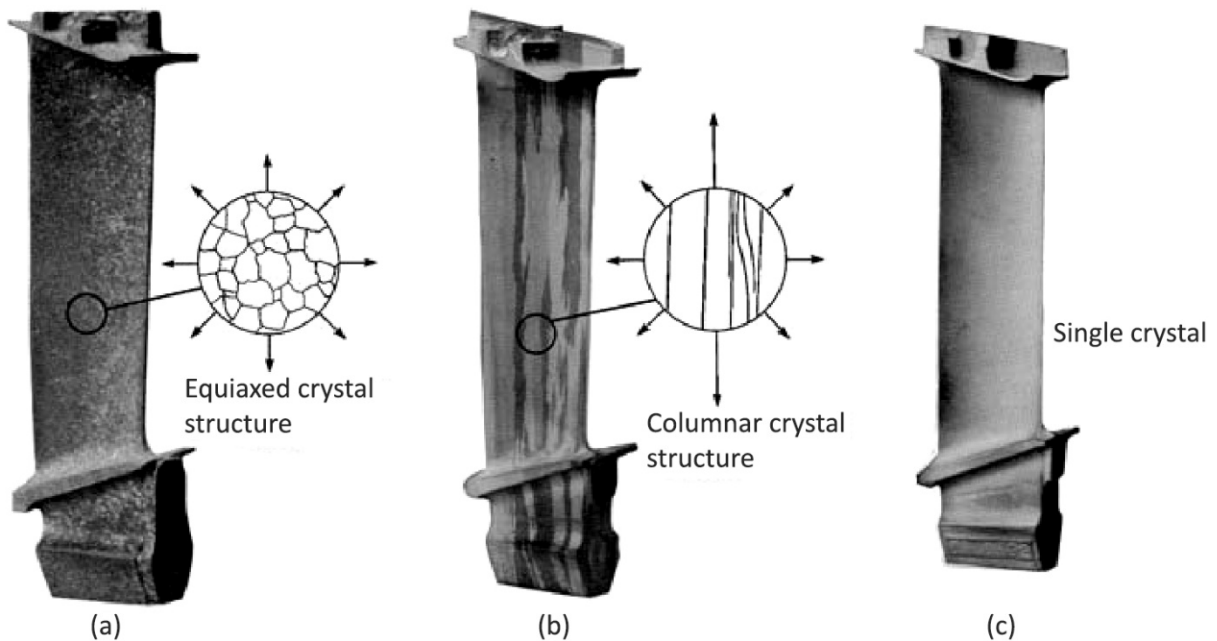


Figure 3 - Turbine blades with (1) equiaxial, (b) columnar and (c) single-crystal microstructures. Figure adapted from Reed, R. C. [35].

The reason why superalloys possess excellent properties at high temperatures, being particularly highlighted for their creep resistance, lies in a combination of factors. Nickel, the primary solvent in superalloys, features a high melting temperature. It also possesses a close-packed, face-centered cubic structure, which high density leads to moderate diffusion rates. Furthermore, the creep activation energy  $Q_c$  in these alloys is high, resulting in elevated microstructural stability at elevated temperatures. While some metals may also offer similar characteristics in this aspect, they are often more expensive, bringing major interest for Nickel. Additionally, polycrystalline superalloys are often produced with large grains, to reduce diffusion paths and the likelihood of grain sliding at high temperatures [2,34,36]. The grain size influence in the creep resistance is further discussed in section 2.3.2.

Nickel-based superalloys can be further strengthened by solid-solution elements, or by the precipitation of intermetallic phases. The alloys that are essentially strengthened by solid solution, such as the polycrystalline Inconel 625, make use of Niobium and Molybdenum, among other

elements. These alloys have the advantage to dispense the need of additional heat treatments for precipitation, making them also highly suitable for welding processes when compared to intermetallic-hardened superalloys. These are strengthened by  $\gamma'$  [ $\text{Ni}_3(\text{Al},\text{Ti})$ ] or  $\gamma''$  [ $\text{Ni}_3(\text{Al},\text{Ti},\text{Nb})$ ], precipitated in the fcc matrix. Common examples of polycrystalline  $\gamma'$ -strengthened alloys are Waspalloy and Inconel 713, whilst a typical  $\gamma''$ -strengthened alloy is the Inconel 718. Some alloys also make use of both precipitates, such as the Inconel 706 [35–37].

Iron-Nickel based superalloys are in general strengthened by  $\gamma'$ , such as the Inconel 901. Less frequent are the modified stainless steels strengthened by solid-solution elements, as the Incoloy 800H, which possesses up to 35 vol.% Ni, while maintaining a minimum of 39,5 vol.% Fe [37]. The premise behind these alloys is a reduction of costs, since nickel is generally a high-valued element in the market, priced at almost 20 times the value of refined iron in the last decade [38].

### 2.2.1 Lattice misfit between matrix and intermetallics

Lattice misfit between the  $\gamma$  matrix and precipitates such as  $\gamma'$  and  $\gamma''$  is common in Ni-based superalloys. The fitting mismatch is generally small, below 1%, thus keeping a low interface energy and promoting the precipitate stability [33,39]. The high degree of coherency between these phases and the matrix leads to the formation of cuboidal precipitates, whose faces are aligned along the cube directions. The development and alignment of  $\gamma'$  precipitates, for instance are highly dependent on the specific degree of lattice misfit and the differences in the elastic moduli of the involved phases [35,40].

The lattice parameters of disordered  $\gamma$  and ordered  $\gamma'$  phases are so similar, that the maxima reflections for both phases, for example  $\{110\}$ ,  $\{200\}$  and  $\{220\}$ , can not be resolved in the electron diffraction patterns. Despite that, some reflections emerge exclusively from the  $\gamma'$  phase, such as  $\{100\}$  and  $\{210\}$ , among others. Generally, the orientation between the  $\gamma$  matrix and  $\gamma'$  precipitates is  $\{100\}_{\gamma'} // \{100\}_{\gamma}$  and  $\langle 010 \rangle_{\gamma'} // \langle 010 \rangle_{\gamma}$ , with  $\gamma/\gamma'$  interfaces having the  $\langle 001 \rangle$  directions as respective plane normal vectors [2].

Some Ni-based superalloys build particularly strongly coherent interfaces between matrix and intermetallics. That is the case with Inconel X-750, which presents a positive lattice parameter misfit between 0.3 and  $0.6 \pm 0.1$  % (with  $a_{\gamma'} > a_{\gamma}$ ) at room temperature and 0.1 % at 900 °C, building favorable coherency fields around  $\gamma'$  precipitates [41,42]. However, during plastic deformation at high temperatures or prolonged aging, misfit dislocations are formed, and the precipitates become semi-coherent. During this process, dislocations are generated in the matrix through internal stresses emerging from the creation and dissolution of carbides. These dislocations glide and bypass big intermetallic particles ( $d > 0.5 \mu\text{m}$ ), forming Orowan loops. Their rotation leaves behind a network of prismatic dislocation, with Burgers vectors of  $a/2\langle 110 \rangle$  and a predominantly

edge character. To better accommodate the changes in the misfit, the precipitates morphology also changes, evolving from a cubic one to a tetradecahedron geometry [40].

A complete loss of coherency is often observed in Ni-based superalloys that present a negative misfit ( $a_{\gamma'} < a_{\gamma}$ ) after long aging [43]. At high temperatures the lattice of the  $\gamma$  matrix increases faster than that of  $\gamma'$ , hence the negative misfit further increases as well [44]. Ultimately, the process leads to the formation of a dendritic morphology, which substitutes the array of cuboids in the microstructure. However, in alloys with positive misfit (such as Inconel X-750) the coherency is never completely lost, even when a dendritic microstructure is formed. The fact is explained by the limited amount of dislocations that can be captured at the  $\gamma/\gamma'$  interface, since they are more easily gathered around the intermetallics in dipole or multipoles configurations [43]. Considering that in general the expansion coefficient tends to be lower in the ordered  $\gamma'$  in relation to the  $\gamma$  matrix, during temperature increase the lattice misfit is indeed expected to grow in alloys with negative misfit, but to be reduced in variants with positive misfit. Nevertheless, it has been observed that in the Inconel X-750 alloy the misfit remains highly stable during long isothermal aging [42].

### 2.3 Inconel X-750

Inconel X-750 is a precipitation hardenable, nickel-based superalloy, with composition detailed in Table 1. It possesses superior tensile and creep resistance, when compared to many other classes of high temperature resistant alloys. It is composed by a face centered cubic (fcc) matrix, based on Nickel, and referred as gamma ( $\gamma$ ). The predominant precipitates include metal carbides, such as MC and  $M_{23}C_6$ , but the primary strengthening phase is the gamma prime ( $\gamma'$ ), an ordered fcc structure  $[Ni_3(Al,Ti)]$  of the  $L1_2$  type, where Ni atoms at the cube edges are replaced predominantly by Al (Figure 4), and to a less extent by Ti [45–48].

Table 1 - Chemical composition of Inconel X-750 (EN 2.4669) [49].

Element	Cr	Fe	Ti	Nb	Al	Si
Wt.%	14.0-17.0	5.0-9.0	2.3-2.8	0.7-1.2	0.4-1.0	0.5 max.
Element	Mn	Co	C	Cu	S	Ni
Wt.%	1.0 max.	1.0 max.	0.08 max.	0.50 max.	0.010 max.	70.0 min.

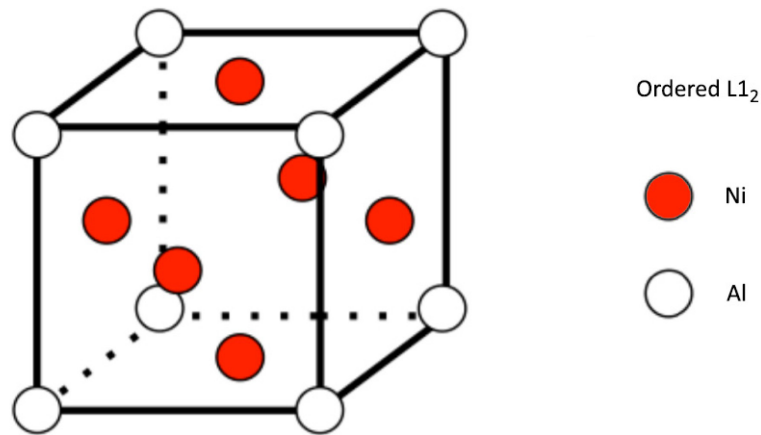


Figure 4 - The long range ordered L1<sub>2</sub> fcc structure of  $\gamma'$ . Figure adapted from Owen [47].

The  $\gamma'$  phase [Ni<sub>3</sub>(Al,Ti)] is formed after a reaction between titanium or aluminum and nickel, and when peak-aged presents a highly coherent interface with the  $\gamma$  matrix. A small lattice misfit with the  $\gamma$  matrix, however, provides the formation of dislocation networks near their interface, already at an early stage of the  $\gamma'$  formation. The degree of misfit between lattice parameters of the  $\gamma$  matrix and the  $\gamma'$  precipitates have a dependence on the solute additions, and their partitioning between precipitate and matrix. The higher the discrepancy among solute atoms and the main phase constituents, the higher is the  $\gamma/\gamma'$  interface misfit [2,34].

The particles of  $\gamma'$  in the Inconel X-750 frequently start growing spherical, to minimize interfacial energy (dependent on surface area), changing later to a cuboid morphology (to accommodate the growth in strain energy). The cubes, for instance, may further grow and split into smaller, connected cubes, and in extreme cases ultimately develop into a dendritic structure. For alloys whose composition results in a low  $\gamma/\gamma'$  misfit, the  $\gamma'$  particle needs to grow further before the effects of the misfit strain can affect the particle shape. However, a strong correlation between positive or negative interface misfit and the resulting  $\gamma'$  morphology is not well established [2,42,50,51].

Generally, ordered intermetallics are composed of two interpenetrating structures: an  $\alpha$  sublattice composed of A atoms, and a  $\beta$  sublattice composed by B atoms, resulting in a superlattice ( $\alpha + \beta$ ). This configuration results in a stronger bonding, compared to disordered alloys, because dislocations need to glide for longer distances to replace identical atoms. A dislocation capable of surpassing this higher energy barrier is often called a "superdislocation", and after the movement the local minimum energy is maintained, since the atoms position remain the same as before the glide [34,35,45,52,53].

Gliding of a superdislocation is, however, not the only possible form of dislocation movement in ordered intermetallics. It is also possible that an atom A occupies the site of an atom B, and vice versa, generating an antisite defect and by this mean increasing the potential energy

of the system. A region of the crystal where the atoms are arranged this way is called an antiphase domain (APD), and its interface with the parent lattice is called an antiphase boundary (APB) [45]. The L1<sub>2</sub> structure type found in the  $\gamma'$  phase provides a significant strengthening by the formation of an antiphase boundary (APB) at the  $\gamma/\gamma'$  interface [33].

While the movement of superdislocations occurs in pairs connected by an APB, they have dissociated stacking faults (SF). Their combination produces a complex stacking fault (CSF). Since the APB energy is lower on {100} than on the {111} plane, the screw super-dislocation cross-slips to the {100} plane, but it leaves its stacking fault on {111}. This situation is known as a Kear-Wilford lock, and it is believed to be responsible for the anomalous temperature-dependence of the yield-stress in Ni-based superalloys containing intermetallic compounds with L1<sub>2</sub> structure. As a result, at temperatures over 500 °C these alloys are harder than at 20 °C, an advantageous characteristic exploited for high temperature applications [34,54].

The size distribution of  $\gamma'$  precipitates is usually not unimodal in the alloy Inconel X-750. The formation of a finer (secondary)  $\gamma'$  occurs during cooling from the solvus temperature, while the coarser (primary)  $\gamma'$  is formed mostly during aging treatment [55]. It is important to note that some Ni-based superalloys also present a tertiary precipitation of  $\gamma'$ . In this work it is adopted the definition of primary  $\gamma'$  for particles that possess an average diameter ( $D_{avg}$ ) over 40 nm, and secondary  $\gamma'$  as particles having  $D_{avg} < 40$  nm.

The occurrence of Ostwald ripening can be observed at temperatures between 700 and 800 °C, with the dissolution of secondary  $\gamma'$  occurring faster at high temperatures and impairing the creep resistance. The elimination of these particles culminates with a transition period where the primary  $\gamma'$  precipitates stabilize in size, establishing a unimodal system. Eventually, these particles start growing again, at even larger rates [56,57].

### 2.3.1 Role of elements

The matrix is composed by  $\gamma$  nickel and solid solution elements. Ni exhibits high temperature strength, and tolerates a high amount of solutes. It also possesses a high stacking fault energy (SFE,  $\sim 150$  mJ/m<sup>2</sup>), thus deforming by glide of dislocations, and leading screw dislocations to cross-slip under low stress. Being able to cross-slip, nickel also does not need to change orientation to accommodate deformations, though some level of reorientation is expected as the result of grain boundaries movement during strain [35,58].

Iron is added to the matrix to reduce the cost of the alloy. Since it possess a metallic radius very close to the one presented by nickel (126 and 124 pm, respectively for Fe and Ni), iron is used as a substitutional element in the  $\gamma$  phase [59]. Aluminum contributes to solid solution strengthening in the matrix, resulting from the differences in atomic diameter to nickel [33].

Cobalt and chromium also give a contribution to mechanical strength as solid solution elements in the matrix, although it is believed to a minor one [58]. Niobium possesses a high atomic mismatch with nickel, so a low solubility of Nb in the  $\gamma$  matrix is observed (e.g. 7% in a Ni-20% Cr alloy at 1000-1200 °C in wt.%) [33,58], and therefore this element is more frequently observed in other phases.

Corrosion resistance is given by chromium, aluminum, and nickel, at different conditions. In common atmosphere, the formation of a superficial Al oxide film is very effective, while in alkaline environments Ni provides a superior protection. Chromium generally improves the surface stability at a larger temperature range through the formation of  $\text{Cr}_2\text{O}_3$ , a durable passive film that suppresses the diffusion of metallic atoms outwards, and of atoms of oxygen inwards. Additionally, chromium also precipitates with carbon in the form of  $\text{M}_{23}\text{C}_6$ , which contributes to immobilize grain boundaries. This precipitate discussed in further detail in section 2.3.3[33,58].

Nickel is also present in the main precipitate in the alloy, the  $\gamma'$  phase. Ni possess the capability to form coherent intermetallics with Nb, Al and Ti, giving the Inconel X-750 a high creep resistance. Titanium and aluminum are the central  $\gamma'$  formers in this alloy [59]. However, a distinction in the composition between different variants of  $\gamma'$  can be made: in similar alloys, the primary  $\gamma'$  is frequently composed by balanced atomic amounts of Al and Ti combined with Ni, while the secondary  $\gamma'$  is mostly composed by Al combined with Ni [60]. The contribution of niobium to form the  $\gamma'$  phase by the substitution of Ti and Al is considered limited, but it adds to the stabilization of MC carbides (Ti,Nb-rich). Nb is also believed to improve the stability of the  $\gamma'$  phase, as well as raising its APB energy and therefore increasing its resistance to cutting [59].

Ti and Nb are present in the MC carbides, which result partially from the stabilization of free carbon in the alloy, after adequate heat-treatment. This process is also a requirement to avoid a surplus of Ti in solution, which may lead to the formation of the undesired (brittle)  $\eta$  phase [59]. The  $\eta$  precipitate is further discussed in section 2.3.3.

### 2.3.2 Role of the grain size

According to the heat treatment applied to the wrought Inconel X-750, it is possible to obtain grain sizes varying significantly. A relation between creep rate and grain size in the alloy is well established [48] (Figure 5), showing that not only diffusion is intensified at the paths provided by the grain boundaries [61], but also the occurrence of grain-boundary sliding facilitates creep. Both mechanisms contribute to increase creep rates, at different moments. During the first stage of creep, cavity nucleation takes place at grain boundaries, resulting in earlier cavity interlinkage in alloys with smaller grain size. Likewise, grain-boundary sliding plays a dominant role in later stages of creep, leading to mechanical tearing and fracture [48].

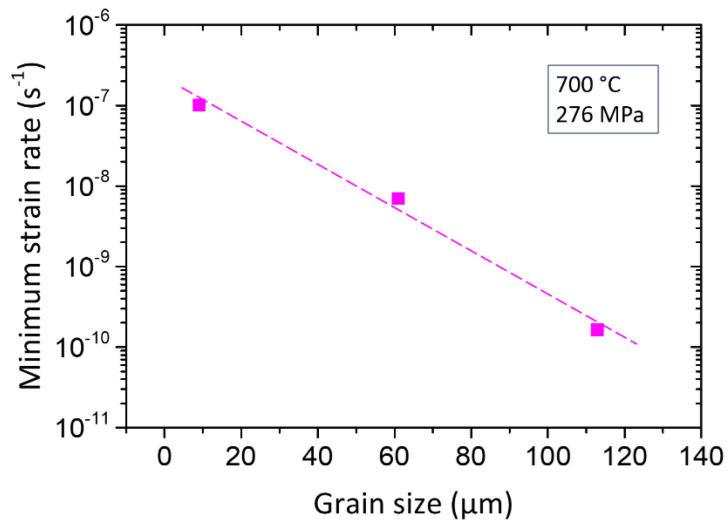


Figure 5 - Correlation between minimum creep rate and grain size in the Inconel X-750 at 700 °C, defined by a linear trendline [46]. Figure adapted from Venkiteswaran and Taplin (1974).

The stress exponent is also affected by the grain size, resulting in lower values for alloys presenting smaller grain sizes. The reduction in the stress exponent is related to the amount of grain-boundary sliding observed during creep, which becomes a dominant deformation mechanism at very fine grain sizes ( $< 10 \mu\text{m}$ ), as observed by Venkiteswaran and Taplin (1974) when testing the Inconel X-750 at 700 °C. It is estimated that the alloy may exhibit superplasticity tendencies if the grain size is reduced below  $1 \mu\text{m}$ , resulting in stress exponent values under 2 [48]. In this case considerable large deformations are expected during creep, caused by strong grain sliding, possibly including grain rotation and Coble diffusional creep [62]. The creep models are further discussed at section 2.5.

### 2.3.3 Typical phases

The MC type carbides are titanium-rich, and control grain refinement during heat treatment and hot work. Niobium may also be present on them, among other refractory elements. After thermal exposure, MC may transform to  $\text{M}_{23}\text{C}_6$  and  $\text{M}_6\text{C}$  type carbides [33,63].

The Cr-rich  $\text{M}_{23}\text{C}_6$  precipitate has a major importance at grain boundaries, counteracting grain boundary sliding in polycrystalline variants. The reaction to form  $\text{M}_{23}\text{C}_6$  occurs partially at the expense of MC carbides, which are rich in Ti and other refractory elements. The chromium carbides form a near-continuous film at grain boundaries, reducing diffusion in the region, thus also decreasing creep rates. However, rupture ductility is reduced as well [33,63,64].

Besides the  $\gamma'$  phase (described in section 2.3), the  $\gamma''$  phase [ $\text{Ni}_3(\text{Nb})$ ] may also be present, resulting from the presence of niobium and iron. Having the form of platelets, and a high coherency with the matrix, it grows around  $\gamma'$  particles, enveloping them. The presence of iron is necessary to the  $\gamma''$  formation, since combined with nickel it provides the necessary electron-to-atom ratio to precipitate  $\gamma''$  [2,34].

Undesirable constituents may also be present, due to variations in chemical composition, processing and exposure to high temperatures during service. Laves ( $\text{AB}_2$ ), a topographically close-packed phase (tcp), is an intermetallic that is detrimental to both rupture strength and ductility properties. Sigma,  $\sigma$  ( $\text{Cr}_2\text{O}_3$ ), is a tcp phase that may be formed in a Ni-depleted matrix, or in a highly segregated microstructure, also decreasing mechanical strength [59,65].

In the Inconel X-750 the  $\gamma''$  phase is rare and more stable than the  $\gamma'$ , but if present it can transform to delta phase [ $\delta$ , ( $\text{Ni}_3\text{Nb}$ )] during service. This orthorhombic phase is non-coherent with the matrix, having the form of platelets or cells. While it contributes to grain control, this phase is considerably less effective to hinder dislocations in comparison to  $\gamma''$  [59,66].

If the alloy is exposed to temperatures between 700 and 800 °C for several thousands of hours,  $\eta$  phase ( $\text{Ni}_3\text{Ti}$ , *eta*) may form. This phase derives from  $\gamma'$  and develops at the expense of Ti, reducing the amount of this element in solid solution. The driving force for this transformation is believed to be the coherency strain energy, associated with the lattice mismatch. Having a cellular form, it is frequently located at grain boundaries, where it significantly reduces their mobility and deteriorates the alloy creep resistance. When present inside the grains it possesses the form of Widmanstätten plates, but in this case, it is not proved to be detrimental to the creep properties. In addition to a loss in ductility,  $\eta$  phase also leads to the formation of  $\gamma'$ -free zones around them [33,59,67].

A high content of niobium may also induce the formation of additional MC phase during service at high temperatures, leading to the development of  $\gamma'$ -depleted zones around these carbides. The solute depletion, due to the formation of the Nb rich MC phase, distinctively affects  $\gamma'$  and  $\gamma''$  precipitates. The concentration of Nb in  $\gamma'$  is lower than in  $\gamma''$ , resulting in larger intermetallic-free zones. The solute depletion issue may also be combined with a vacancy depletion. This effect derives from the volume misfit between the MC phase and the  $\gamma$  matrix, that facilitates vacancy migration to the growing carbides. Ultimately, the deficiency of vacancies around the carbides also contributes to inhibit both  $\gamma'$  and  $\gamma''$  growth in the region [59,63,65].

#### 2.3.4 Fabrication methods

A diversity of fabrication methods is used to produce polycrystalline Ni-based superalloys, including  $\gamma'$ -strengthened varieties such as the Inconel X-750. Among the most common processes



are investment casting, forging and forming, and the powder metallurgy routes [1,68]. When designing the microstructure, it is possible to opt for a production method that enables tailoring the alloy mechanical behavior. These involve controlling the  $\gamma'$  amount and size, the dispersion of carbides, the grain size, the  $\gamma$  matrix chemistry and the grain boundaries morphology [69].

Fabrication of Ni-based superalloys by powder metallurgy routes became notorious with the production of highly alloyed variants, producing fine grained preforms that also possess a high degree of microstructure homogeneity. The route allows the production of near-net shapes, which reduces the amount of secondary processing. It also allows superior control over the resulting microstructure, compared to ingot metallurgy wrought products [1].

Among common powder consolidation processes are uniaxial sintering under vacuum, hot isostatic pressing followed by forging, and direct isostatic pressing. Powder sizes between 45 to 250  $\mu\text{m}$  are frequently used in these routes [1]. The powder routes are also frequently used to produce Ni-based superalloys reinforced by a dispersion of oxides or ceramic particles. Often, high energy ball milling processes are also utilized to prepare the powders to produce these variants, aiming at a microstructure with higher creep resistance [70].

Spark plasma sintering (SPS) is a field assisted sintering technique that presents advantages over more traditional powder metallurgy fabrication methods. It is characterized by the repeated high voltage charges on a metallic powder compacted under relatively low pressures, during a process that lasts only a few seconds. Commonly, spark plasma sintering is conducted under an atmosphere of argon, hydrogen, or under vacuum. During the process, oxides, absorbents and other impurities are frequently broken and moved from the powder surface. Among the highlighted features from the SPS process are the possibility to generate super saturated solid solutions, produce materials with high densities and the use of very short sintering times, saving time and energy [71].

It is important to note that the SPS process can produce heating rates up to 800 K per minute, resulting in instantaneous temperature gradients that make difficult to assess the real temperature achieved in the specimen interior [71–73]. In Ni-based superalloys, the SPS process may also cause the formation of a liquid film at particles boundaries, that helps to achieve high densification values [71,74]. The method is proven as fabrication route for  $\gamma'$  strengthened Ni-based superalloys [75] and oxide dispersion strengthened Ni-based superalloys [76,77].

## 2.4 Metal Matrix Composites (MMCs)

Composite materials offer a way to combine the properties and manufacturing advantages of two different material classes. Among them are the Metal Matrix Composites (MMCs), who greatly benefit from metal properties such as ductility and fabrication versatility, together with a

ceramic reinforcement, which often adds high stiffness, wear and corrosion resistance to the metallic alloy. Furthermore, the addition of a reinforcement with a superior Young's Modulus (compared to the matrix phase) also enhance the alloy strength, by transferring part of the load to the reinforcement. Given the right materials combination, the total strength resistance of an MMC is situated between that observed for the non-reinforced alloy, and the ceramic phase alone. But beyond bearing the load, the addition of a reinforcement phase may also improve the temperature stability, reducing the creep rate by several orders of magnitude [6,78–80].

The MMCs emerged in the 1950's, as result of the strong demand for advanced materials by the military and aerospace sectors. By the 1960's, the development of ceramic whiskers and *in-situ* eutectics found their first applications in aircraft engines. Particle reinforced MMCs would receive stronger attention only in the early 1980's, motivated by a combination of affordable costs of processing, the blooming post-recession market and a stronger demand for new engineering designs. After the late 1980's, both continuously and discontinuously reinforced MMCs gained a new boost from research programs around the world, culminating in several commercial applications. Today MMCs can be found in transportation (trains, automobiles and airspace), energy generation, industrial infrastructure and recreational products, among other segments [5,78,79].

In general, the MMCs may be classified in continuous and discontinuous reinforced types. Examples of continuous reinforcements, such as short and long fibers, are graphite, alumina and silicon carbide, among others. Carbon fibers are particularly renowned for their high strength resistance in several consumer appliances. As discontinuous reinforcements, a variety of shapes may be employed, such as particles, very short fibers and whiskers. When the aspect ratio between their longer and shorter axis is situated around 1 and 4, the reinforcement is considered to be a particle [80]. The most common hard phases added to these alloys are SiC, Al<sub>2</sub>O<sub>3</sub>, B<sub>4</sub>C, TiC, TiB<sub>2</sub> and ZrO<sub>2</sub>, among others. When using fibers as reinforcement, it is observed a strong strengthening effect in the direction of the fibers axis (anisotropy). This directional behavior, however, is not observed with the use of particles as reinforcement, where the strengthening effect is mainly isotropic [5,78].

As the matrix material, a softer, more ductile metallic phase is utilized. Structural aluminum alloys, such as the 6000 and 7000 series, are widely employed. For higher temperatures, however, refractory metals are preferred. Among them, titanium, cobalt and nickel occupy a prominent position, since these alloys possess also high corrosion and creep resistance, but still retain some ductility. For the microstructure, in general coarse grains are preferred when aiming at elevated creep resistance, since they provide less paths to diffusion along the grain boundaries [4,81].

The load transfer from the matrix to the reinforcement occurs through shear-lag [82] or Eshelby models [13,24,83]. While the shear-lag model offers a scalar mathematical treatment,

that is effective to predict the behavior of composites reinforced with asymmetrical rigid phases, the Eshelby model is tensor-based and gives better estimations on MMCs that possess particles of low aspect ratio [13,14]. This approach considers the existence of a complex state of stress involving both the reinforcing particle, and the surrounding material [24]. The amount of load transfer can be obtained with Equation 2 [84].

$$\sigma_{LT} = (\sigma_{com} - \sigma_{TH,com}) - \sigma_{alloy}^{eff} \tag{2}$$

where  $\sigma_{com}$  and  $\sigma_{TH,com}$  are respectively the applied stress and the threshold stress in the composite, and  $\sigma_{alloy}^{eff}$  is the effective stress for creep to occur in the matrix alone.

In order to properly calculate the load transfer, it is essential that no differences are observed between the microstructure of the non-reinforced reference and the matrix in the composite [84]. The Eshelby model accounts for a strain field that results from thermal expansion and phase changes, inducing stresses that are not only limited to the matrix, but also present in the reinforcing particle. To model the complex state of strain in the matrix, Eshelby [24] conceived the possibility to hypothetically remove the inclusion, restore its original stress equilibrium by allowing morphology changes, and reintroduce the particle in the matrix (Figure 6).

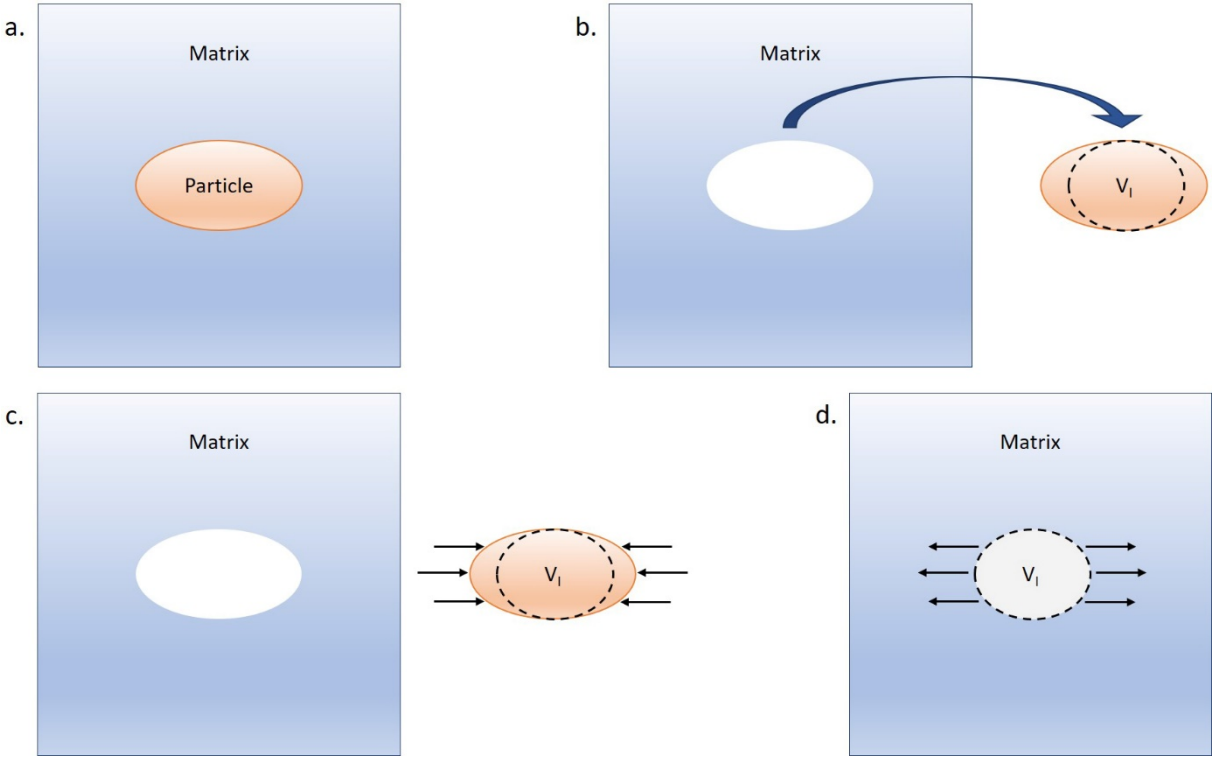


Figure 6 - Schematics of a simplified Eshelby's inclusion model. The sequence shows a hypothetical removal of a reinforcing particle, with shape and size restored after stress relief, followed by reinsertion in the matrix. Figure adapted from Meyer [85].

### 2.4.1 Influence of Size and Volume of Particles

Regarding the amount of reinforcement, MMCs can be divided in two main groups: high volume fraction, having over 40 vol.% of particles, and low volume fraction, having a content below this limit. The first group is composed mainly by ceramic preforms infiltrated with liquid metal, used for thermal management in electronic packaging. In this configuration, the particles are inevitably in contact with each other, resulting in a network arrangement. In the second group, however, the particles are commonly surrounded by the metallic matrix, retaining some ductility and manufacturing capacities of the original alloy. These are often used in structural and wear-resistant applications, having usually less than 30 vol.% of reinforcement phase [86].

Reinforcing particles can be nearly spherical, or possess any other geometrical form, provided that the aspect ratio between their axis length is kept close to 1. It is shown [87], theoretical and experimentally, that discontinuous reinforcements with an aspect ratio further from 1, such as whiskers and platelets, yield a stronger contribution to raise the dislocation density during strain, when compared to equiaxial particles. However, if sharp edges are present, they may contribute to the premature formation of cracks, diminishing the MMC life under creep. Furthermore, cracks can also originate within the reinforcement itself, through preexisting inner defects, or from particles that suffered damage during the plastic strain. If the damage results in acute shaped fragments, these will also act as stress concentrators, contributing to lower the creep resistance [88].

Frequently, increasing the particle size results in lower strengthening effect [87,89,90]. When testing pure aluminum reinforced with 10 to 20 vol.% SiC<sub>p</sub>, Whitehouse *et al.* (1999) observed that 10 μm sized particles improved the material creep resistance, but when using 20 μm particles the life under creep was strongly reduced. The authors attributed the early failure to a stronger tendency to cavitation when using the larger reinforcement [91]. In general, the larger the particle size, the higher the tendency to observe particle fracture in creep tests [92,93].

Other properties, such as the Young's Modulus, may also be affected by the particle size, with some MMCs being particularly prone to present a high variation in Dynamic Young's Modulus. Since the metallic matrix and the ceramic reinforcement often possess different thermal expansion coefficients (CTEs), an additional strengthening mechanism can further improve the mechanical properties of these materials. During cooling, tension-compression forces generated in the system raise the dislocations density, increasing both the hardness and the Young's Modulus (via Eshelby's stress field model, as discussed in section 2.4). Such effect is dependent on the particle size, with smaller particles producing a higher strengthening effect [94,95].

Conversely, the Young's modulus may decrease during creep plastic straining, with particle damage appointed as the cause. The larger particles are the first to suffer damage, followed by the smaller particles with increasing strain [96–98]. It is also known that cracked particles, which generate penny shaped cracks, are less detrimental to the Young's modulus than shattered particles, which produce voids [87]. The particle size, however, does not significantly affect dislocation density in the crack region, since the increase in dislocations is restricted to a very small area close to the fracture surface [99].

Regarding the volume of reinforcement, several researchers [89,92,100–102] experimenting with different combinations of matrix and particle materials, observed that in general the addition of a higher vol.% of reinforcement – up to a certain limit – will increase the stress exponent and lower the steady state creep rate. However, the longest time to rupture is typically observed with a lower vol.% of particles, with appointed values situated between 5 to 10 vol.%. Other researchers [6,90,103] also found that a volume of reinforcement higher than 30% often results in overall worse creep resistance. The result is attributed to the formation of a particle network, with the reinforcement phase not being surrounded by the matrix anymore, but instead forming large clusters (as seem in Figure 7). During creep, a more localized deformation in the clusters zone sets off the early formation of cracks, leading to failure [99]. It was also observed that the combination of higher volume and higher particle size results in the shortest creep life [103].

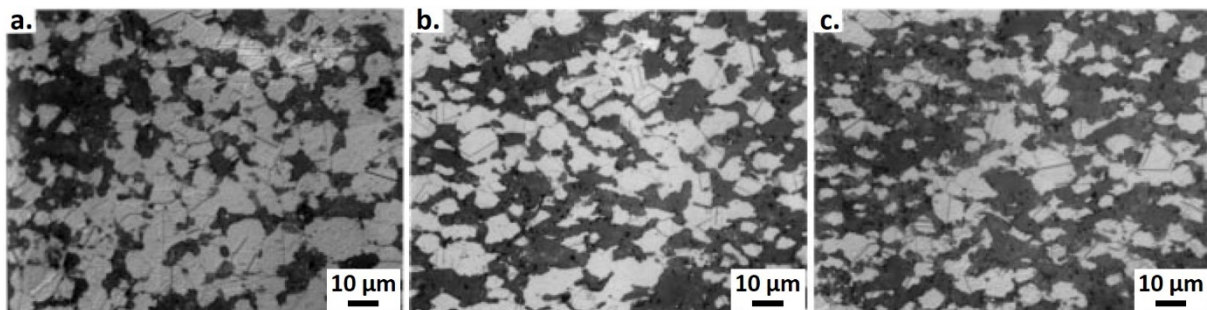


Figure 7 - Ni/Y<sub>2</sub>O<sub>3</sub> composites with a) 30, b) 40 and c) 50 vol.% of reinforcing particles, often forming large clusters. Figure adapted from Sun and Shaw (1998) [103].

The volume of reinforcement and the matrix creep resistance are parameters that significantly influence the MMC steady state creep rate, concluded Davis and Allison (1995). The authors observed that, during creep tests of 2219 aluminum alloy reinforced with 15 vol.% TiC<sub>p</sub>, a simple polynomial could be used to describe the steady state rate in the reinforced material. Furthermore, the authors observed that changes in the Young's Modulus, in the matrix or particles, would affect the initial stress distribution and initial creep rate, but not significantly impact the steady state creep rate. They determined that the strain in the first stage of creep occurs more rapidly when there is a larger ratio mismatch of the thermal expansion coefficient

between matrix and reinforcement, which can lead to an early development of defects during heating [104].

## 2.5 Creep in Ni-based superalloys

Creep can be defined as the progressive deformation of a material under a constant load. While creep may occur at lower temperatures, in alloys it is usually only significant over  $0.4 T_m$  (in Kelvin degrees). A typical creep response can be examined in strain vs. time and strain rate vs. strain plots, divided into three creep stages (Figure 8) [9,105].

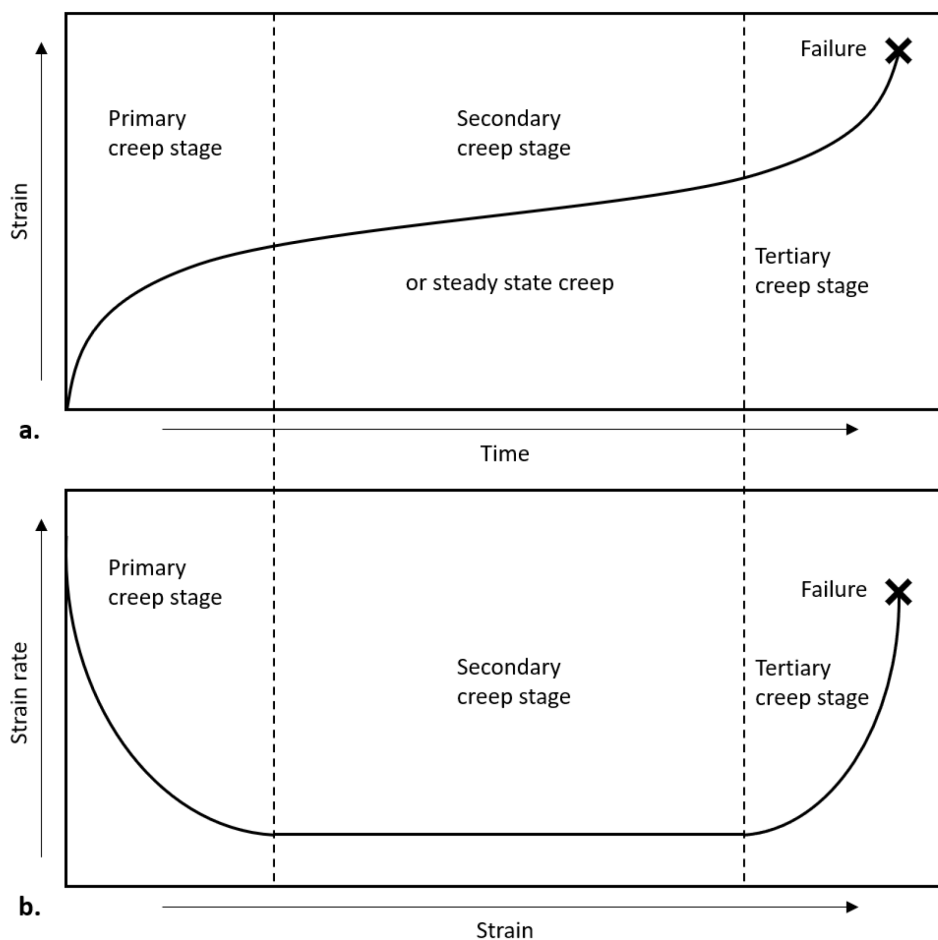


Figure 8 - Typical creep vs. time and strain rate vs. strain plots of a specimen submitted to constant tensile load and constant temperature. Figure adapted from Whitehouse [105].

The process initiates with a rapid deformation, observed during a relative short time, before it achieves a constant strain rate. During this phase, known as primary or transient creep, a stress redistribution occurs due to a microstructural unbalance [9,105,106], which is generally due to changes in the dislocation substructure [34]. It is also well documented that the initial state

of the microstructure significantly affects the transient creep, as a result from carbides precipitation or coarsening, before and during this stage. The application of a pre-straining also has strong influence in the primary creep, especially during multi-axial creep tests [107].

The secondary creep, also called steady-state creep, is considered by many the most important creep stage. During this period, there is a relative equilibrium between processes that cause hardening and softening in the material, leading to a condition where the minimum strain rate is achieved. This stage is also, in general, the longest during creep, reflecting the stationary condition observed in long-term work [105,106]. In Ni-based superalloys strengthened by intermetallics, however, the steady-state creep state is frequently replaced by a single point of minimum creep rate [34].

In the tertiary stage the deformation rate increases. The loss of creep strength at this regime is often due to a combination of causes, such as coarsening of precipitates, grain growth or recrystallization, among other possible factors [105]. Ultimately, the mechanical stability reaches a limit, triggering damage processes such as cavitation, necking and crack formation, which leads to failure. The shape of the tertiary part of the creep curve and its duration is dependent on the material composition, the temperature and the applied stress. For some alloys, the tertiary creep stage may represent the major part of the creep process [106].

Voids might also nucleate during any stage of the creep process, and their multiplication decrease the material load-bearing capacity, eventually leading to failure by coalescence of these cavities or the propagation of micro-cracks [106].

Fracture in creep is usually intergranular, and can be categorized as strain-induced, thermal-induced, and environment-induced damage. The strain-induced damage is characterized by excessive straining at constant load, grain-boundary cavitation, and multiplication of dislocation substructures. Thermal-induced damage results from the material aging processes, while the environment-induced damage develops from corrosion and oxidation by chemical attack from the surrounding medium. Whilst usually there is a dominance of one creep damage mechanism, they all might act in association and interact with each other, making the physical modelling often complex and restrict to specific material and service conditions [106].

### 2.5.1 Diffusional Creep

Also known as linear viscous creep, occurs at low stresses, or generally in situations where dislocation motion is highly inhibited. The observed creep, thus, is due only to the diffusion of matter. The dominant path for diffusion is conditional to the temperature: grain boundaries at low temperatures (Coble creep, defined in equation 3) and through the lattice at high temperatures (Nabarro-Herring creep, defined in equation 4). As a result, the stress exponent

( $n \approx 1$ ) is also low for diffusional creep. Additionally, Harper-Dorn creep also exhibits a low stress exponent, but involving the movement of dislocations inside grains [105,108–111].

$$\dot{\epsilon}_{ss} = [D_{sd}\sigma b^3]/[kTg^2] \quad (3)$$

where  $D_{sd}$  is the activation energy for self-diffusion,  $b$  is the burgers vector and  $g$  is the grain size.

$$\dot{\epsilon}_{ss} = [\alpha_3 D_{gb}\sigma b^4]/[kTg^3] \quad (4)$$

where  $D_{gb}$  is the diffusion coefficient along grain boundaries and  $\alpha_3$  is a constant.

Nabarro proposed that creep at high temperatures (close to  $T_m$ ) and low stresses in metals with very fine grains took place through the grains (from one boundary to another) [111]. This proposition was refined by Herring, that suggested that mass vacancies were produced at the grain boundaries perpendicular to the tensile axis [110]. The excess of vacancies would, therefore, diffuse through the grain until sinking on the other side. Later, Coble proposed that at lower temperatures ( $T < 0.7 T_m$ ) the grain-boundary could contribute more than the self-diffusion through the grains [34].

Diffusional creep is often connected to the formation of precipitate-denude zones. In dispersion-hardened alloys, these areas form adjacent to grain boundaries that are normal to the tensile axis, and are the result of the diffusion of atoms to the opposite grain boundary [34].

## 2.5.2 Power Law Creep

In pure metals and class M alloys, which behave similarly to pure metals under creep, the strain rate at low stresses is determined by the rate of dislocations climbing over obstacles. They may be incoherent particles in the lattice, or long range stress fields surrounding dislocations [105,112,113]. These metals experience creep through a power law relationship between steady-state creep rate and strain rate [34,108,114–116]. This relationship can be described by the equation 5:

$$\dot{\epsilon}_{ss} = A (\sigma/E)^n \cdot \exp[-Q_c/RT] \quad (5)$$

where  $\dot{\epsilon}_{ss}$  is the steady-state creep rate,  $A$  is a material constant,  $R$  is the universal gas constant (8.314 J/mol·K),  $n$  is the stress exponent and  $E$  is the Young's modulus.



A vital component to define the creep mechanism in metals is the stress exponent  $n$ , defined by Norton and Bailey [115] as a relation between the steady-state creep rate and applied stress (Equation 6), varying between 1 and 8 [34,105].

$$n = [\delta \ln \dot{\epsilon}_{ss} / \delta \ln \sigma_{ss}]_T \quad (6)$$

where  $\dot{\epsilon}_{ss}$  is the steady-state creep rate,  $\sigma_{ss}$  is the applied stress and  $T$  is the temperature.

For diffusional creep,  $n \approx 1$  is expected, while  $n \approx 3$  is common in glide-controlled creep below  $0.5 T_m$ . A  $n \approx 5$  is predicted for creep controlled by a combination of glide and climb. At low temperatures, creep controlled by core diffusion results in  $n \approx 7$ , while a control by lattice diffusion through an invariant substructure results in  $n \approx 8$  [34,105,117]. In the last case, the model considers the subgrain size as constant and independent from the applied stress, as very fine particles would be able to immobilize subgrain boundaries [118,119].

Over a wide range of strain rates and temperatures in these materials,  $n$  is constant and has a value of 5. Because of that, this behavior is also known as the “five power law” [34,120]. Nevertheless, when analyzing different Ni-based superalloys, the stress exponent during power law regime may still vary from values of 4 to 7. The apparent activation energy  $Q_{app}$  for creep in these alloys is often the same necessary for self-diffusion of the pure metal [34], and can be determined with the equation 7:

$$Q_{app} = -k[\delta(\ln \dot{\epsilon}_{ss})/\delta(1/T)]_{\sigma_{ss}/E,s} \quad (7)$$

While determining the apparent activation energy is enough for pure alloys, it is insufficient for materials strengthened by a dispersion of particles. In this case, a correction that considering the temperature dependence of the modulus and the existence of threshold stress [105,121] leads to the true creep activation energy, as defined by equation 8:

$$Q_c = Q_{app} + RT + \frac{RT^2}{G} \left( -\frac{\partial G}{\partial T} \right) (n - 1) + \frac{nRT^2}{\sigma - \sigma_{TH}} \left( -\frac{\partial \sigma}{\partial T} \right) \quad (8)$$

where  $G$  is the shear modulus,  $n$  is the true stress exponent and  $\sigma_{TH}$  is the total threshold stress.

Therefore, the power law relation can be modified [122] to account for the existence of the threshold stress, as described by equation 9:

$$\dot{\epsilon}_{ss} = A (\sigma - \sigma_{TH}/E)^n \cdot \exp[-Q_c/RT] \quad (9)$$

Within power law creep (PLC), the activation energy usually decreases as the stress exponent increases. When reducing temperature and/or raising stress, the movement of dislocations with jogs creates vacancy supersaturation, increasing  $n$  and decreasing  $Q_c$ . Because of that  $Q_c$  matches the energy necessary for self-diffusion, but dislocation climb is still the governing mechanism in PLC [34,109,113]. The climb mechanism is also observed in  $\gamma'$  strengthened Ni-based superalloys at lower regime stresses (< 500 MPa), where active matrix dislocations are not able to penetrate and cut fine and highly coherent  $\gamma'$  particles [123–125].

Creep strength increases with the Young's modulus. The normalization of the stress  $\sigma_{ss}$  by  $E$  makes possible to more accurately describe the power law creep in metals. Some opt for compensating the stress with the use of the shear modulus ( $G$ ). The change is not critical to describe phenomenological equation, but simply a common preference among several researchers [34].

### 2.5.3 Power Law Breakdown

In Ni-based superalloys strengthened by  $\gamma'$  particles, creep in the high stress regime occurs through glide of dislocations followed by shearing or bowing at the obstacles. The result is an exponential dependency of the strain rate on the applied stress [51,105]. When the  $\gamma'$  precipitates are coherent with the matrix, the dominant creep mechanism at high stress is the cutting of  $\gamma'$  particles by superdislocations [34,51,126–128].

Power law breakdown (PLB) in these alloys occurs below  $0.6 T_m$ , with an increase in  $n$  and often a decrease in  $Q_c$ . This is evidenced through the plot  $\dot{\epsilon}_{ss}$  vs.  $\sigma_{ss}$ , where the slope increases with increasing stress, thus also affecting the stress exponent. A creep equation for the PLB regime was proposed by Garofalo [129,130] with the equation 10, proposing a hyperbolic sine relationship between strain rate and stress.

$$\dot{\epsilon}_{ss} = A[\sinh(\alpha\sigma)]^n \cdot \exp[-Q_c/RT] \quad (10)$$

where  $A$  and  $\alpha$  are material constants.

In the PLB regime, smaller and highly coherent  $\gamma'$  particles are easier bypassed through cutting [127,131]. During exposure to high temperatures for prolonged periods, growth of  $\gamma'$  leads to a precipitate radius that surpasses a critical value ( $r_{critical}$ ), which is often accompanied by a loss of coherency. Ultimately, the development changes the obstacles bypass mechanism to Orowan bowing [126].

More specific creep mechanisms are also observed in certain alloys. A linear creep rate vs. stress relation is sometimes achieved at very low stresses, involving dislocation motion. This

situation is known as Harper-Dorn creep, and occurs with climb-controlled creep, while maintaining a constant density of dislocations [105].

#### 2.5.4 Negative Creep in Tension

Many hypotheses to explain the negative creep phenomena in some Ni-based superalloys were developed by several authors [132–138]. The most common accepted explanations consider changes in the precipitates volume fraction and size distribution, in addition to the relief of internal stresses in the matrix. A definitive answer is, however, not yet reached in consensus between researchers in the field. The phenomena manifest itself as a negative strain rate, or serration, under relatively low, unidirectional stress. It is more pronounced in the early stages of creep, and ceases above recrystallization temperature.

Negative strain-rate during tensile creep testing was studied by Timmings *et al.* (1986) on a Nimonic 90 superalloy. It was observed a volumetric contraction under low stress testing, due presumably by changes in the  $\gamma'$  fraction. This effect would apply to superalloys with a large positive misfit ( $\alpha_{\gamma'} > \alpha_{\gamma}$ ), when heated above its final aging temperature [135,138]. Stevens and Flewitt (1979) observed that an IN-738, after aging treatment at 603 °C for 16 h, presented a bimodal distribution of  $\gamma'$  precipitates (0,05 and 0,5  $\mu\text{m}$  in diameter). Further aging treatments, at 550 and 606 °C, showed a coarsening of the larger particles (cuboidal shaped), at the expense of the smaller precipitates (spherical shaped). The study showed that the time of disappearance of the smaller  $\gamma'$  particles matches a significant reduction of serrations and creep resistance [139].

Changes in hardness and electrical resistivity are also indicators of a secondary phase precipitation or dissolution, which may also cause volumetric changes. Lang *et al.* (1989) investigated an Inconel X-750 alloy, aged at 700 °C for 40 h, observing a complex composition of ordering, precipitation and recrystallization affecting the material hardness and electrical resistivity. After further isothermal heat treatment, a sharp decay in hardness was observed for temperatures above 700 °C, corresponding to a reduction of the smaller  $\gamma'$  precipitates fraction. The electrical resistivity also varied, but a strong reduction on conduction was only observed with further growth of the larger  $\gamma'$  particles, matching the depletion of solute elements in the matrix [140,141].

Sondhi *et al.* (2004) proposed, for an IN-100 – a  $\gamma'$  strengthened superalloy – the existence of an internal stress field in the non-aged alloy, that would cause a volumetric mismatch between matrix and coherent precipitates particles. It is known that geometrical changes under constant load decrease the stress in creep compression, but increase it in a tension creep test. An isothermal aging test, without any applied stress, may be performed to measure the shrinkage of a specimen over long periods at high temperature. The shrinkage displacement differences

measured during compressive and tensile creep tests can be, by this method, considered twice the amount of linear shrinkage. The observed difference was, however, far greater than expected by the authors, thus accounting for a dependence between creep and shrinkage phenomena [135].

The coherency stresses at  $\gamma/\gamma'$  interface vary for alloys with negative ( $a_{\gamma'} < a_{\gamma}$ ) and positive misfits ( $a_{\gamma'} > a_{\gamma}$ ), as illustrated in Figure 9. The internal stress field model proposed accounts for the presence of a compressive stress within the matrix, and a tensile stress within  $\gamma'$  particles. In this case the lattice parameter of the  $\gamma'$  particle is smaller than the matrix, so the lattice distortion generates a compressive stress in the matrix. The authors also observed that the stress can be relieved by a long aging treatment, after obtaining an almost complete internal stress relief in the alloy after 600 h of aging at 704 °C. However, it was also observed a strong coarsening of  $\gamma'$  particles – 70 to 80% – during the process, which could also account for the loss in creep resistance under tension. It is speculated that a dissolution of the smallest  $\gamma'$  could also contribute to the observed reduction in the creep resistance [135].

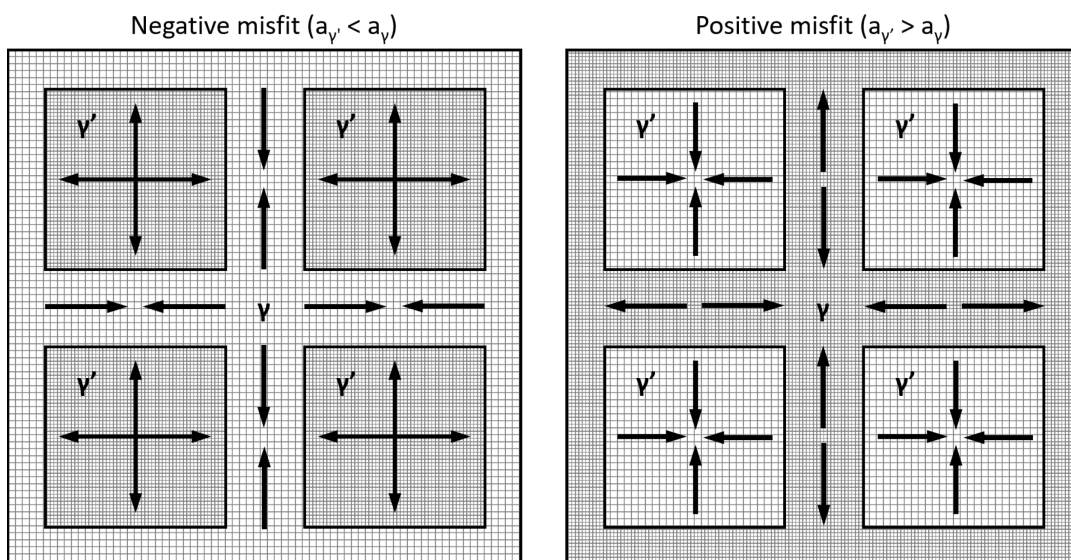


Figure 9 – Representation of coherency stresses at  $\gamma/\gamma'$  interface in Ni-based superalloys with negative and positive misfits, respectively. Figure after Kuhn *et al.* [142].

### 2.5.6 Creep of Inconel X-750

Generally the Inconel X-750 presents a creep strain vs. time behavior similar to several other  $\gamma'$  reinforced alloys (Figure 10). But also similarly to many variants, it exhibits an anomalous yield stress when deformed at high temperatures. When increasing the temperature, up to approximately  $0.6 T_m$ , the flow stress also increases. When studying  $L1_2$  ordered alloys, such as the  $Ni_3Al$  phase ( $\gamma'$ ), Kear and Wilsdorf (1962) observed the presence of long screw dislocations

gliding on {111} locked by cross slip on to {100}. Instead of strain aging or precipitation hardening, the increase in the flow stress could then be explained by a mechanism known as Kear-Wiltsdorf lock (Figure 11), which can be summarized as the locking of screw dislocations by thermally activated cross-slip [111,113,143–145].

While initially it was believed that the flow stress anomaly derived only from the mechanism of Kear-Wiltsdorf lock in the  $\text{Ni}_3\text{Al}$  phase ( $\gamma'$ ), further studies showed that structural changes also played a significant role in the abnormality. Between 700 and 1100 °C, part of the  $\text{L}_{12}$  structure go through a transformation, experiencing a tetragonal distortion of the parent  $\text{L}_{12}$  lattice. This leads to the development of internal stresses, increasing the drag resistance for the motion of dislocations. Both modified and original  $\text{L}_{12}$  structure co-exist in this temperature range, and the higher the amount of the distorted phase, the higher the anomalous strengthening effect [146].

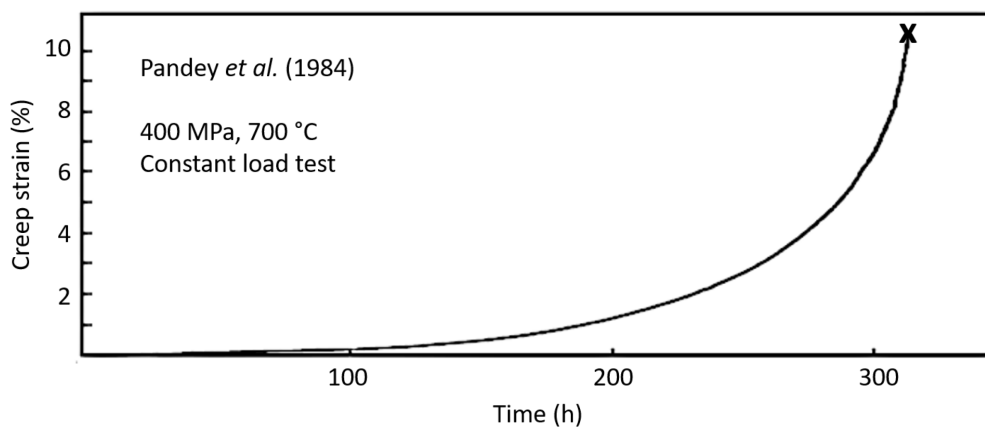


Figure 10 - Typical creep strain vs. time plot of an Inconel X-750 superalloy. Figure adapted from Pandey *et al.* [147].

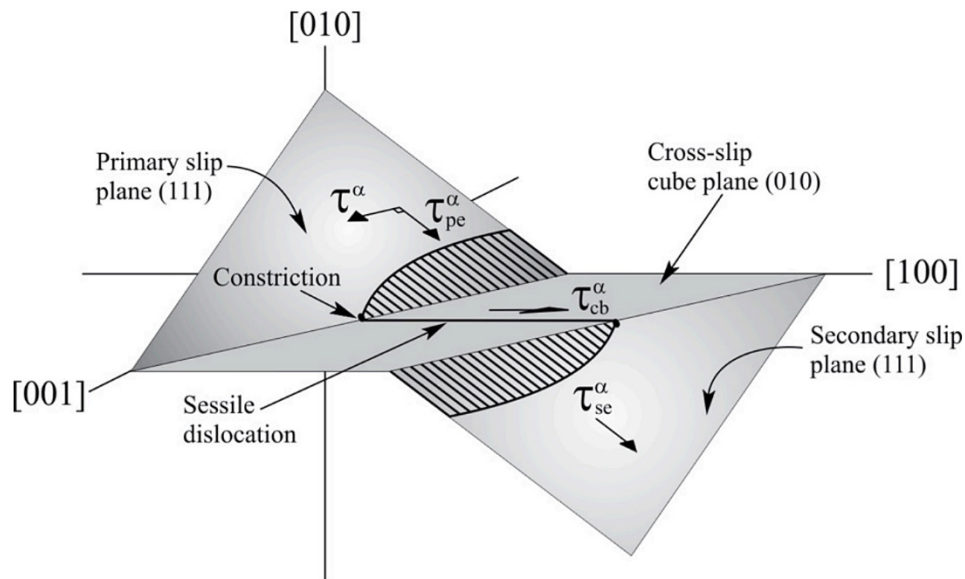


Figure 11 - 3D schematics of a Kear-Wilksdorf lock, commonly observed in  $\gamma'$ -strengthened Ni-based superalloys such as the Inconel X-750. Figure from Keshavarz *et al.* [145], license [CC BY 4.0](https://creativecommons.org/licenses/by/4.0/).

Other singular features are also observed in the creep of X-750. Unusually high values of stress exponent and activation energy observed in  $\gamma/\gamma'$  alloys, regardless of possessing grain boundaries or not, have been explained by Tien *et al.* (1972). It is proposed that during steady-state creep, a very fine mesh of dislocations forms around the  $\gamma'$  particles, generating an excess of jogs on the mobile dislocations and depleting the area of vacancies. This leads the creep rate to be controlled by higher energy processes, involving interstitials. In an opposite manner, if the dislocations mesh near  $\gamma'$  particles is coarse or absent, the vacancy diffusion will control the motion of jogs, and thus of creep [113,148].

To determine which mechanism is controlling the creep in  $\gamma'$  strengthened Ni-based superalloys, it is necessary to consider the precipitate fraction, size and morphology. At high stress regime, if the interparticle distance is small,  $\gamma'$  is more likely be cut by dislocations. At large particle spacing, however, the dislocations bypass  $\gamma'$  through looping or climb mechanisms [51,109,113]. The transition between the creep modes is also dependent on the deformation rate and temperature, as well as the APB and fault energy of  $\gamma'$ , the coherency strains and the solute diffusivity in both  $\gamma$  and  $\gamma'$  [33,51]. Furthermore, it is necessary to consider that in alloys such as the Inconel X-750 a bimodal size distribution of  $\gamma'$  particles is present, each one affecting the flow of dislocations differently [149].

The secondary  $\gamma'$  particles play an important role at creep onset. Fine  $\gamma'$  precipitates act by pinning dislocation lines, thus significantly contributing to the alloy creep resistance. However, during creep evolution the multimodal system is disrupted, and the larger primary  $\gamma'$  particles become the major responsible for immobilizing dislocations. A loss in the creep resistance is also expected, as the inter-particle distance increases. At 700 °C, the dissolution process of secondary  $\gamma'$  at low stresses can take thousands of hours, but at 800 °C only tens of hours are necessary for

their elimination. It is believed that at these high temperatures in the low stress regime the dominating creep mechanism is the particle bypass via dislocation climb-glide. At higher stresses, particle shearing takes over as controlling creep mechanism [51,113,123,124,149,150].

Another role often played by the secondary  $\gamma'$  particles during creep leads to the development of an apparent threshold stress,  $\sigma_{TH}$ . When the applied stress decreases to a value close to the threshold, the strain rates decline strongly, and creep by dislocation motion ceases. The threshold stress possesses a correlation with the Orowan stress, which is also valid when considering the resistance to climb [109,151]. In superalloys strengthened by highly coherent nanoscale intermetallics, it is observed that the dislocations surpass the particles by local climb at low stress regime, with the amount of precipitates and their distribution in the matrix strongly affecting the threshold stress [51,113,126]. In superalloys strengthened by  $\gamma'$  and  $\gamma''$  particles the threshold stress can be higher than  $0.6 \times \sigma_a$ , where  $\sigma_a$  is the applied stress, at temperatures around 700 °C. When in the power law regime, the threshold stress is proportional to the applied stress. Additionally, it decreases with increasing temperature, which is attributed to a temperature dependence of the shear modulus [113,152].

It is also important to consider the influence of grain size to define the governing creep mechanism [153,154]. In age-hardened Inconel X-750, grain sizes between 100 and 200  $\mu\text{m}$  in diameter are common. When specimens are submitted to creep tests at 700 °C with stresses around 500 MPa, a dislocation-climb mechanism operates to surpass the  $\gamma'$  particles. However, when producing the same material with a significant smaller grain size, the dominant deformation mechanism at the same conditions changes to grain-boundary sliding. That is evidenced through a decrease in the stress exponent, from values between 5 and 6 in the alloy with grain sizes around 100 to 200  $\mu\text{m}$ , to values below 3 in the alloy with grains smaller than 10  $\mu\text{m}$  [112].

### 2.5.7 Creep of Particle Reinforced MMCs

A ceramic particulate reinforced metal will often present, relative to the non-reinforced material, higher stiffness and reduced thermal expansion. Additionally, many systems also present high isotropic behavior, when compared to alloys reinforced with fibers. Within a certain range, variations on the particulate size and their fraction allow the obtainment of application-tailored properties. For instance, the creep resistance may be enhanced with the addition of a small fraction of reinforcement (as seem in the example of Figure 12), whereas a substantial gain in stiffness or reduction in thermal expansion can be achieved with a higher amount of particulate added to the alloy [86,89,91,100,101,155,156].

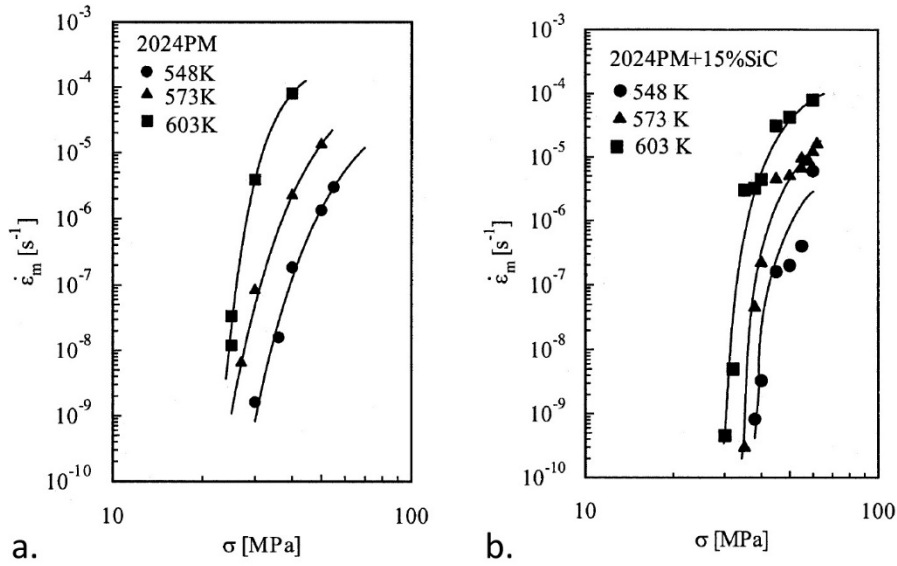


Figure 12 - Minimum creep strain rate vs. stress curves showing the creep resistance of an Al 2024 alloy at different temperatures, with a) the non-reinforced material and b) after the introduction of 15 vol.% SiC particles. Figure adapted from Spigarelli *et al.* (2001) [157].

Frequently a confusion between particle reinforced MMCs and dispersion or precipitation strengthened materials occurs. While in the former the main strengthening mechanism is the load transfer from the matrix to the reinforcement, in the latter the strengthening results essentially from impeding dislocations mechanisms, such as the Orowan bowing stress [158,159] and dislocation climb [101]. Dispersion strengthened metals [160] also often experience unusual high values of stress exponent ( $n$ ) and creep activation energy ( $Q_c$ ), better explained by the concept of a threshold stress ( $\sigma_{TH}$ ). The existence of such stress may be attributed to: i) Orowan bowing between particles; or ii) the presence of a back-stress associated with dislocation climb; or iii) attractive forces between particles and dislocations, near the reinforcement/matrix interface. However, in many MMCs the load transferred to the reinforcement mitigates the shear stress on dislocations in the matrix, lowering it to a point below the required for Orowan bowing. During creep, MMCs may present higher values of stress exponent – when compared to the non-reinforced metal – but they can be partly explained by the mechanism of load transfer to the reinforcement, and not solely by the threshold stress attributable to the immobilization of dislocations. The total threshold stress, therefore, can be obtained by the sum of two components, as indicated in the equation 11 [80,93].

$$\sigma_{TH}^{MMC} = \sigma_{TH}^{LT} + \sigma_{TH}^{[\gamma+\gamma'] matrix} \quad (11)$$

where  $\sigma_{TH}^{MMC}$  is the total threshold stress measured,  $\sigma_{TH}^{LT}$  is the load transfer component and  $\sigma_{TH}^{[\gamma+\gamma'] matrix}$  is the threshold stress resulting from dislocations obstructed by  $\gamma'$  precipitates.



The concept of two sources for the measured threshold stress was also investigated by other authors. Despite the different mechanisms governing the strengthening of particle reinforced MMCs and dispersion strengthened metals, Park *et al.* (1990) proposed that MMCs produced by conventional powder metallurgy route could present a hybrid strengthening system. The idea is that small particles serve as barriers to dislocation motion, giving origin to a threshold stress for creep. When experimenting with a 30 vol.% SiC<sub>p</sub> reinforced 6061 Al alloy, they observed that the SiC particles alone would not be capable to account for the obtained threshold stress, and that fine incoherent oxide particles present in the matrix would likely to serve as dislocation barriers [161]. The same conclusion was achieved by Lin and Mohamed (2012), when a 15 vol.% SiC<sub>p</sub>-2009 MMC presented higher than expected stress exponent and activation energy. The authors identified the presence of ultra-fine particles, originated from particle cracking during the hot press processing, as the cause for the additional threshold stress measured [162].

The true threshold stress in materials that follow a five-power law creep, such as many composites, can be obtained by plotting the strain rate vs. the stress and applying a power fitting. The extrapolation of the curve towards a very low creep rate (close to 1E-10 or 1E-11, in many instances) will lead to near-flat lines, converging on the true threshold stress. If the extrapolation takes place over no more than two orders of magnitude, the method [163,164] is adequate to estimate  $\sigma_{TH}$  in these materials. Examples of the method application are shown in Figure 13.

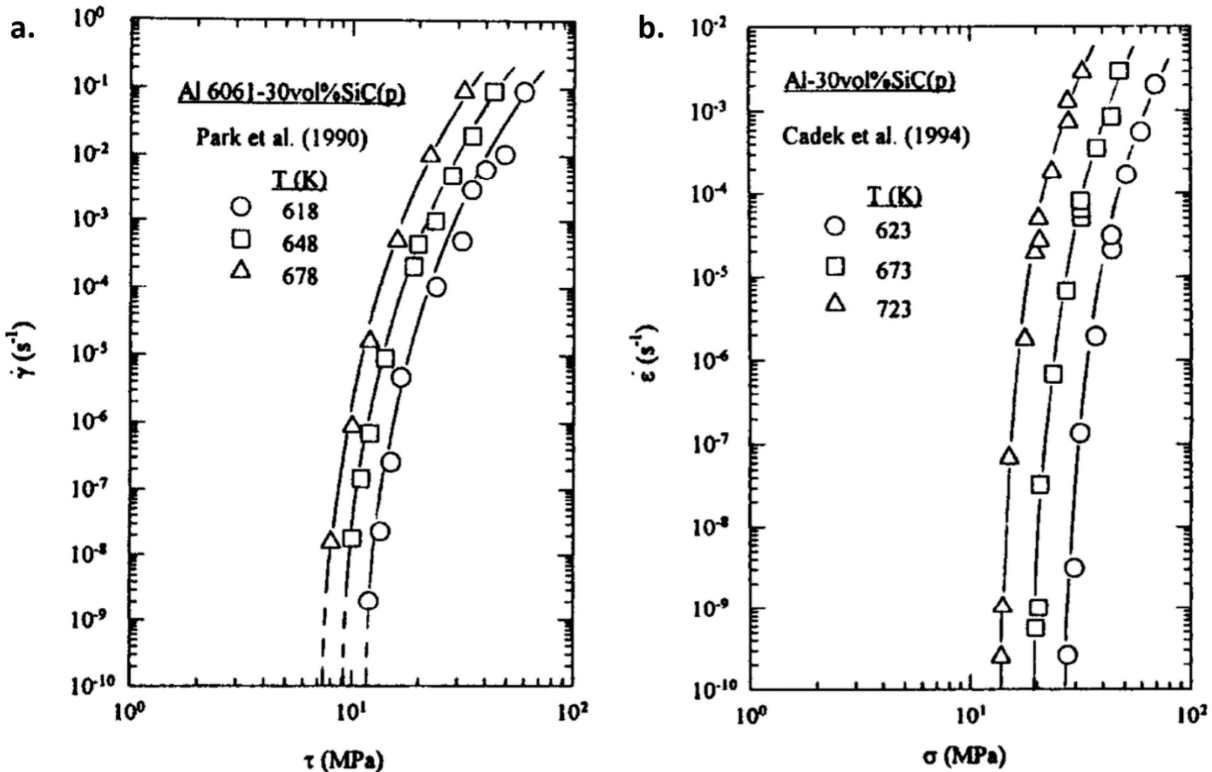


Figure 13 - Determination of the true threshold stress by Li and Langdon method [164], with plots of strain rate vs. stress leading to near-flat lines at  $\dot{\epsilon} = 10^{-10} \text{ s}^{-1}$ , using other authors data [161,165]. Figure from Li and Landon [164].

The tensile behavior of particle reinforced MMCs also differs from the non-reinforced metals in many aspects. In MMCs microplasticity occurs at a relative lower stress, especially when using a low volume of reinforcement. Contrary to most unreinforced metal alloys, they do not present an abrupt transition from the elastic to the plastic stage in the stress-strain curves. Instead, a smooth transition is observed and followed by state of work-hardening saturation, with the matrix evolving to accommodate further strain. This leads to the nucleation and expansion of voids, culminating with the propagation of cracks and the material failure [4,87]. Additionally, the presence of rigid reinforcing particles often impairs the grain boundaries ductility, which may decrease strain before rupture in MMCs with a high reinforcement content. The effect can be observed in the work of Hui *et al.* (2000) with a Fe-Cr-Ni alloy [101], where an increase in the amount of TiC particles remarkably affected the ductility in creep tests (Figure 14).

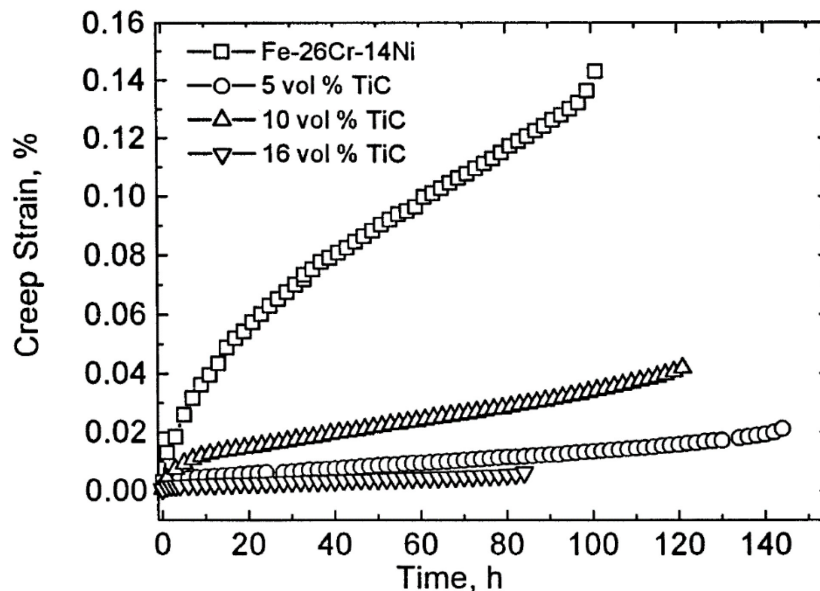


Figure 14 - Creep strain vs. time curves from a Fe-Cr-Ni alloy with different amounts of TiC particles. Figure from Hui *et al.* [101].

Not only the fraction of reinforcing particles affect the creep parameters, but also their size. The apparent creep exponent often increases when reducing the particle size, as shown by Tjong and Ma [166] when investigating the creep parameters of Al-2618/SiC<sub>p</sub> composites. The outcome is attributed to the existence of a threshold stress, that is frequently associated with small reinforcing particles distributed in the matrix, which offset the apparent creep exponent to higher values [87,89–91].

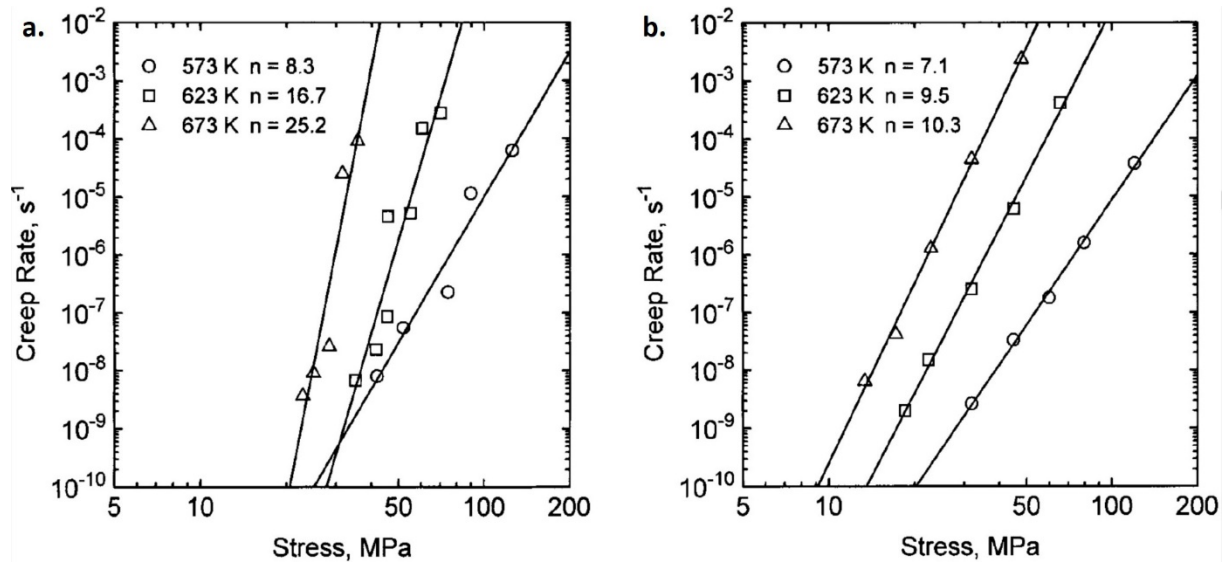


Figure 15 - Steady-state creep rate vs. stress plots from Al-2618/SiC<sub>p</sub> composites with 15 vol.% of reinforcing particles measuring a) 3.5  $\mu\text{m}$  and b) 10  $\mu\text{m}$ , showing their size effect on the apparent creep exponents. Tests conducted between 300 and 400 °C. Figure from Tjong and Ma [166].

### 3. Materials and Methods

The materials investigated were divided in reference alloys (non-reinforced variants) and composites produced (through different routes), for comparison purposes.

#### 3.1 Reference materials

As references, two Inconel X-750 non-reinforced alloys were used in selected examinations. The first non-reinforced alloy consisted of a commercial, hot-rolled variety (composition in Table 2), provided in the form of round bars with a diameter of 10 mm.

Table 2 - Chemical composition (wt.%) of Inconel X-750 hot-rolled.

Element	Cr	Fe	Ti	Nb	Al	Si	Mn	Co	C	Cu	S	Ni
Wt.%	15.5	7.0	2.5	1.0	0.7	0.5	0.1	0.02	0.04	0.01	0.003	Bal.

The second reference material was produced through a powder metallurgy route, using a commercial powder of Inconel X-750 (composition in Table 3) atomized under Argon atmosphere, resulting in particles with an average diameter of  $D_{80} = 22 \mu\text{m}$ . The particle size was measured with laser diffraction analysis, using a Malvern 2000 instrument. The powder was submitted to a high energy milling (HEM) process, conducted in a planetary mill Pulverisette 6 with Fe-Cr-Ni balls. The process was handled under Argon atmosphere for several hours, with breaks to keep the powder under 60 °C.

Table 3 - Chemical composition (wt.%) of Inconel X-750 powder.

Element	Cr	Fe	Ti	Nb	Al	Si	Mn	Co	C	Cu	S	Ni
Wt.%	15.3	6.5	2.7	1.1	0.7	0.2	0.1	0.03	0.02	0.01	0.003	Bal.

A high energy milling (HEM) process can be described as a mill process where the constant collisions between the powders and the grinding balls are strong enough to generate cold welding. The powder clusters are subsequently broken again into fragments, often resulting in particles with smaller size in comparison to their initial state. During the process, the likelihood of reactions between the different powders involved increase, and stresses are induced in the ensuing particles [70,167].

After the milling process, the powder of the second reference material was consolidated by spark plasma sintering with an FCT Type HP D/HHP D system (Figure 16), using a cylindrical mold with a diameter of 30 mm. A pressure force of 50 kN and a current of 5500 A were utilized, aiming at a sintering temperature of 1250 °C, measured at the sample die.

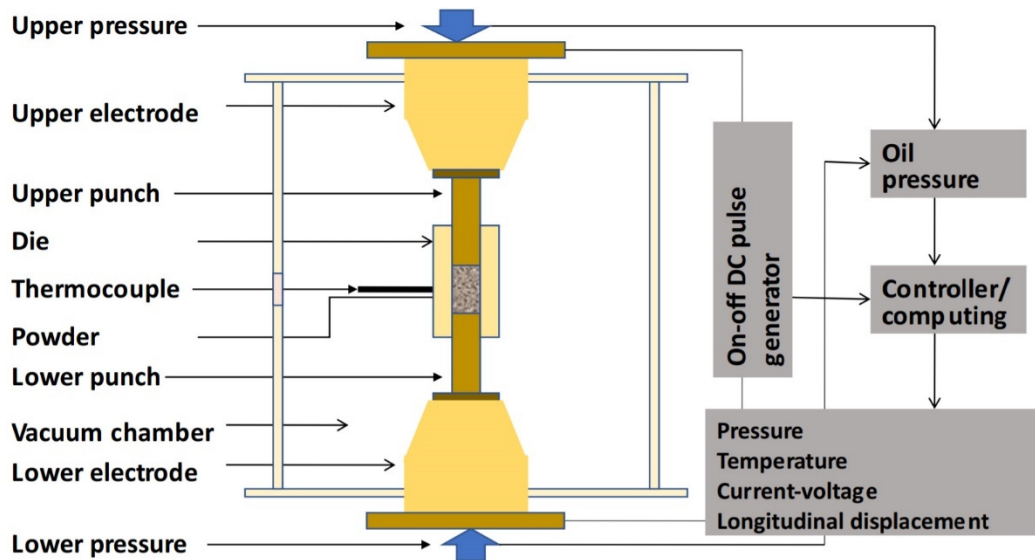


Figure 16 – Schematic of spark plasma sintering system FCT Type HP D/HHP D. Figure from Ogunbiyi *et al.* [75].

Both non-reinforced variants obtained, respectively still in the form of bars and plate, were submitted to a triple heat-treatment (Figure 17) without the use of special atmosphere or vacuum. An initial solution step was applied to dissolve  $\gamma'$  and  $M_{23}C_6$  precipitates, followed by a stabilization treatment to reduce levels of Nb and Ti in solution. Lastly, an aging step was performed to promote the precipitation of  $\gamma'$  and  $M_{23}C_6$ .

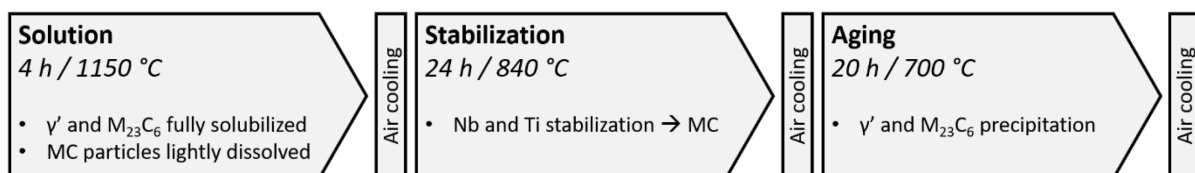


Figure 17 - Triple heat-treatment applied to all investigated materials, without atmosphere control.

The final forms of both variants were achieved through distinct processes. The round bards from the hot-rolled variety were machined via CNC turning lathe into the final geometry for creep tests (Figure 21), while the pressure sintered variety resulted in a rectangular block, that was cut

into smaller cubes with  $l = 2.5 \text{ mm}$  subsequently. This variant was utilized exclusively in isothermal treatment studies, and not in creep tests.

### 3.2 Composites produced

Two metal matrix composites were fabricated via powder metallurgy routes, both holding the combination of 85 wt.% Inconel X-750 as matrix material, and 15 vol.% TiC particles ( $\text{TiC}_p$ ) as reinforcing phase. The first composite was manufactured by mixing the powders of non-reinforced Inconel X-750 with titanium carbides, using a Turbula T2F mixer for 15 minutes. This process was denominated “Low Energy Mixing” (LEM), for further reference. The original TiC particles presented a trimodal distribution (Figure 18), with average sizes of 0.3, 1.1 and 3.1  $\mu\text{m}$ . The overall diameter was adopted as  $d_{80} = 2.7 \mu\text{m}$ , for a cumulative percentile of 80% of the total number of particles.

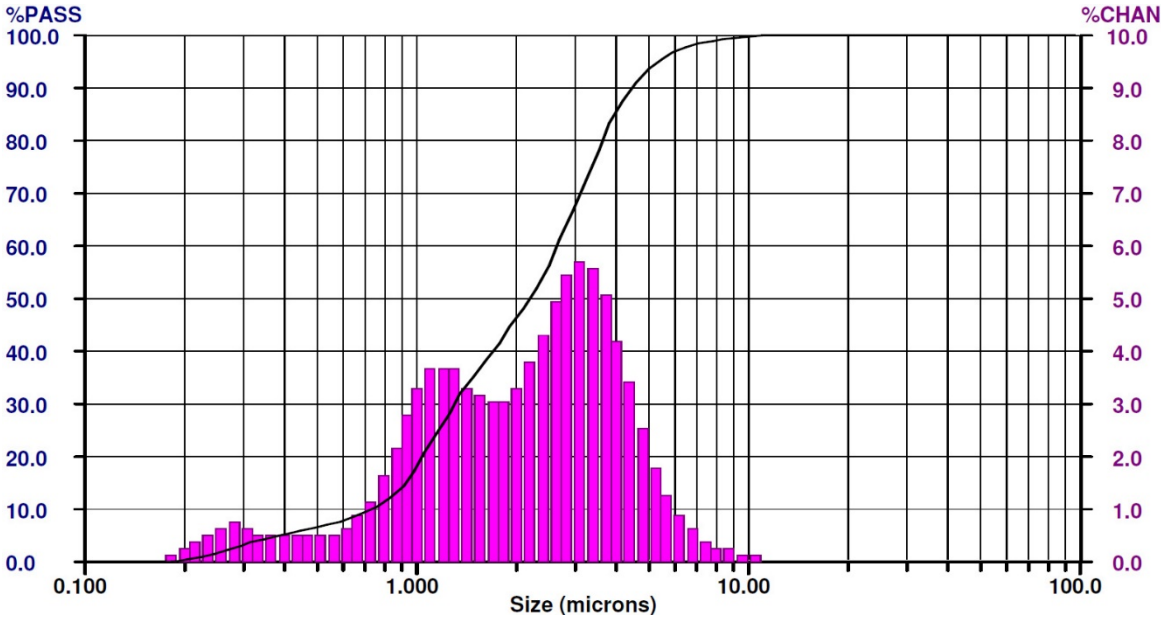


Figure 18 - Particle-size distribution of original  $\text{TiC}_p$  powder. %PASS is the cumulative percentile, indicated by the black line. %CHAN refers to the distinct percentile of each column, in magenta.

After the mixing step, the mixed powders of the first composite were laid in a rectangular mold and submitted to uniaxial pressure sintering under vacuum, at 1523 K (1250 °C) and 35 MPa for 1 h. The resulting plate (Figure 19) achieved the calculated complete densification of 7.8  $\text{g}/\text{cm}^3$ .

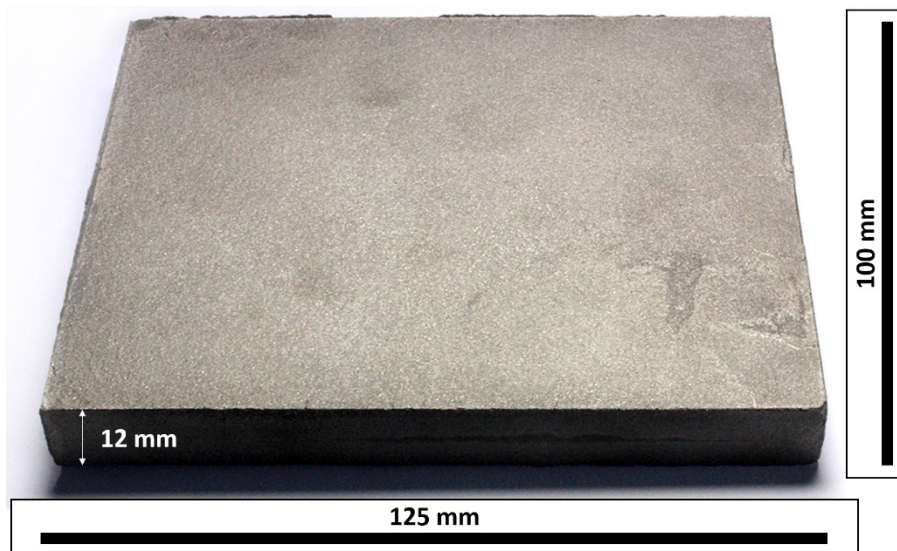


Figure 19 – First composite plate, produced by low energy mixing and uniaxial pressure sintering.

The second composite was prepared with a high energy ball milling process, using the same parameters utilized to produce the second non-reinforced material. Powders of both Inconel X-750 and TiC were milled together, and submitted subsequently to spark plasma sintering, following again the parameters used to produce the reference material (the final  $\text{TiC}_p$  size distribution was evaluated in the section 0). The resulting specimen (Figure 20) density was measured at  $7.7 \text{ g/cm}^3$ , reaching 99% of the calculated expected value ( $7.78 \text{ g/cm}^3$ ).

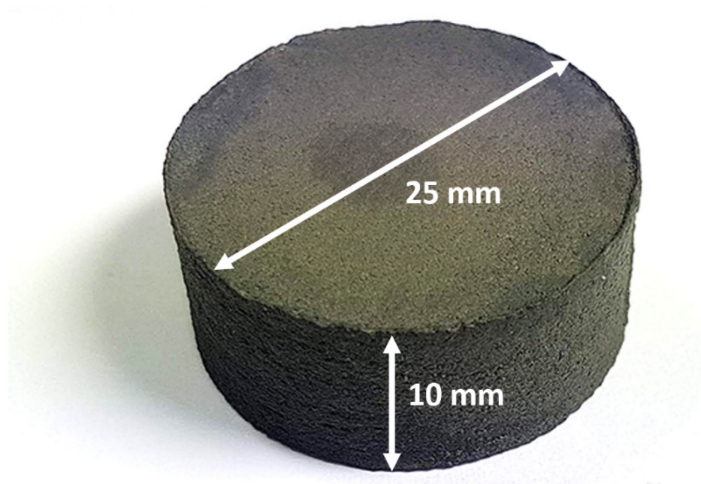


Figure 20 – Second composite plate, produced by high energy milling and spark plasma sintering.

The resulting plates were submitted to the same heat-treatment applied to the non-reinforced variants, followed by different machining processes. The first composite (produced by press sintering) was machined via CNC turning lathe, while the second one (produced by spark

plasma sintering) was finished via electrical discharge machining (spark erosion). In both cases long cylinders with a diameter of 5 mm were obtained, and subsequently cut at a length of 7.5 mm to produce compression creep specimens. In addition, from the first composite were also obtained specimens for tensile creep tests, following the dimensions shown in Figure 21. All produced materials and their respective codes used in this work are summarized in Table 4.

Table 4 - Summary of all materials investigated, along with their respective processing routes.

Material	Powder Comminution	Production Method
<b>Inconel X-750 non-reinforced</b>	—	Hot rolling (commercial ref.)
<b>Inconel X-750/TiC<sub>p</sub> 15 vol.%</b>	Low Energy Mixing ( <b>LEM</b> )	Pressure Sintering ( <b>PS</b> )
<b>Inconel X-750 non-reinforced</b>	High Energy Milling ( <b>HEM</b> )	Spark Plasma Sintering ( <b>SPS</b> )
<b>Inconel X-750/TiC<sub>p</sub> 15 vol.%</b>	High Energy Milling ( <b>HEM</b> )	Spark Plasma Sintering ( <b>SPS</b> )

### 3.3 Microstructure Analysis

Materials submitted to light and electron microscopy, as well as to X-ray diffraction (XRD), were beforehand embedded in Bakelite Struers Multifast Black at 180 °C. Subsequently, these specimens were grinded in a Struers Tegramin-25 equipment, using the following sequence of discs and lubricants: Piano 220 (water), Allegro 9 μm (DP-Lubricant blue), Mol 3 μm (DP-Lubricant blue) and Chem polishing (OP-S). Between each grinding step and after polishing, the specimens were cleaned with a mixture of deionized water and a short sprinkle of ethanol in an ultrasonic cleaning device, for 60 s. After the last step the specimens were dried out with cotton pads under a stream of hot air.

For specimens submitted to light and electron microscopy, except those destined to Electron Backscatter Diffraction (EBSD) analysis, the surface was etched with a mixture devised to reveal γ' particles. The solution was composed by 60 ml HCl, 1 g Molybdc acid (85%), 15 ml distilled water, 15 ml HNO<sub>3</sub> (65%) and 5 drops of neutral dish soap. The etching was performed with immersion in the solution for 20 s, and the samples were washed immediately afterwards with deionized water.

Light microscopy (LM) was conducted using a Leica DM-LM device coupled to a camera Axiocam 305. The images were taken with the aid of the software ZEN 2 Core, with magnifications from 50 to 1000 times. Specimens for scanning electron microscopy (SEM) received a gold layer (except those destined to EBSD analysis), deposited with the device Edwards Scancoat 6, using vacuum of  $8 \times 10^{-1}$  mbar and a sputtering current of 30 mA, for 90 s. SEM investigation was then carried out on both microscopes LEO 1430 and Zeiss Sigma 300, using accelerating voltages between 5 and 15 keV, with beam diameter varying between 150 and 500 nm. Topographic images



were obtained with a normal SE detector in the Leo device and an in-lens detector in the Zeiss instrument.

Additional SEM investigations were carried out. Energy-dispersive X-ray spectroscopy (EDS) was performed with a Bruker x-Flash 6130 module, while EBSD analysis was conducted with a Bruker e-Flash HR+ detector. For the EBSD analysis a vibratory polishing preparation was employed, with the device ATM Saphir Vibro and the solution Eposil M-11. The polishing was conducted for times between 6 h (composites) and 12 h (reference materials), using a frequency of 90 Hz and intensity of 80%. The EBSD analysis was carried out with an acceleration voltage of 20 kV, work distance of 20 mm and pixel size of 0.16  $\mu\text{m}$ .

The size of grains,  $\gamma'$  precipitates and other microstructural features was measured with the aid of the software ImageJ. The average grain size was obtained after 100 observations from SEM-SE images, comprised by 50 linear measurements in the same axis and 50 linear measurements with 90° to the chosen axis. Average  $\gamma'$  size was determined after 60 linear measurements in the same axis. Whenever possible, the measurements were taken from several different grains in a central region of each specimen. Confidence intervals were calculated for a significance value ( $\alpha$ ) of 0.05.

Further observation of nanostructures was conducted with the aid of transmission electron microscopy (TEM), coupled with a module for selected area electron diffraction (SAED). For the analysis the samples were prepared according to Williams and Carter [168] method. Discs with 10 mm in diameter and 500  $\mu\text{m}$  of thickness were extracted from the material using a low speed diamond saw, and grinded with SiC papers of 300, 600, 800 and 1200 mesh, until a thickness of 100  $\mu\text{m}$  was reached. A polishing step was carried out afterwards using  $\text{Al}_2\text{O}_3$  of 1.0 and 0.3  $\mu\text{m}$  of size, in order to produce a smooth surface. From each specimen smaller discs were cut, with 3 mm in diameter. Subsequently, the samples were electro etched with a solution of  $\text{HNO}_3$  -  $\text{CH}_3\text{OH}$  electrolyte on Struers TENUPOL-5 device, using 3 V for 50 s. The discs were immediately cleaned after the procedure with immersion in a sequence of  $\text{CH}_3\text{OH}$  and  $\text{C}_2\text{H}_6\text{OH}$  solutions, respectively. The TEM analysis was carried out with a JEOL JEM-1011 device, using a Tungsten filament and an electron acceleration of 100 kV.

Phases were also characterized with X-ray diffraction (XRD) using a Panalytical Empyrean device using three different arrangements: mirror, lens and Bragg-Brentano setups. All investigations were conducted using a Cobalt anode as X-rays emitter, and an Iron filter before the detector. Resulting diffractograms were analyzed with the software Highscore Plus 4.5, using three databases for the qualitative investigation: ICSD FIZ 2016-1, COD 2016 Conv 45 and PDF-2 Release 2004. Quantitative analysis was carried out with Rietveld fitting using the same software, but in conjunction solely with the ICSD FIZ 2016-1 database. Due to overlapping of the diffraction peaks of  $\text{Cr}_{23}\text{C}_6$ , this phase was not characterized with XRD. In view of that, the results from Rietveld analysis are to be considered an approximation, as the fraction of chromium carbides is

not accounted for. Likewise, larger grain sizes are expected to impact the refinement quality, due to the restricted amount of different orientations in the analyzed area. Literature guidelines [169–171] were followed to ensure a suitable fitting in the given conditions.

### 3.4 Mechanical Analysis

The composites produced and their non-reinforced references were tested for creep resistance, and had their hardness measured. Additionally, to obtain the elastic modulus ( $E$ ) a nanoindentation device was used. The test settings and equipment used in the mechanical analysis are subsequently detailed.

#### 3.4.1 Creep tests

Creep tests were conducted with both tensile and compression setups following the ASTM E139-11 standard. For tensile tests, the specimens were machined following a modified ASTM E8M-13 standard to obtain sub-sized variants (Figure 21). Compression creep tests on all materials were conducted on cylinders with 5,0 x 7,5 mm (diameter x height), obtained by machining in the case of hot-rolled or pressure sintered variants, and by electrical discharge machining (wire erosion) in the case of materials produced by spark plasma sintering.

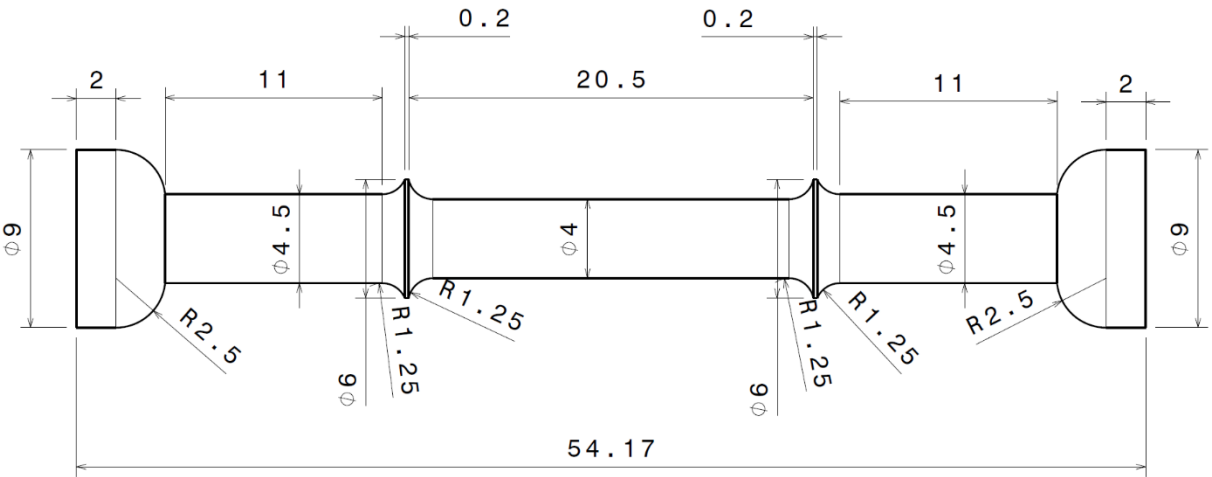


Figure 21 - Drawing of the tensile creep specimens produced in the CNC turning lathe, with measure values in mm.

Two materials were submitted to tensile creep tests: Inconel X-750 hot rolled (reference) and the composite X-750/TiC 15 vol.% prepared by LEM + PS route, following processing codes described in Table 4. The temperature range was defined as 700 to 800 °C, and the stress as 215 to 440 MPa. Compression creep tests were conducted in the same materials, with the addition of the composite X-750/TiC 15 vol.% prepared by HEM + SPS route. The same temperature range was utilized, and the stress range defined as 200 to 500 MPa.

Specimens from compression creep tests destined to microstructure analysis were tested with a stress of 280 MPa, and the tests were interrupted after 4 to 6 percent of creep strain. The remaining specimens had their tests terminated after 0.3 to 33 percent of creep strain, after the secondary creep regime was clearly identifiable.

For both tensile and compression setups, a Denison Mayes TC-50 machine working with the principle of constant load was used. For heating, a vertical tubular furnace Reetz with triple zone and proportional–integral–derivative (PID) controller (Eurotherm 2116) was employed. The temperature was measured in three points, at the upper, middle and lower parts of the specimen submitted to deformation, using type K thermocouples. The maximum variation from the target-temperatures was limited to  $\pm 1$  °C.

Tensile creep tests were conducted using a setup with contact clamps and two vertical-mounted inductive extensometers. The signal was further acquired with a National Instruments DAQ System, and processed with the software NI LabVIEW 2016. The compression creep tests were conducted using only one extensometer, model Heidenhain 1288, attached to an ATS compression device, model 4057. The signal was acquired with a module Heidenhain EIB 741 and processed with the software NI LabVIEW 2016.

The resulting data was manipulated with the software Origin 2019. The initial movement of the extensometer, before the total load was released on the load plate, was disregarded. Deformation and time data were submitted to a reduction to evenly spaced points, and smoothed using an adjacent-averaging algorithm. Further, the plotted deformation vs. time curve was differentiated to produce the creep rate vs. time plots, thereby determining the minimum creep rate values.

While the amount of adjacent points taken in the smoothing filter varied with the frequency of acquisition selected for every test, the criteria for the filter application considered that no changes in the secondary creep stage slope should be allowed. Nevertheless, the filter is essential to eliminate periodic variations that arise from the furnace temperature fluctuation. Although this variation is small on the specimen itself, it affects more significantly the long extensometer tubes, thus generating a systematic background noise.

Creep results were also used in parametrizations. A Monkman-Grant relationship was established to estimate creep life, using data from all temperatures and stresses tested under both

tensile and compression conditions. A Larson-Miller (LM) parametrization was also conducted, using constant values  $C_{LM}$  calculated according to Manson and Mendelsohn [172].

### 3.4.2 Hardness and Elastic Modulus Measurements

All specimens had their hardness measured using a device Microhardness Leica VMHT 30M with a Vickers indenter, using a load of 300 g for 10 s. The measurement was conducted with the aid of the Brück VMS 2 software, version 2.6. To obtain the average hardness, a total of 5 measurements were taken from each specimen submitted to thermal aging tests, and 10 measurements for all other specimens.

The elastic modulus at room temperature was measured using a Nanoindenter Zwick/Roell ZHN, and analyzed with the software InspectorX version 4. A pyramidal indenter was utilized with a force of 50 mN, over 50 different regions in each specimen. Regions with and without carbides were also selected and compared. The obtained values were compared with literature and extrapolated to high temperatures, using a polynomial fitting from a non-reinforced variant as reference.

## 4. Results

To evaluate the microstructure evolution and creep resistance of the proposed composites and the non-reinforced references, the study was divided in the topics: initial state characterization, development over long isothermal aging, tensile creep results and compression creep results.

### 4.1 Initial state characterization

#### 4.1.1 Inconel X-750 hot-rolled (reference material)

The non-reinforced variant produced by hot rolling presented large amounts of twin boundaries (Figure 22 a), as observed through light microscopy. Fine precipitates were present along the grain boundaries (Figure 22 b). These particles were further observed with SEM (Figure 23 a), measuring about 0.1  $\mu\text{m}$  in diameter. Inside grains and at their boundaries larger polygonal precipitates were observed (Figure 23 b), having diameter varying between 0.5 and 10  $\mu\text{m}$ . The size and morphology of both precipitates were consistent with Cr-rich  $\text{M}_{23}\text{C}_6$  and Ti,Nb-rich MC, as established in literature [1,33,46,173–176].

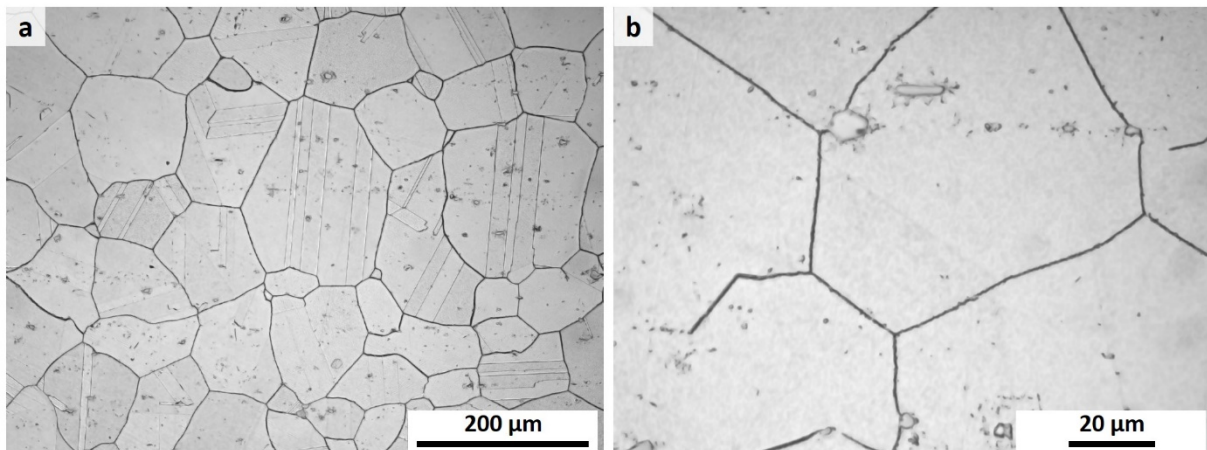


Figure 22 - Light microscopy images of Inconel X-750 hot-rolled, highlighting a) multimodal grain size distribution and twinning patterns; b) carbides at grain boundaries.

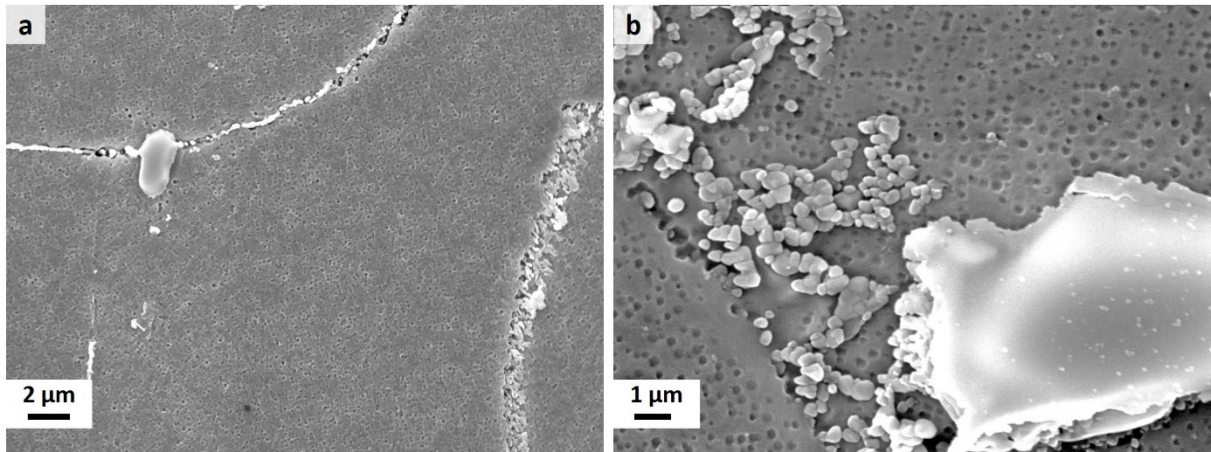


Figure 23 – SEM-SE images of Inconel X-750 hot-rolled, showing a) carbides at grain boundaries and b)  $\gamma'$  precipitates near a grain-boundary containing different carbides.

The average grain size was measured at  $D_{avg} = 106.9 \mu\text{m}$ . A fine dispersion of cuboidal precipitates, predicted as  $\gamma'$  particles [1,46,175,176], was observed inside the grains. Their average diameter was measured with the aid of TEM, resulting in  $D_{avg} = 67.4 \text{ nm}$ . Both the grain and  $\gamma'$  particle sizes have their distribution detailed in the section 0. Close to grain boundaries, a region depleted of such particles was occasionally observed, having a width varying between 0.1 and 0.3  $\mu\text{m}$ .

Upon close inspection, the regions near grain-boundaries were not always depleted in  $\gamma'$ . An even finer dispersion of  $\gamma'$  ( $D_{avg} < 10 \text{ nm}$ ), predicted for this alloy [35,51,177], is clearly present (Figure 24 a). Higher magnifications showed that the smaller particulate is also present between the primary  $\gamma'$  precipitates (Figure 24 b).

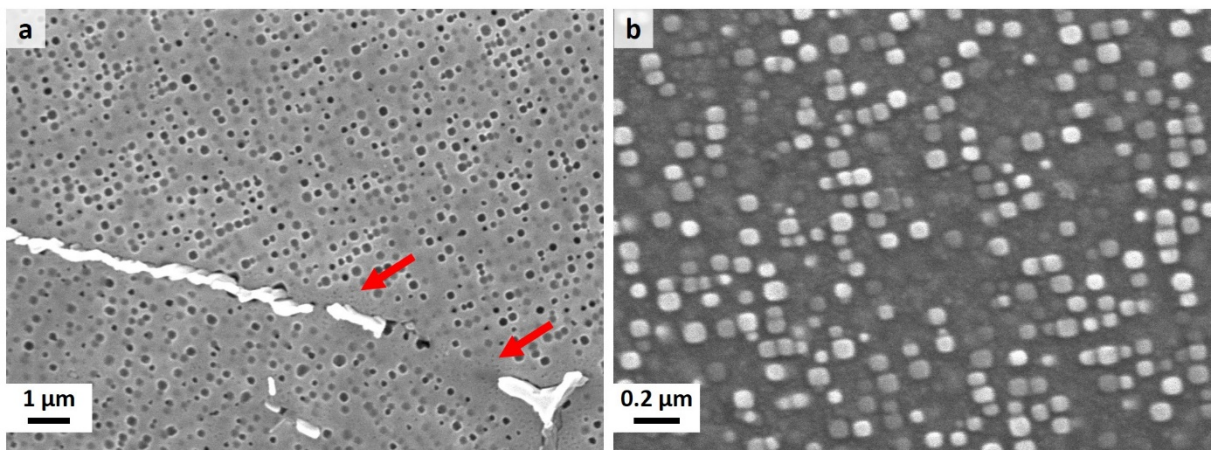


Figure 24 - SEM images of Inconel X-750 hot-rolled, showing secondary  $\gamma'$  a) near grain boundaries (marked) and b) homogeneously dispersed as a fine particulate between primary  $\gamma'$ .

The large MC precipitates were further investigated with EDS elements mapping and punctual analysis (Figure 25). It was observed that they were enriched with Nb (40 at.%) and Ti (41 at.%) in similar amounts (1:1), containing yet small amounts of Al (1 at.%) and Cr (2 at.%). It was also noticed that Nb levels were higher in peripheral areas of the carbide, while Ti was more prevalent in internal areas.

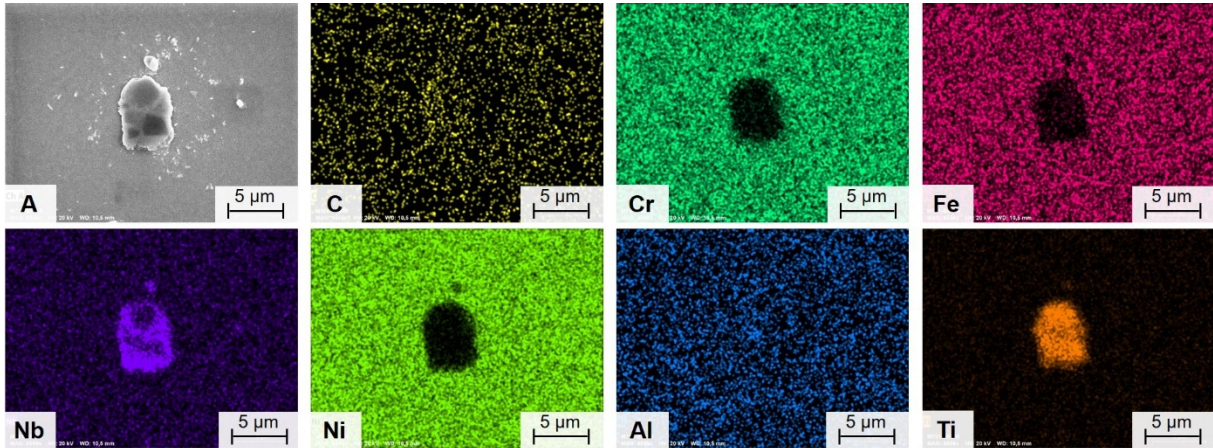


Figure 25 - EDS elements map of Inconel X-750 hot rolled, showing region containing a large MC precipitate rich in Nb and Ti. The original SE image is represented by A.

With the aid of transmission electron microscopy, it was identified that the fine squared precipitates (thus far presumed  $\gamma'$ ) presented a cubic structure (Figure 26). Selected area electron diffraction revealed d-spacings of 2.04 Å and 2.79 Å, consistent with the  $\gamma'$  phase in the family planes of  $\{111\}$  and  $\{200\}$ , respectively.

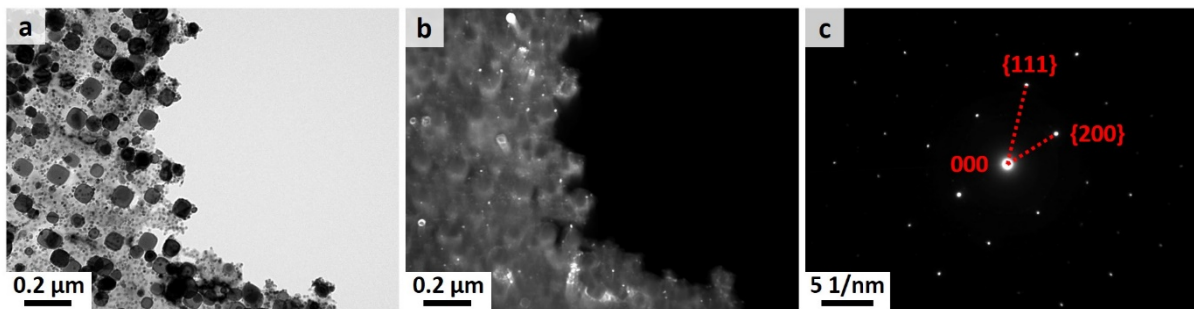


Figure 26 - TEM images of Inconel X-750 hot-rolled with a) bright field, b) dark field and c) selected area electron diffraction, highlighting the  $\gamma'$  phase in the family planes  $\{1,1,1\}$  and  $\{200\}$ .

Bright field images also confirmed the presence of a secondary precipitation of  $\gamma'$ , having  $D_{avg} < 10$  nm (Figure 27). This even finer particulate was homogeneously dispersed between the bigger  $\gamma'$  particles, further increasing the whole phase amount in the matrix.

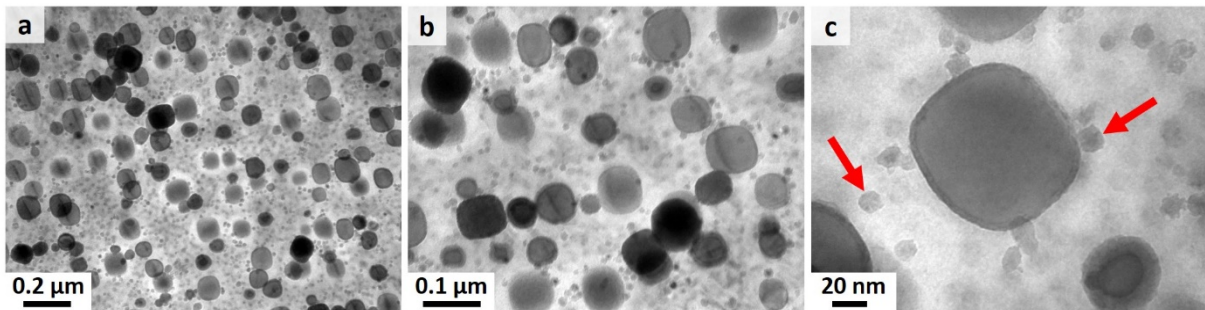


Figure 27 - TEM images of Inconel X-750 hot-rolled showing primary and secondary  $\gamma'$  dispersions over the  $\gamma$  matrix, at different magnifications. To illustrate, selected secondary  $\gamma'$  are marked by arrows.

EBSD analysis confirmed the initial assumption on grain size and the presence of twinning (Figure 28). Scattered data on family planes distribution did not show any preferential orientation.

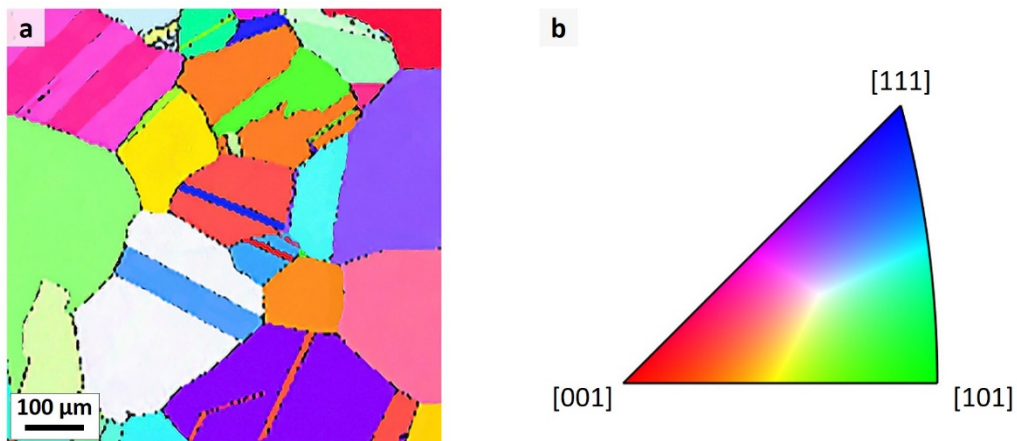


Figure 28 – EBSD image of Inconel X-750 produced by hot rolling process, showing a) orientation map from direction Z; b) IPF color key.



#### 4.1.2 Inconel X-750 (high energy milling + spark plasma sintering)

Relative to the non-reinforced variant produced by hot-rolling process, the Inconel X-750 submitted to high energy milling followed by spark plasma sintering presented a much finer microstructure (Figure 29 a). Grain size was reduced to  $D_{avg} = 3.7 \mu\text{m}$ , with the size distribution detailed in section 4.1.5. Precipitates were also present along the grain boundaries, but in a discrete pattern. Larger precipitates were occasionally spotted (Figure 29 b), presenting irregular shapes.

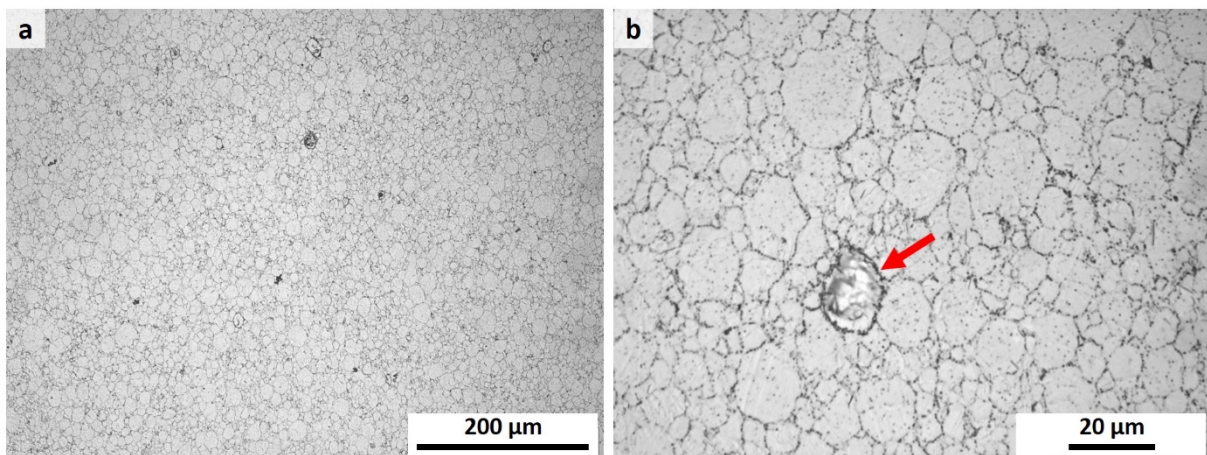


Figure 29 - Light microscopy images of Inconel X-750 produced by HEM + SPS process, showing a) fine grain structure and b) carbides at grain boundaries, in addition to larger sporadic precipitates (marked).

Upon close inspection by scanning electron microscopy (Figure 30 a), a substantial amount of lath-shaped precipitates was found in the grain boundaries, and sporadically inside the grains. These structures presented up to  $5 \mu\text{m}$  in length and  $1.6 \mu\text{m}$  in width. Their minimum thickness was established as  $65 \text{ nm}$ . Frequently the laths vicinity was depleted of primary  $\gamma'$  precipitates (Figure 30 b), along a width measuring between  $0.2$  to  $1 \mu\text{m}$ . The primary  $\gamma'$  present inside the grains presented a size of  $D_{avg} = 57.6 \text{ nm}$ . The complete distribution of  $\gamma'$  particle size is detailed in section 4.1.5.

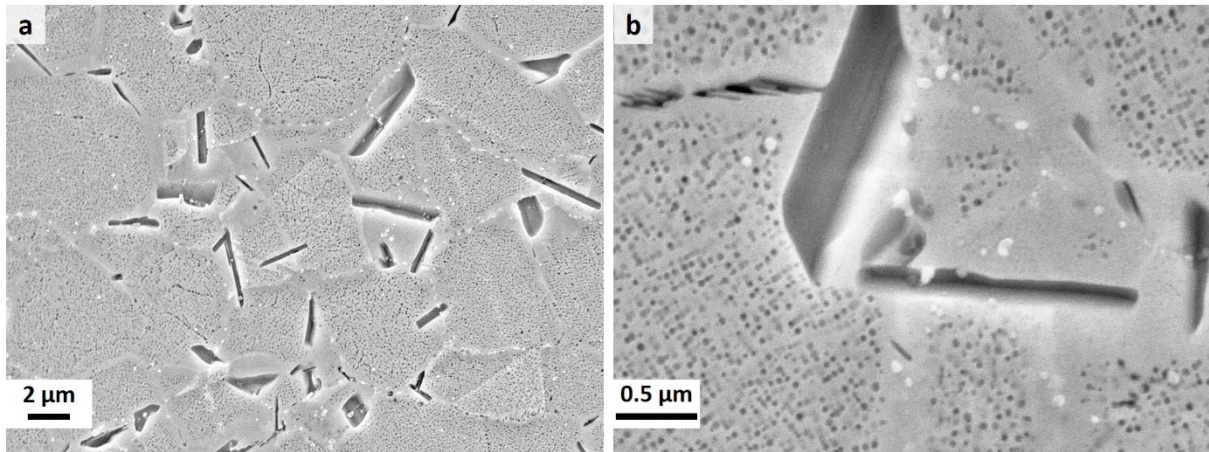


Figure 30 - SEM-SE images of Inconel X-750 produced by HEM + SPS process showing a) dispersion of lath-shaped precipitates and b) primary  $\gamma'$ -free zone near  $\eta$  laths.

A higher SEM magnification revealed that  $\gamma'$  precipitates are partially aligned within grains, having a cuboid-shape and round edges (Figure 31 a). It also reveals that grain boundaries are not devoid of intermetallics, as a fine precipitation of secondary  $\gamma'$  is clearly seen in these regions (Figure 31 b). These particles are also observed between the larger  $\gamma'$ , away from the grain boundary.

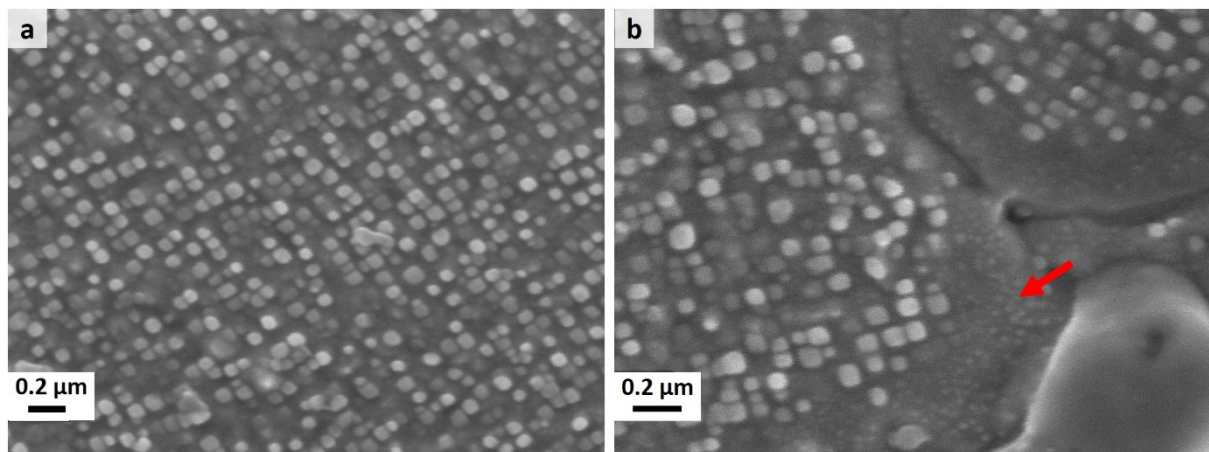


Figure 31 - SEM-SE images of Inconel X-750 produced by HEM + SPS process showing a) dispersion of primary  $\gamma'$  over the matrix and b) detail of secondary  $\gamma'$  near grain boundary (marked by arrow).

Examination by EDS elements mapping (Figure 32) and punctual analysis showed that the laths were mostly rich in Ti and Ni, bearing also smaller amounts of Nb and Al. These precipitates presented reduced amounts of Cr, Fe and C, in relation to the matrix.

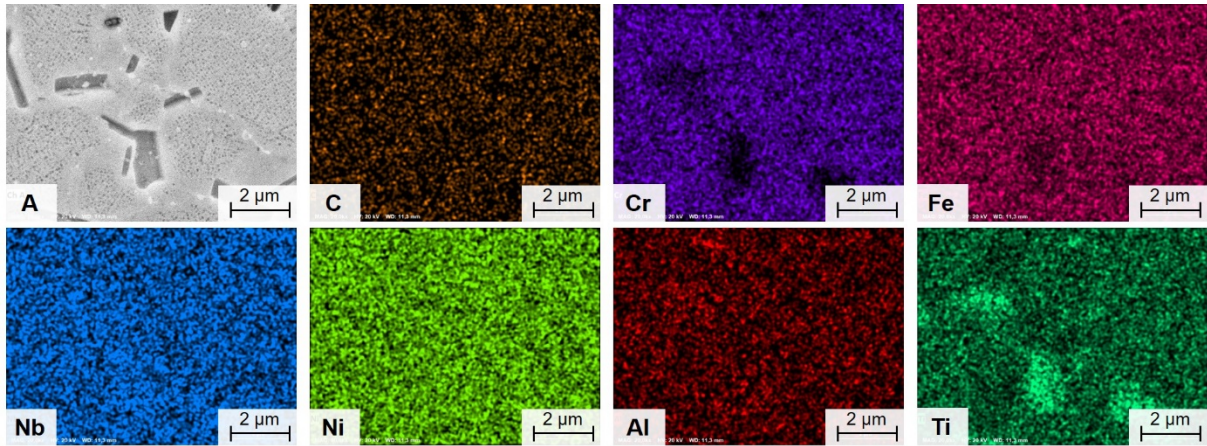


Figure 32 - EDS elements map of Inconel X-750 produced by HEM + SPS, showing a region containing laths. The original SE image is represented by A.

With the aid of transmission electron microscopy, a closer examination of both primary and secondary  $\gamma'$  over the  $\gamma$  matrix (Figure 33 a) was conducted. A diffraction on selected precipitates, comprising mostly of secondary  $\gamma'$  intermetallics (Figure 33 b, c) revealed d-spacings of 2.05 Å and 1.78 Å, belonging to the family planes {111} and {200}, respectively.

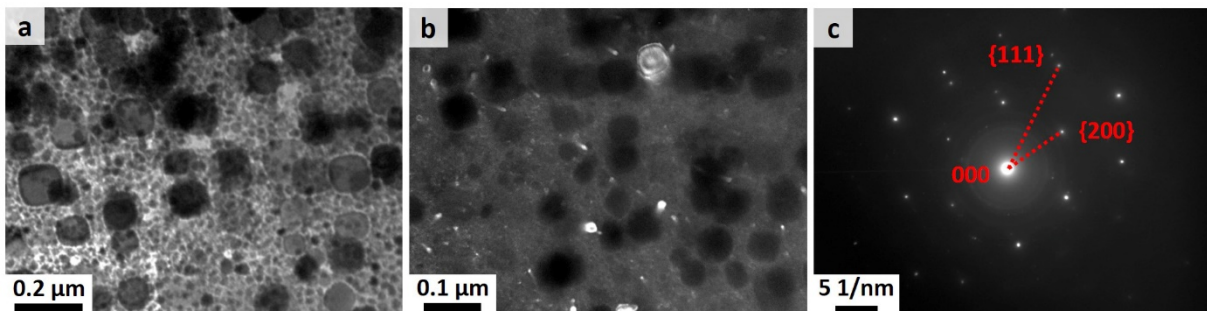


Figure 33 - TEM images of Inconel X-750 produced by HEM + SPS process, with a) bright field, b) dark field of magnified area and c) selected area electron diffraction, highlighting  $\gamma'$  phase in the family planes {1,1,1} and {200}.

The crystallographic orientation was also investigated, through ESDB analysis. A mapping showed no existence of texture (Figure 34), with grains randomly oriented in the samples. As with the Inconel X-750 hot rolled, the variety produced by the HEM + SPS process also presented a high amount of crystal twinning.

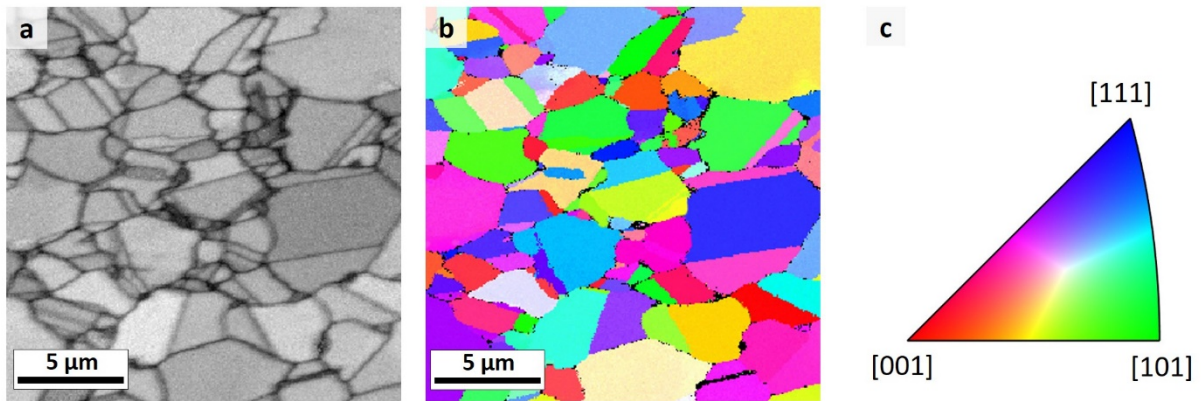


Figure 34 - EBSD image of Inconel X-750 produced by HEM + SPS route, showing a) quality map; b) orientation map from direction X; c) IPF color key.

#### 4.1.3 X-750/TiC 15 vol.% (low energy mixing + pressure sintering)

The combination of mixing and pressure sintering produced a fine microstructure, with a grain size of  $D_{avg} = 8.9 \mu\text{m}$ , but it also led to agglomeration of TiC particles at the grain boundaries. Light microscopy images (Figure 35 a) revealed a distribution of  $\text{TiC}_p$  of different sizes, matching the original powder size distribution. Many of them were in direct contact with each other. Larger polygonal particles, with up to  $10 \mu\text{m}$  in diameter, were also occasionally observed (Figure 35 b).

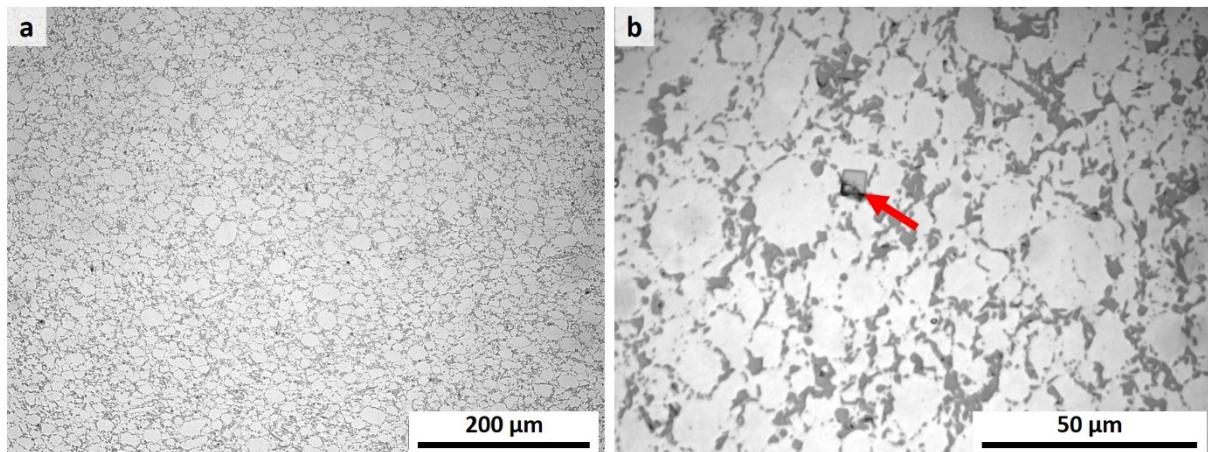


Figure 35 - Light microscopy images of X-750/TiC 15 vol.% produced by LEM + PS, showing a) fine grain structure and b) carbides at grain boundaries, in addition to sporadic larger precipitates (marked).

SEM images (Figure 36 a) confirmed that a significant number of  $TiC_p$  clusters formed at grain boundaries, but also showed that the added particles did not impact considerably the formation of  $\gamma'$  precipitates. On rare occasions  $\gamma'$ -free zones were identified (Figure 36 b), but not presenting a distinguishable pattern of appearance in relation of proximity to  $TiC_p$ . The average primary  $\gamma'$  size was determined at  $D_{avg} = 71.8$  nm, with its distribution detailed in section 4.1.5.

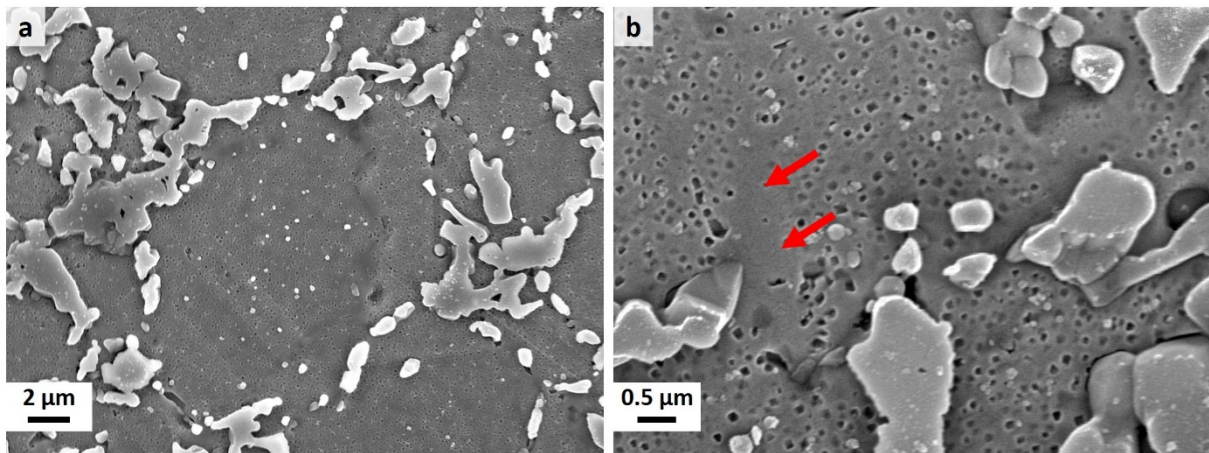


Figure 36 - SEM-SE images of X-750/TiC 15 vol.% produced by LEM + PS process showing a) TiC at grain boundaries and b)  $\gamma'$ -free zones near TiC particles.

Higher magnifications in SEM, with the aid of an in-lens detector, revealed a secondary precipitation of finer  $\gamma'$  between the larger  $\gamma'$  cuboids. Both were observed in the vicinity of carbides (Figure 37 a) and grain boundaries (Figure 37 b), confirming that the formation of  $\gamma'$ -free zones is not necessarily conditional to the proximity to these areas. The average composition of  $TiC_p$  was obtained by punctual EDS measurements, resulting in 67.8 at.% Ti, 2.8 at.% Nb, 2.6 at.% Cr and 0.7 at.% Al.

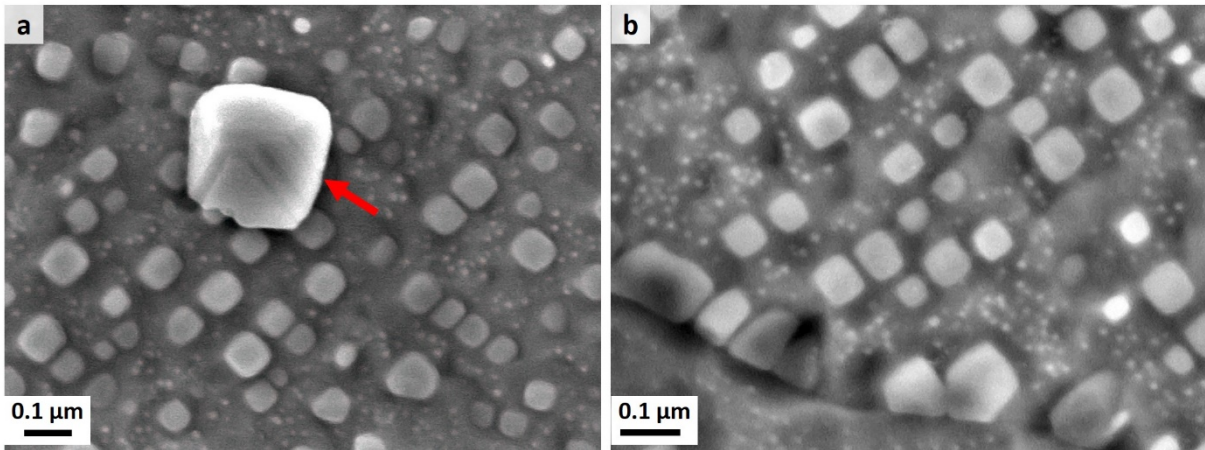


Figure 37 - SEM-SE images of X-750/TiC 15 vol.% produced by LEM + PS process showing a) primary and secondary  $\gamma'$  precipitates around a carbide (marked); b)  $\gamma'$  precipitates near a grain boundary (below).

The added TiC particles were examined with EDS elements mapping (Figure 38) and punctual measurements. These were still composed mostly by Ti (70 at.%), but also enriched with Nb (3 at.%). Further elements observed are Cr (3 at.%) and Al (1 at.%).

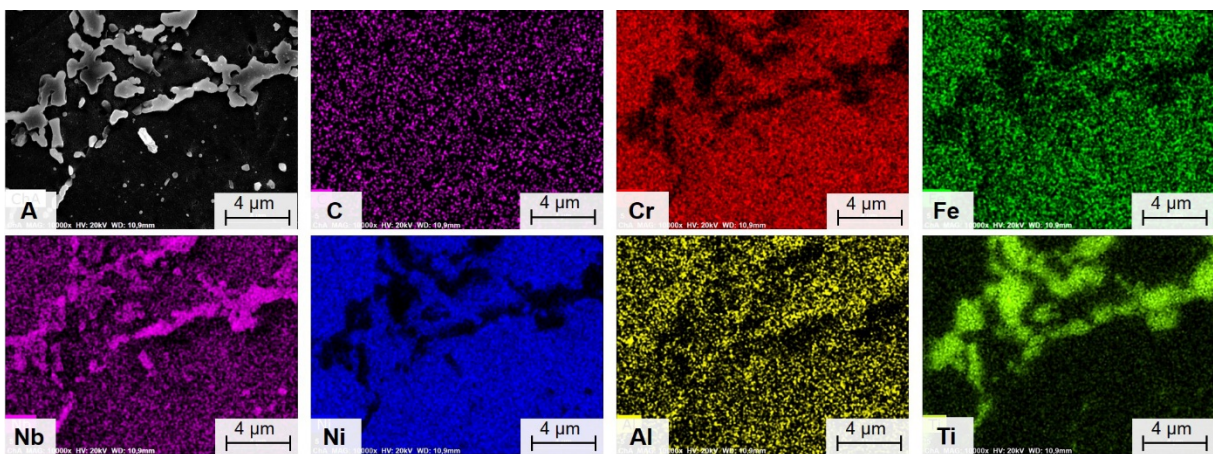


Figure 38 - EDS elements map of X-750/TiC 15 vol.% produced by LEM + PS process, showing region containing the added TiC particles, enriched in Nb. The original SE image is represented by A.

The small intermetallics and the matrix were further characterized with transmission electron microscopy. With the aid of TEM-SAED, an examined d-spacings of 2.04 Å and 1.78 Å was established as belonging to the family planes {111} and {200}, respectively, in the  $\gamma + \gamma'$  phases (Figure 39 and Figure 40). Secondary  $\gamma'$ , presenting  $D_{avg} < 10$  nm, were also observed in the analysis (Figure 40 a, marked by arrow).

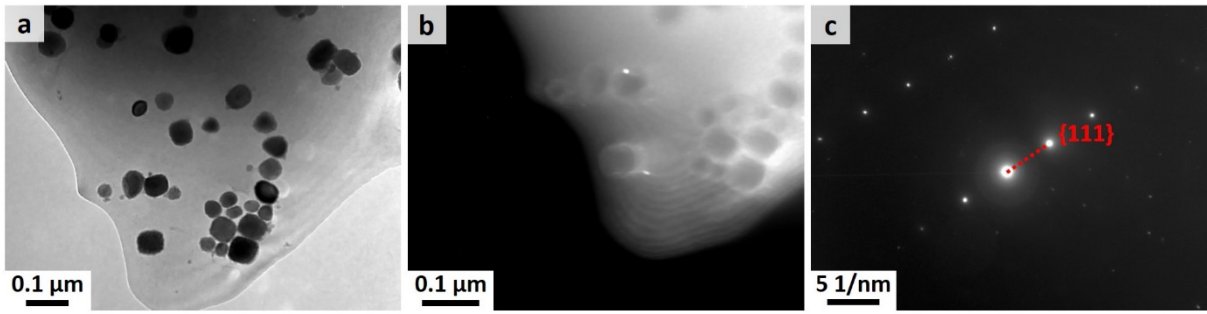


Figure 39 - TEM images of X-750/TiC 15 vol.% produced by LEM + PS process, with a) bright field, b) dark field and c) selected area electron diffraction, highlighting  $\gamma + \gamma'$  phases in the family plane  $\{1,1,1\}$ .

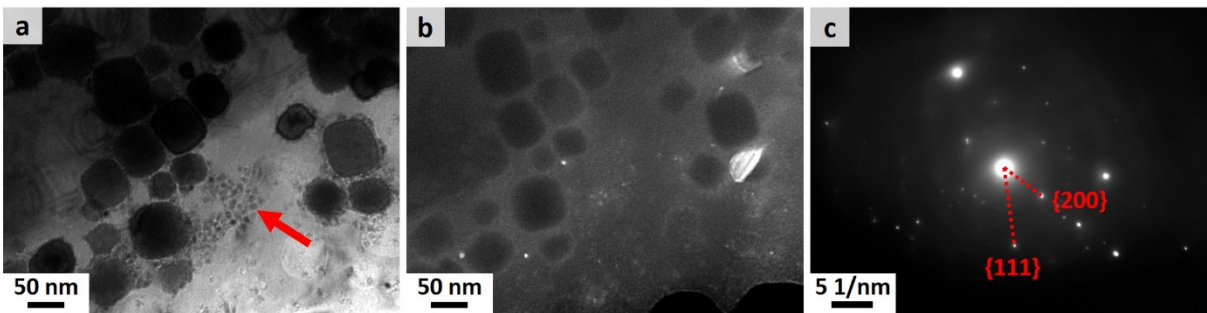


Figure 40 - TEM images of X-750/TiC 15 vol.% produced by LEM + PS process, with a) bright field, b) dark field and c) selected area electron diffraction, highlighting  $\gamma'$  phase in the family planes  $\{1,1,1\}$  and  $\{200\}$ .

EBSD analysis showed the presence of twins in quality maps (Figure 41 a, with an example marked) and orientation images (Figure 41 b). No texture was observed in the matrix. Furthermore, TiC particles also presented random orientation, even when agglomerated at grain boundaries.

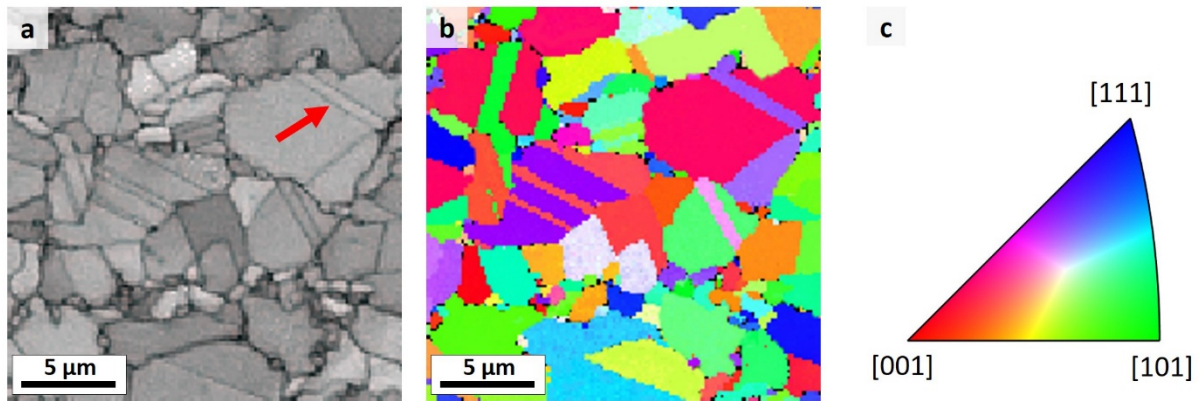


Figure 41 - EBSD image of X-750/TiC 15 vol.% produced by LEM + PS route, showing a) quality map; b) orientation map from direction X; c) IPF color key.

#### 4.1.4 X-750/TiC 15 vol.% (high energy milling + spark plasma sintering)

The most refined microstructure was obtained with the combination of high energy milling and spark plasma sintering. Light microscopy images (Figure 42) showed the presence of occasionally elongated grain-like structures, oriented at 90° with the compression axis in the spark plasma sintering process.

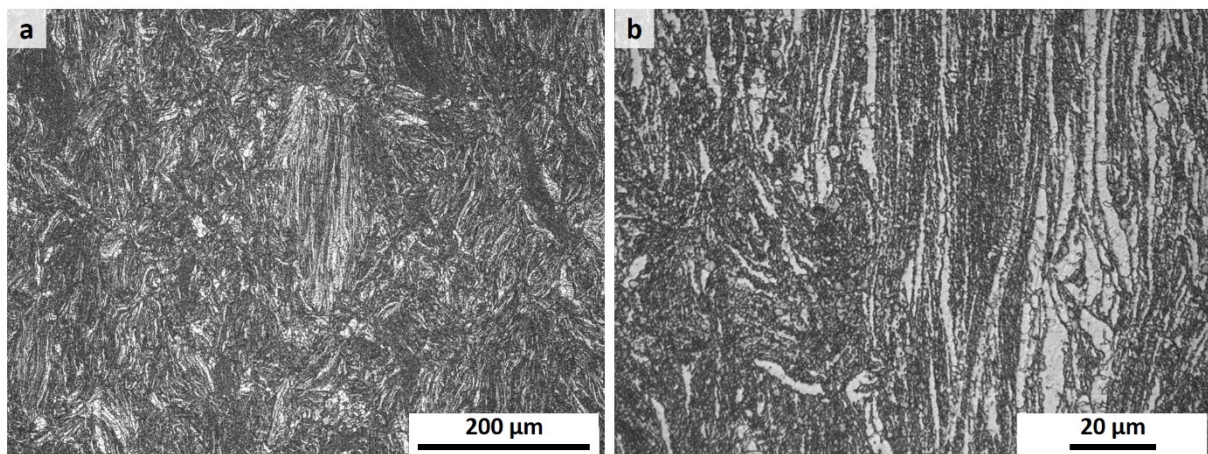


Figure 42 - Light microscopy images of X-750/TiC 15 vol.% produced by HEM + SPS process, showing a very fine and occasionally elongated grain-like structure at different magnifications in a) and b).



Upon close inspection with the use of SEM, two domains were identified: regions with a high amount of small TiC particles near-homogeneously dispersed (Figure 43 a), and regions containing areas deprived of TiC<sub>p</sub> (Figure 43 b). TiC<sub>p</sub> size varied between 0.1 and 0.4 μm, but also sporadically presented particles as large as 0.7 μm. Their average size was determined as  $D_{avg} = 0.33 \pm 0.12 \mu\text{m}$ , with the size dispersion shown in Figure 44.

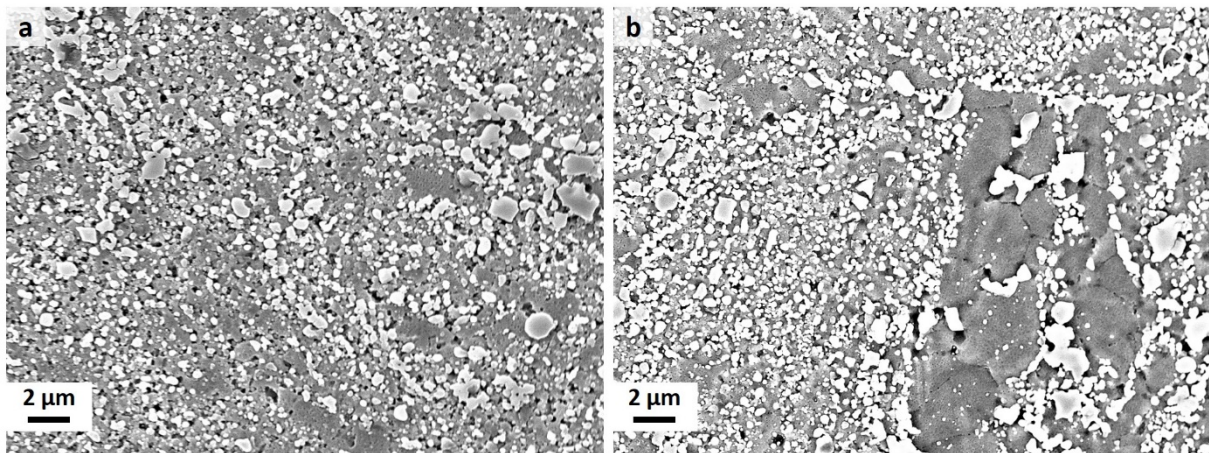


Figure 43 - SEM-SE images of X-750/TiC 15 vol.% produced by HEM + SPS process showing a) TiC<sub>p</sub> fine dispersed over the matrix and b) region containing areas devoid of TiC<sub>p</sub>.

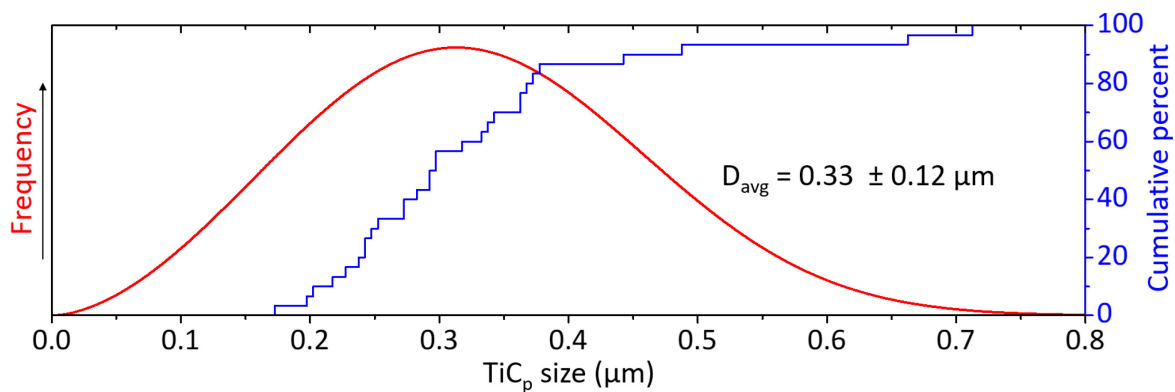


Figure 44 - Weibull distribution of TiC<sub>p</sub> size in X-750/TiC 15 vol.% produced by HEM + SPS.

Regions holding a high amount of consistently dispersed TiC<sub>p</sub> frequently exhibited areas scarce in  $\gamma'$  between the carbides (Figure 45 a). In contrast, regions poor in TiC<sub>p</sub> presented the highest amount of  $\gamma'$  particles (Figure 45 b). The  $\gamma'$  primary particle size was established at  $D_{avg} = 51.3 \text{ nm}$ , with the size distribution detailed in section 4.1.5.

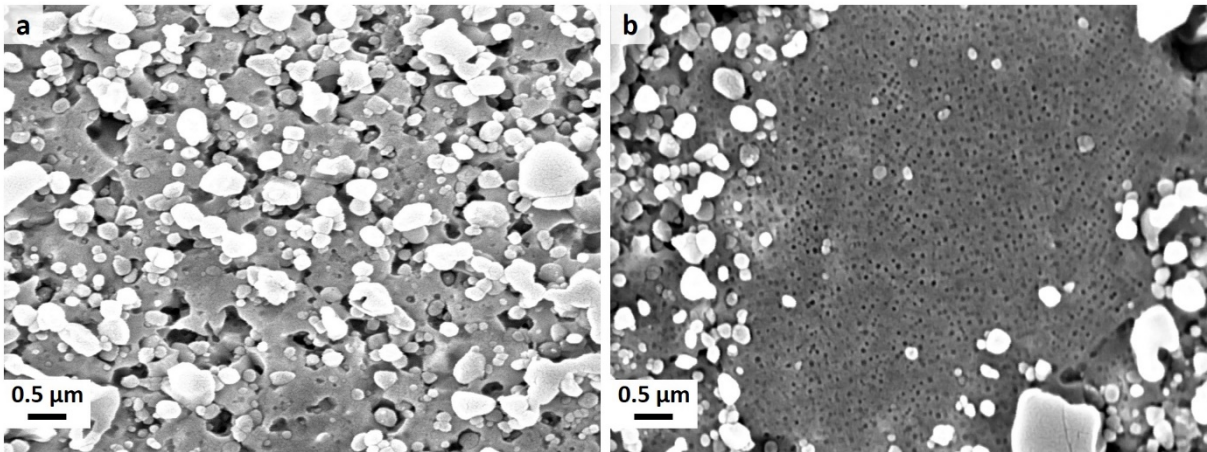


Figure 45 - SEM-SE images of X-750/TiC 15 vol.% produced by HEM + SPS process showing a) region deficient in  $\gamma'$  between  $TiC_p$ ; b) region with near-homogeneously dispersed  $\gamma'$ .

Despite that, not all areas containing a high amount of  $TiC_p$  presented a lower occurrence of  $\gamma'$  precipitates. Some regions still showed a homogeneous dispersion of intermetallics, even close to agglomerations of carbides (Figure 46 a). A higher magnification of these areas also revealed that a secondary precipitation of  $\gamma'$ , with finer size, was also present (Figure 46 b).

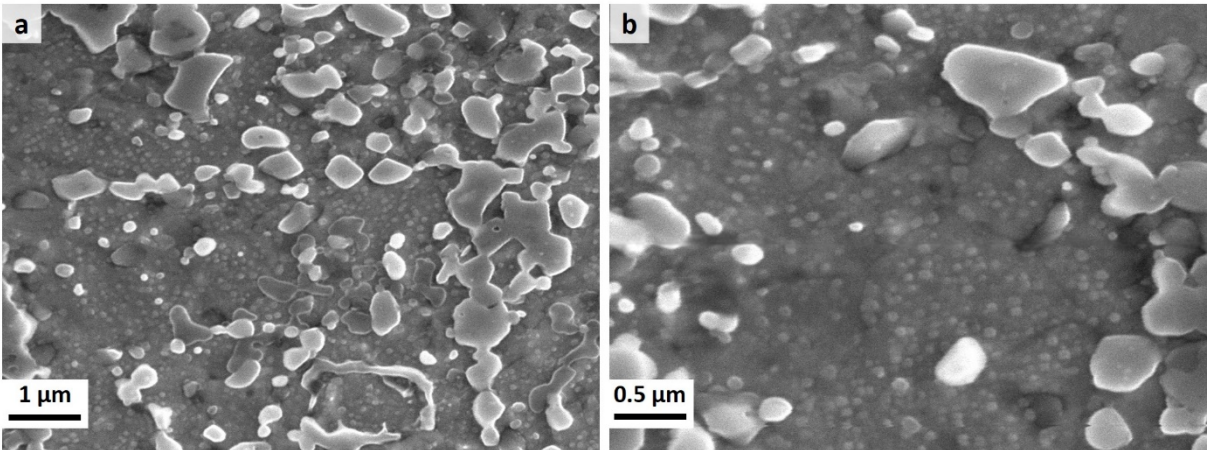


Figure 46 - SEM-SE images of X-750/TiC 15 vol.% produced by HEM + SPS process showing a) closer detail of  $\gamma'$  particles between  $TiC_p$  and b) mixture of primary and secondary  $\gamma'$  dispersion over  $\gamma$  matrix.

EDS elements mapping measurements (Figure 47) revealed that  $TiC_p$  had an average composition of 57 at.% Ti, 5 at.% Cr, 5 at.% Nb and 0 at.% Al. Chromium and aluminum oxides were also observed. Chromium oxides were present near chromium carbides, while aluminum oxides were less frequent and occurred surrounded by fine  $TiC$  particles.

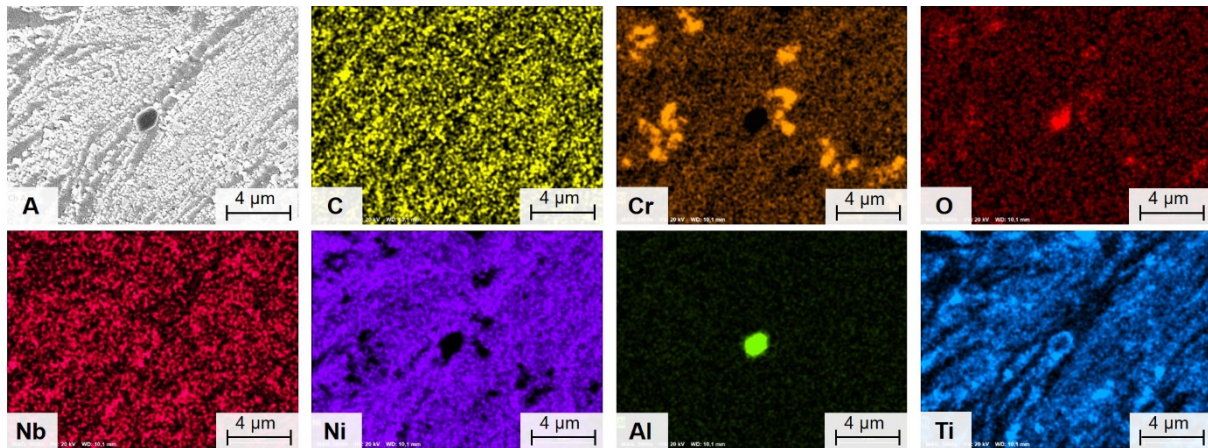


Figure 47 - EDS elements map of X-750/TiC 15 vol.% produced by HEM + SPS process, showing region containing the added TiC particles, chromium carbides and oxides, in addition to a single aluminum oxide. The original SE image is represented by A.

Transmission electron microscopy images revealed that the distribution of  $\gamma'$  precipitates is not homogeneous near carbides (Figure 48 a), with the formation of pockets of secondary  $\gamma'$  (Figure 48 b, marked by arrow) and areas free of intermetallics in the vicinity of the grain boundary.

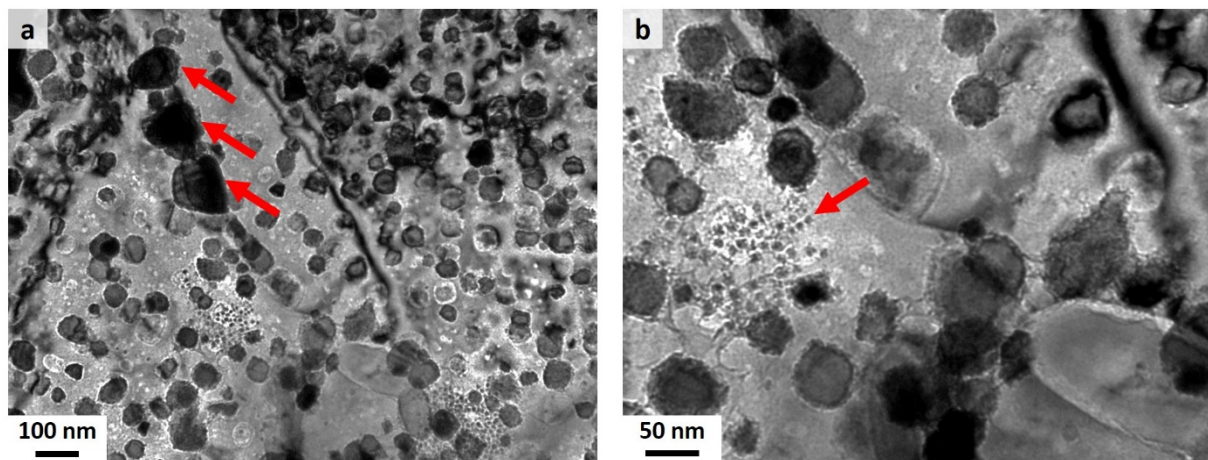


Figure 48 – Bright field TEM images of X-750/TiC 15 vol.% produced by HEM + SPS process, showing a)  $\gamma'$  intermetallics over  $\gamma$  matrix, near carbides (marked by arrows) at a grain boundary; b) magnified area, showing heterogeneous dispersion of secondary  $\gamma'$  (marked by arrow).

Grain size was estimated with the aid of EBSD analysis (Figure 49). A significant dispersion of size was obtained, varying from 0.3 to 2.0  $\mu\text{m}$  in the regions rich in TiC particles, that compose the major part of the material. The average diameter was established as  $D_{\text{avg}} = 0.6 \pm 0.5 \mu\text{m}$ , with the size distribution detailed in section 4.1.5. No texture was observed in the material within the scope of the EBSD analysis.

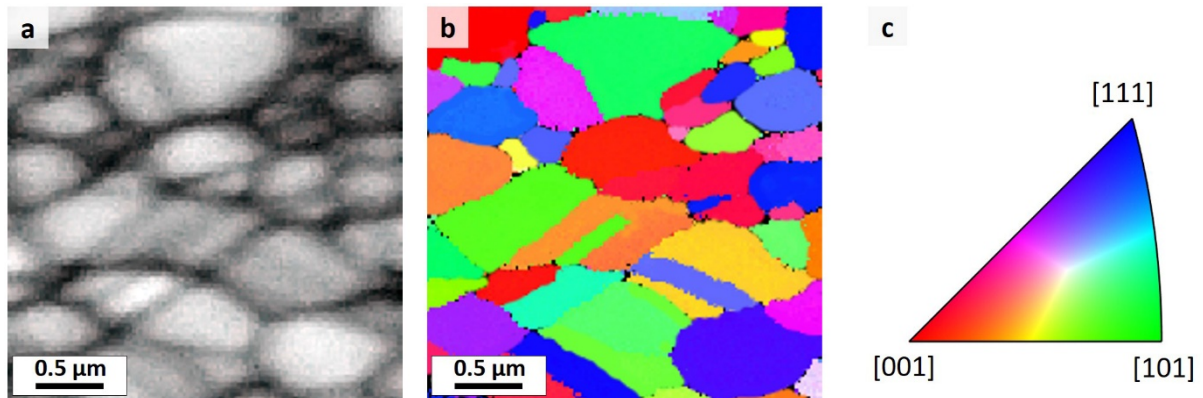


Figure 49 - EBSD image of X-750/TiC 15 vol.% produced by HEM + SPS route, showing a) quality map; b) orientation map from direction X; c) IPF color key.

#### 4.1.5 Distribution of grain and primary $\gamma'$ size

A direct comparison of grain size (Table 5) and  $\gamma'$  size (Table 6) was made, for all non-reinforced and composite variants at initial state. A Weibull distribution from both grain size (Figure 50) and  $\gamma'$  size (Figure 51) was also conducted, together with the cumulative percent. Secondary  $\gamma'$  size and distribution were not evaluated, as resolution constraints in the SEM instrument did not allow the acquisition of reliable measurements.

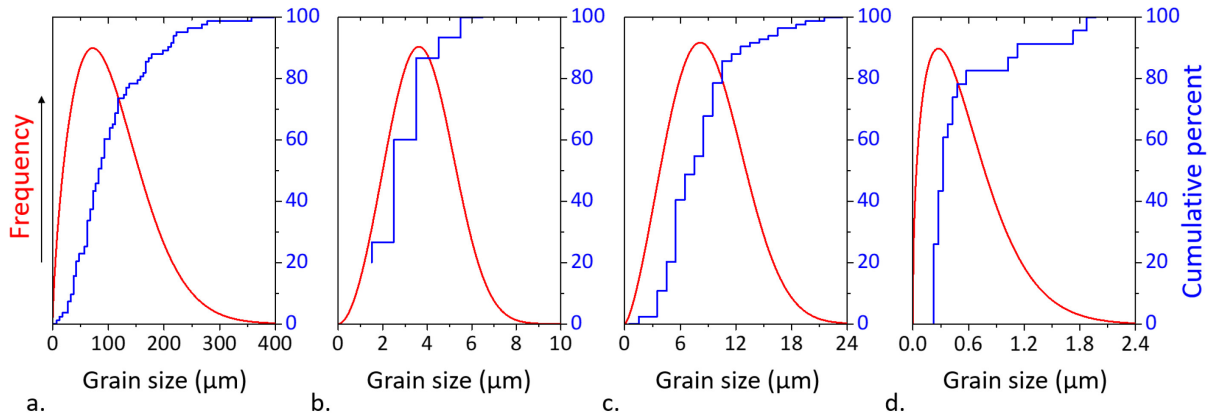


Figure 50 – Weibull distribution of grain size (diameter) at initial state from a) Inconel X-750 hot-rolled; b) Inconel X-750 [HEM + SPS]; c) X-750/TiC<sub>p</sub> [LEM + PS] and d) X-750/TiC<sub>p</sub> [HEM + SPS].

Table 5 - Average grain size (diameter, μm) of all investigated materials at initial state.

	<b>Inconel X-750 hot-rolled</b>	<b>Inconel X-750 [HEM + SPS]</b>	<b>X-750/TiC<sub>p</sub> [LEM + PS]</b>	<b>X-750/TiC<sub>p</sub> [HEM + SPS]</b>
Mean size	106.9	3.7	8.9	0.6
Standard deviation	67.3	1.4	3.8	0.5
Minimum size	14.2	1.7	2.2	0.3
Maximum size	361.08	6.8	22.9	1.9

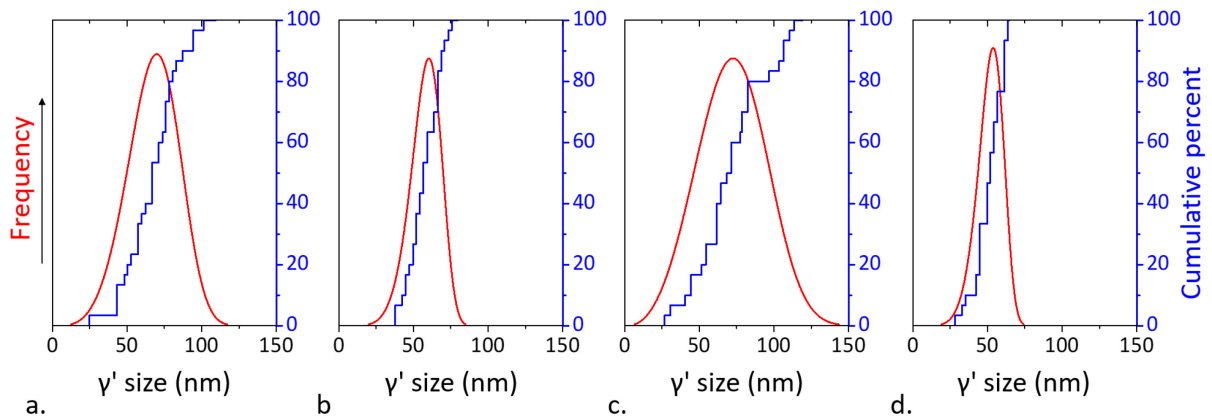


Figure 51 – Weibull distribution of  $\gamma'$  size (diameter) at initial state from a) Inconel X-750 hot-rolled; b) Inconel X-750 [HEM + SPS]; c) X-750/TiC<sub>p</sub> [LEM + PS] and d) X-750/TiC<sub>p</sub> [HEM + SPS].

Table 6 - Summary of primary  $\gamma'$  size (diameter, nm) of all investigated materials at initial state.

	<b>Inconel X-750 hot-rolled</b>	<b>Inconel X-750 [HEM + SPS]</b>	<b>X-750/TiC<sub>p</sub> [LEM + PS]</b>	<b>X-750/TiC<sub>p</sub> [HEM + SPS]</b>
Mean size	67.4	57.6	71.8	51.3
Standard deviation	17.3	10.3	23.0	9.2
Minimum size	25.4	38.0	27.8	38.1
Maximum size	101.8	76.2	114.6	76.2

#### 4.1.6 Phases identification and quantification with XRD

When analyzing the diffractograms of all investigated materials, five phases were identified and had their weight fraction measured with Rietveld refinement [169,178] method:

- $\gamma$ -Ni<sub>4</sub>, a mixed-crystal phase that composes the matrix having a fm-3m space group symmetry and an A1 structure (fcc). The high amount of substitutional elements provoked small distortions on the lattice parameters, causing the shifts observed in diffractograms. This phase was present on all analyzed specimens;
- $\gamma'$ -Ni<sub>3</sub>(Al,Ti), an intermetallic that also possesses a fm-3m symmetry and precipitates with a L1<sub>2</sub> structure (ordered fcc). As with  $\gamma$ , distortions on the lattice parameters of  $\gamma'$  caused small shifts in the XRD peaks. The phase was found on all examined specimens;
- $\eta$ -Ni<sub>3</sub>Ti, a precipitate with hexagonal structure, belonging to the p6<sub>3</sub>/mmc space group. This phase presents a DO<sub>24</sub> order was identified only in samples of X-750/TiC 15 vol.% produced by the combination of high energy milling and spark plasma sintering processes;
- TiC, the reinforcing carbide added to the produced composites. This phase possesses a cubic structure, of fm-3m group and B1 type order, and was found only in the MMCs.
- (Al,Nb,Ti)C, a mixed carbide of hexagonal structure, of p6<sub>3</sub>/mmc group. The phase was present only in samples from Inconel non-reinforced variants of X-750 and in the X-750/TiC 15 vol.% produced by LEM + PS process.

All produced materials, their identified phases and weight percentages are summarized in Table 7. All diffractograms with their respective phase quantifications conducted by Rietveld refinement can be observed as follows: X-750 hot rolled (Figure 52), X-750 HEM + SPS (Figure 53), X-750/TiC LEM + PS (Figure 54) and X-750/TiC HEM + SPS (Figure 55). It is important to note that large grain sizes ( $D_{avg} > 10 \mu\text{m}$ ), as well as microstructures that present any degree of texture, might affect the quality of the Rietveld refinement. These conditions were found in all investigated materials. Therefore, quantification results obtained in these circumstances must be assumed as approximations and analyzed in conjunction with other examinations.

Table 7 - Phases characterized with XRD and their respective amounts (in wt.%), obtained with Rietveld refinements. Accuracy might be affected by the absence of specific phases.

Material	Process	$\gamma$ (Ni <sub>4</sub> )	$\gamma'$ (Ni <sub>3</sub> Al)	$\eta$ (Ni <sub>3</sub> Ti)	TiC	(Al,Nb,Ti)C
Inconel X-750	Hot rolling	55.4	42.6	0.0	0.0	2.0
Inconel X-750	HEM + SPS	66.4	28.7	3.8	0.0	1.1
X-750/TiC 15 vol.%	LEM + PS	49.4	38.9	0.0	10.9	0.8
X-750/TiC 15 vol.%	HEM + SPS	50.0	37.0	0.0	13.0	0.0

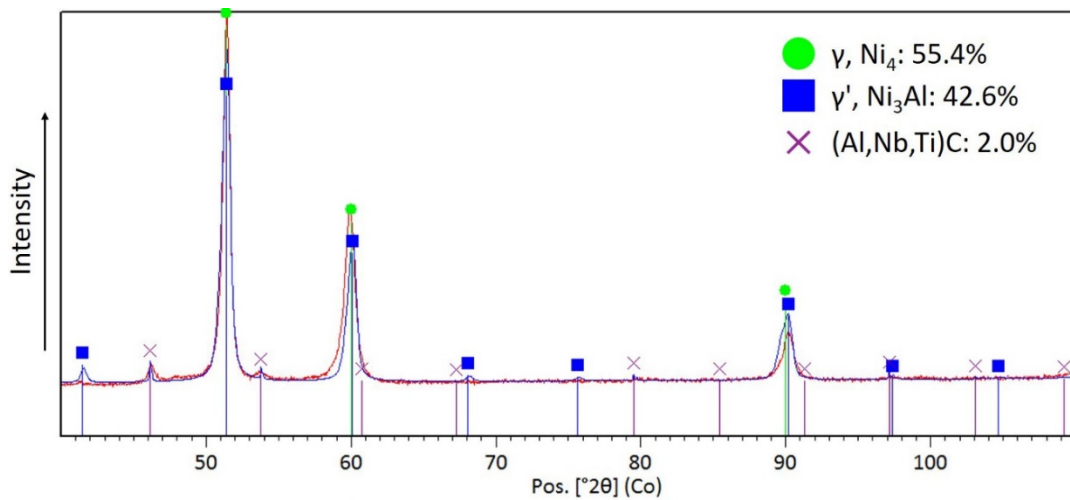


Figure 52 - XRD profile of Inconel X-750 hot rolled, with phases fitted with Rietveld refinement.

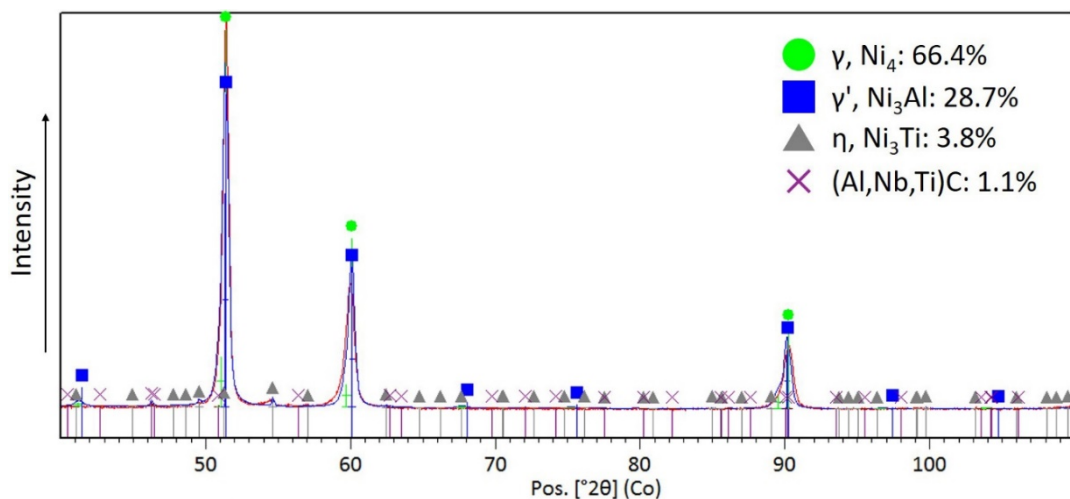


Figure 53 - XRD profile of Inconel X-750 produced by HEM + SPS process, with phases fitted with Rietveld refinement.

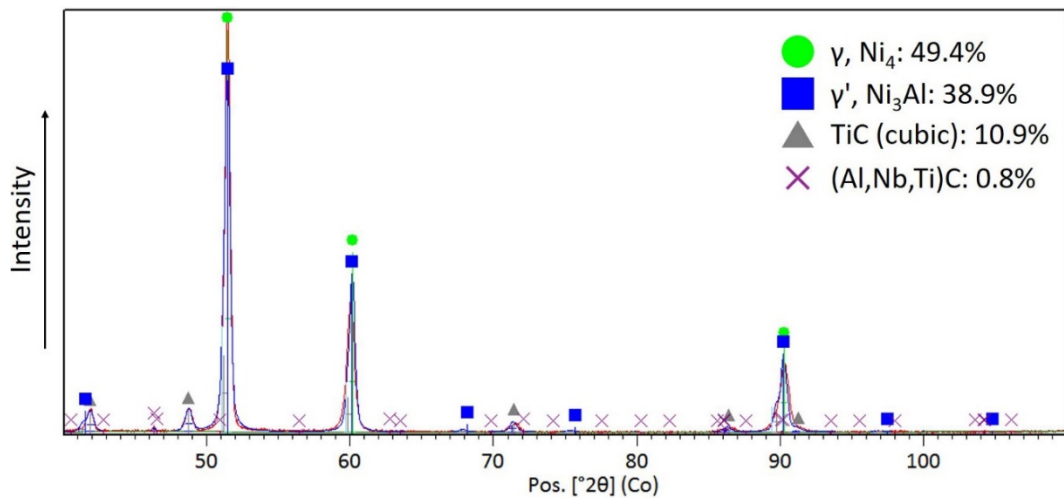


Figure 54 - XRD profile of X-750/TiC 15 vol.% produced by LEM + PS process, with phases fitted with Rietveld refinement.

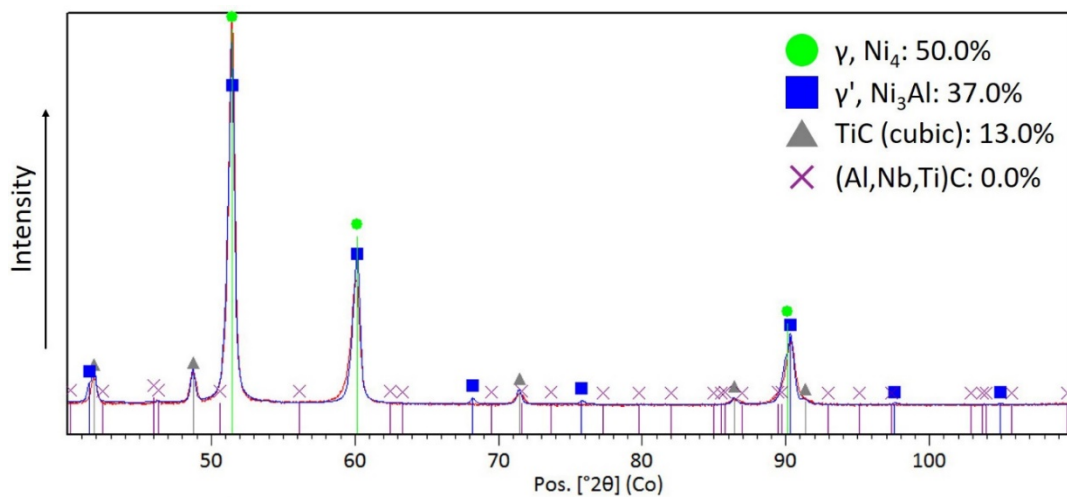


Figure 55 - XRD profile of X-750/TiC 15 vol.% produced by HEM + SPS process, with phases fitted with Rietveld refinement.



#### 4.1.7 Elastic modulus estimation with nanoindentation

The dispersion of indentation marks successfully reached areas with and without carbides on all materials tested (Figure 56 a, b, c), allowing the acquisition of average values from all samples. Furthermore, different grains were favorably targeted on all investigated materials.

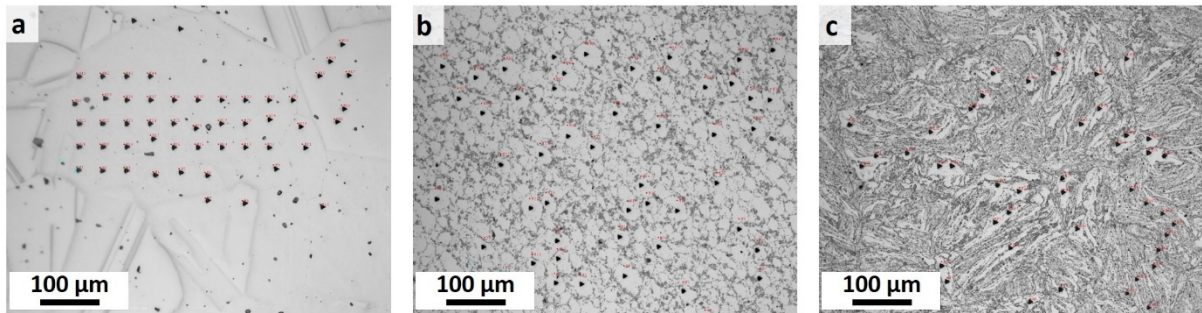


Figure 56 - Areas submitted to nanoindentation in a) X-750 hot rolled; b) X-750/TiC 15 vol.% LEM + PS and c) X-750 15 vol.% HEM + SPS. Areas with and without carbides were equally targeted.

The average value of elastic modulus ( $E$ ) obtained from samples of Inconel X-750 hot rolled (Table 8) did not presented a significant variation from values provided in literature [49], thus validating the method for room temperature measurements. Using high temperature values provided in literature for the Inconel X-750 [49], a polynomial fitting (Equation 12) was extracted and applied to extrapolate the expected values for all produced materials:

$$E = -0.00009351 \times T^2 - 0.02661730 \times T + 213.46220383 \quad (12)$$

where  $T$  is the temperature, in the range of 260 to 815 °C [49].

Table 8 - Elastic modulus (in GPa) at room and high temperatures. Significance value ( $\alpha$ ) is 0.05.

Material	$E$ measured (GPa)			$E$ calculated (GPa)		
	room temperature			700 °C	750 °C	800 °C
	Average	St. Dev.	Confidence interval	Value		
Inconel X-750 (literature)	214 <sup>a</sup>	—	—	149 <sup>a</sup>	141 <sup>a</sup>	132 <sup>a</sup>
Inconel X-750 (hot-rolled)	215	7	5	150 <sup>b</sup>	142 <sup>b</sup>	133 <sup>b</sup>
X-750/TiC (LEM + PS)	229	8	6	160 <sup>b</sup>	151 <sup>b</sup>	142 <sup>b</sup>
X-750/TiC (HEM + SPS)	251	15	11	175 <sup>b</sup>	165 <sup>b</sup>	155 <sup>b</sup>

<sup>a</sup> values provided in literature [49], for reference; <sup>b</sup> based on extrapolation over the fitted data.

To assess the test accuracy concerning regions in the composites with different contents of TiC particles, measurements conducted on these areas in X-750/TiC 15 vol.% (produced by HEM + SPS) were separated in two groups and compared. Areas showing a high concentration of TiC<sub>p</sub> presented  $E_{avg} = 248$  GPa and a confidence interval of 14 GPa, while areas visually free from these carbides exhibited  $E_{avg} = 253$  GPa and a confidence interval of 9 GPa. This result indicates that concerning the carbides distribution, the average  $E$  can be safely determined regardless of the region tested in the composite, since the visual distribution of TiC<sub>p</sub> does not account for the presence of carbides positioned right below the matrix. The accuracy of the result, therefore, is dependent only on the number of measurements conducted on each specimen.

A rule of mixture for particle reinforced composites was used to establish a comparison with the experimental results, obtaining estimated values for higher (equation 13) and lower (equation 14) limits of elastic modulus at room temperature. The calculation is valid for both composites, since only the amount of reinforcement and the elastic modulus of matrix and ceramic particles are necessary for the estimation.

$$E_{sup} = (E_m \times V_m) + (E_p \times V_p) \quad (13)$$

where  $E_{sup}$  is the MMC estimated superior limit of the elastic modulus,  $E_m$  is the matrix elastic modulus,  $V_m$  is the volume percent occupied by the matrix,  $E_p$  is the particle reinforcement elastic modulus, and  $V_p$  is the volume percent occupied by the particle reinforcement.

$$E_{inf} = (E_m \times E_p) / [(E_p \times V_m) + (E_m \times V_p)] \quad (14)$$

where  $E_{inf}$  is the MMC estimated inferior limit of the elastic modulus.

The results obtained with the rule of mixture,  $E_{sup} = 248$  GPa and  $E_{inf} = 232$  GPa, were also in good agreement with the extrapolation obtained after experimental results. Therefore, based on Table 8 the average value from nanoindentation tests with both composites was calculated and adopted in the work as single values for each temperature, as shown in Table 9.

Table 9 – Elastic modulus (in GPa) at high temperatures adopted in the work, calculated from average values obtained for composites (as detailed in Table 8).

Material	$E_{average}$ (GPa)		
	700 °C	750 °C	800 °C
Metal matrix composites produced	168	158	149

## 4.2 Development over long isothermal aging

Carbides and oxides found both in composites and non-reinforced variants were measured, at initial state and after 1000 h of aging at 800 °C. A significant increase in the size of chromium carbides was observed in the composite produced by LEM + PS route, while in other materials it remained unchanged. Chromium oxides were identified in specimens produced by HEM + SPS route, also presenting growth in size after the overaging treatment. Titanium carbides added as reinforcement in the composites did not present visually dissolution with time, holding their original particle sizes.

Table 10 - Average diameter\* ( $\mu\text{m}$ ) of carbides and oxides, after isothermal aging at 800 °C.

Material	Processing	Overaging	TiC	Cr <sub>x</sub> C <sub>y</sub>	Cr <sub>x</sub> O <sub>y</sub>
Inconel X-750 non-reinforced	Hot rolled	Initial state	—	0.2	none
		After 1000 h	—	0.2	none
Inconel X-750 + TiC <sub>p</sub> 15 vol.%	LEM + PS	Initial state	3.2	0.2	none
		After 1000 h	3.2	1.4	none
Inconel X-750 non-reinforced	HEM + SPS	Initial state	—	0.1	none
		After 1000 h	—	0.1	1.8
Inconel X-750 + TiC <sub>p</sub> 15 vol.%	HEM + SPS	Initial state	0.3	n/d	0.8
		After 1000 h	0.3	n/d	1.9

\* Standard deviations: TiC =  $\pm 0.1 \mu\text{m}$ ; Cr<sub>x</sub>C<sub>y</sub> =  $\pm 0.4 \mu\text{m}$ ; Cr<sub>x</sub>O<sub>y</sub> =  $\pm 0.3 \mu\text{m}$ .

During isothermal aging at 700°, the microstructure at steps between the initial state condition and 1000 h of overaging were examined, comprising of 50, 100, 200, 400 and 700 h. The size of  $\gamma'$  precipitates was observed to remain almost constant in the composite produced by LEM + PS (Figure 57), and presented only a small growth in the variant produced by HEM + SPS (Figure 58). Contrastingly, at 800 °C both variants presented a large growth of  $\gamma'$ , with the composite prepared by LEM + PS (Figure 59) showing a faster pace of evolution, and the variant produced by HEM + SPS (Figure 60) catching up only after 700 h of isothermal treatment. The average diameter at each step, including initial state and after 1000 h, is shown in Figure 62.

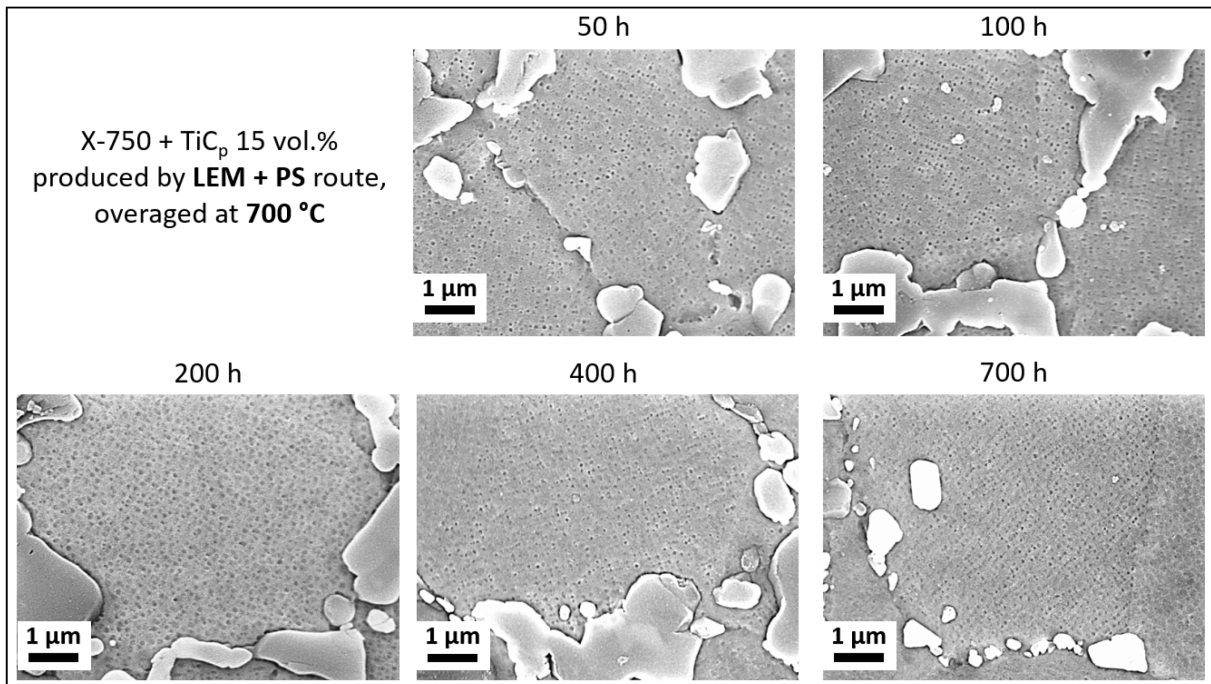


Figure 57 - Images taken at intermediate steps during long isothermal aging at 700 °C from the composite X-750/TiC 15 vol.% produced by LEM + PS route, showing a negligible evolution of  $\gamma'$ .

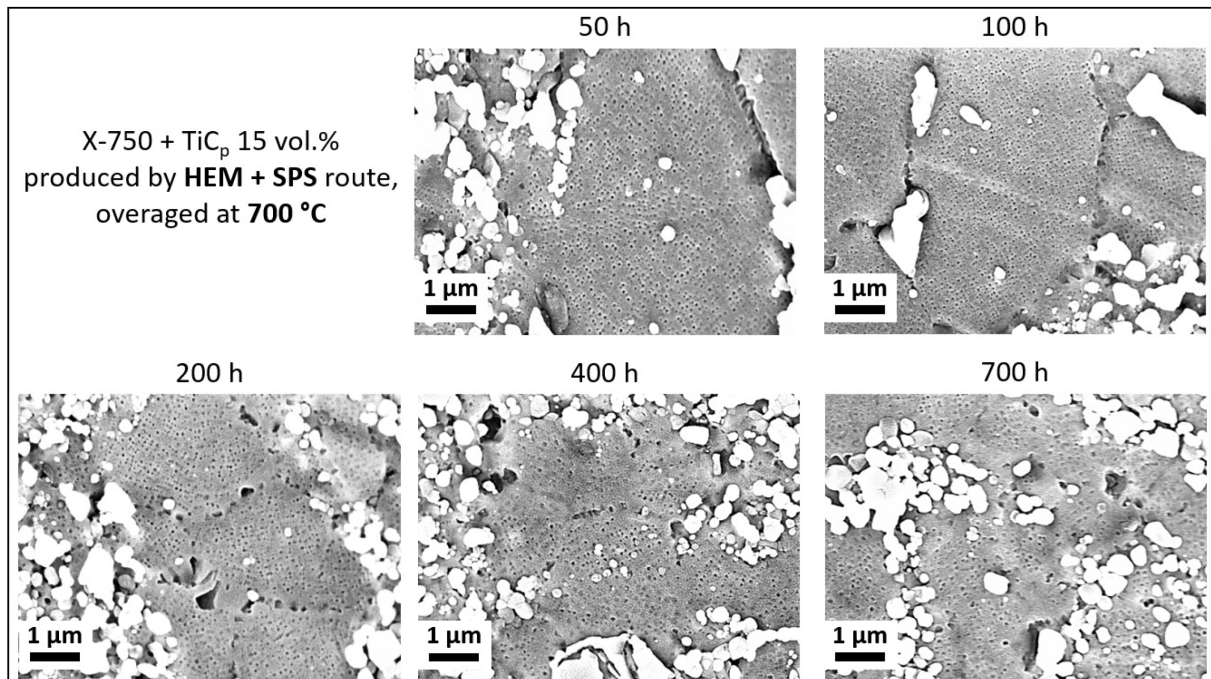


Figure 58 - Images taken at intermediate steps during long isothermal aging at 700 °C from the composite X-750/TiC 15 vol.% produced by HEM + SPS route, showing a modest evolution of  $\gamma'$ .

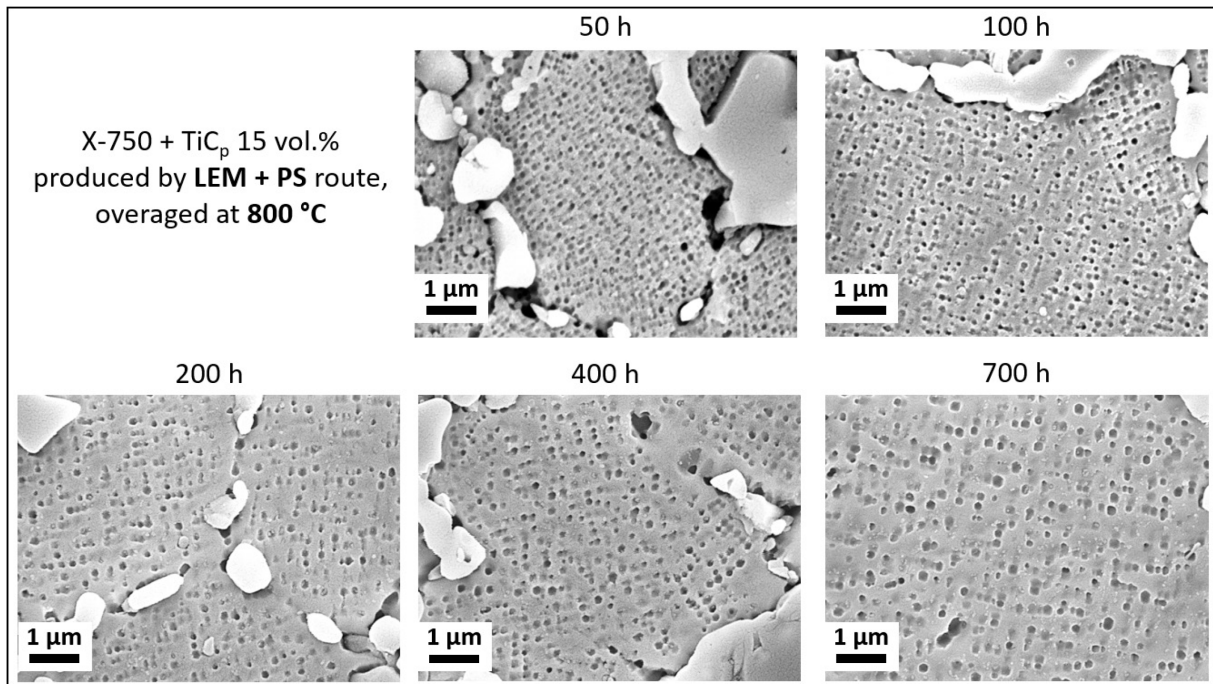


Figure 59 - Images taken at intermediate steps during long isothermal aging at 800 °C from the composite X-750/TiC 15 vol.% produced by LEM + PS route, showing the evolution of  $\gamma'$ .

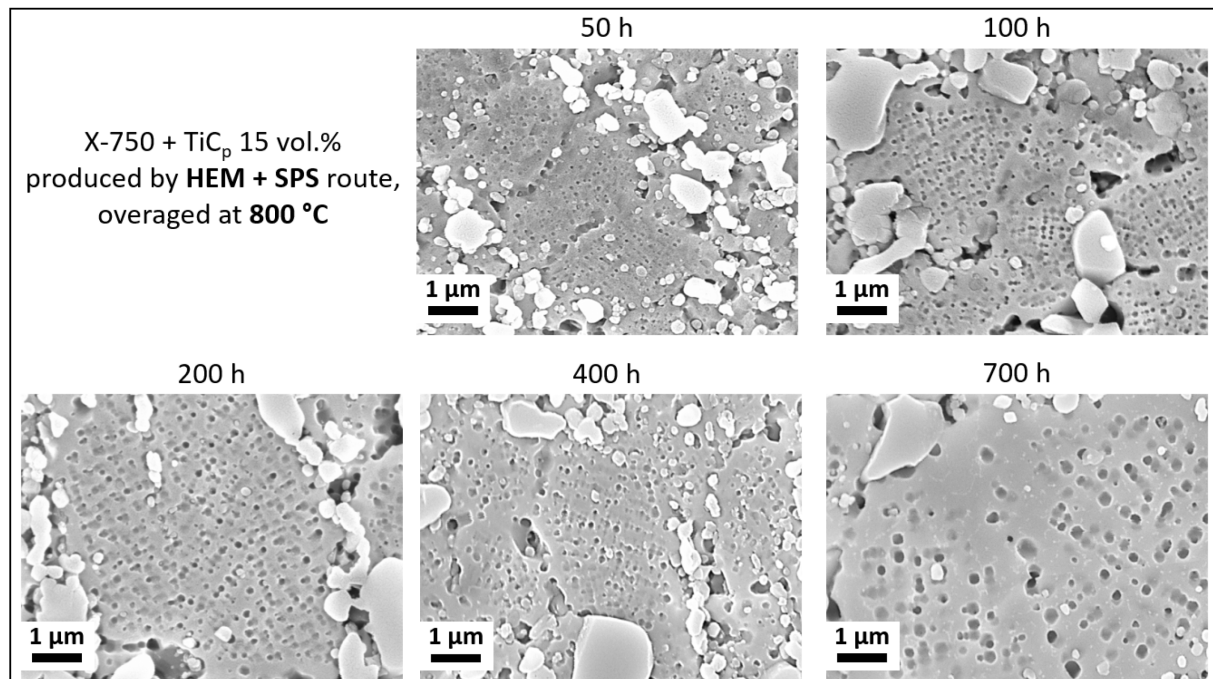


Figure 60 - Images taken at intermediate steps during long isothermal aging at 800 °C from the composite X-750/TiC 15 vol.% produced by HEM + SPS route, showing the evolution of  $\gamma'$ .

The presence of  $\gamma'$  was still confirmed in all overaged materials after 1000 h of exposure to 700 and 800 °C (Figure 61). Among the composites, the variant produced by the LEM + PS route presented the smallest particle size after 1000 h of aging at 700 °C, while at 800 °C the composite produced by HEM + SPS exhibited the smaller  $\gamma'$  size in average (Figure 62). When considering only the non-reinforced variants, the X-750 produced by hot rolling showed the highest growth of particles after 1000 h at both tested temperatures, while the variant produced by HEM + SPS exhibited the lowest  $\gamma'$  growth at 800 °C.

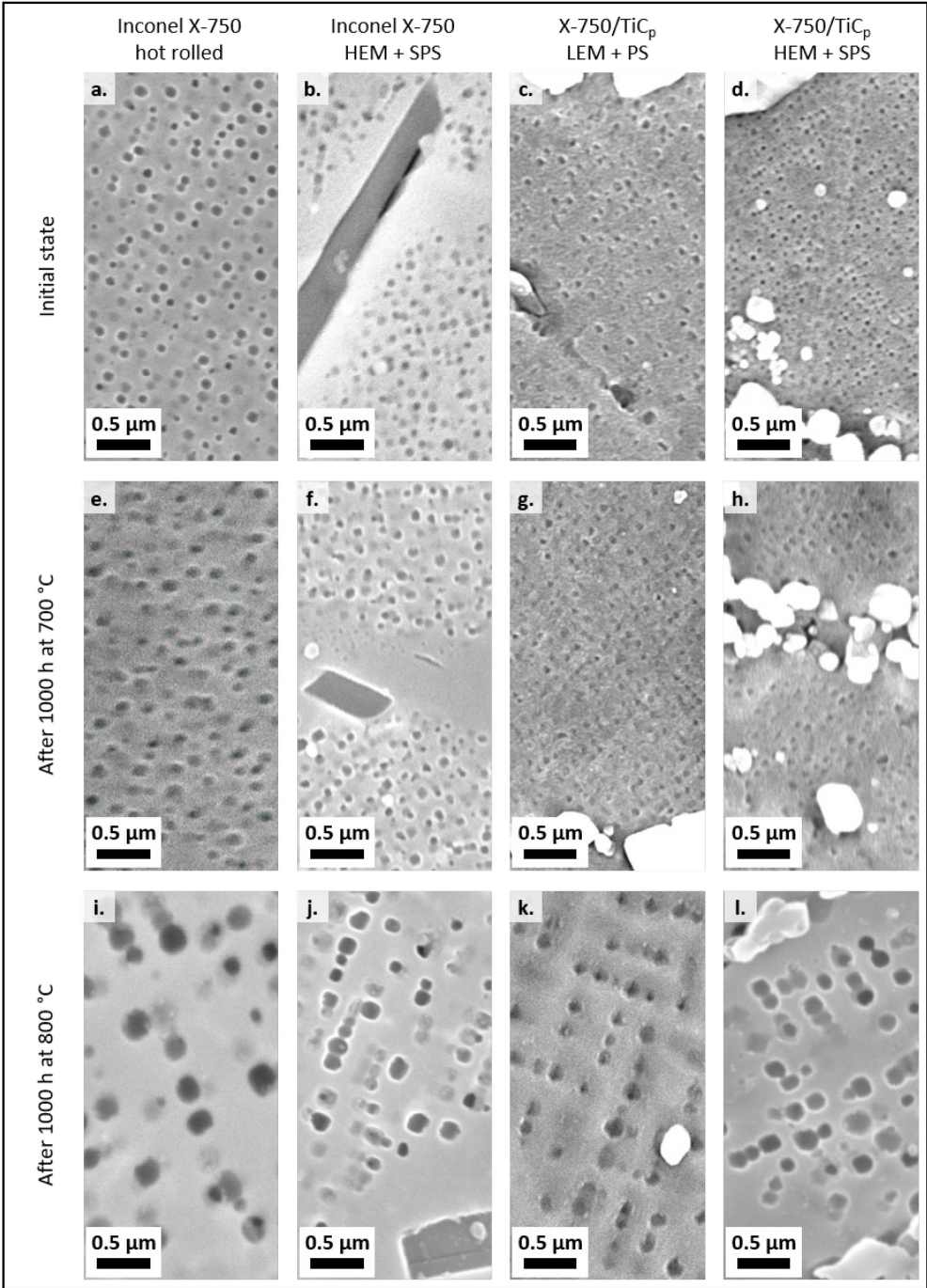


Figure 61 – Comparison between different materials (columns) and conditions of treatment (lines), at initial state (a, b, c, d), after 1000 h at 700 °C (e, f, g, h) and after 1000 h at 800 °C (i, j, k, l).

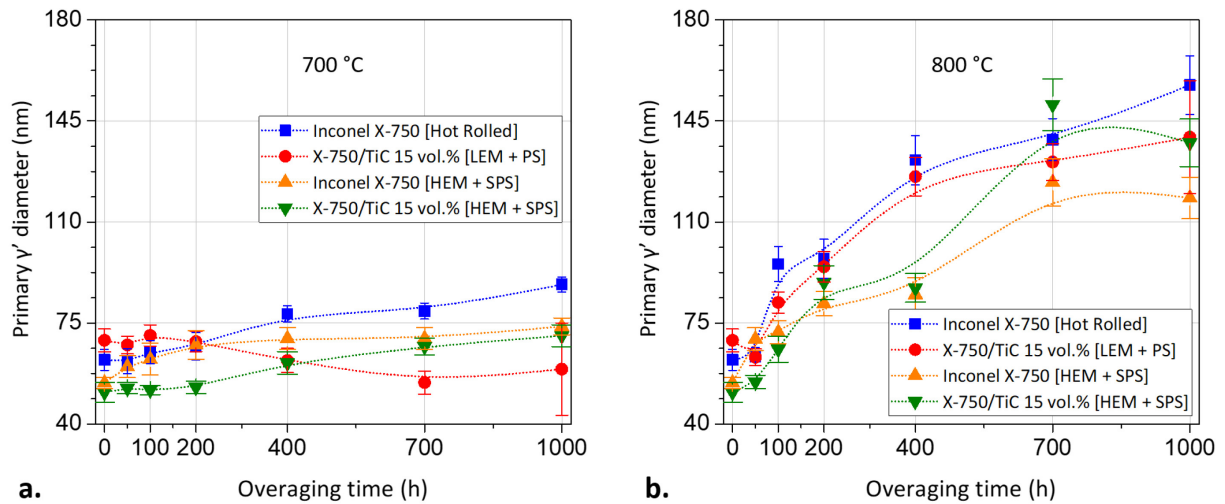


Figure 62 - Evolution of average size of primary  $\gamma'$  precipitates, after aging at a) 700 °C and b) 800 °C. Bars represent the confidence interval, for a significance level ( $\alpha$ ) of 0.05.

MC particles in the composite produced by LEM + PS route, that includes both the added  $TiC_p$ , but also the hexagonal (Al,Nb,Ti)C form that occurs in the non-reinforced hot rolled variant, were all observed to be enriched in Nb and Al during the overaging treatment. However, the partition of these elements in MC is not homogeneous, often presenting an irregular distribution (Figure 63).

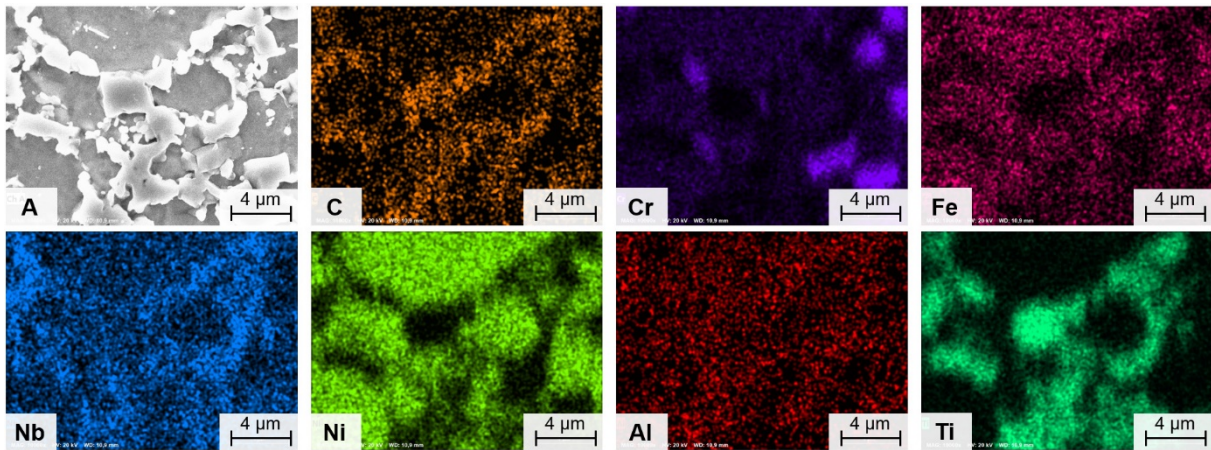


Figure 63 - EDS elements map of X-750/TiC 15 vol.% produced by LEM + PS, after aging for 1000 h at 800 °C. The original SE image is represented by A.

Chromium oxides observed in the composite produced by HEM + SPS route and submitted to overaging were frequently located in the vicinity of large Chromium and Titanium carbides (Figure 64). Punctual EDS analysis showed that MC particles in this material were enriched in Ti and Al, but also contained higher amounts of Nb and Cr in comparison to specimens produced by the LEM + PS route.

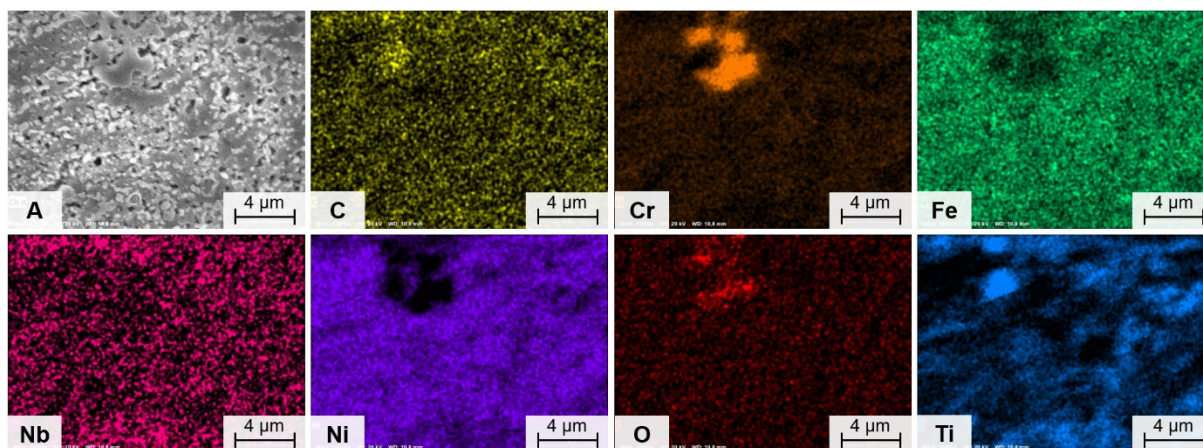


Figure 64 - EDS elements map of X-750/TiC 15 vol.% produced by HEM + SPS, after aging for 1000 h at 800 °C. The original SE image is represented by A.

The content of Ti, Nb, Al and Cr in  $TiC_p$  was measured with EDS punctual analysis, to obtain the average amount of these elements in the carbide (Table 11). At the initial state, the composite produced via LEM + PS route showed the highest content contents of Ti and Al, while the variant produced by the HEM + SPS process exhibited increased amounts of Nb and Cr, relative to its counterpart. After the long isothermal aging, both composites were enriched in Ti, but the variant produced by HEM + SPS showed also an increase in the Nb content. A precise amount was not determined, once the very fine  $TiC_p$  in this variant leads to a large distribution of values in punctual analysis. However, the measurements generally suggest a consistently higher quantity of the element on this composite. The investigation on the  $TiC$  particles makes possible to infer the availability of elements in  $\gamma$  solution.

Table 11 - Average content of selected elements (at.%) measured with EDS punctual analysis at  $TiC$  particles. In the non-reinforced alloy, the measurement was conducted on the MC precipitates.

		Ti	Nb	Al	Cr
<b>Initial state</b>	Inconel X-750 hot rolled	40.5	39.5	0.9	1.7
	X-750/TiC 15 vol.% [LEM + PS]	69.8	2.8	0.7	2.6
	X-750/TiC 15 vol.% [HEM + SPS]	56.9	4.6	0.0	4.6
<b>After 1000 h at 700 °C</b>	Inconel X-750 hot rolled	19.4	20.5	0.8	9.1
	X-750/TiC 15 vol.% [LEM + PS]	79.3	1.3	0.0	0.7
	X-750/TiC 15 vol.% [HEM + SPS]	Enriched in Ti and Nb			
<b>After 1000 h at 800 °C</b>	Inconel X-750 hot rolled	30.8	42.6	0.1	1.6
	X-750/TiC 15 vol.% [LEM + PS]	79.2	2.4	0.0	0.6
	X-750/TiC 15 vol.% [HEM + SPS]	Enriched in Ti and Nb			



XRD results (Figure 65) confirmed that both composites presented  $\gamma'$  precipitates also after 1000 h of aging treatments, at 700 and 800 °C. However, the variant produced by HEM + SPS route also displayed the presence of  $\eta$  phase, in addition to the hexagonal close-packed MC precipitate.

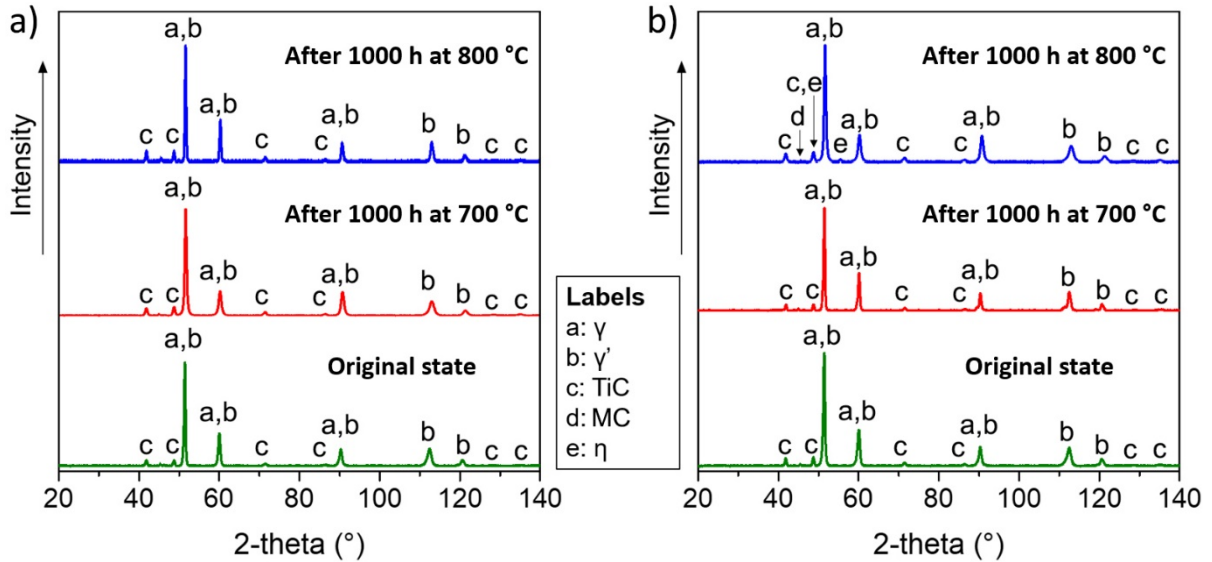


Figure 65 - XRD diffractograms of composites produced by a) low energy mixing + pressure sintering and b) high energy milling + spark plasma sintering, submitted to different aging times.

Hardness measurements (Figure 66) revealed a significant decrease in values on all investigated materials in the first 100 h of aging, for specimens treated at 800 °C. This behavior was not observed when the aging was performed at 700 °C. The composite prepared by LEM + PS route was particularly affected by a loss of hardness after 1000 h at both temperatures. In contrast, the variant produced by HEM + SPS exhibited a high stability in hardness, presenting only a marginal fluctuation at both tested temperatures.

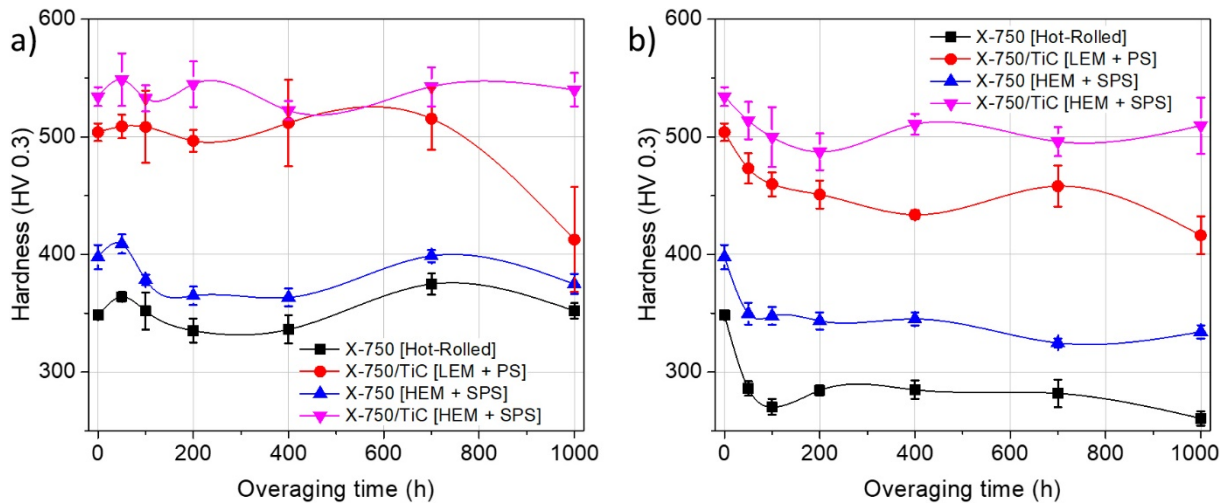


Figure 66 - Average hardness evolution of specimens submitted to aging at a) 700 °C and b) 800 °C. Bars represent the confidence interval, for a significance level ( $\alpha$ ) of 0.05.

### 4.3 Tensile creep results

Results from tensile creep tests were divided in microstructure analysis after fracture and mechanical properties. The tests were conducted only in two selected materials: a non-reinforced variant, Inconel X-750 hot rolled, and a composite, X-750/TiC 15 vol.% produced by LEM + PS route.

#### 4.3.1 Microstructure after rupture

All specimens submitted to tensile creep tests presented semi-fragile rupture, with intergranular fracture. At the temperature range used for the tests (700 to 800 °C), the fracture occurred always perpendicular to the strain axis. The Inconel X-750 hot rolled underwent failure through cracks originating at MC carbides, that grew through the grain boundaries filled with chromium carbides (Figure 67 a). In a similar fashion, the composite failed by the spread of a cracks through grain boundaries adorned with  $TiC_p$  (Figure 67 b), but in this case the origin is harder to establish. In some areas an agglomeration of  $TiC_p$  suggests the point of origin, but that is not always clearly the case.

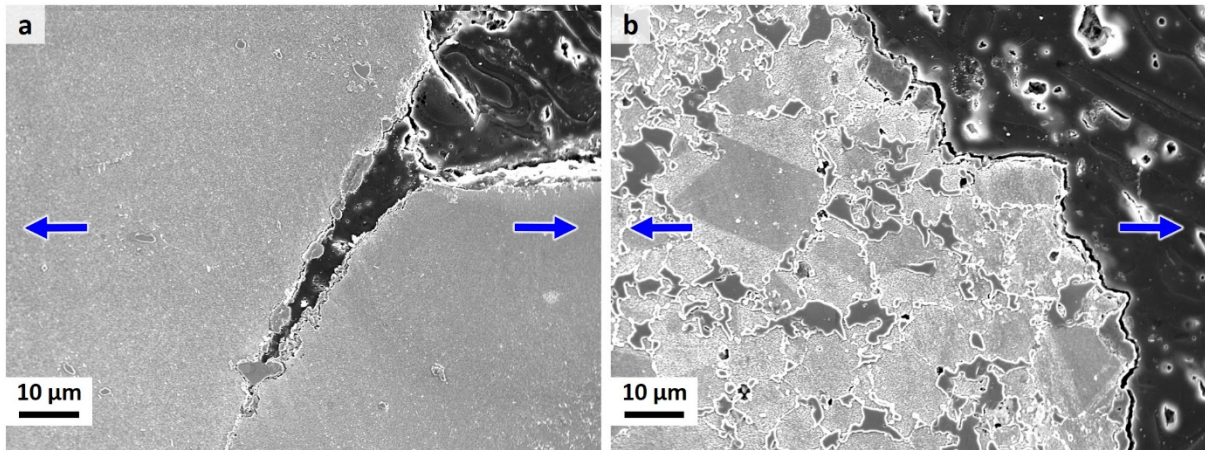


Figure 67 - SEM-SE image of longitudinal cut of tensile creep specimens tested at 800 °C with 340 MPa, showing the ruptured area near the surface of a) Inconel X-750 hot rolled and b) X-750/TiC 15 vol.% produced by LEM + PS route. The tension axis is indicated by arrows.

Cracks measuring up to 600 µm in length were frequently observed in the composite, near approximately 1 µm from the parallel surface of rupture (Figure 68 a). The cracks also exhibited small ramifications and presented an intergranular path (Figure 68 b). No changes in the grains geometry were observed. Likewise, around the cracks path no other microstructural or chemical changes were noticed. The dark areas in the images are due to inconsistencies in the etching.

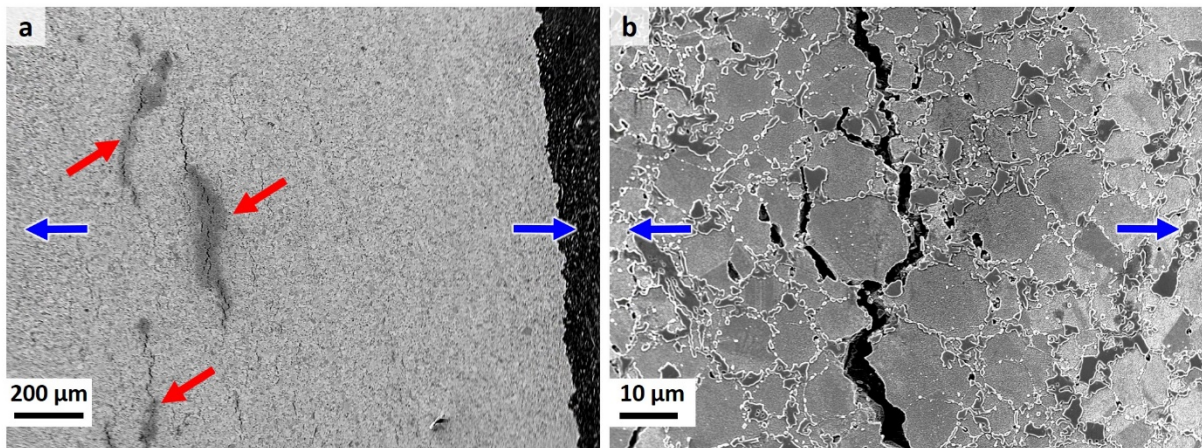


Figure 68 - SEM-SE image of longitudinal cut of ruptured X-750/TiC 15 vol.% produced by LEM + PS after tensile creep test conducted at 800 °C with 340 MPa, showing a) low magnification view of region near rupture, with cracks marked by red arrows; b) detail of intergranular crack initiating at circa 1 µm from the ruptured surface. The tension axis is indicated by blue arrows.

A closer observation of the microstructure revealed  $\gamma'$  precipitates enlarged in both materials (Figure 69), still presenting also a fine dispersion of secondary  $\gamma'$  between the bigger precipitates. The primary  $\gamma'$  particles were occasionally aligned at distinct directions in relation to strain axis, but not coalesced. No change in the amount of  $\gamma'$ -free zones was observed.

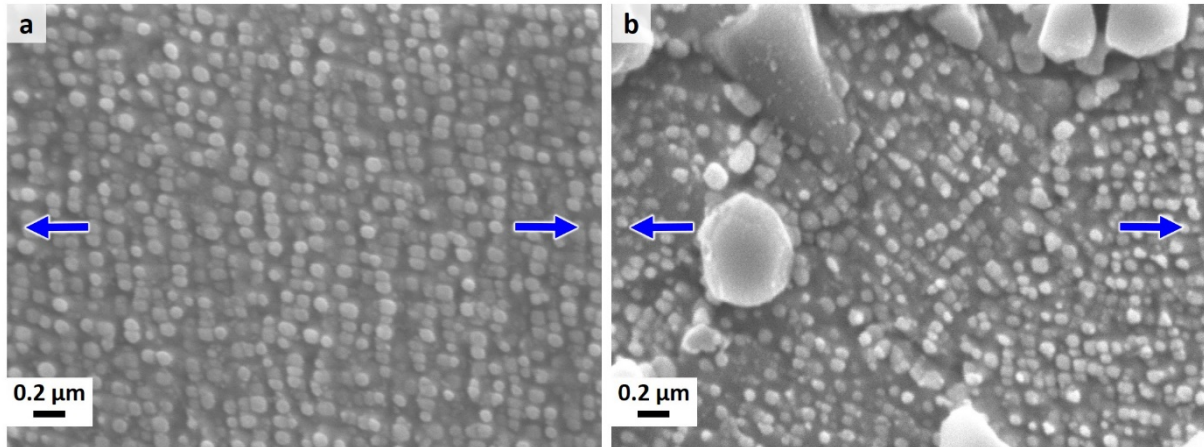


Figure 69 - SEM-SE image of longitudinal cut of ruptured tensile creep specimens after test at 800 °C with 340 MPa, showing a) Inconel X-750 hot rolled and b) X-750/TiC 15 vol.% produced by LEM + PS route. The tension axis is indicated by arrows.

#### 4.3.2 Creep-rupture curves and determination of parameters

The non-reinforced reference presented longer times to rupture in comparison to the composite X-750/TiC 15 vol.% produced by LEM + PS route, particularly at 800 °C (Figure 70). The disparity between them, however, diminished when the stress was increased. Conversely, the time to rupture differences between both materials diminished with a decrease in temperature, as observed in results from 750 °C (Figure 71 b). At 700 °C (Figure 71 a) was observed the highest proximity between both materials.

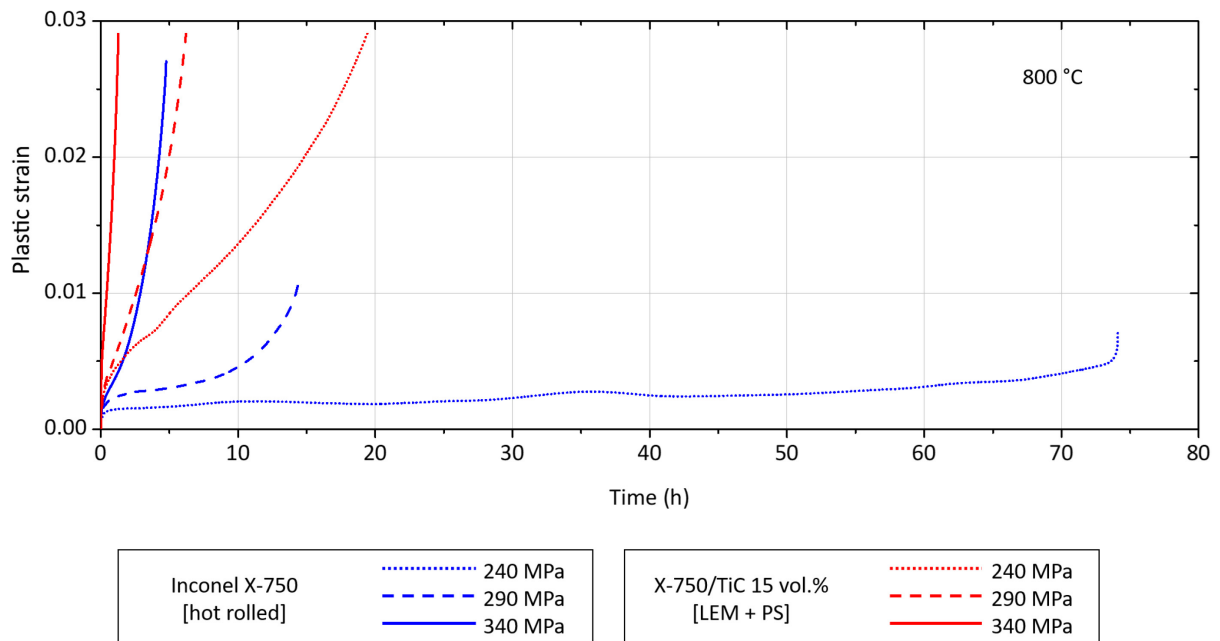


Figure 70 - Strain vs. time curves from tensile creep to rupture tests of Inconel X-750 hot rolled and X-750/TiC 15 vol.% produced by LEM + PS route at 800 °C.

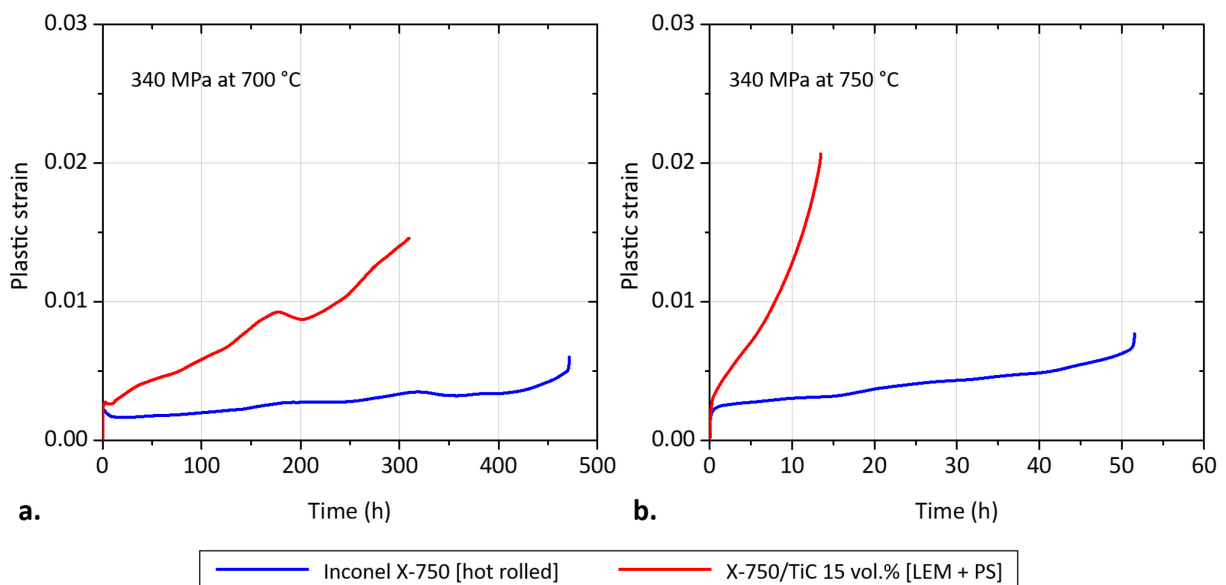


Figure 71 - Strain vs. time curves from tensile creep to rupture tests of Inconel X-750 hot rolled and X-750/TiC 15 vol.% produced by LEM + PS route with 340 MPa at a) 700 °C and b) 750 °C.

Ductility was improved in the composite, particularly at lower stresses and lower temperatures. All tests conducted in the MMC resulted in creep strain values over 1%, while the non-reinforced variant surpassed this limit only when tested at 800 °C with stresses over 290 MPa. Tests conducted at 700 °C resulted in particularly low deformation values for the non-reinforced alloy, in addition to serrated yielding in the plot of strain creep vs. time. The severity of the effect

was higher in tests conducted at lower stresses, situation when the serrations were also observed in experiments conducted at higher temperatures.

The serrated yielding produced periods of negative creep strain, particularly in the second stage of creep. The evolution to the tertiary creep stage was shorter in the non-reinforced variant, notably at lower temperatures (Figure 72). The minimum creep rates observed on this material were also lower at all tested stresses, compared to the composite produced by LEM + PS (Figure 73). Notwithstanding, at 700 °C the differences between reinforced and non-reinforced variants were significantly smaller, with both materials reaching the same power ( $10^{-9} \text{ s}^{-1}$ ) of strain rate.

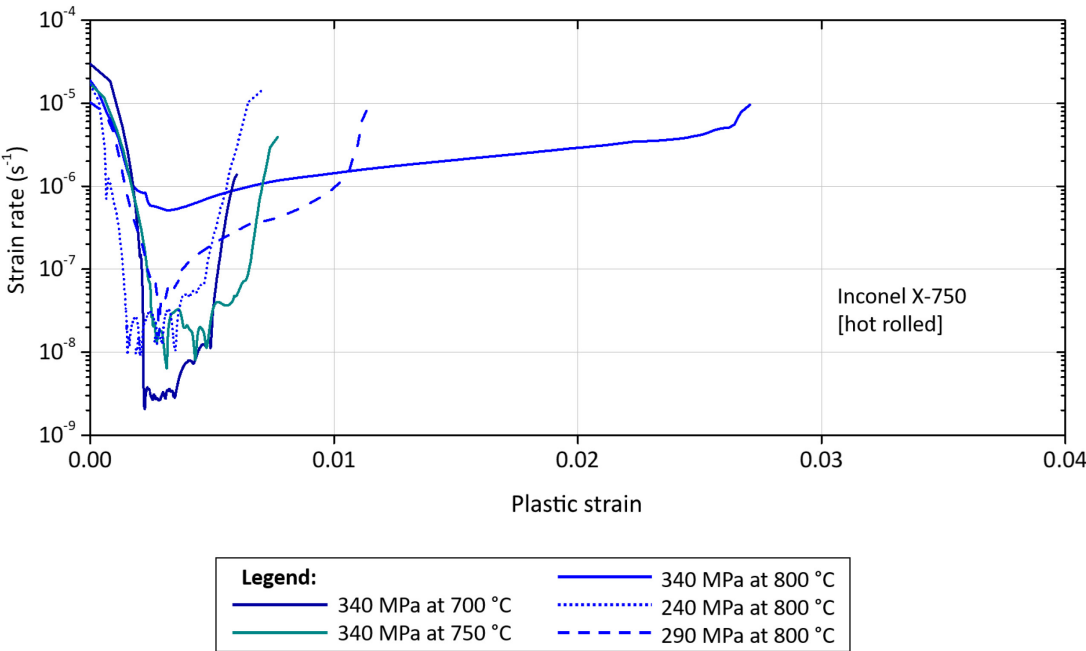


Figure 72 - Strain rate vs. strain curves from tensile creep to rupture tests of Inconel X-750 hot rolled, tested between 700 and 800 °C.

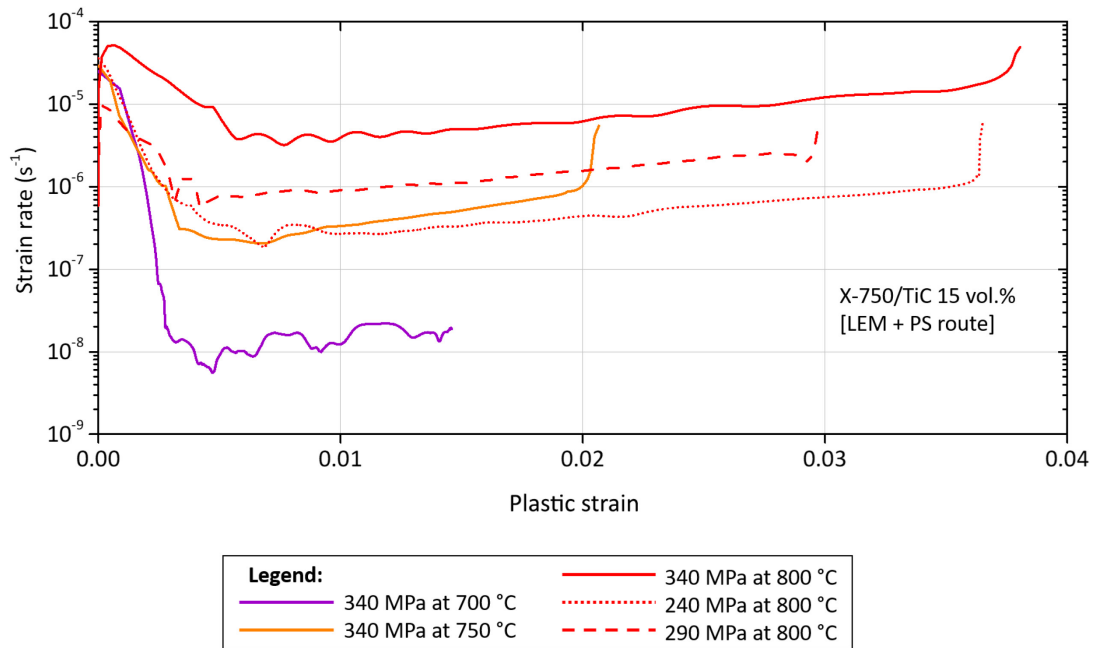


Figure 73 - Strain rate vs. strain curves from tensile creep to rupture tests of X-750/TiC 15 vol.% produced by LEM + PS route, tested between 700 and 800 °C.

A threshold stress was observed on both tested variants. An estimation of the true total threshold stress using the approximation method (power fitting) [164] resulted in lower values in the composite (Figure 74 a). An increase in  $\sigma_{TH}$  with the decrease in temperature of test was also observed, with the non-reinforced alloy presenting  $\sigma_{TH} = 132$  MPa at 800 °C and 222 MPa at 700 °C. The variation was investigated in this variant alone since it was the sole one to provide enough specimens for the analysis.

The apparent activation energy ( $Q_{app}$ ) was in the same order for both variants (Figure 74 b), but to obtain the true creep activation energy ( $Q_c$ ) it is necessary to take into account the threshold stress, the true stress exponent and the temperature dependence, as provided by Equation 8. Therefore, for the Inconel X-750 hot rolled it was obtained  $Q_c = 333$  kJ/mol. For the composite produced by LEM + PS route obtaining  $Q_c$  was not feasible, since at least two different stress at three temperatures must be tested to calculate the true creep activation energy. Therefore, these experiments were conducted with compression creep tests, as examined in section 4.4.2.

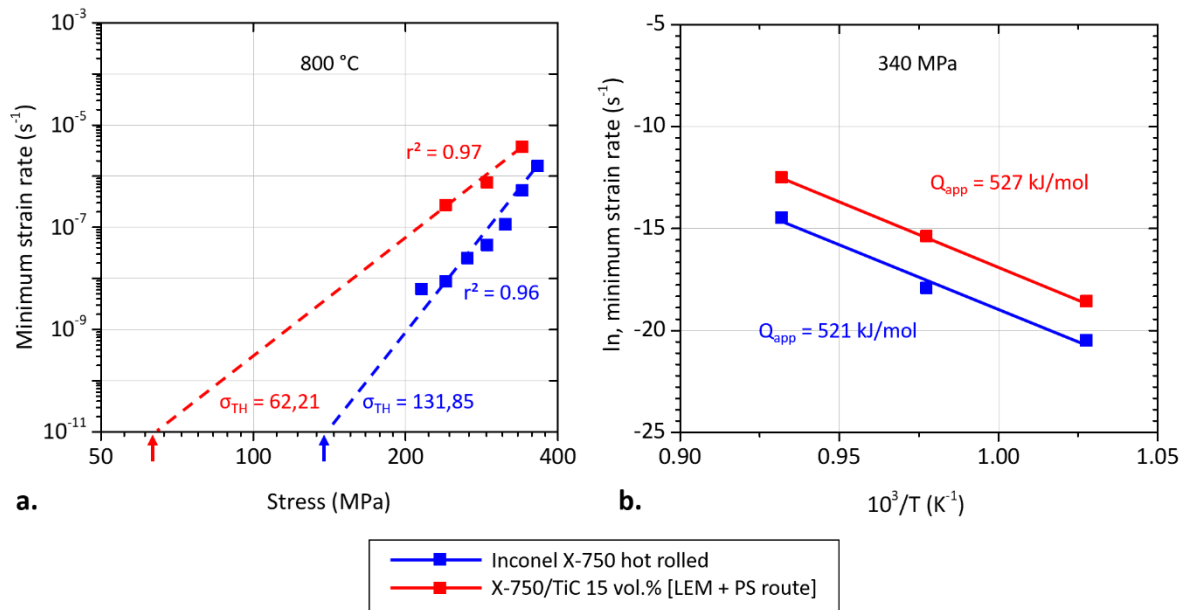


Figure 74 – Creep parameters: a) true total stress  $\sigma_{TH}$  estimated at  $800\text{ }^{\circ}\text{C}$  (indicated by arrows) and b) apparent creep activation energy  $Q_{app}$ , obtained with  $\sigma = 340\text{ MPa}$  between  $700$  and  $800\text{ }^{\circ}\text{C}$ .

The apparent Norton stress exponent was obtained for both varieties tested at  $800\text{ }^{\circ}\text{C}$ , resulting in significantly large values (Figure 75). The composite presented a slightly higher exponent ( $n \approx 13$ ), compared to the non-reinforced reference ( $n \approx 11$ ).

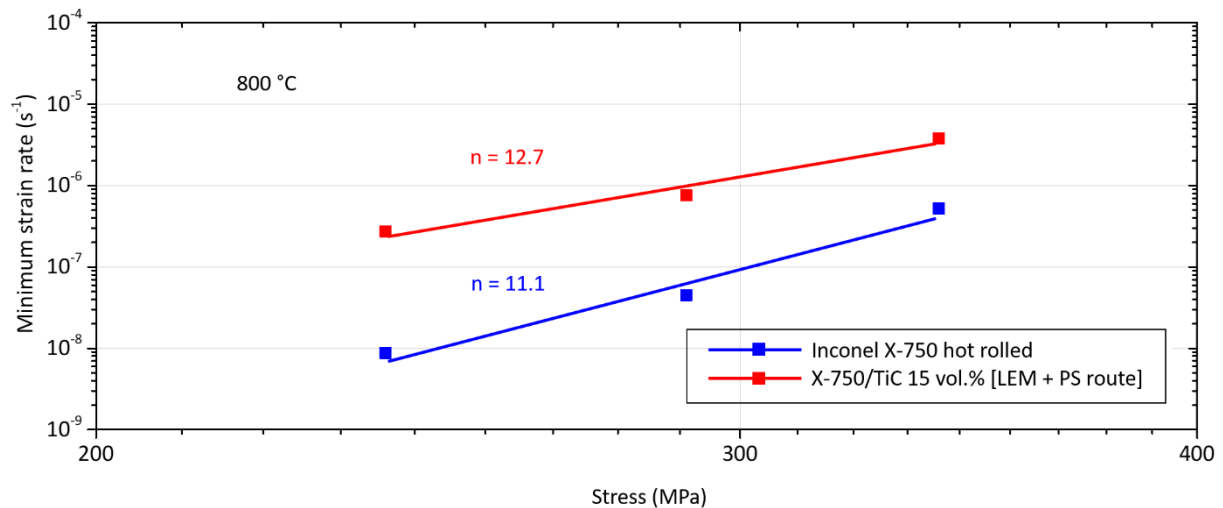


Figure 75 - Apparent stress exponents, given by the minimum strain rate vs. applied stress plot.



When considering the effective stress ( $\sigma - \sigma_{TH}$ ), the calculation of the true stress exponents resulted in values in the same range for both non-reinforced and reinforced variants at 800 °C, with  $n \approx 6$ . (Figure 76 a). A Monkman-Grant relationship covering temperatures between 700 and 800 °C was also established (Figure 76 b), resulting in linear approximations with a  $r^2$  value of 0.98 for both analyzed variants.

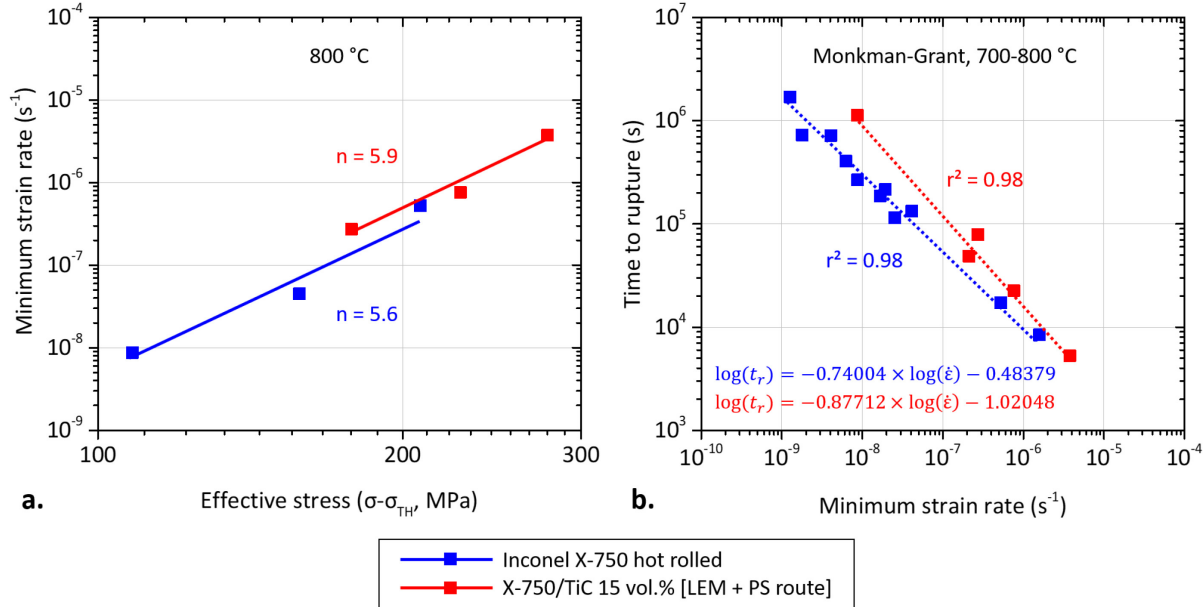


Figure 76 – Creep parameters: a) minimum strain rate vs. effective stress, showing true stress exponents obtained at 800 °C and b) Monkman-Grant relationship for creep tests conducted between 700 and 800 °C, including coefficient of determination ( $r^2$ ).

Creep life was also estimated with a Larson-Miller parametrization (Figure 77), considering results from all temperatures and stresses tested. A polynomial fitting was made, resulting in equations with determination coefficients of 0.98 and 1.00, respectively for the non-reinforced and the composite variants. A Larson-Miller constant  $C_{LM} = 20$  was calculated for the non-reinforced reference, and  $C_{LM} = 23$  was obtained for the composite produced by LEM + PS route, according to Manson and Mendelson method [172,179].

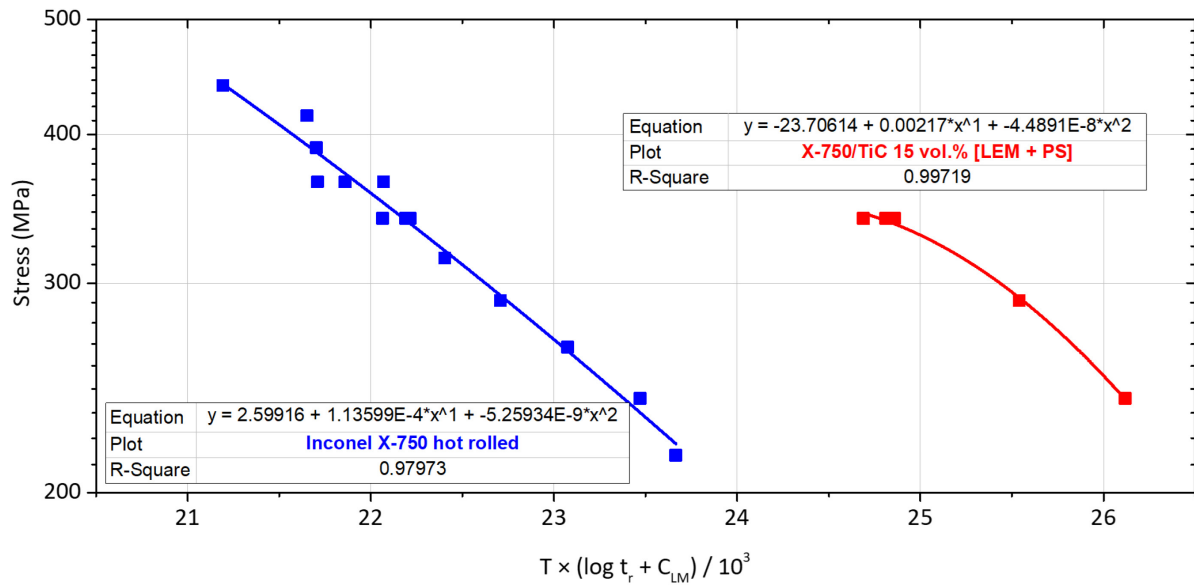


Figure 77 - Larson-Miller parametrization of specimens investigated in tensile creep tests.

To predict the effective creep rates in a turbine blade submitted to centripetal forces, the material density was considered as a parameter in a relation between the turbine rotations per minute (rpm) and the achievable minimum creep rates, extrapolated from tensile creep tests at 800 °C. Adopting the turbine blade parameters from the example given in section 2.1.1, a hypothetical case was conceived. From the relation, a crossing point between both materials curves was obtained at  $\dot{\epsilon} = 3.02 \times 10^{-5} s^{-1}$  (Figure 78 a), after which for higher revolutions per minute the non-reinforced variant is predicted to creep faster than the composite. A relation between the expected creep rates and the stress predicted at a turbine blade section was also established (Figure 78 b), resulting in an even point at 458 MPa, above which faster creep rates are anticipated in the non-reinforced alloy, in relation to the composite.

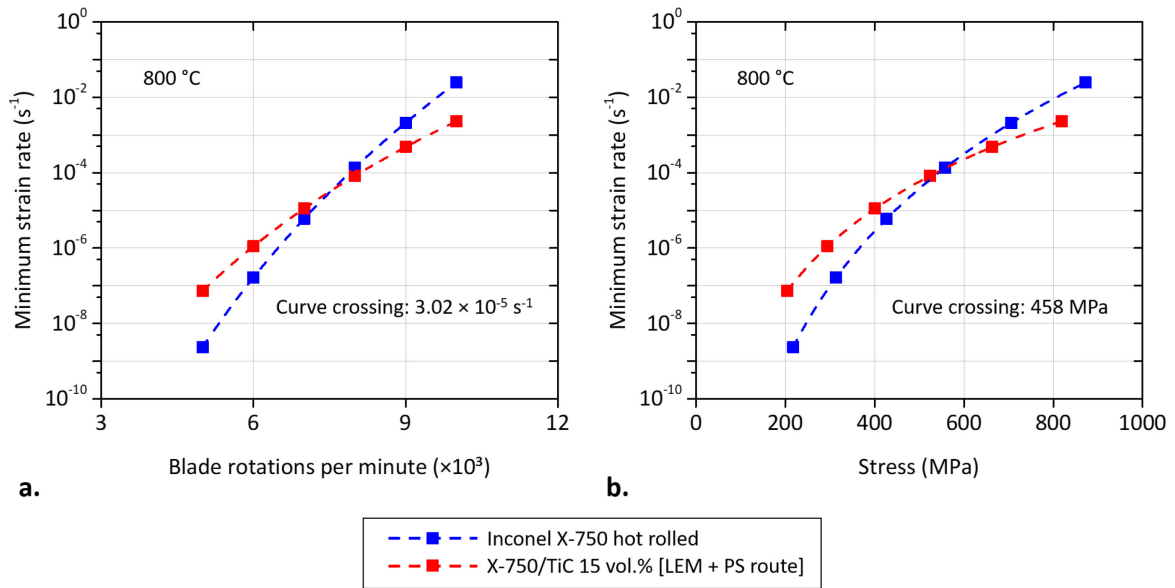


Figure 78 - Exemplification of minimum creep rates and stresses acting on a working turbine blade, showing crossing values between the non-reinforced and the composite variants at 800 °C.

## 4.4 Compression creep results

### 4.4.1 Microstructure after test

After compression creep tests conducted at 700 °C with 280 MPa (Figure 79), no significant changes to the grains morphology were observed. It is noted that the elongated segments devoid of TiC and aligned against the strain axis were still present in the composite produced by HEM + SPS after the compression test (Figure 79 c), as already observed in the specimens at initial state.

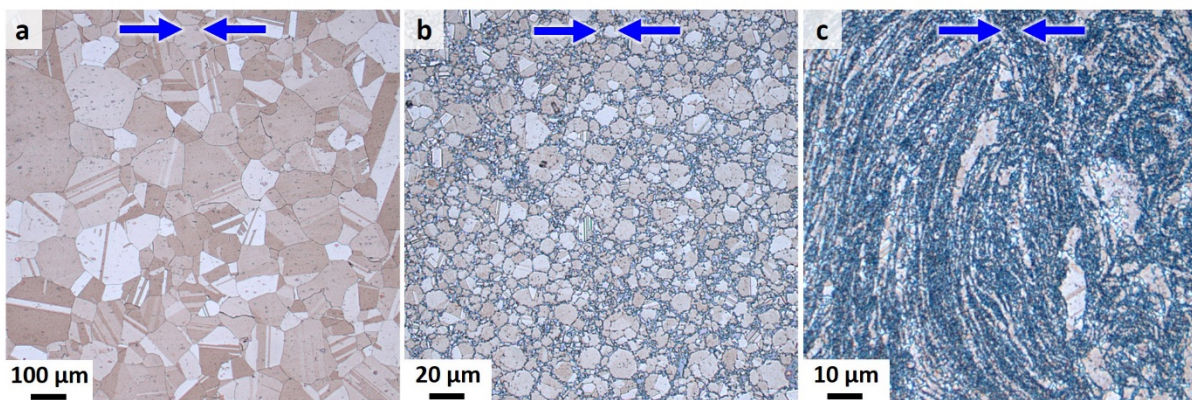


Figure 79 - Light microscopy images of longitudinal cuts of compression creep specimens tested at 700 °C and 280 MPa, showing a) Inconel X-750 hot rolled, b) X-750/TiC 15 vol.% produced by LEM + PS, c) X-750/TiC 15 vol.% produced by HEM + SPS. Arrows indicate the compression axis.

Subsequent to the compression tests at 700 °C with 280 MPa the growth of  $\gamma'$  particles in specimens from all investigated materials was observed, but the original morphology of both  $\gamma'$  and grain boundaries was largely preserved (Figure 80). No evident signs of particle breakage were found.

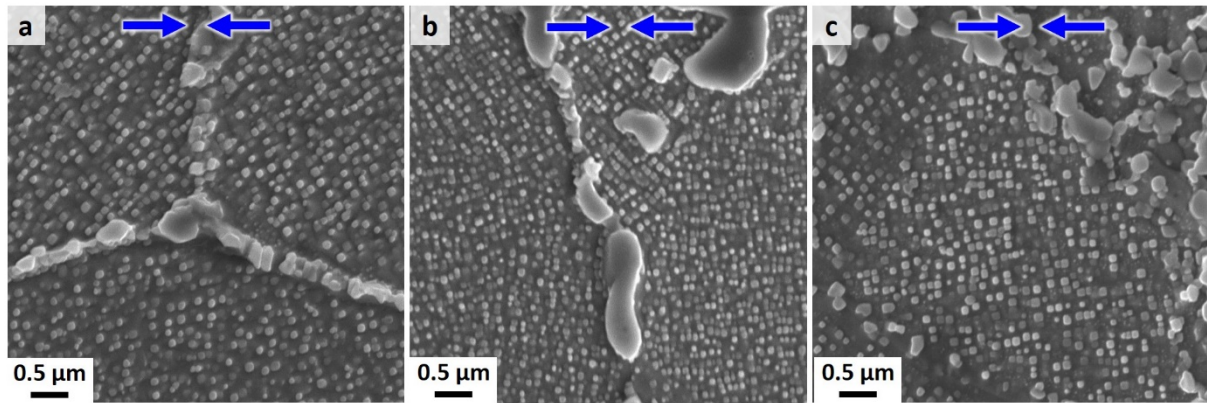


Figure 80 - SEM-SE images of longitudinal cuts of compression creep specimens tested at 700 °C with 280 MPa, showing a) Inconel X-750 hot rolled, b) X-750/TiC 15 vol.% produced by LEM + PS, and c) X-750/TiC 15 vol.% produced by HEM + SPS. Blue arrows indicate the compression axis.

Compression creep tests conducted at 750 °C with 280 MPa resulted in grains moderately deformed (Figure 81), showing evidence of a small elongation at 90° with the axis of compression. The composite produced by HEM + SPS presented elongated grain-like segments comparable to the conditions already observed in the material at initial state.

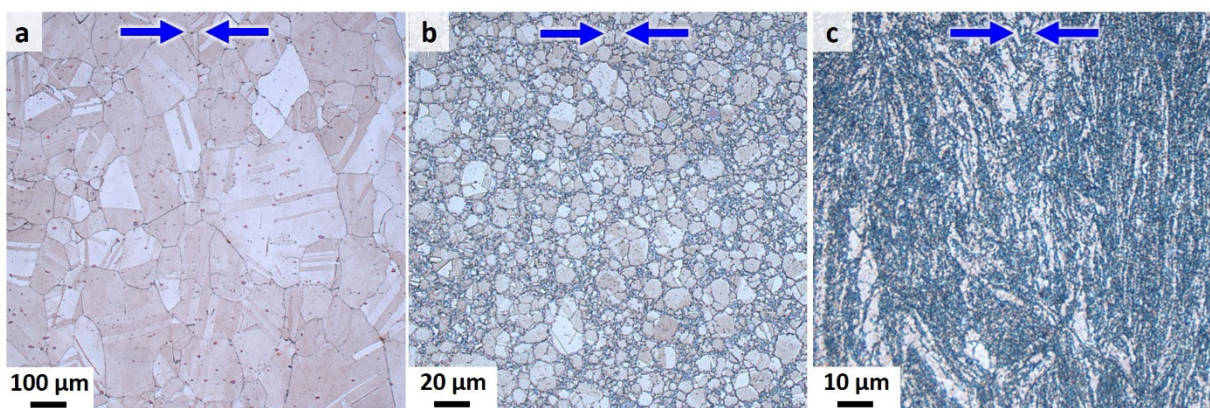


Figure 81 - Light microscopy images of longitudinal cuts of compression creep specimens tested at 750 °C with 280 MPa, showing a) Inconel X-750 hot rolled, b) X-750/TiC 15 vol.% produced by LEM + PS, and c) X-750/TiC 15 vol.% produced by HEM + SPS. Blue arrows indicate the compression axis.

Among specimens tested for creep at 750 °C with 280 MPa (Figure 82), the non-reinforced reference presented  $\gamma'$  particles elongated. The feature was only moderately observed in the composites, which exhibited this intermetallic with a predominantly equiaxial morphology. However, growth of  $\gamma'$  was observed in all tested materials, as evidenced in Table 12.

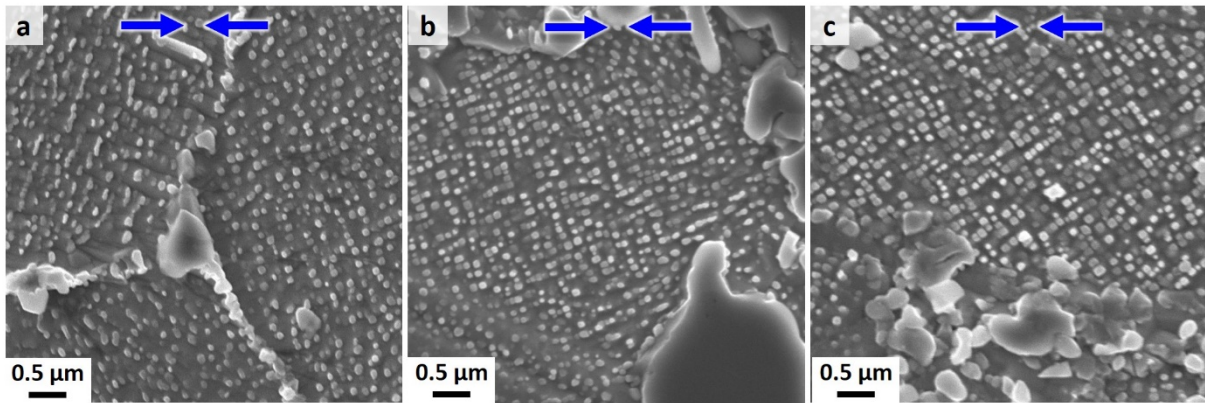


Figure 82 - SEM-SE images of longitudinal cuts of compression creep specimens tested at 750 °C with 280 MPa, showing a) Inconel X-750 hot rolled, b) X-750/TiC 15 vol.% produced by LEM + PS, and c) X-750/TiC 15 vol.% produced by HEM + SPS. Blue arrows indicate the compression axis.

Compression creep tests conducted at 800 °C with 280 MPa induced more significant changes in the microstructure of all tested materials. The non-reinforced reference showed the presence of occasional serrated grain boundary (Figure 83 a). A higher magnification (Figure 83 b) also revealed that  $\gamma'$  precipitates were enlarged and elongated in relation to the material in the original state. These precipitates were also inconsistently oriented in relation to the axis of compression, exhibiting a different direction in each grain.

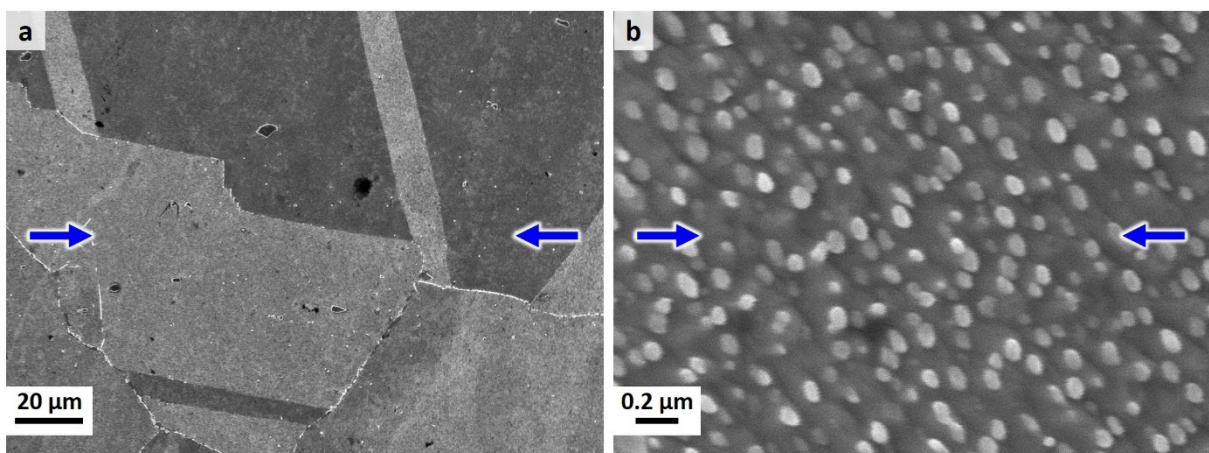


Figure 83 - SEM-SE images of longitudinal cuts of compression creep specimens from Inconel X-750 after test at 800 °C with 280 MPa. Blue arrows indicate the compression axis.

A stronger orientation of  $\gamma'$  intermetallics after the creep test at 800 °C with 280 MPa was observed in the composite X-750/TiC 15 vol.% produced by LEM + PS route, but again without the presence of a clear preferential orientation in relation to the axis of compression (Figure 84 a). However, it is reasonable to affirm that the majority of the precipitates presented themselves aligned within the range of 45° to 90° in reference to the stress axis. A closer look at  $\gamma'$  particles also reveals enlarged precipitates in this variant, presenting the elongated shape (Figure 84 b). Occasionally some of these particles were arranged in a near-touching pattern.

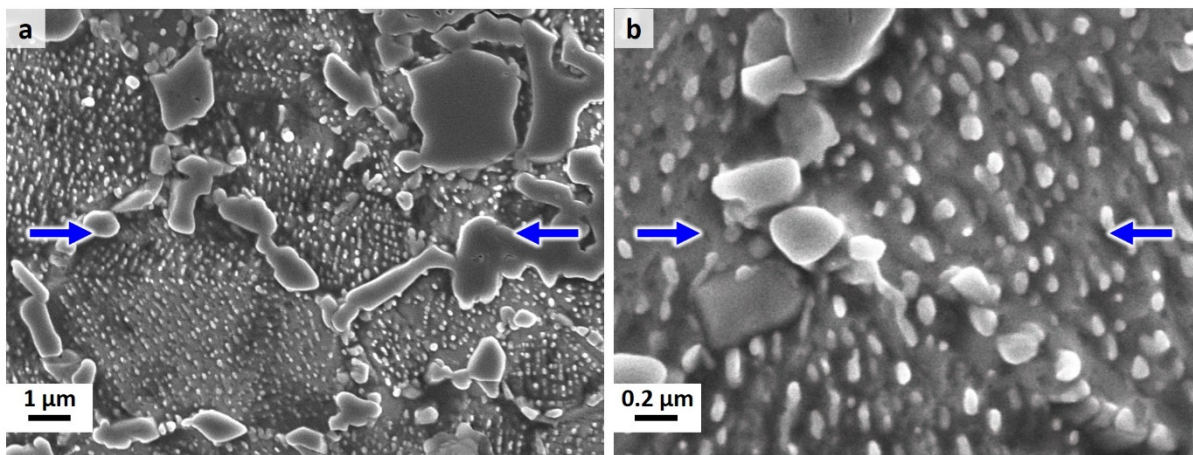


Figure 84 - SEM-SE images of longitudinal cuts of compression creep specimens from X-750/TiC 15 vol.% produced by LEM + PS after test at 800 °C with 280 MPa. Blue arrows indicate the compression axis.

Specimens from the composite X-750/TiC 15 vol.% produced by HEM + SPS route did not present a significant realignment of carbides after the test at 800 °C with 280 MPa. Closer to the surface, nonetheless, a flow of TiC at 90° with the axis of compression can be observed (Figure 85 a). A closer inspection also show a minor effect on  $\gamma'$  precipitates, but without apparent coalescence (Figure 85 b).

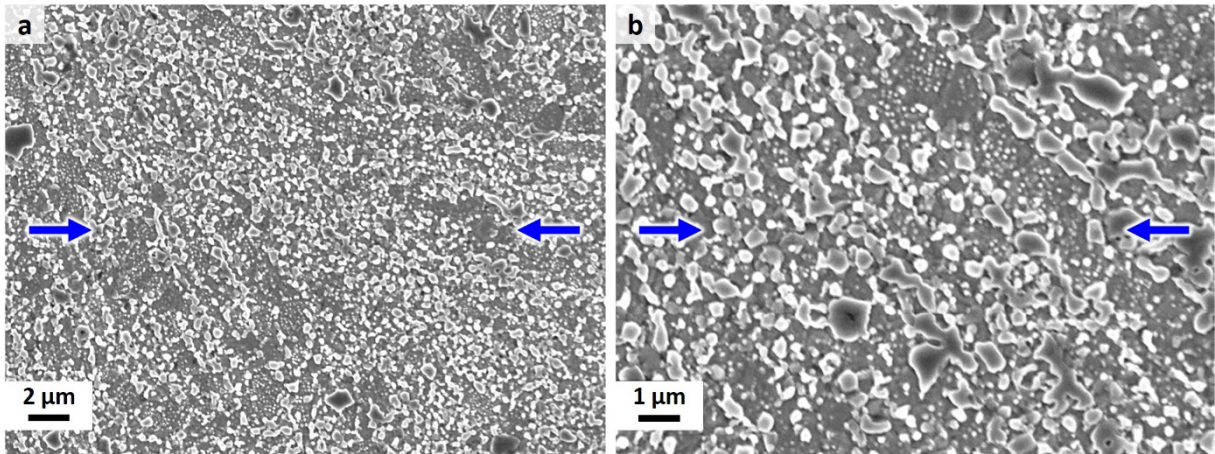


Figure 85 - SEM-SE images of longitudinal cut of compression creep specimens from X-750/TiC 15 vol.% produced by HEM + SPS after test at 800 °C with 280 MPa. Blue arrows indicate the compression axis.

Areas depleted of  $\gamma'$  were also frequently observed in all tested materials tested at 800 °C with 280 MPa (Figure 86). These zones were always situated near titanium and chromium carbides, often located at grain boundaries.

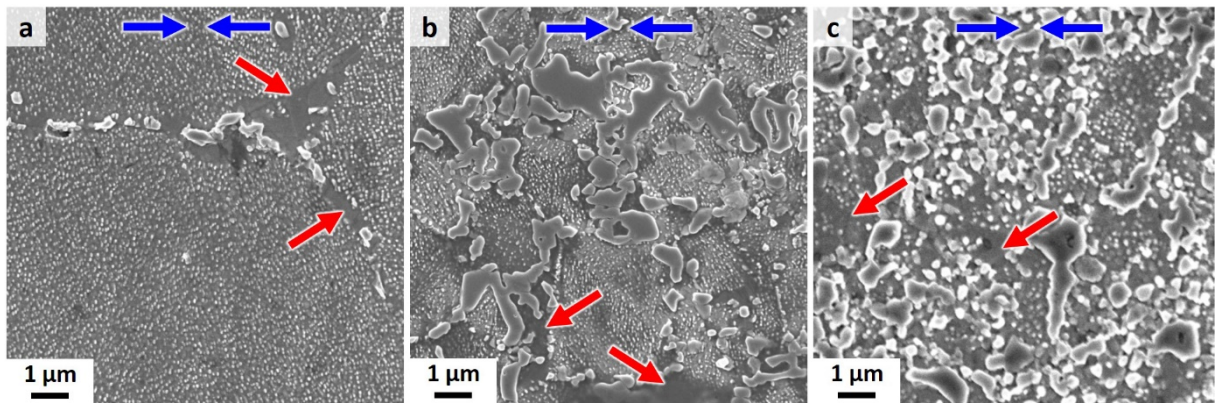


Figure 86 - SEM-SE images of longitudinal cut of compression creep specimens after test at 800 °C with 280 MPa, with red arrows indicating primary  $\gamma'$ -free zones in a) Inconel X-750 hot rolled, b) X-750/TiC 15 vol.% produced by LEM + PS, and c) X-750/TiC 15 vol.% produced by HEM + SPS. Blue arrows indicate the compression axis.

Rietveld refinement analysis combined with image quantification allowed the measurement of primary and secondary  $\gamma'$  volumes, before and after compression creep (Table 12). The volume of primary  $\gamma'$  was generally increased in all investigated alloys after creep tests conducted at 700 °C with 280 MPa, after 500 h. In contrast, volumes of secondary  $\gamma'$  diminished in all examined specimens.

Table 12 - Volume percent of primary and secondary  $\gamma'$  in specimens before and after compression creep at 700 °C and 280 MPa, after 500 h.

		$\gamma$ + carbides	Primary $\gamma'$	Secondary $\gamma'$
<b>Inconel X-750 hot-rolled</b>	Initial state	58.1	29.2	12.7
	After creep	54.0	38.3	7.7
<b>X-750/TiC<sub>p</sub> [LEM + PS]</b>	Initial state	58.1	27.8	14.1
	After creep	60.1	33.8	6.1
<b>X-750/TiC<sub>p</sub> [HEM + SPS]</b>	Initial state	60.6	28.4	11.0
	After creep	62.3	29.6	8.1

4.4.2 Creep curves and determination of parameters

Strain vs. time curves from compression creep tests conducted at 700 °C with 280 MPa show the composite produced by HEM + SPS route straining in the shortest time, followed by the non-reinforced reference and the composite produced by LEM + PS route, respectively (Figure 87 a). The test was interrupted after approximately 500 h, before some specimens could achieve 1% of strain. Serrations, which are often manifested as sections showing negative strain rates, were present in curves of all materials tested at 700 °C. When repeating the experiment with 440 MPa (Figure 87 b), the order of results was the same, but the composite produced by LEM + PS presented behavior closer to the non-reinforced material.

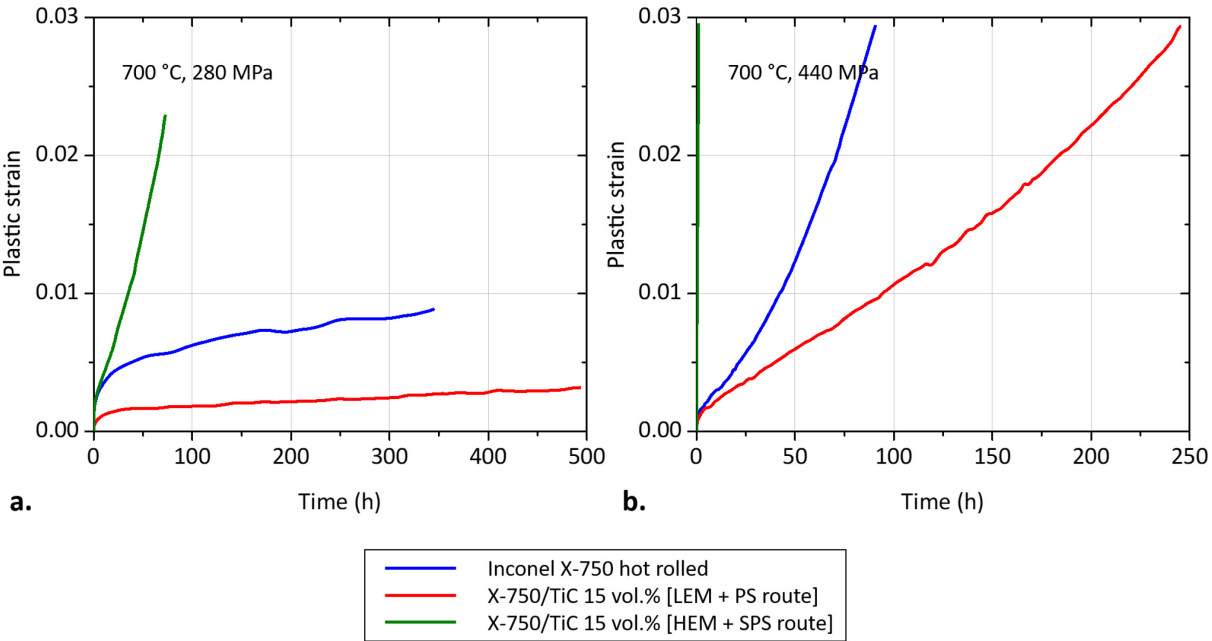


Figure 87 - Strain vs. time curves from interrupted compression creep tests conducted at 700 °C with applied stresses of a) 280 MPa and b) 440 MPa.



When observing strain rate vs. strain plots, the serrations are evident in the curves of all variants, but more severe at lower stresses (Figure 88 a). The composite produced by the LEM + PS route exhibited the slowest minimum strain rates, followed by the non-reinforced reference, and lastly by the composite produced by HEM + SPS method. Again at higher stress (Figure 88 b) the two last variants presented closer performance in relation to tests conducted at lower stresses.

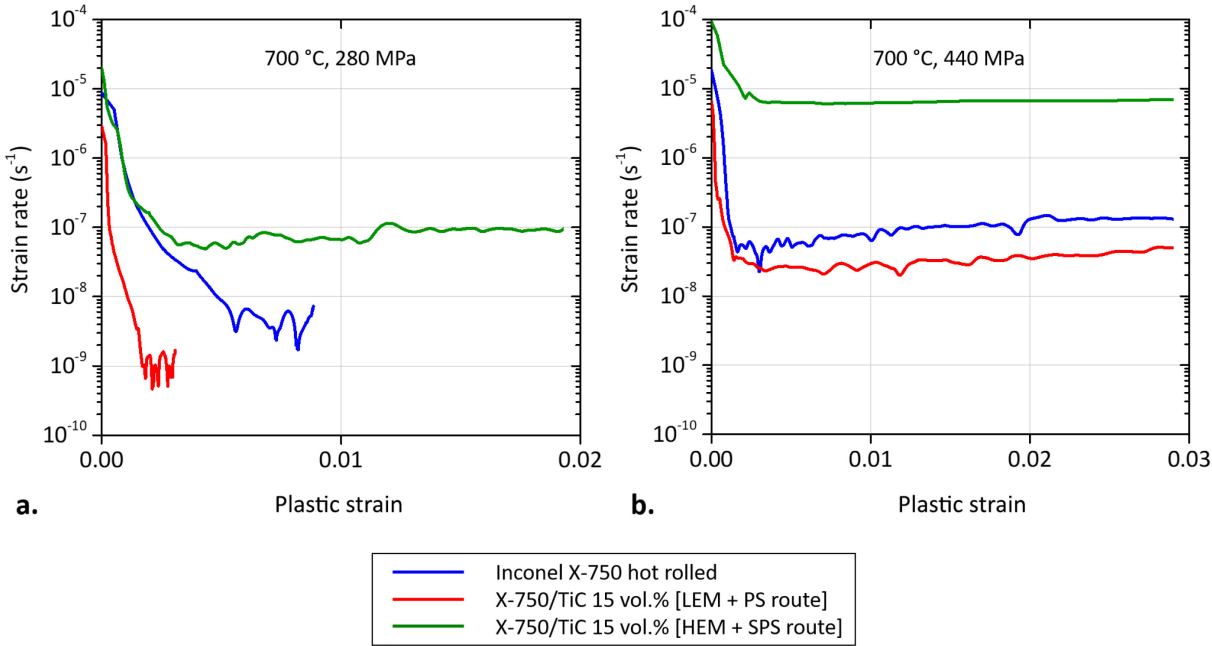


Figure 88 – Strain rate vs. strain curves from interrupted compression creep tests conducted at 700 °C with applied stresses of a) 280 MPa and b) 440 MPa.

At 750 °C the serrations in strain vs. time plots were reduced, and the composite produced by the HEM + SPS route experienced creep strain in even shorter times compared to other tested variants (Figure 89 a). However, at this temperature the non-reinforced reference also took a longer time to show the same creep strain levels, compared to the composite produced by LEM + PS. When observing strain rate vs. strain curves (Figure 89 b), the variant produced by HEM + SPS shows a creep rate two orders of magnitude faster than other tested materials, while the non-reinforced variant performs only marginally slower than the composite produced by LEM + PS route.

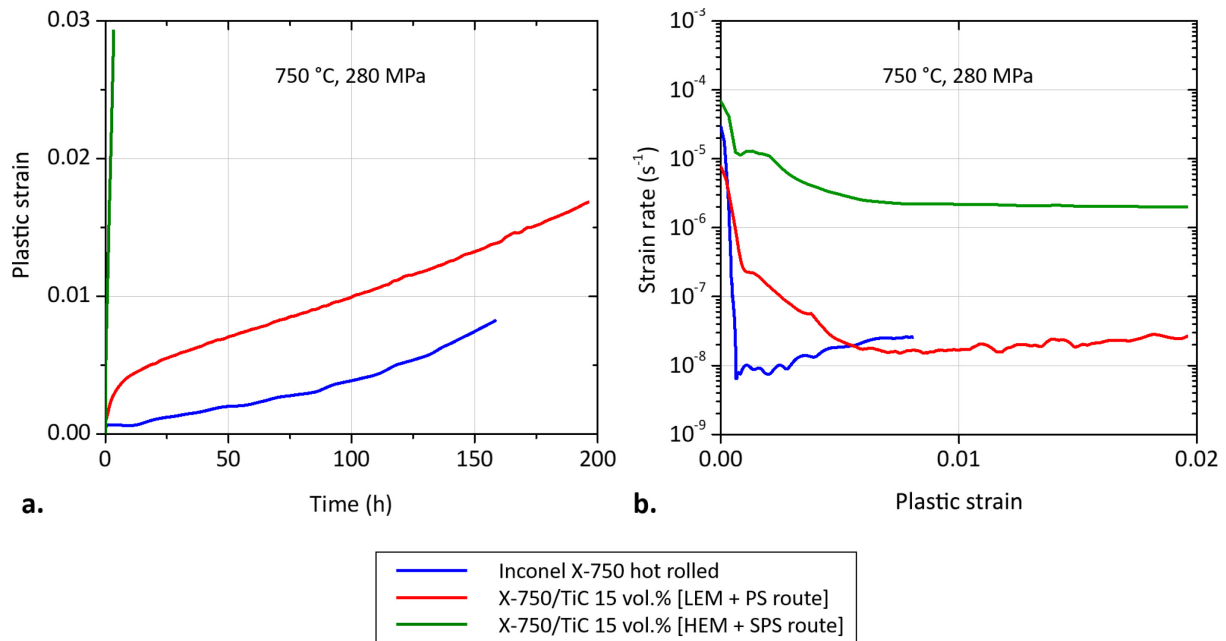


Figure 89 – Creep curves from interrupted compression creep tests conducted at 750 °C with applied stresses of 280 MPa, showing a) strain vs. time plots and b) strain rate vs. strain plots.

The behavior in strain vs. time curves between the non-reinforced reference and the composite produced by LEM + PS is the closest at 800°C (Figure 90), while differences from both materials to the variant produced by HEM + SPS method are once again widened. Serrations are also still present, but largely subdued at this temperature.

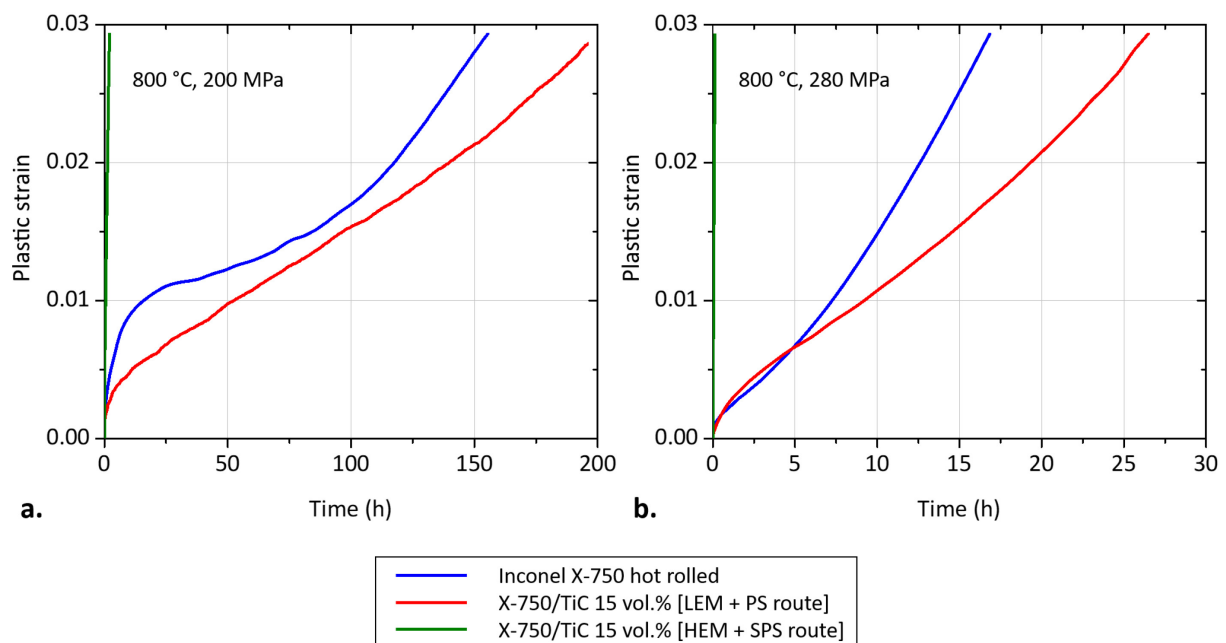


Figure 90 - Strain vs. time curves from interrupted compression creep tests conducted at 800 °C with applied stresses of a) 200 MPa and b) 280 MPa.

Minimum strain rates at 800 °C with 200 and 280 MPa from the non-reinforced reference and the composite produced by LEM + PS route are in the same order of magnitude (Figure 91). The non-reinforced variant, however, presents a different behavior, with a more punctual minimum creep rate. When considering the steady-state values, the composite produced by LEM + PS presents slightly slower rates. In contrast, the variant produced by HEM + SPS method strains considerably faster than both other variants, by a difference of two orders of magnitude.

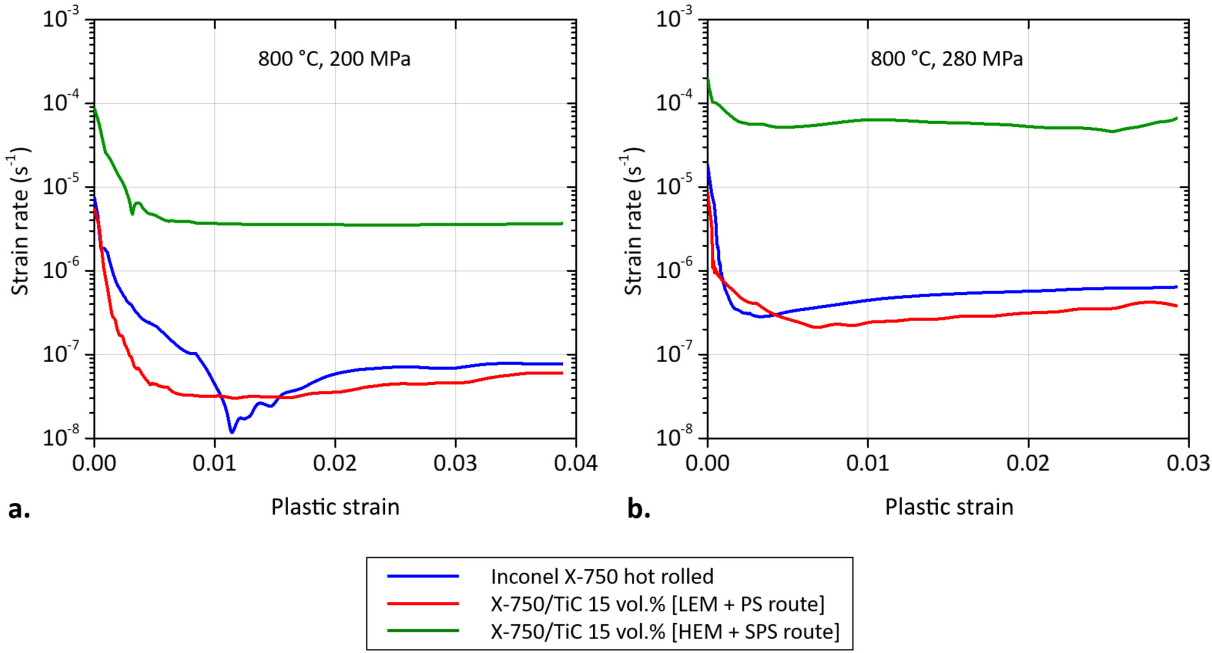


Figure 91 - Strain rate vs. strain curves from interrupted compression creep tests conducted at 800 °C with applied stresses of a) 200 MPa and b) 280 MPa.

Tests conducted with stresses in the range of 220 to 280 MPa at 700 °C (Figure 92 a) and 800 °C (Figure 92 b) with the non-reinforced reference and the composite prepared by LEM + PS, were also used in a direct comparison to observe the effect of the temperature on these variants. At both temperatures, the composite presents longer time to reach 2 and 3% of creep strain, but at 700 °C the differences are significantly larger in favor of the MMC at higher stress levels.

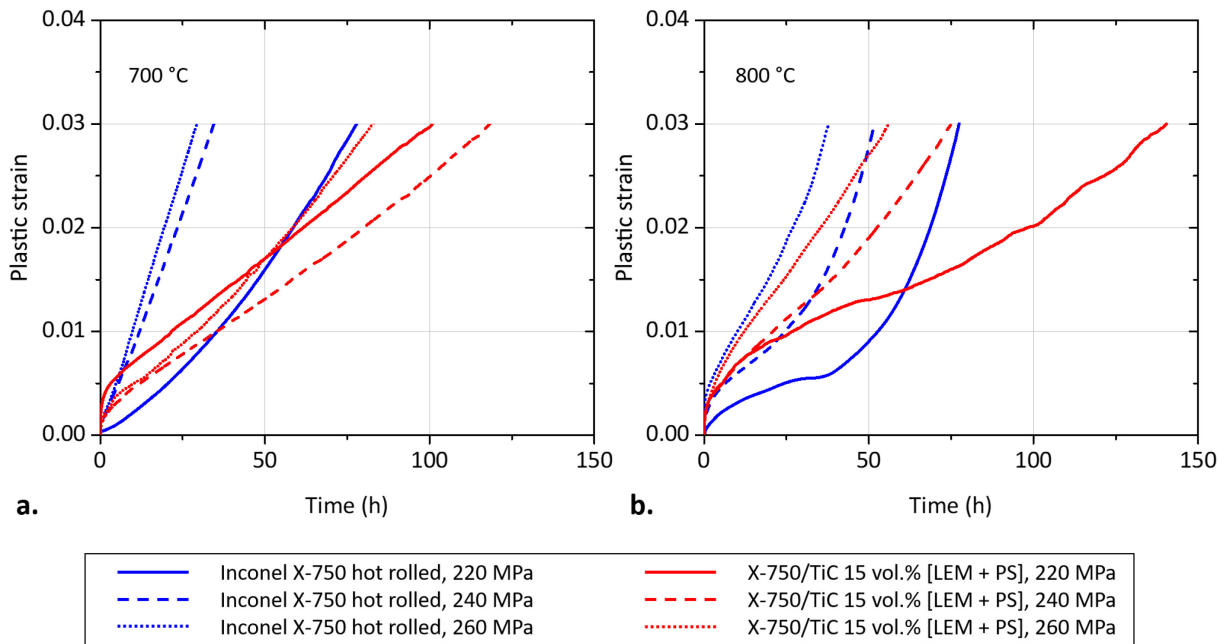


Figure 92 - Strain vs. time curves from interrupted compression creep tests conducted at 700 and 800 °C, from intermediate applied stresses of 220, 240 and 280 MPa.

The time necessary to reach 2% creep strain for all tested variants at 700 and 800 °C (Figure 93) shows a large discrepancy between the composite produced by HEM + SPS route and the other materials, with that variant reaching the strain target significantly faster. Oppositely, the composite prepared by LEM + PS took the longest times to reach 2% strain at both tested temperatures, showing a more significant improvement over the non-reinforced variant at 700 °C.

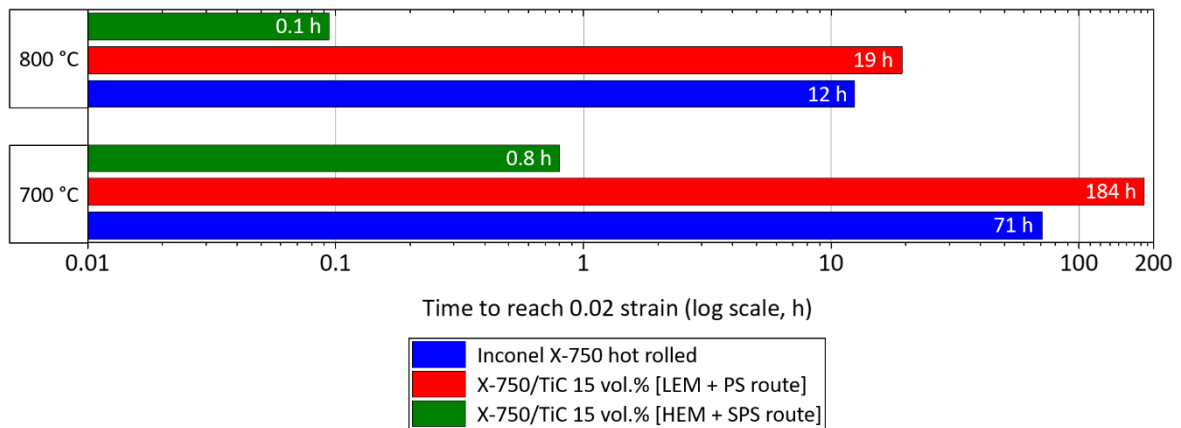


Figure 93 – Time necessary to reach 2% creep strain in compression creep tests conducted at 800 °C with 280 MPa, and at 700 °C with 440 MPa, respectively.

The true total threshold stress calculated for 700 °C (Figure 94 a) through the approximation method (power fitting), resulted in the lowest value observed in the composite prepared by the HEM + SPS process ( $\sigma_{TH} = 123$  MPa), while the variant produced by the LEM + PS route exhibited the highest value ( $\sigma_{TH} = 153$  MPa). Apparent creep activation energies, calculated for a stress of 280 MPa (Figure 94 b), presented higher values in the composites in relation to the non-reinforced reference. The apparent values are necessary for the calculation of the true creep activation energies, determined by equation 8. For the Inconel X-750 hot rolled a  $Q_c = 375$  kJ was obtained, while for X-750/TiC 15 vol.% produced by LEM + PS a  $Q_c = 295$  kJ was determined, and for X-750/TiC 15 vol.% produced by HEM + SPS a  $Q_c = 311$  kJ was calculated.

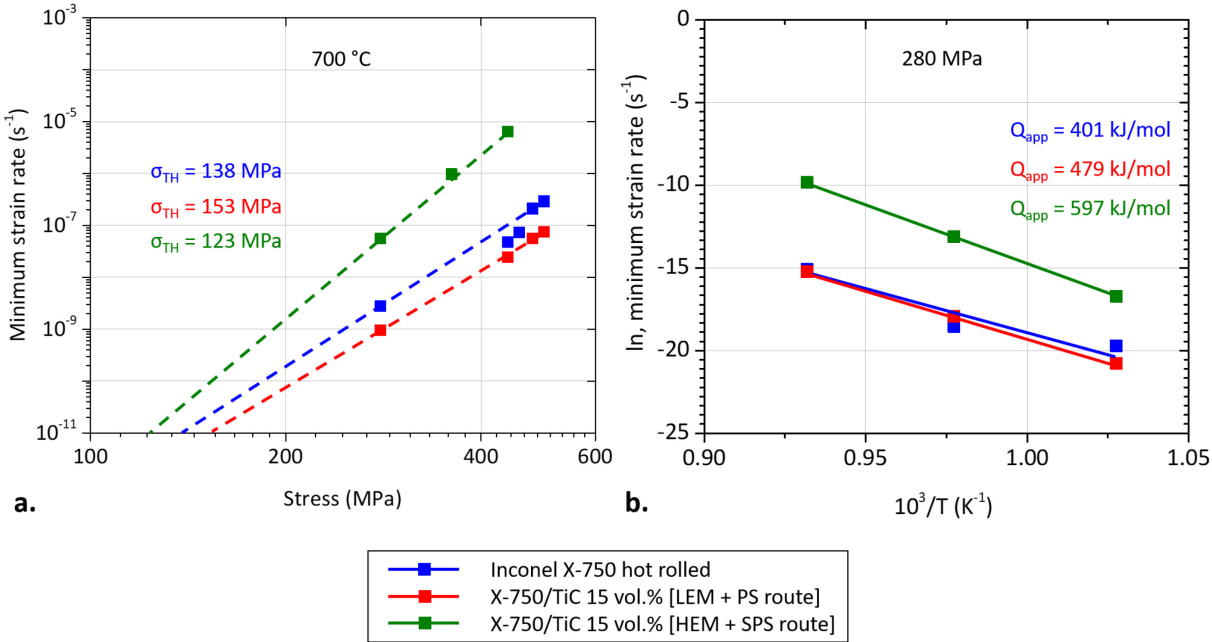


Figure 94 – Creep parameters: a) true total threshold stress  $\sigma_{TH}$  estimated with approximation method at 700 °C and b) apparent creep activation energy  $Q_{app}$ , obtained with  $\sigma = 280$  MPa.

The apparent Norton creep stress exponent was calculated for all tested materials (Figure 95), resulting in particularly high values in the composite produced by HEM + SPS ( $n \approx 11$ ). The non-reference variant and the composite prepared by LEM + PS also presented elevated stress exponents ( $n \approx 8$  for both materials).

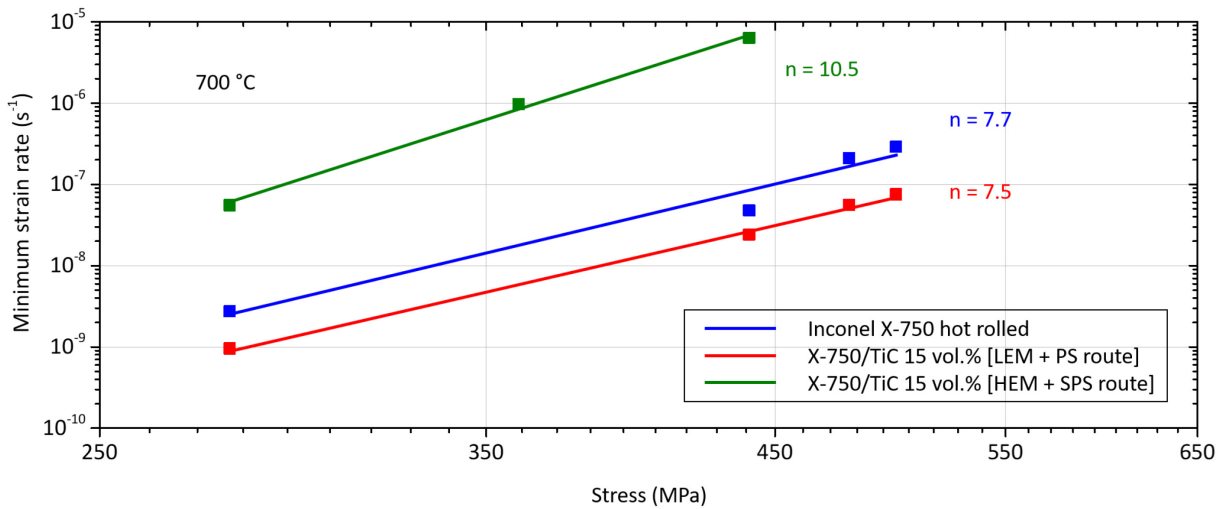


Figure 95 - Apparent stress exponents, given by the minimum strain rate vs. applied stress plot.

When considering the threshold stress, it was possible to obtain the true stress exponent at 700 °C for the composites and the non-reinforced reference (Figure 96 a). Both the composite prepared by LEM + PS route and the Inconel X-750 presented true stress exponents between 4 and 5, while the composite produced by HEM + SPS method exhibited a  $n$  value close to 7. Additionally, a Monkman-Grant parametrization (Figure 96 b) was conducted for all three investigated materials in the range of 700 to 800 °C, resulting in linear relations with coefficients of determination between 0.95 (for the non-reinforced variant) and 1.0 (for both composites).

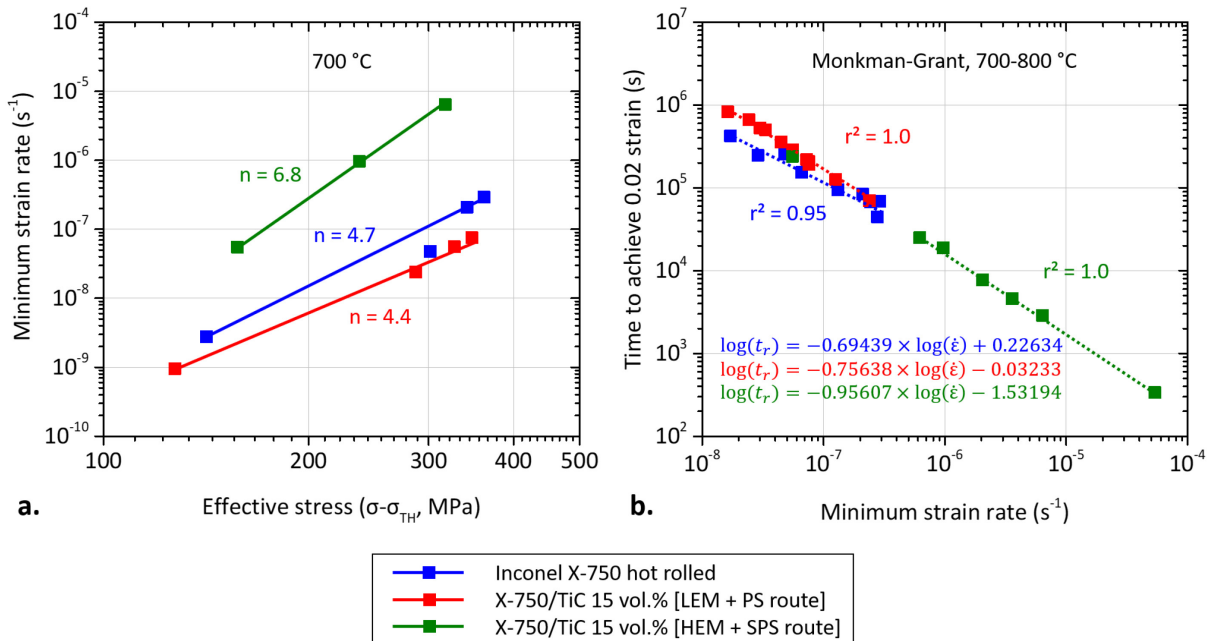


Figure 96 – Creep parameters: a) minimum strain rate vs. effective stress, showing true stress exponents obtained at 700 °C and b) Monkman-Grant relationship for creep tests conducted between 700 and 800 °C, including coefficient of determination ( $r^2$ ).

In addition to the Monkman-Grant parametrization, coefficients of Larson-Miller parameter were also calculated and fitting equations extracted (Figure 97) using data from at all temperatures and stresses tested, but modified to consider the criteria of time necessary to reach 2% strain instead of rupture time. A polynomial fitting resulted in equations with determination coefficients of 0.99, 1.00 and 1.00, respectively for the composite prepared by LEM + PS, the variant produced by HEM + PS and the non-reinforced X-750 alloy. A Larson-Miller constant of  $C_{LM} = 20$  was calculated for non-reinforced reference,  $C_{LM} = 23$  for the composite produced by LEM + PS, and  $C_{LM} = 28$  for the composite produced by HEM + SPS, according to Manson and Mendelson method [172,179]. With this method (plot of  $\log t$  vs.  $1/T$ ), when the temperature influence is small, shorter rupture times will result in elevated values for the constant  $C_{LM}$ . As a result, the composite values are displaced to the left in relation to the non-reinforced reference in the plot stress vs. modified Larson-Miller Parameter.

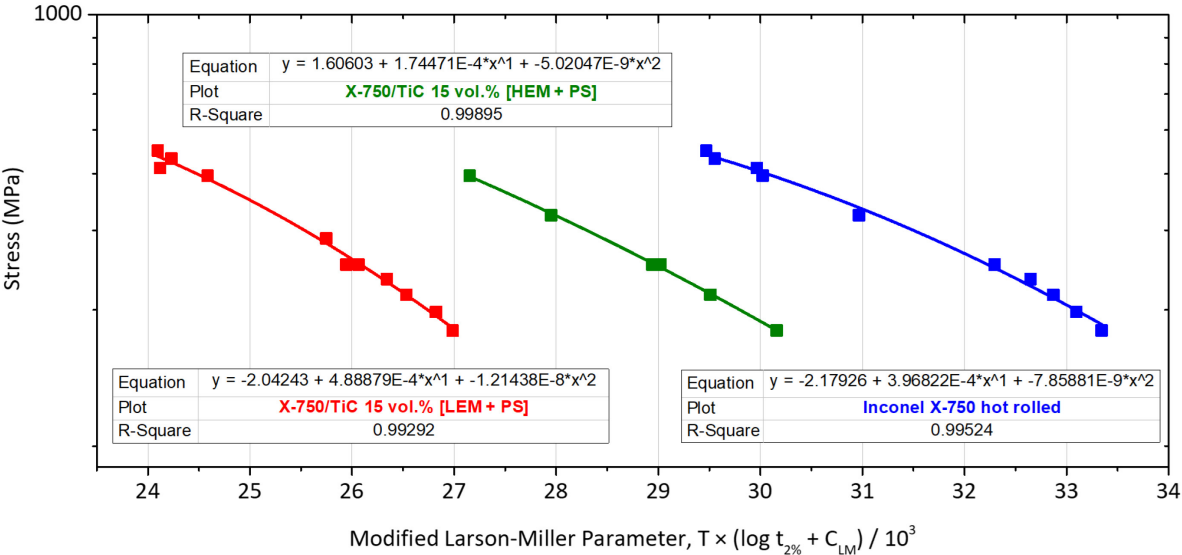


Figure 97 - Larson-Miller parametrization of specimens submitted to creep in compression.

A case was made taking the density into consideration as a parameter, by adopting the example of a turbine blade submitted to centripetal forces described in section 2.1.1. In this scenario a correlation between rotations per minute and the effective minimum strain rate at 700 °C was obtained Figure 98 a), showing a crossing point between the non-reinforced reference and the composite produced by LEM + PS route at  $4.84 \times 10^{-24} \text{ s}^{-1}$  at 650 rpm. At any revolutions rate over this point the composite is expected to present slower strain rates. Similarly, when correlating the predicted minimum strain rates and the applied stress to the turbine blade (Figure 98 b), a crossing point at 3 MPa was identified, stress above which the composite is also expected to strain at slower rates. Oppositely, the variant produced by HEM + PSP method is predicted to present a slower rate in comparison to the non-reinforced reference only when applying less than 112 MPa, at a crossing point of  $2.53 \times 10^{-12} \text{ s}^{-1}$ .

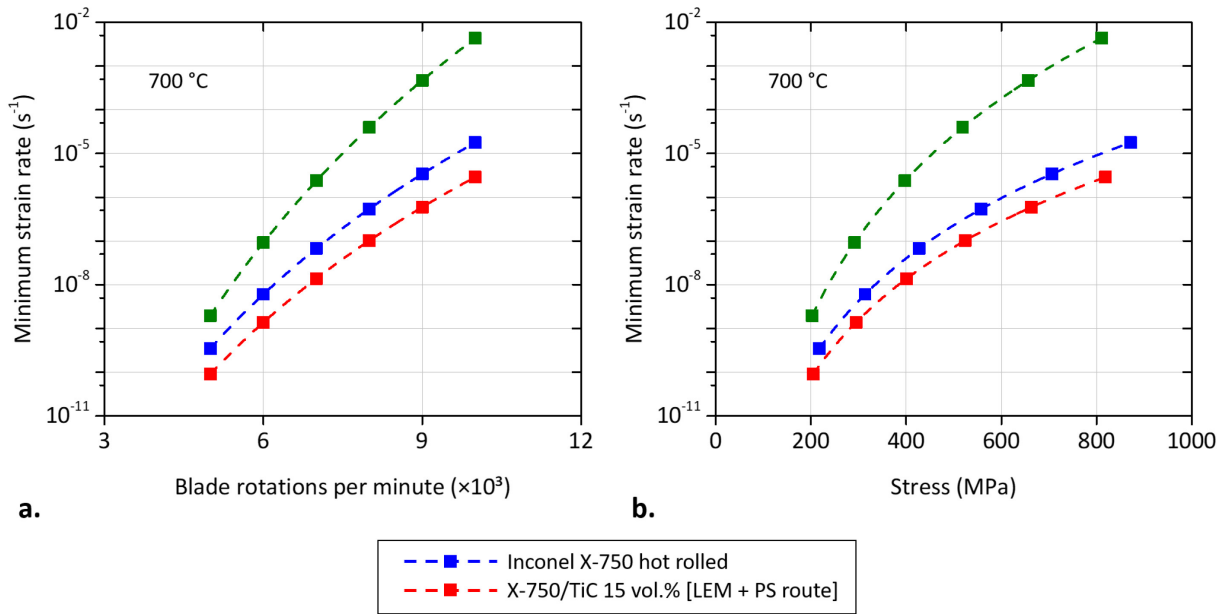


Figure 98 - Exemplification of a working turbine blade at 700 °C, showing a) minimum creep rates related to revolutions per minute and b) minimum creep rates for expected stresses.

#### 4.4.3 Estimation of load transfer in the composites

The load transferred from the matrix to the reinforcing particles can be obtained with the equation 11, described in section 2.5.7. As observed in Figure 94, the non-reinforced X-750 alloy tested at 700 °C presented a true total threshold stress of 138 MPa. Since only the immobilization of dislocations by the  $\gamma'$  precipitates can be considered as source of the threshold stress in this material, it is reasonable to assume that it corresponds a measurement of the threshold stress occurring exclusively at the matrix  $\gamma + \gamma'$  of the X-750 alloy, as described in equation 15:

$$\sigma_{TH}^{[\gamma+\gamma']\text{ matrix}} = \sigma_{TH}^{X-750} = 138 \text{ MPa} \quad (15)$$

where  $\sigma_{TH}^{[\gamma+\gamma']\text{ matrix}}$  is the threshold stress acting exclusively in the matrix, as a result of dislocations immobilized by  $\gamma'$ , and  $\sigma_{TH}^{X-750}$  is the total threshold stress measured in the alloy.

The composites, however, present an additional threshold stress component, attributable to the load transferred to the reinforcing particles. To obtain this value is necessary to subtract the threshold stress component that occurs exclusively at the  $\gamma + \gamma'$  matrix, already calculated in equation 15, and adjust it to the relative volume of  $\gamma'$  phase observed in the composites. Using the data from Table 12, it is observed that the composite X-750/TiC [LEM + PS] possess only 85 vol.% of the  $\gamma'$  present in the matrix of the non-reinforced reference. Likewise, the composite



X-750/TiC [HEM + SPS] also presents a lower amount of  $\gamma'$ , corresponding to 80 vol.% of the reference matrix. Applying these values to the equation 11, it is possible to estimate the remaining threshold stress in the composites, as observed in the developments in equations 16 and 17:

$$\sigma_{TH}^{LT} = \sigma_{TH}^{MMC} - (0.85 \cdot \sigma_{TH}^{X-750}) = 153 - (0.85 \cdot 138) = 36 \text{ MPa} \quad (16)$$

$$\sigma_{TH}^{LT} = \sigma_{TH}^{MMC} - (0.80 \cdot \sigma_{TH}^{X-750}) = 123 - (0.80 \cdot 138) = 13 \text{ MPa} \quad (17)$$

where the  $\sigma_{TH}^{LT}$  is the load transfer estimated, and  $\sigma_{TH}^{MMC}$  is the total threshold stress measured, respectively in the X-750/TiC [LEM + PS] (equation 16) and X-750/TiC [HEM + SPS] (equation 17) composites.

## 5. Discussion

### 5.1 Initial and overaged microstructures

Twin boundaries, observed in both non-reinforced variants, are a common trait of several polycrystalline Ni-based superalloys. Often in fcc metals the stress required for slip is significantly lower than the necessary for twinning, but in Ni-based superalloys reinforced by  $\gamma'$  twinning occurs more easily [180], resulting in a high amount of these structures. Similarly, short range planar defects such as stacking faults are also common on Ni-based superalloys, often acting as favorable sites for the nucleation of MC precipitates [181]. These were observed in both non-reinforced references. In the composites these carbides are not readily distinguishable from the added TiC particles, but could be differentiated with XRD analysis. Likewise, the presence of twinning was also observed in the reinforced variants with the use of EBSD examination, determining that the most frequent planar defects were still present even in MMCs produced by more complex fabrication methods.

The final grain size is a consequence of both raw powder characteristics and the processing route. Generally, it is of great interest to obtain a coarse microstructure, in order to reduce diffusion through grain boundaries during creep. The powder metallurgy route enables the work with coarse grained powders, but this course of action often leads to an intense agglomeration of reinforcing particles, which is highly detrimental to the material general resistance. Likewise, very fine powders may result in a very refined microstructure, which can also be detrimental to creep resistance [153]. Therefore, a compromise was made with the composite produced through the LEM + PS route, aiming at a good distribution of TiC<sub>p</sub>, and avoiding excessive refinement of the final microstructure. But for the composite produced by the HEM + SPS method, a more drastic combination of milling and spark plasma sintering was chosen, seeking to improve the reinforcement dispersion, and therefore avoiding the development of defects that are commonly associated with hard particle clusters.

As expected, the resulting grain size varied considerably between all evaluated materials, as a consequence of the different processing routes. The desired coarse microstructure was present in the commercial non-reinforced variety produced by hot rolling. However, it derives from chemical and processing developments that were not optimized in the devised composites. Therefore, a potentially suboptimal grain size was obtained in these variants. Nevertheless, it is important to note that under specific conditions refining the microstructure can be beneficial to the creep life of polycrystalline Ni-based superalloys. A smaller grain size is associated to a large number of triple junctions, that restrict crack propagation [112]. Consequently, a longer tertiary creep stage was indeed observed in tensile creep tests of both composites. Additionally, an

improvement of ductility was observed, which under strict limits such as 1 to 2% creep strain [9,30] it is known to benefit the design of turbine blades [27].

The strong grain size reduction in the composite produced by HEM + SPS method ( $D_{avg} = 0.33 \mu\text{m}$ ) had an extreme impact in creep rates, as observed in compression creep tests (section 4.4.2). The result is a consequence of grain boundary sliding and diffusion through grain boundaries, both aspects favored by an intense refinement of the microstructure [48]. The issue was less significant in the composite produced by LEM + PS method, which presented larger grains ( $D_{avg} = 8.9 \mu\text{m}$ ) and significantly lower creep rates. The subject is discussed in further detail in sections 5.3 and 5.4.

Despite the adverse effect of a reduced grain size on creep rates of the composite produced by HEM + SPS route, the outcome contributed to the achievement of a semi-homogeneous distribution of reinforcing TiC particles, dispersed at the grain boundaries. At first glance, the composite produced by the HEM + SPS method produced a more uniform dispersion of TiC (Figure 42), but the process also generated clustering and areas devoid of reinforcing particles. Furthermore, it was shown in EDS and XRD investigations that a higher amount of reactions occurred during the manufacture of this material, leading to the formation of undesired phases, such as oxides. In contrast, the composite produced by LEM + PS route exhibited a cleaner and more consistent microstructure (Figure 35), maintaining the  $\text{TiC}_p$  composition closer to its original state.

The initial size of  $\gamma'$  was measured in all specimens, showing discrepancies. Variants produced by the HEM + SPS method exhibited  $\gamma'$  with the lowest average diameter. The outcome can be attributed to the swiftly character of the spark plasma process [72], that presents extremely high rates of heating and cooling, in addition to a very short soaking period. As a result, the growth of precipitates in alloys based on the Inconel X-750 is hindered by the matrix diffusion rates of Al and Ti [59,67]. Oppositely, the composite produced by LEM + PS route presented slightly larger  $\gamma'$  particles in comparison to the non-reinforced hot rolled variant, but still adequate when considering the standard deviation observed in measurements. It must be observed as well that the conventional pressure sintering presents significantly slower heating rates, soaking time and cooling rates, allowing time for the diffusion of elements that constitute the  $\gamma'$  precipitates.

The presence of areas depleted of primary  $\gamma'$  was noted in all investigated materials, but showing different degrees of prevalence. In general, the vicinity of carbides and grain boundaries presented most frequently an apparent lack of these intermetallics. However, upon close inspection with SEM and TEM techniques, it was possible to detect in these areas the presence of a secondary precipitation of  $\gamma'$  (as depicted in Figure 31 b). These particles are considerably finer ( $D_{avg} < 10 \text{ nm}$ ) in comparison to the primary  $\gamma'$  ( $40 < D_{avg} < 60 \text{ nm}$ ), and are known to be highly effective to restrain the movement of dislocations [149]. Furthermore, when located at the grain boundaries, the secondary  $\gamma'$  precipitates are capable to significantly strengthen them. It is

established that during cooling from super-solvus temperatures, protrusions between reformed intermetallics and the grain boundary are formed. These promote the formation of serrations at the boundaries that limit grain sliding, particularly during high temperature creep [182–186].

Regions free of primary  $\gamma'$  were mostly observed in non-reinforced specimens produced by HEM + SPS route, along laths of hexagonal  $\text{Ni}_3\text{Ti}$ , known as  $\eta$  phase (Figure 30). The precipitation of  $\eta$  depletes the vicinity of Ti [59], both increasing the matrix solubility and reducing the availability of one of the most common  $\gamma'$  constituents. Nevertheless, even in this case a secondary precipitation of  $\gamma'$  was observed in these areas, albeit limited to the fine particle size that characterizes this precipitate. It is established that the secondary  $\gamma'$  is mostly formed during relatively fast cooling rates (1 °C/s) from the solvus temperature, and that it presents a highly coherent interface with the matrix [182]. Additionally, the secondary  $\gamma'$  stability is improved by the presence of Nb in solution in the matrix, which substitutes part of Al and Ti in the precipitate [59]. But ultimately, it can be assumed that the strong local depletion of Ti by the formation of the  $\eta$  phase hinders the growth of the larger  $\gamma'$  cuboids in the vicinity of  $\eta$  laths.

The composite prepared by the HEM + SPS process did not present  $\eta$  laths. It is hypothesized that this phase results from the partial dissolution of small Ti-rich MC carbides, that leads to a great amount of Ti in solution [59]. The process is triggered by the brief and exceptionally high temperatures reached during the SPS process, but in this case the presence of a much finer added  $\text{TiC}_p$  is likely to mitigate the outcome [67]. It is established that TiC and NbC particles present high affinity for Ti and Nb in solution, often occurring further enrichment by these elements at high temperatures [59,187]. The result is a mixed cubic carbide (Nb,Ti)C, that tends to remain rather stable even after long isothermal treatments [67]. It can be hypothesized that in the SPS process the fine distribution of the reinforcing carbide reduces the diffusion path for the Ti in solution to reach  $\text{TiC}_p$ . The arrangement can be considered effective to recover the excess of the element in  $\gamma$  produced by the high temperatures reached in the SPS process, and by doing so also lowering the tendency to form the  $\eta$  phase. It is acknowledged that transitory temperature differences between the graphite die, where the thermocouples are localized, and the material core, can add as much as 450 °C to the temperature target (1250 °C) during spark plasma sintering [72]. Considering this scenario, for a short period the exceedingly elevated temperatures (close to 1700 °C) are likely to favor a partial dissolution of TiC and enrich the matrix with Ti.

Examination of non-reinforced references by SEM-SE and EDS showed that chromium carbides are often located at grain boundaries, while MC particles are frequently observed both at boundaries and inside grains. In the composite prepared by LEM + PS it can be assumed that the same situation takes place, since no significant manipulation is conducted to blend X-750 and  $\text{TiC}_p$  powders at such level. In this case, triple junctions were most often populated with carbides. The composites produced by HEM + SPS method present a much more refined and complex microstructure, making it difficult to distinguish between the very fine chromium and titanium

carbides. Yet, an observation is made that that all carbides are generally located at grain boundaries, prominently at junctions of smaller grains. Therefore, it can be affirmed that the high energy milling processes did not achieve the objective of placing  $TiC_p$  inside the grains, despite being followed by the same heat treatment applied to the non-reinforced references.

No texture was observed in the composites, but the variety produced by HEM + SPS route presented random elongated segments almost deprived of  $TiC_p$ . While generally no preferential crystallographic orientation was noted, the issue led to a microstructure less homogeneous than the one observed in the variety prepared by LEM + PS method, resulting in a potentially anisotropic behavior. Considering this possibility, it should be noted that creep tests were conducted only in the same axis of compression and sintering in both investigated composites. In the variant produced by LEM + PS route no texture was expected, since it did not present elongated grain-like structures. This expectation was indeed confirmed, with the EBSD results. In face of these facts, the inconsistencies in the composite produced by HEM + SPS are to be considered in a future investigation of creep properties, by conducting tests at different orientations to evaluate the impact of the elongated segments on mechanical properties.

TiC particles also did not present preferred crystallographic orientation. The result from EBSD analysis confirms the expectation that the added titanium carbides possess good microstructural stability at usual sintering temperatures (1250 °C), for the relatively short times used in the process. Even when positioned closely in clusters, individual orientations were preserved. Nonetheless, it should be noted that TiC might dissolve partially at the high momentary temperatures that take place during the SPS process, as previously discussed following investigations on this technique conducted by other researchers [72]. Accordingly, also in studies using traditional pressure sintering with Fe-Si + TiC powders at 1410 and 1430 °C for 1 h, a partial dissolution of TiC was observed [188]. Therefore, these carbides should be considered as relatively stable only at lower temperatures.

After long isothermal aging, the microstructures of non-reinforced references and composites were compared to their original states. Regarding the non-reinforced hot rolled alloy and both composites, no statistical changes were observed in the size of primary  $\gamma'$  particles after 200 h at 700 °C or 50 h at 800 °C (Figure 62). But as the treatment progressed, a consistent growth of primary  $\gamma'$  ensued up to 1000 h of aging, when the investigation was discontinued. The non-reinforced reference produced by HEM + SPS method was the only variant to present statistical growth of primary  $\gamma'$  after just 50 h at 700 °C. The finding is in line with the assumption that the high cooling rates provided by the spark plasma sintering [73] process hinder the initial growth of primary  $\gamma'$  [55,189], which was promptly resumed with the isothermal aging. Since the standard heat-treatment does not bring the particle size to the same baseline observed in the variants produced by other routes, it is possible to infer that cooling rates from solvus temperature play a substantial role in that outcome. This was indeed observed by other researchers, showing that below 970 °C the nucleation and growth kinetics of primary  $\gamma'$  are significantly slower, particularly

when considering particles in the size range observed. The result is attributed to the lower diffusion rates observed at these temperatures [189].

Although the non-reinforced alloy produced by HEM + SPS presented a fast growth of primary  $\gamma'$  during overaging tests, the behavior was not observed in the composite prepared by the same route. This variant presented the slowest increase in the particle size, only approaching the primary  $\gamma'$  diameter observed in the composite produced by LEM + PS and the non-reinforced hot rolled reference after 400 h at 800 °C. The development can be linked to the Ti-enriched matrix, which reduces the diffusion rates in the matrix and hinders the  $\gamma'$  growth [174].

Punctual EDS analysis was conducted on TiC particles (Table 11) present in the composite produced by LEM + PS, showing that at initial state they possessed a higher content of Al in comparison to the particles observed in the variant produced by HEM + SPS. As a major constituent of  $\gamma'$  ( $\text{Ni}_3\text{Al}$ ) [2], it can be conceived that a restricted availability of Al in solution contributed to limit the growth of this phase during overaging at 700 °C (Figure 62 a). As a consequence, the composite produced by the LEM + PS route was the only one to present a  $\gamma'$  particle size that remained stable in relation to its initial state (in the statistical range, considering a confidence level with  $\alpha = 0.05$ ), even after 1000 h of treatment.

Elements mapping on the composite prepared by LEM + PS at initial state also showed that TiC particles were fairly enriched by aluminum (Table 11). Niobium was additionally observed as part of MC particles in both composites, at initial state and after 1000 h of isothermal aging at the two tested temperatures. Both elements are important to  $\gamma'$  growth [59,174], and their diffusion from the  $\gamma$  matrix to the carbides might hinder the intermetallic development, as indeed observed.

Only the variant produced by HEM + SPS exhibited chromium oxides (Table 10), that doubled in size after the overaging treatment. Since no component bearing oxygen was involved in the MMC concept, the likelihood of contamination during the high milling energy process must be acknowledged. The amount of oxides in the material, nevertheless, can be deemed restricted enough to be reasonably neutral to the creep resistance. It is shown that a fine oxide dispersion ( $D_{\text{avg}} < 0.5 \mu\text{m}$ ) has the potential to even contribute to the Ni-based superalloys strength [167].

The  $\text{M}_{23}\text{C}_6$  precipitates formed between 650 and 820 °C are mostly enriched by niobium, titanium and chromium, given the proper availability of these elements in solution [59]. Since this carbide precipitates mostly at grain boundaries, it has the potential to take a significant amount of Nb and Ti from solution in the region, thus impacting the local stability of  $\gamma'$ . To avoid it, a stabilization treatment must be conducted at a temperature over 820 °C, where the formation of Nb- and Ti-rich MC carbides occurs more easily than of  $\text{M}_{23}\text{C}_6$ . Since MC carbides tend to be better dispersed in the microstructure, with this step the formation of  $\gamma'$ -free zones along grain boundaries can be largely avoided [59].

During overaging of the composite produced by LEM + PS the chromium carbides presented a consistent growth with time (Table 10), displaying an average diameter seven times larger after 1000 h at 800 °C. It was observed that at initial state the reinforcing TiC particles in the composite presented chromium in its composition, that diminished during the long isothermal treatments. As with Al and Nb, Cr is also partially arrested by TiC particles during sintering [67]. It can be conceived that the element diffuses back to the matrix during overaging at both 700 and 800 °C, affecting the solubility and leading to the precipitation of additional carbides. A modest dissolution of the reinforcing TiC particles also has the potential to provide further carbon for the reaction. In the composite produced by HEM + PS route the observation of the effect was not favorable, since the chromium carbides present in this variant are fairly small and less homogeneously dispersed, resulting in measurements with large intervals of confidence. But even in this case the initial enrichment of TiC<sub>p</sub> by Cr during the MMCs fabrication process was largely confirmed by EDS analysis, presenting between 5 and 10 at.% of the carbide composition and supporting the general assumption. Further investigation of the chromium carbides evolution in composites produced by SPS process, nevertheless, is advised in future studies.

Phases were additionally characterized with XRD. Both composites exhibited at their original conditions the presence of a  $\gamma$  matrix,  $\gamma'$  precipitates and cubic TiC particles. Additionally, a very small amount of hexagonal MC phase was detected in the composite prepared by LEM + PS method. After 1000 h at 700 °C no changes to this constitution was observed, but after the same treatment time at 800 °C the composite produced by HEM + SPS route presented also hexagonal MC phase, in addition to  $\eta$  phase. The occurrence of this carbide is prevalent in the non-reinforced X-750 hot rolled (Table 7), which experienced slow cooling rates during production, promoting its precipitation over 820 °C [59]. Relatively moderate cooling rates are also observed in the traditional pressure sintering process, favoring the development of a small amount of the phase. Contrarily to both cases, the spark plasma sintering process presents much faster cooling rates, hindering the formation of hexagonal MC precipitates [72]. But in this case, a long isothermal aging at 800 °C proved enough to cause its precipitation.

Compared to the cubic TiC variant added to create the composite, the hexagonal MC precipitate is highly enriched in Nb and Ti, also having Al in its composition. Therefore, it can be referred as a mixed (Al,Nb,Ti) carbide. While it was not identified in the composite prepared by HEM + SPS at its original condition, it could be argued that a very small fraction of the precipitate might always be present in this variant, since after the longest heat treatment only a reduced amount of it was quantified by Rietveld analysis. In contrast,  $\eta$  phase was uniquely observed in the composite produced by HEM + SPS after 1000 h of treatment at 800 °C, but in a substantial amount. This intermetallic is predicted to form after long time in the non-reinforced alloy, and is often associated with a loss in the creep resistance, since it severely reduces ductility at grain boundaries [59,174].

The possible influence of  $\eta$  phase in the performance under creep of the composite prepared by HEM + SPS must be considered. It is known that the precipitation of  $\eta$  occurs at the expense of  $\gamma'$ , since both compete for the Ti available in solution [59]. After 1000 h of isothermal treatment at 800 °C, only that composite variant presented  $\eta$ , as observed in XRD results (Figure 65). The outcome suggests a probable premature weakening of creep resistance in this variant. The outline of elements in  $\gamma$  solution and in  $TiC_p$  that influence the formation of  $\eta$  and  $\gamma'$ , among other aspects, is summarized in Figure 99.

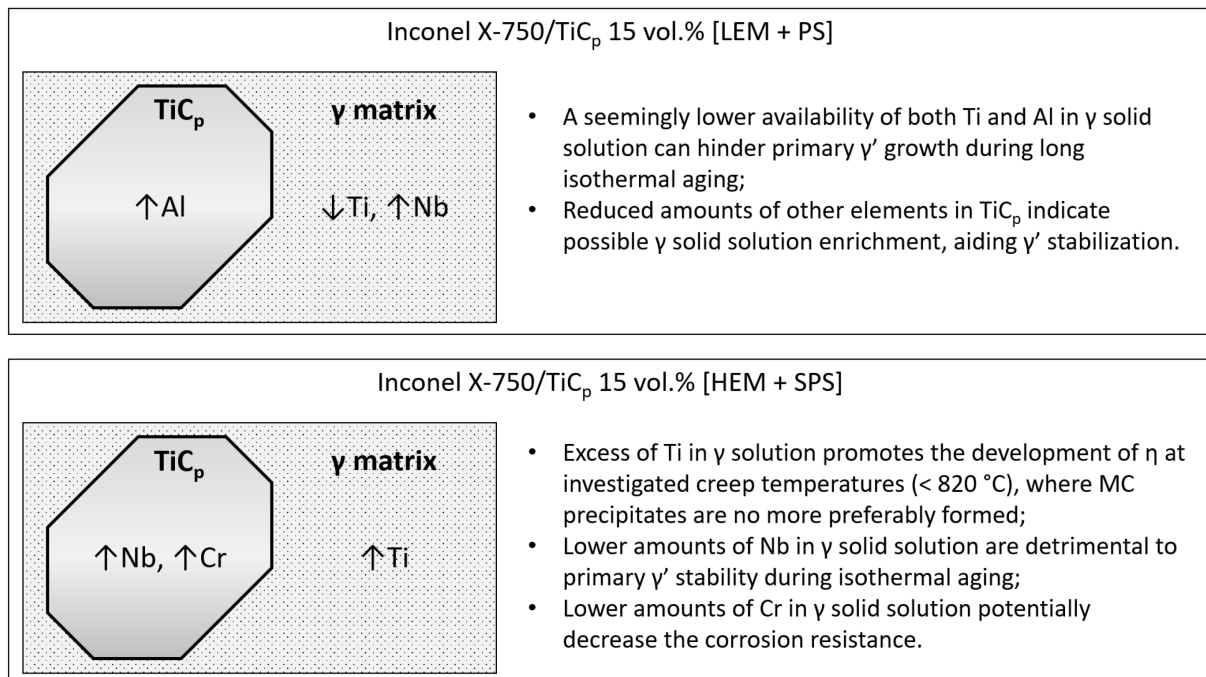


Figure 99 – Comparison of highlighted elements quantified in composites, with arrows indicating higher or lower amounts in relation to its counterpart. Potential roles of each element are also presented.

The total amount of  $\gamma'$  (primary + secondary) in all specimens at initial state was also quantified with Rietveld analysis (Table 7). The maximum amount of this intermetallic is observed in the non-reinforced reference produced by hot rolling. Both composites presented lower quantities of the precipitate, due to the volume shared with  $TiC_p$  in the microstructure, in addition to more areas devoid of primary  $\gamma'$  in the vicinity of carbides. The presence of secondary  $\gamma'$ , however, seems to generally compensate for the lack of the larger primary  $\gamma'$  in these areas. It is also important to note that while no composition measurement was taken at the intermetallics, it is acknowledged that the fine secondary  $\gamma'$  is mostly enriched in Al, while primary  $\gamma'$  often presents additionally a high amount Ti in its composition [60]. Therefore, a balanced offer of both elements is important to achieve a microstructure with a high amount of both primary and secondary  $\gamma'$  precipitates.



The non-reinforced variant prepared by HEM + SPS route presented the most primary  $\gamma'$ -deficient microstructure in Rietveld analysis, due to the formation of large laths of  $\eta$  phase. As previously discussed, it displaces large amounts of Ti from the  $\gamma$  solid solution, impairing the conditions for growth of primary  $\gamma'$ . In this case, the existence of very small secondary  $\gamma'$  in the affected regions does not seem to compensate for the absence of primary  $\gamma'$ , resulting in lower total volume of the phase in the variant.

Hardness measurements (Figure 66) in all variants investigated after long isothermal treatments showed similarities. All materials presented a relatively stable hardness evolution with time at 700 and 800 °C, with the exception of the composite prepared by LEM + PS route, which exhibited a larger decrease after 1000 h at both temperatures. The result can be linked with the primary  $\gamma'$  size evolution, as clearer noted when establishing a correlation between average hardness and primary  $\gamma'$  diameter at 800 °C (Figure 100). In this case the larger interparticle distances contribute to a reduction in the stress calculated for Orowan stresses, which are used for an estimation of the threshold stress occurring at the ( $\gamma + \gamma'$ ) matrix [126,151]. Ultimately, the strength loss can also be expected to be observed in hardness measurements [190]. It is worth noting that also in creep tests conducted at 700 °C, after 500 h the composite prepared by LEM + PS exhibited a considerably larger increase in primary  $\gamma'$  volume (+25.6 vol.%) compared to the variant produced by HEM + SPS (+4.2 vol.%), as observed in Table 12. Therefore, the stronger coalescence of primary  $\gamma'$  in the composite LEM + PS over time at high temperature can be asserted.

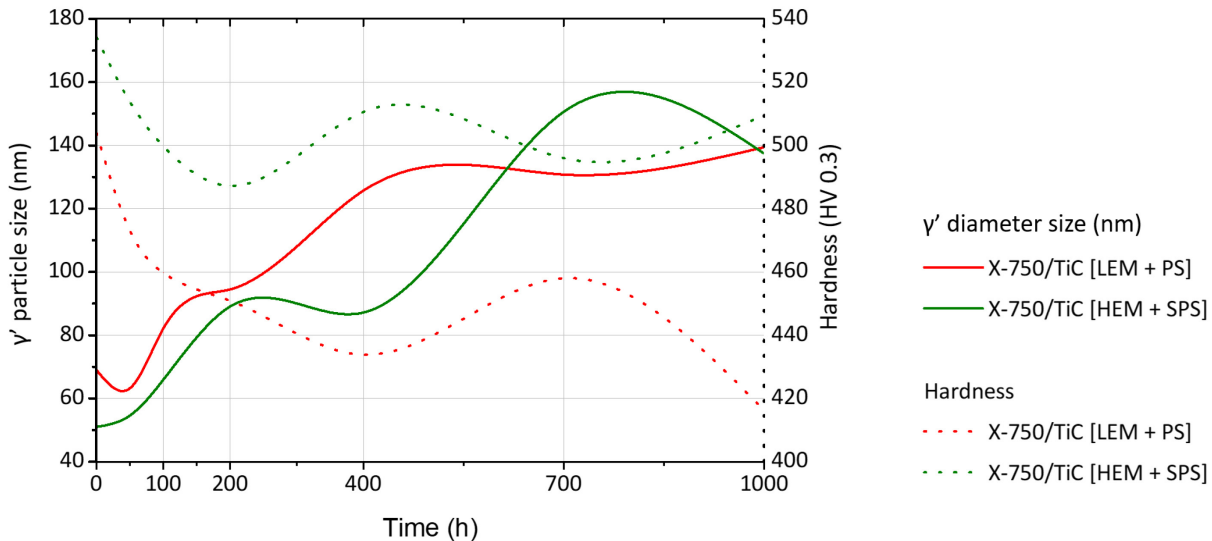


Figure 100 - Correlation between primary  $\gamma'$  size and hardness during long isothermal aging at 800 °C in composites produced by different routes, highlighting an inverse relationship.

A particular aspect from results obtained with 700 °C tests must also be noted: at this temperature, after 1000 h of treatment, a more prominent decrease in both hardness and  $\gamma'$  size

was observed in the composite prepared by LEM + PS route. A hypothesis can be made regarding the evolution of secondary  $\gamma'$ , that becomes larger with the overaging time. The measurement of intermetallics did not consider very small particles ( $< 10$  nm), since these are not clearly distinguishable or not visible at all in most SEM analysis, during initial stages of overaging. After long time in isothermal treatment, however, these particles either dissolve or grow enough to become evident in SEM results and affect the measurements, in this case leading to a lower size average. As consequence, a large statistical confidence interval was also observed at this specific condition. Therefore, a suggestion is made for a future investigation with the use of Rietveld refinement and transmission electron microscopy over long isothermal aging times ( $> 1000$  h), to better assess the evolution of both primary and secondary  $\gamma'$ .

In the result evaluated above, it also must be considered that primary  $\gamma'$  alone remained mostly stable, which can be linked to the limited amounts of Ti and Al available in  $\gamma$  solution for further development of cubic  $\text{Ni}_3(\text{Al,Ti})$  [42]. It is known that larger coherent intermetallics contribute less to strengthen the X-750 alloy in comparison to smaller, peak aged  $\gamma'$ , as their associated APB energy decreases with an increase in particle size [191]. Therefore, even a small growth of these precipitates may affect the hardness negatively.

## 5.2 Creep fracture and microstructure

Creep test results also showed significant microstructure differences between the investigated materials. After rupture in tensile creep tests both materials selected for this examination, a non-reinforced hot rolled variant and a composite produced by LEM + PS, exhibited intergranular fracture (Figure 67). The roots were determined to be cracks initiating at large intergranular hexagonal  $(\text{Nb,Ti})\text{C}$  precipitates in the non-reinforced variety, while in the composite no single origin was established. Yet, both presented a clear propagation path along chromium carbides, situated at grain boundaries. The result is consistent with a semi-fragile rupture, with both analyzed materials showing very limited ductility, but still without the presence of transgranular fracture that is frequently associated with brittle alloys [192–195].

The composite produced by LEM + PS exhibited additional cracks in its interior (Figure 68), close to the region of rupture. These were parallel to the fracture, but also followed an intergranular path. In the vicinity more cracks were observed, frequently near larger  $\text{TiC}$  carbides. It is known that in the polycrystalline X-750 alloy the nucleation of cavities initiates already in the primary creep stage, progressing continuously through creep tests at  $700$  °C, when applying stresses between  $200$  and  $400$  MPa [112]. It is also acknowledged that residual stresses between the matrix and carbides, resulting from differences in the coefficient of thermal expansion, leads to sliding at grain boundaries during heating. In this case, even a small displacement of circa  $5$  nm is already sufficient to form stable cavities in the X-750 alloy, even prior to the creep test start

[112]. It can be assumed that in composites based on this alloy an analogous behavior arises, but amplified by the amount of present carbides.

After tensile creep, both non-reinforced and composite variants presented primary  $\gamma'$  precipitates partially aligned, but inconsistently oriented in relation to the strain axis (Figure 69). While no apparent coalescence of primary  $\gamma'$  was observed, the particles were coarsened and frequently closely positioned. The result suggests the onset of a rafting process (Figure 101), that occurs only after a certain amount of creep deformation takes place [190,196].

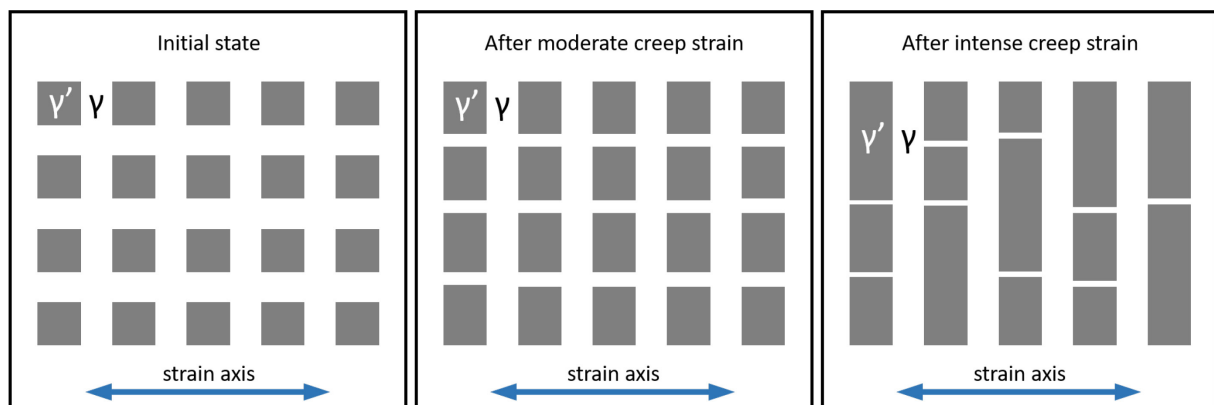


Figure 101 – Expected development of rafts in the investigated alloys, in progression order.

For comparison purposes, it is worth noting that in single crystal alloys rafting develops along the  $\gamma$  channels less populated with dislocations, which in this case (positive misfit,  $a_{\gamma'} > a_{\gamma}$ ) would be expected to be along the tensile axis. This plane is also the less stressed, where coalescence of  $\gamma'$  would be expected to follow [196,197]. Additionally, it is important to note that a raft structure perpendicular to the strain axis is considered poorly effective to reduce creep rates in single crystal alloys, since they are most easily surpassed by climb [125,190,198–201].

With polycrystalline superalloys, however, a different interpretation is possible. In the case of the current investigation the alignment of primary  $\gamma'$  was observed both in the non-reinforced reference and the composite submitted to tensile creep tests, but generally closer to  $45^\circ$  in relation to the strain axis (as illustrated in Figure 102). This configuration is acknowledged to be prevalent in polycrystalline Ni-based alloys [202], where  $\gamma'$  precipitates are frequently located along slip bands aligned at  $45^\circ$  with the strain axis, influenced by the maximum shear stress in the specimen. Nevertheless, the composite frequently presented deviations in the alignment direction of  $\gamma'$  cuboids, particularly in regions populated by small grains. These areas also contain a high amount of TiC particles, which are presumed to affect the local creep flow to a larger extent. Therefore, it can be assumed that both the maximum shear stress and the presence of disorderly placed carbides in smaller grains contributed to the mixed alignment of  $\gamma'$  cuboids observed in the investigated alloys.

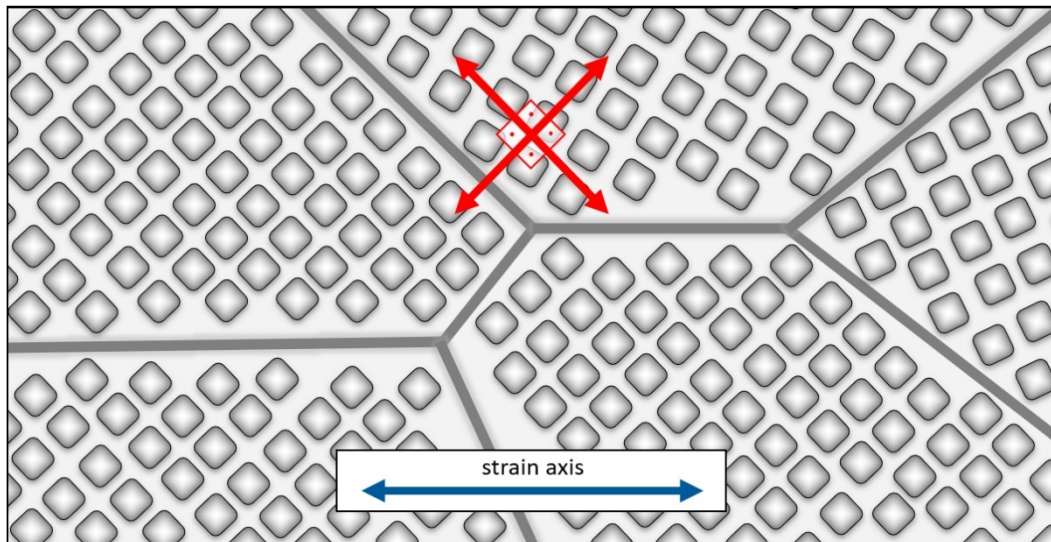


Figure 102 – Representation of the close relationship between the maximum shear stress (represented by red arrows) in the arrangement of  $\gamma'$  cuboids in a polycrystalline Ni-based superalloy, resulting in precipitates alignment generally close to 45° in relation to the strain axis during creep deformation.

Serrated grain boundaries were identified only in the non-reinforced X-750 produced by hot-rolling (Figure 83 a). The development of jagged boundaries in the alloy is connected to slow cooling rates, that promote heterogeneous precipitation of  $\gamma'$  in the region. These grow and induce the irregularities along the boundaries [182]. While the serrations are generally associated with a positive effect to limit boundary mobility, it is unknown if their presence in composites offer a potential for further strengthening. Moreover, the present study did not explore variations in the heat-treatment, so the subject remains to be addressed in forthcoming investigations.

The microstructure of materials submitted to compression creep tests exhibited an evolution trend similar to variants tested under tension conditions. The  $\gamma'$  particles presented once again a partial alignment close to 45° in relation to the strain axis, which is due to the influence of the maximum shear stress expected in the specimen [202]. It is known that in circumstances where a high amount of geometric distortions is present in certain regions of single crystal variants, rafting may develop uncommonly at 45° with the strain axis [203], but in polycrystalline variants a limited 45-degree rafting is often the most prevalent result. In this case the distinct grain orientations provide an asymmetry that leads the  $\gamma'$  cuboids to be differently aligned at each grain before the test. During creep deformation, only a very restricted directional coalescence of  $\gamma'$  is observed in these variants, generally matching the maximum shear stress applied to the specimen [202].

The composite prepared by LEM + PS (Figure 84), however, showed additionally signs of coalescence of  $\gamma'$ . The finding was more evident in regions close to the specimen border, in a lengthwise center position with the compression axis, since the creep flow reaches a maximum in this region. It is acknowledged that coalescence is highly influenced by diffusion kinetics, that allow a partial local dissolution of  $\gamma'$  and a flow of alloying elements to the adjacent matrix channel [197]. Therefore, a connection can be made with the earlier presented evidence that this composite possesses a  $\gamma$  matrix with a reduced amount of solid solution elements, which would hinder the diffusion process. Further evidence of coalescence of  $\gamma'$  during creep is shown in results summarized in Table 12. As creep progresses, the volume of primary  $\gamma'$  increases, while simultaneously the volume of secondary  $\gamma'$  diminishes.

The presence of  $\text{TiC}_p$  reinforcements also affected the alignment of  $\gamma'$  in the composite prepared by LEM + PS in tensile tests, leading the angle with the strain axis to vary mostly between  $45^\circ$  and  $90^\circ$ . The complex creep flow in the composite indicate an isotropic potential in the material, that can be advantageous to applications that are involves a multiaxial stress state. The variant produced by HEM + SPS (Figure 85), meanwhile, exhibited only a moderate degree of alignment, without signs of coalescence. The lower amount of primary  $\gamma'$  in this material might be considered as a limiting factor for the onset of a rafting process.

### 5.3 Creep parameters

Tensile creep test results revealed common aspects in the examined materials. Both non-reinforced and composite variants presented a considerably short first stage of creep (Figure 70), observed at all temperatures. The step was followed by an inflection that marked a punctual minimum creep rate at  $800^\circ\text{C}$ , promptly changing to a long tertiary stage of deformation, which was particularly lengthier in the composite. When reducing the temperature, the point of inflection was gradually replaced by a steady state step in both variants, which once again was lengthier in the composite. This pattern achieved a peak at  $700^\circ\text{C}$ , where the secondary stage was the longest in relation to the complete creep-to-fracture curve, but simultaneously the total strain also became the shortest among all tested temperatures.

The appearance of a lengthier secondary creep stage in the composite can be explained by a competition between two mechanisms. In metal matrix composites, the microstructural evolution of the matrix during creep is often counterbalanced by strains continuously developed at the matrix/reinforcement interface, resulting in a longer stationary stage of creep [61]. During this steady-state regime, the aging of  $\gamma'$  precipitates leads to dislocations overcoming those barriers with less effort [127], but at the same time a load transfer mechanism acts in the strain fields generated around reinforcing particles, slowing down the deformation process. In this case,

a state of apparent creep equilibrium can be temporarily achieved, delaying the beginning of the tertiary stage of creep [61].

Another common aspect was the occurrence of serrations in strain vs. time curves. These were not only expressed as steps, but often also as negative strain. The effect is significantly more pronounced at 700 °C, temperature where the stability of the  $\gamma'$  phase reaches a maximum [204]. The serrations were observed mostly in lower stress tests, particularly in the early stages of creep. It is established that Inconel X-750 intermetallics presents a positive misfit of  $0.3 \pm 0.1$  % with the  $\gamma$  matrix at room temperature [41] and close to 0.1 % at 900 °C [42], which induces the formation of coherency fields around the precipitates. During creep, geometrical changes caused by the increase of dislocations density at the interface induce the expansion of such fields, leading to volumetric changes in the precipitate adjacency, and thus to a transitory contraction in the material [135,138,139]. The high amount of primary and secondary  $\gamma'$  present at 700 °C is in agreement with the observed prevalence of the effect at this temperature.

It is established that at 700 °C the tensile creep strain of a non-reinforced Inconel X-750 produced by hot rolling and presenting a grain size of approximately 100  $\mu\text{m}$  is kept below 1% when tested with stresses over 200 MPa [112]. Also in conventional hot tensile tests, conducted at a constant strain rate of  $3 \times 10^{-5} \text{s}^{-1}$ , the lowest strain is achieved at approximately 700 °C. It is believed that the strong reduction in ductility is due to the highest stability of  $\gamma'$  at this temperature, causing dislocations to be more effectively locked by the  $\gamma'$  phase. Those are abruptly released afterwards during the test, generating extensive dislocation activity through slip bands. Ultimately, the bands initiate localized separation that leads to the development of cracks [204].

Despite the observation of a reduced ductility at 700 °C in tensile creep tests, at this temperature both reinforced and non-reinforced alloys presented the longest times to rupture. The composite produced by LEM + PS process, however, did exhibit a shortened secondary creep stage followed by longer tertiary step, when compared to the non-reinforced reference. The divergence can be attributed to the finer grain microstructure observed in this composite, which presented a tenfold reduction in grain size compared to the original alloy (decreasing from 107 to 9  $\mu\text{m}$  in average diameter). The extremely refined microstructure facilitates creep strain by promoting both intergranular diffusion and grain boundary sliding, which are generally detrimental to the creep resistance [153]. However, an assessment is that a possible compromise between a favorable higher ductility and good creep resistance could be achieved, provided that an excessively refinement of the microstructure could be avoided. It is important to consider that certain amount of ductility is advantageous for an optimal adjustment of the blade connection to the disc, thus reducing the likelihood of undesired resonant vibrations [205].

Time to rupture in tensile creep tests was generally shorter for the composite produced by LEM + PS route. The differences in relation to the non-reinforced reference are larger at higher

temperatures, and become significantly smaller at 700 °C. The reduced performance of the composite in this aspect can be attributed to presence of  $\text{TiC}_p$  clusters, the reinforcement morphology and the higher material ductility, that induces particles collision and breakage. The resulting sharp-edged fragments are well known as stress concentrators, contributing to voids generation and consequently to the reduction of creep life [87]. Furthermore, the relatively large angular particles added to this composite are prone to easier break, in comparison to fine rounded ones [96,97].

The minimum creep rates obtained from tensile creep tests at 700 °C were similar between the non-reinforced reference (Figure 72) and the composite produced by LEM + PS (Figure 73), both achieving the power of  $10^{-9} \text{ s}^{-1}$ . While the high amount of grain boundaries favors the intergranular diffusion, it can be inferred that the load transfer mechanism counteracts the effect to a significant extent. In contrast, higher temperatures promoted faster rates in the composite, with even larger discrepancies when applying lower stresses. The condition favors higher diffusion rates and promotes the flow through grain boundaries in the fine microstructure observed in the composite [153,206]. At these circumstances, it is considered that the load transfer mechanism is no more capable to compensate for the intense intergranular diffusion.

Further investigation was conducted with compression creep tests at 700 °C (Figure 88), which involved additionally the composite produced by HEM + SPS method. The reduced severity of this experiment on the microstructure, regarding the odds of particle breakage and development of voids, resulted in the lowest minimum creep rates to be observed in the composite produced by LEM + PS route. In such conditions, the load transfer to the reinforcement by shear stress is favorable for a reduction in the creep rates [83], particularly in composites that present a neat matrix/reinforcement interface. It is acknowledged that the optimal load transfer occurs when the contact between metallic and ceramic phases is free from artifacts or surface imperfections, which eventually arise from the manufacturing process [4,14,15,207].

The composite produced by HEM + SPS process did not present the same performance of its counterpart fabricated by LEM + PS method at 700 °C, exhibiting compression creep rates 2 to 2.5 orders of magnitude faster in the range of stress investigated. The outcome is related to the extremely refined microstructure resulting from the high energy milling process, which promoted more diffusion paths. However, the aftermath is in contrast with the improvements observed in the LEM + PS variety, which also present a fine microstructure, when submitted to compression tests at the same conditions. Hence, another aspect can be hypothesized as playing a major role in this case: the existence of flaws in the matrix/reinforcement interface in the variant produced by the HEM + SPS, particularly resulting from reactions during the high energy milling process. It is shown in the microstructure analysis that reactions between metallic and ceramic phases occur more frequently in this processing route, which may lead to worse  $\text{TiC}_p$ /matrix pairing and consequently to poor load transfer during creep.

At 750 °C in compression creep tests conducted with 280 MPa (Figure 89), the non-reinforced reference achieved momentary lower creep rates, but entered the tertiary creep stage after taking roughly the same amount of time as required by the composite produced by LEM + PS. It also must be noted that the non-reinforced variant presented faster creep rates in the tertiary regime, which can be used to predict both materials reaching 2% of strain in similar time, and the composite attaining 3% of strain in a longer time. Therefore, at this temperature a near-tie situation between both variants can be observed. The composite produced by HEM + SPS route again produced significantly faster creep rates, as well as initiating the tertiary regime very prematurely in relation to the other tested varieties. The case is explained by the same premises that lead to a very similar stand at 700 °C.

Compression creep tests conducted at 800 °C (Figure 90) resulted in generally faster creep rates in all evaluated materials, but affected notably the composite produced by HEM + SPS, which presented the largest discrepancies to its counterparts at this temperature. While differences were already observed at 700 and 750 °C, the potential for intense grain boundary diffusion at higher temperatures leads to even poorer performance of this variant. In contrast, the composite produced by LEM + PS was able to still display lower steady-state creep rates in comparison to the non-reinforced reference. It should be noted again that the reference exhibited a punctual minimum creep rate, before promptly entering the tertiary regime. The composite produced by LEM + PS, oppositely, exhibited a longer lasting steady-state step, notably at lower stresses. A more suitable grain size (not excessively refined) and a better  $\text{TiC}_p$ /matrix interface in this variant are probable causes that must be considered to justify the superior performance of this composite.

A correlation between grain size and the minimum strain rate can also be made using literature data, to verify the existence of a correspondence in behavior between the non-reinforced X-750 alloy and the composites. Tensile creep data from Venkiteswaran (1974) [112], using variants with different grain sizes, was employed to establish the behavior expected from the non-reinforced alloy used in the present study, and compared to experimental data from both composites (Figure 103). For the comparison, it was assumed initially that only the grain size could affect the creep strain rates. However, it was observed that the slope in the trendline between the composites varied significantly from the slope observed between the non-reinforced variants. Therefore, the initial premise would be inaccurate, and additional factors would be responsible for the more severe change in strain rates in the composites, when varying the grain size.



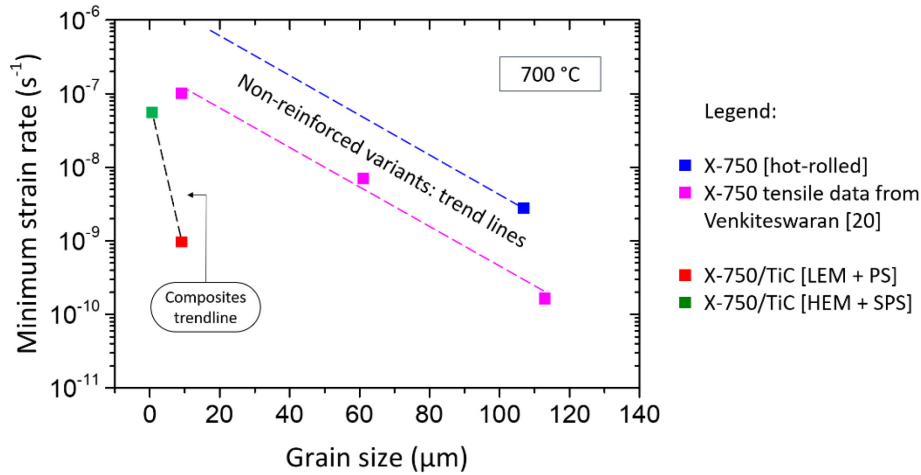


Figure 103 - Comparison between creep data from Venkiteswaran (1974) with 276 MPa [112], the expected (extrapolated) behavior of the non-reinforced X-750 used as reference in this work, and the devised composites. The remainder results were obtained with the application of 280 MPa.

The hypothesis of a load transfer process applies in this case to support explaining the observed difference, but the effectiveness of the mechanism could be related to both changes in the TiC morphology and the microstructure of the  $\gamma + \gamma'$  matrix, conditional on the production route chosen for each variant. This proposition is further discussed in chapter 5.4, in addition to the creep mechanisms expected to occur at the  $\gamma + \gamma'$  matrix exclusively.

## 5.4 Creep mechanisms

In order to establish the governing creep mechanism, it is necessary to consider the temperature, stress,  $\gamma/\gamma'$  interface coherency and interparticle spacing, as well as the true Norton stress exponent. Possible ways for dislocations to overcome obstacles, namely primary and secondary  $\gamma'$  precipitates, involve mechanisms such as particle climb, Orowan bowing and particle cutting [35,46,51,113,123,124,150,151,177,208–210].

To investigate the feasibility of Orowan bowing taking place in the investigated materials, first it is required to define the most probable course of slipping in the matrix lattice. In Ni-based superalloys, slip occurs most efficiently on the {111} plane in the  $\langle 110 \rangle$  direction [2], where the shortest lattice vector is  $(a_0/2)[110]$ . One common observed slip direction is  $b = (a_0/2)[10\bar{1}]$ , which is not the most energetically favorable shear displacement in this system. Therefore, the dislocation in this case must decompose into two partial ones, as seen in equation 18, to achieve the lowest energy necessary to slip.

$$(a_0/2)[10\bar{1}] \rightarrow (a_0/6)[2\bar{1}\bar{1}] + (a_0/6)[11\bar{2}] \quad (18)$$

As a result, the effective Burgers vector was calculated as  $b = a_0/\sqrt{6} + a_0/\sqrt{6} = 2.91 \text{ \AA}$ .

The Orowan stress can be obtained using the equation 19, in its simplest form [151]:

$$\sigma_o = Gb / \lambda \quad (19)$$

where  $G$  is the shear modulus,  $b$  the Burgers vector and  $\lambda$  the interparticle spacing.

By using the elastic modulus results obtained with nanoindentation tests in the composites, it is possible to obtain the approximate shear modulus with the relation  $E = 2G \times (1 + \nu)$ , where  $\nu$  is the Poisson ratio [211]. From the relation are obtained  $G = 66 \text{ GPa}$  at  $700 \text{ }^\circ\text{C}$  and  $62 \text{ GPa}$  at  $800 \text{ }^\circ\text{C}$ , respectively. The measured mean spacing between primary  $\gamma'$  was observed to be  $610 \text{ \AA}$ , and between secondary  $\gamma'$  to be  $235 \text{ \AA}$ . Therefore, the necessary energy for Orowan bowing to occur at  $\gamma'$  precipitates was calculated, and the results are shown in Table 13.

Table 13 – Stress estimated for Orowan bowing to occur at  $\gamma'$  in the investigated alloys at initial state, given all necessary conditions. Values obtained with equation 19.

	At 700 °C			At 800 °C		
	Minimum	Maximum	Average	Minimum	Maximum	Average
Interparticle distance (Å)	120	1100	610	120	1100	610
$\sigma_o$ at primary $\gamma'$ (MPa)	1601	175	315	1504	164	296
$\sigma_o$ at secondary $\gamma'$ (MPa)	1281	601	818	1203	564	768

It is acknowledged that at high stresses the preferential  $\gamma'$  bypass mechanism in Ni-based superalloys with highly coherent intermetallics is particle cutting, transitioning to Orowan bowing when overaged  $\gamma'$  precipitates become incoherent with the matrix [127]. At lower stresses, particle climb is the governing mechanism [109,113,122–124,131,150,151,209,212,213], particularly in alloys with lower  $\gamma/\gamma'$  misfit ( $\sim 0.1 \%$ ) at creep temperatures [51], which is precisely the case with the Inconel X-750 [42]. Consequently, the calculated Orowan stresses are valid once the  $\gamma/\gamma'$  interface evolves to an incoherent one, commonly after thousands of hours in isothermal treatment at high temperatures. In this scenario, considering the interparticle size as unchanged, Orowan bowing would be feasible only at primary  $\gamma'$  for the stress range investigated. But when considering the initial microstructure of both non-reinforced references and composites, the alloy with a highly coherent  $\gamma'/\gamma$  interface is expected to provide as creep governing mechanism a combination of glide and climb at lower stresses. The statement is supported by literature evidence that shows the existence of stress fields around the coherent  $\gamma'$  intermetallics, which

create opportunity for dislocations to climb locally over the obstacles at low stress regime [33,34,101,113,126,149].

The stress necessary for local climb to occur is roughly half of the calculated Orowan stress. Below this value, dislocations remain immobilized at the particles, and creep does not occur [51,151]. That is known as the threshold stress in particle reinforced alloys. At 700 °C, the investigated varieties present an average calculated Orowan stress of 315 MPa for primary  $\gamma'$  and 818 for secondary  $\gamma'$  (Table 13). At this same temperature, it was observed at the not-reinforced Inconel X-750 hot rolled had a threshold stress of 304 MPa, obtained through the approximation method after compression creep tests. Therefore, it can be hypothesized that the threshold stress observed takes place when dislocations are immobilized by the secondary  $\gamma'$ , since these particles are in better agreement with the stress expected for local climb to occur ( $\sigma_{TH} \approx 0.5 \times \sigma_0$ ) [151].

The possibility of  $\gamma'$  cutting to occur at the range of temperatures and stresses tested must also be investigated. Pollock and Argon [214] obtained both theoretically and experimentally at 800 °C the stress necessary for a leading screw dislocation to enter a  $\gamma'$  particle before leaving an APB behind it, therefore initiating the cutting process. With the equation 20 [215], they observed the resolved shear stress obtained to be 21% lower than the stress measured experimentally.

$$\hat{\sigma}_c = \chi_{APB} / b \quad (20)$$

where  $\hat{\sigma}_c$  is the resolved shear stress to start  $\gamma'$  cutting by a leading screw dislocation,  $\chi_{APB}$  is the APB energy and  $b$  is the Burgers vector of the slip plane.

The same approach was applied to the results of this work, using the APB energy necessary for glide on the {111} plane of 0.111 J/m<sup>2</sup> [216], and the respective Burgers vector of 0.291 nm, as previously calculated. As a result,  $\chi_{APB} = 381$  MPa was obtained. However, when applying the offset to experimental results obtained by Pollock and Argon [214], a resolved shear stress in the vicinity of 480 MPa should be expected. Considering that creep experiments conducted in this work were limited to stresses below 500 MPa,  $\gamma'$  particle cutting is generally not expected to occur.

Additional evidence of dislocation climb as governing creep mechanism for the stress and temperature range selected in the investigation is the Norton creep exponent. A mixture of glide and climb is commonly reported as dominating mechanisms for  $n$  values between 4 and 7, while in power-law breakdown regime higher creep exponents are expected [34,105,117,129,130]. True stress exponents obtained for all investigated materials were situated in the range of 4 to 7, supporting the assumption.

There is also indication that diffusion through grain boundaries affect considerably the strain rates in the composites. The true creep activation energy determined for the hot-rolled non-reinforced reference was established as 375 kJ/mol at 700 °C in compression creep tests. While in pure and low alloyed metals the creep activation energy is close to the value necessary to provoke

self-diffusion, in highly mixed crystal systems and particle reinforced composites  $Q_c$  is significantly higher [126,217]. Therefore, true values over 280 kJ/mol, the energy for self-diffusion of Ni in pure polycrystalline Nickel, are expected [218]. The composites, however, presented values of 295 and 311 kJ/mol in specimens produced by LEM + PS and HEM + SPS, respectively. The lower activation energies, in relation to the non-reinforced variant, are expected as a result of facilitated diffusion through the higher amount of grain boundaries, since this process is thermally activated.

The existence of a threshold stress was expected in both reinforced and non-reinforced variants, mainly as a result of the fine  $\gamma'$  dispersed in the matrix, and evidenced by the anomalously elevated apparent Norton stress exponents. The extent of the threshold stress can also be linked to the amount of  $\gamma'$  present in each investigated material. In compression creep tests, the composite produced by HEM + PS method displayed the lowest  $\sigma_{TH}$  value at 700 °C. The variant also presented the lowest amount of total  $\gamma'$  in analysis conducted by Rietveld refinement, among all tested materials. It is established that the presence of fine precipitates and dispersoids in the matrix leads to the development of a threshold stress, below which creep does not occur by the movement of dislocations (though diffusional processes might still occur) [153,177]. When reducing the amount of  $\gamma'$  in the matrix, therefore, a drop in the threshold stress is also expected. It is important to note that, as shown before, at the conditions of test the threshold stress is expected to occur due to immobilization of dislocations mainly by the secondary  $\gamma'$  particles, since climb is still feasible at primary  $\gamma'$  at these circumstances.

It is important to observe that the threshold stress declined with an increase in temperature. Considering results from compression creep tests, raising the temperature from 700 to 800 °C caused a decline of 39% in  $\sigma_{TH}$  in the non-reinforced variant, while the composite produced by LEM + PS route presented a reduction of 34%. The outcome is linked to the partial dissolution of secondary  $\gamma'$  [197], which were observed in this work to be the primary source of the threshold stress at the range of stresses and temperatures investigated.

A divergence in the true total threshold stress, however, was observed between the two composite variants submitted to compression creep tests. An approximation with the equation 11 was used to isolate two components of the threshold stress: the load transfer to reinforcing particles, and the threshold stress deriving exclusively from the dislocations immobilized at  $\gamma'$  precipitates in the  $\gamma + \gamma'$  matrix. As calculated in section 4.4.3, it was identified that the composite X-750/TiC [LEM + PS] presented almost three times more load transferred from the matrix to the reinforcing carbides, compared to the X-750/TiC [HEM + SPS] variant. The outcome derives from two major dissimilarities in the composites: reinforcement size and a reduced amount of reactions between the matrix and the added carbides. It is acknowledged that to bear load, an optimal range of particle size must be used, where reinforcements with diameter below 1  $\mu\text{m}$  (as observed in the X-750/TiC [HEM + SPS] variant) present a considerably lower contribution to the effect [87,89,90]. Likewise, the presence of  $\eta$  phase in the X-750/TiC [HEM + SPS] composite is evidence of a stronger reaction between the TiC particles and the matrix in the variant, originating with the

partial dissolution of the carbides during the SPS process. The  $\eta$  phase is known to cause the formation of  $\gamma'$ -free zones by the depletion of solute elements [33,59,67], which can be attested by the lower volume of  $\gamma'$  observed in this composite.

Both non-reinforced reference and composite prepared by LEM + PS exhibited true stress exponents in the same order ( $n \approx 6$ ), when submitted to tensile creep tests. The value is consistent with power law creep, and indicate that the addition of reinforcing TiC particles did not affected the main creep mechanism. When analyzing compression creep results, the equivalence between both materials was kept, but the composite produced by HEM + SPS process (tested only under compression) exhibited a higher stress exponent,  $n \approx 6$ , against  $n \approx 4.5$  for the other tested varieties. While the value is still inside the range expected for a  $\gamma'$ -strengthened superalloy at the stress level investigated [177], the difference can be attributed to statistical variances originated from the limited amount of specimens submitted to compression creep tests.

The power law equation for the composite produced by LEM + PS route, tested under tensile creep stress at 800 °C, is summarized in equation 21. Likewise, for the compression creep tests conducted at 700 °C the relationships of the composites produced by LEM + PS and HEM + SPS routes are defined in equations 22 and 23, respectively.

$$\dot{\epsilon}_{ss} = A \left( \frac{\sigma - \sigma_{TH}}{E} \right)^n \cdot \exp \left[ -\frac{Q_c}{RT} \right] = 9.83 \cdot 10^{-8} \left( \frac{\sigma - 62}{149} \right)^{5.9} \cdot \exp \left[ -\frac{295}{R \cdot 1073} \right] \quad (21)$$

$$\dot{\epsilon}_{ss} = A \left( \frac{\sigma - \sigma_{TH}}{E} \right)^n \cdot \exp \left[ -\frac{Q_c}{RT} \right] = 2.89 \cdot 10^{-9} \left( \frac{\sigma - 153}{168} \right)^{4.4} \cdot \exp \left[ -\frac{295}{R \cdot 973} \right] \quad (22)$$

$$\dot{\epsilon}_{ss} = A \left( \frac{\sigma - \sigma_{TH}}{E} \right)^n \cdot \exp \left[ -\frac{Q_c}{RT} \right] = 8.98 \cdot 10^{-8} \left( \frac{\sigma - 123}{168} \right)^{6.8} \cdot \exp \left[ -\frac{311}{R \cdot 973} \right] \quad (23)$$

where  $\dot{\epsilon}_{ss}$  is the steady state creep rate,  $A$  is a material constant,  $\sigma$  is the applied stress,  $\sigma_{TH}$  is the threshold stress,  $n$  is the stress exponent,  $E$  is the elastic modulus,  $Q_c$  is the creep activation energy,  $R$  is the universal gas constant (8.314 J/mol·K) and  $T$  is the temperature in Kelvin.

## 5.5 Estimation of life under creep

A Monkman-Grant parametrization conducted for both tensile (Figure 76 b) and compression creep results (Figure 96 b) showed a high coefficient of determination for the composites produced. The relationship facilitates the life estimation of both variants, for the temperature and stress range tested. It also reveals an opposite behavior between the two kind of creep tests conducted, with the composite prepared by LEM + PS route frequently presenting the fastest times-to-rupture in the tensile tests, and the slowest in compression tests. While this

result concerns only the range of investigation, the outcome can be attributed to the faster build-up of critical defects in the tensile test, such as micro voids [204], resulting the of combination particle sliding [112] and damage to the reinforcing phase. Regarding damage, it is established that angular-shaped reinforcements and particles positioned in direct contact with each other are also sources of cavities, that leads to failure prematurely when large voids are formed [105].

Creep life was also estimated with a Larson-Miller parametrization. The equations resulting from a polynomial data fitting exhibited satisfactory determination coefficients from both tensile (Figure 77) and compression creep tests (Figure 97), allowing the estimation of time to rupture on all investigated composites. When analyzing compression creep tests specifically, the parameter was modified to account for 2% of strain, instead of rupture. It is important to note that the capability of a Larson-Miller parametrization to estimate the creep life is limited to the conditions of test, and therefore the creep life projection on compression creep tests are not be translated to an estimation on tensile creep tests, and *vice-versa*. Likewise, only the ranges of temperature and stress adopted in the investigation are feasible as parameters for an accurate creep life estimation with the given equations.

## 5.6 Functional effect of density reduction

An important aspect in metal matrix composites that must not be neglected is the potential for a material density reduction, in comparison to the non-reinforced alloy. When considering the attainable weight deduction of a turbine blade made from the proposed MMCs, it is necessary to account for a subsequent reduction in the stress acting at any section of it during work, regarding the direct proportionality between these parameters ( $\rho \propto \sigma$ ). The composites produced by LEM + PS and HEM + SPS routes exhibited density reductions of 5.8 and 7.0%, respectively, in relation to the non-reinforced hot rolled variant. As result, corresponding declines in the creep rates of a blade submitted to centripetal forces are expected.

An example was presented to elucidate the potential of the material density reduction. The case illustrates a hypothetical rotating blade, demonstrating not only the effects of the achievable decrease on the effective creep rates, but also pointing intersections between the non-reinforced reference and the composites, using fitted data from tensile creep tests (Figure 78) and extrapolated data from compression creep tests (Figure 98). When considering strain rates from tensile experiments conducted at 800 °C, a parity point between the non-reinforced material and the composite produced by LEM + PS was achieved at  $3.02 \times 10^{-1} \text{ s}^{-1}$ , for an estimated rotational speed. The curve was generalized for a minimum strain rate vs. stress plot, showing that for any applied stress above 458 MPa the composite is expected to creep slower in relation to the non-reinforced variant. Considering that many gas turbines blades present tension stresses at this

range during operation [12], the MMC conceived can be considered a feasible candidate to replace the original alloy at the conditions of temperature and stress indicated.

Still considering the density reduction, the MMC behavior in a hypothetical work situation at 700 °C was also investigated. In this case the data obtained does not present crossing points, but an extrapolation was conducted to consider a presumptive situation. Generally the differences between the non-reinforced variant and the composite produced by LEM + PS are larger when the density is considered as a parameter. Therefore, it is expected that the MMC variant will always present slower strain rates in comparison to the original alloy at this temperature, for any applied stress over 3 MPa. The differences also grow with the stress, favoring even lower rates in the composite in this situation. In contrast, the reinforced variation produced by HEM + SPS is expected to present always the highest creep rates, with differences in relation to the other variants growing with the stress.

In light of the general creep data, and the consideration of the density reduction influence in a working turbine blade, the performance of the composite produced by LEM + PS method has the potential to exceed the one presented by the original alloy at 700 °C, and possibly at even lower temperatures. But contrary to this result, the composite prepared by HEM + SPS route did not surpass its counterparts at any metric in both tensile and compression creep tests. Despite indications of a possibly good microstructural stability, the excessively refined microstructure and a possibly flawed TiC<sub>p</sub>/matrix interface failed to achieve an effective reduction on creep rates.

## 6. Conclusions

The concept of a Ni-based superalloy reinforced with TiC particles was presented, resulting in two metal matrix composites produced through different powder metallurgy routes: a low energy mixing step combined with uniaxial press sintering, and a high energy milling process combined with spark plasma sintering. Both variants presented primary and secondary  $\gamma'$  intermetallics, planar defects (such as twin boundaries) and refined microstructures, in relation to non-reinforced references.

The process of powders comminution resulted in intense refinement in the composite prepared by HEM + SPS method, leading to more reactions between the metallic matrix and reinforcing particles. The absence of  $\eta$  laths in the composite produced by SPS, in contrast to the result observed in the non-reinforced variant prepared by the same method, derives from the presence of the high amount of well dispersed Ti-rich MC particles. These present a high affinity for Ti and Nb, and were able to capture the excess of these elements in solution during the sintering process. Additionally, primary  $\gamma'$  denuded zones in the composite produced by HEM + SPS resulted from the partial depletion of Al and Ti near  $TiC_p$ , but secondary  $\gamma'$  remained present.

Long isothermal aging treatments revealed how the composites microstructure develops at 700 and 800 °C, after up to 1000 h of overaging. The presence of  $TiC_p$  delayed the growth of primary  $\gamma'$  in the composite prepared by LEM + PS, by limiting the initial availability of Al and Ti in solid solution. However, the dispersion of highly refined  $TiC_p$  in the variant prepared by HEM + SPS led to a dissolution of Ti into the matrix during isothermal overaging, inducing the formation of the undesired  $\eta$  phase after 1000 h at 800 °C. At this temperature, the MC precipitates are no more preferably formed. Therefore, it is assumed that an overall larger surface area of fine dispersed  $TiC_p$  prompts the process in the variant produced by the HEM + SPS method.

Power law creep was observed in the composites, in the range of temperature and stress tested, with the preferential  $\gamma'$  bypass mechanism determined to be climb and glide. A higher stress exponent ( $n \approx 7$ ) in the variety produced by HEM + PS was related to both a lower amount of the  $\gamma'$  intermetallic, favoring glide, and the presence of a significant smaller grain size. Likewise, the threshold stress was lower in this variant as a result of less  $\gamma'$  available to hinder dislocations.

In relation to the non-reinforced hot rolled alloy, the creep resistance of the composites declined sharply with a temperature increase, due to the high amount of grain boundaries inducing intergranular diffusion. Accordingly, creep activation energies were also comparatively lower in both composites. However, the variant produced by LEM + PS method showed strain rates in the same order of magnitude of the non-reinforced reference at 700 °C, in tensile creep tests, and exhibited the lowest rates at all tested temperatures and stresses in compression creep tests. Furthermore, when considering the material density as a parameter for an estimation of the effective stress acting on a rotating turbine blade, the composite produced by LEM + PS method



exhibited the lowest strain rates above 458 MPa at 800 °C under tension, and above 3 MPa at 700 °C, when extrapolating values from compression creep tests. The outcome is attributed to a favorable load transfer to the reinforcing particles in this composite variant, effectively counterbalancing the diffusion through grain boundaries.

The investigation suggests that by adding a highly compatible ceramic phase, in the form of particles, the creep resistance of Ni-based superalloys can be improved. Yet, aggressive powder milling and sintering processes that cause momentary high temperatures must be avoided, in order to reduce interactions between matrix and reinforcing particles, which lead to the formation of undesired phases and excessively refinement of the microstructure. Conclusively, the study also demonstrates how even a modest decrease in the alloy density, by adopting a concept of a metal matrix composite, has the potential to significantly reduce creep rates in a working turbine blade.

Perspectives for the research continuity include the use of advanced fabrication methods, such as laser assisted additive manufacturing, to attempt an intragranular dispersion of reinforcing particles. The approach has the potential to produce a coarser microstructure, with reduced intergranular diffusion. Additionally, raising the niobium content in the composite mixture is also considered, since the formation of very stable Nb-rich MC precipitates was observed in the developed MMCs. The aim is to provide further opportunity for the enrichment of TiC by Nb, thereby potentially raising the carbide compatibility with the  $\gamma$  matrix.

## 7. References

- [1] M.J. Donachie, S.J. Donachie, *Superalloys - A Technical Guide*, 1st ed., ASM International, 2002.
- [2] R.C. Reed, *The Superalloys - Fundamentals and Applications*, 1st ed., Cambridge University Press, Edinburgh, 2006.
- [3] The World Bank, *Air Transport and Energy Efficiency*, Washington, 2012.
- [4] B.N. Chawla, Y. Shen, *Mechanical Behavior of Particle Reinforced Metal Matrix Composites*, *Adv. Eng. Mater.* 3 (2001) 357–370.
- [5] Department of Defense. United States of America., *Metal Matrix Composites*, in: *Compos. Mater. Handb.*, 2002: p. 304.
- [6] K.U. Kainer, *Custom-made Materials for Automotive and Aerospace Engineering: Metal Matrix Composites*, Wiley, 2006.
- [7] A. Evans, C. San Marchi, A. Mortensen, *Metal matrix composites in industry, an introduction and a survey*, Springer Science, 2003. <https://doi.org/10.1007/978-1-4615-0405-4>.
- [8] United States Congress. Office of Technology Assessment., *Metal Matrix Composites*, in: *Adv. Mater. by Des.*, DIANE Publishing, Washington, 1988: pp. 99–117.
- [9] A.P. Mouritz, *Creep of aerospace materials*, in: *Introd. to Aerosp. Mater.*, Woodhead Publishing, 2012: pp. 521–533. <https://doi.org/10.1533/9780857095152.521>.
- [10] C. Soares, *Gas Turbines - A Handbook of Air, Land and Sea Applications*, Elsevier, 2014.
- [11] K. Volkov, *Efficiency, Performance and Robustness of Gas Turbines*, InTech, Rijeka, 2012.
- [12] Donna J. Ciafone, *Gas Turbines: Technology, Efficiency and Performance*, Nova Science, New York, 2011.
- [13] R. Fernández, G. González-Doncel, *Creep fracture and load transfer in metal-matrix composite*, *Scr. Mater.* 59 (2008) 1135–1138. <https://doi.org/10.1016/j.scriptamat.2008.07.038>.
- [14] R. Fernández, G. González-Doncel, *Threshold stress and load partitioning during creep of metal matrix composites*, *Acta Mater.* 56 (2008) 2549–2562. <https://doi.org/10.1016/j.actamat.2008.01.037>.
- [15] R. Fernández, G. González-Doncel, *Additivity of reinforcing mechanisms during creep of metal matrix composites: Role of the microstructure and the processing route*, *J. Alloys Compd.* 475 (2009) 202–206. <https://doi.org/10.1016/j.jallcom.2008.07.053>.
- [16] Elisabetta Gariboldi, *Metal Matrix Composites: Discontinuously Reinforced, Microstructure and Mechanical Property Correlations*, in: L. Nicolais, A. Borzacchiello (Eds.), *Wiley Encycl. Compos.*, 2nd ed., John Wiley & Sons, 2012: pp. 1–16.

- [17] P. Andresen, B. Antolovich, S.D. Antolovich, S. Becker, *Fatigue and Fracture*, ASM International, 1996.
- [18] M. e Meyers, K. Chawla, *Mechanical behavior of materials*, 2nd ed., Cambridge University Press, 2009.
- [19] J.D. Mattingly, H. Von Ohain, J. a Schetz, *Elements of Propulsion: Gas Turbines and Rockets* Department of Mechanical Engineering, AIAA, Virginia, 2006. <https://doi.org/10.2514/4.861789>.
- [20] H.J. Ryu, K.H. Chung, S.I. Cha, S.H. Hong, Analysis of creep behavior of SiC/Al metal matrix composites based on a generalized shear-lag model, *J. Mater. Res.* 19 (2004) 3633–3640. <https://doi.org/10.1557/JMR.2004.0472>.
- [21] L.H. Dai, Z. Ling, Y.L. Bai, Size-dependent inelastic behavior of particle-reinforced metal-matrix composites, *Compos. Sci. Technol.* 61 (2001) 1057–1063. [https://doi.org/10.1016/S0266-3538\(00\)00235-9](https://doi.org/10.1016/S0266-3538(00)00235-9).
- [22] Y. Huang, T.G. Langdon, The creep behavior of discontinuously reinforced metal-matrix composites, *Jom.* 55 (2003) 15–20. <https://doi.org/10.1007/s11837-003-0187-7>.
- [23] M.J. Starink, S. Syngellakis, Shear lag models for discontinuous composites: fibre end stresses and weak interface layers, *Mater. Sci. Eng. A.* 270 (1999) 270–277.
- [24] J.D. Eshelby, The determination of the elastic field of an ellipsoidal inclusion, and related problems, *Proc. R. Soc. A.* 241 (1957) 376–396. <https://doi.org/10.1016/j.msea.2007.08.046>.
- [25] M.J. Tan, X. Zhang, Powder metal matrix composites: selection and processing, *Mater. Sci. Eng. A.* 244 (1998) 80–85. [https://doi.org/10.1016/S0921-5093\(97\)00829-0](https://doi.org/10.1016/S0921-5093(97)00829-0).
- [26] J.W. Kaczmar, K. Pietrzak, W. Wlosinski, The production and application of metal matrix composite materials, *J. Mater. Process. Technol.* 106 (2000) 58–67. [https://doi.org/doi:10.1016/S0924-0136\(00\)00639-7](https://doi.org/doi:10.1016/S0924-0136(00)00639-7).
- [27] M.P. Boyce, *Gas Turbine Engineering Handbook*, 2nd ed., Gulf Professional Publishing, 2002.
- [28] Rolls-Royce plc, *The Jet Engine*, 5th ed., Derby, 1986.
- [29] G.A. Kool, Current and future materials in advanced gas turbine engines, *J. Therm. Spray Technol.* 5 (1996) 31–34. <https://doi.org/10.1007/BF02647514>.
- [30] J. Liburdi, J.O. Stephens, Experience in Extending the Life of Gas Turbine Blades, *ASME.* (1980) 1–10.
- [31] M. Azadi, M. Azadi, Evaluation of high-temperature creep behavior in Inconel-713C nickel-based superalloy considering effects of stress levels, *Mater. Sci. Eng. A.* 689 (2017) 298–305. <https://doi.org/10.1016/j.msea.2017.02.066>.
- [32] G. Lemos, M.C. Fredel, F. Pyczak, U. Tetzlaff, Development of a TiCp Reinforced Ni-Based Superalloy MMC, with High Creep Resistance and Reduced Weight, *Key Eng. Mater.* 742 (2017) 189–196. <https://doi.org/10.4028/www.scientific.net/KEM.742.189>.

- [33] J.H. Weber, *Encyclopedia of Materials: Science and Technology*, in: Elsevier Science Ltd., 2001: pp. 1–4.
- [34] M. Kassner, *Fundamentals of creep in metals and alloys*, 2nd ed., Elsevier, 2008.
- [35] R.C. Reed, *The Superalloys: Fundamentals and applications*, 2006. <https://doi.org/10.1017/CBO9781107415324.004>.
- [36] K. Yagi, G. Merckling, T. U. Kern, *Creep properties of heat resistant steels and superalloys*, 2004.
- [37] J. Davis, *Metals Handbook Desk Edition*, 2nd ed., ASM International, 1998. <http://www.bcin.ca/Interface/openbcin.cgi?submit=submit&Chinkey=204840> (accessed February 10, 2014).
- [38] L.G. Ehrlich, *What Drives Nickel Prices - A structural VAR Approach*, 2018.
- [39] A. Sarkar, P. Mukherjee, P. Barat, T. Jayakumar, Mahadevan S., S.K. Rai, Lattice Misfit Measurement in Inconel 625 By X-Ray Diffraction Technique, *Int. J. Mod. Phys. B.* 22 (2008) 3977–3985. <https://doi.org/10.1142/S0217979208048772>.
- [40] A.K. Singh, N. Louat, K. Sadananda, Dislocation Network Formation and Coherency Loss around Gamma-Prime Precipitates in a Nickel-Base Superalloy, 19 (1988).
- [41] T.G. FERENCE, S.M. Allen, Dislocation / Precipitate Interactions during Coarsening of a Plastically Strained High-Misfit Nickel-Base Superalloy, 17 (1986).
- [42] H. Hisazawa, Y. Terada, M. Takeyama, Morphology evolution of  $\gamma'$  precipitates during isothermal exposure in wrought Ni-based superalloy Inconel X-750, *Mater. Trans.* 58 (2017) 817–824. <https://doi.org/10.2320/matertrans.M2016376>.
- [43] R.A. Ricks, A.J. Porter, R.C. Ecomb, The growth of  $\gamma'$  precipitates in nickel-base superalloys, *Acta Metall.* 31 (1983) 43–53.
- [44] F. Pyczak, B. Devrient, H. Mughrabi, The effects of different alloying elements on the thermal expansion coefficients, lattice constants and misfit of nickel-based superalloys investigated by X-ray diffraction, *Proc. Int. Symp. Superalloys.* (2004) 827–836. [https://doi.org/10.7449/2004/superalloys\\_2004\\_827\\_836](https://doi.org/10.7449/2004/superalloys_2004_827_836).
- [45] N.S. Stoloff, R.G. Davies, The mechanical properties of ordered alloys, *Prog. Mater. Sci.* 13 (1968) 1–84. [https://doi.org/10.1016/0079-6425\(68\)90018-2](https://doi.org/10.1016/0079-6425(68)90018-2).
- [46] R.C. Reed, *The Superalloys: Fundamentals and Applications*, Cambridge University Press, 2006.
- [47] L.R. Owen, H.Y. Playford, H.J. Stone, M.G. Tucker, A New Approach to the Analysis of Short-range Order in Alloys using Total Scattering, *Acta Mater.* 115 (2016) 155–166.
- [48] P.K. Venkiteswaran, D.M.R. Taplin, The Creep Fracture of Inconel X-750 at 700 °C, *Met. Sci.* 8 (1974) 97–106.
- [49] Special Metals Corporation, *Inconel X-750*, Huntington, 2004.
- [50] E. Arzt, D.S. Wilkinson, Threshold stresses for dislocation climb over hard particles: The effect of an attractive interaction, *Acta Metall.* 34 (1986) 1893–1898.

[https://doi.org/10.1016/0001-6160\(86\)90247-6](https://doi.org/10.1016/0001-6160(86)90247-6).

- [51] A.J. Goodfellow, Strengthening mechanisms in polycrystalline nickel-based superalloys, *Mater. Sci. Technol.* (United Kingdom). 34 (2018) 1793–1808. <https://doi.org/10.1080/02670836.2018.1461594>.
- [52] R.E. Smallman, R.J. Bishop, *Modern Physical Metallurgy and Materials Engineering: Science, Process, Applications*, BH, 1999.
- [53] D.A. Porter, K.E. Easterling, M.Y. Sherif, *Phase Transformations in Metals and Alloys*, 2009.
- [54] B.L.M. Paul Haasen, Peter Haasen, *Physical Metallurgy*, Cambridge University Press, Cambridge, 1996.
- [55] R.J. Mitchell, M. Preuss, S. Tin, M.C. Hardy, The influence of cooling rate from temperatures above the  $\gamma'$  solvus on morphology, mismatch and hardness in advanced polycrystalline nickel-base superalloys, *Mater. Sci. Eng. A.* 473 (2008) 158–165.
- [56] J. Coakley, H. Basoalto, D. Dye, Coarsening of a multimodal nickel-base superalloy, 58 (2010) 4019–4028. <https://doi.org/10.1016/j.actamat.2010.03.017>.
- [57] P.W. Voorhees, The Theory of Ostwald Ripening, *J. Stat. Phys.* 38 (1985) 231–252. <https://doi.org/10.1295/kobunshi.48.140>.
- [58] J. Davis, *ASM Specialty Handbook: Heat-Resistant Materials*, ASM International, 1997.
- [59] G.D. Smith, S.J. Patel, The Role of Niobium in Wrought Precipitation-Hardened Nickel-Base Alloys, *Superalloys 718, 625, 706 Var. Deriv.* (2005) 135–154. [https://doi.org/10.7449/2005/Superalloys\\_2005\\_135\\_154](https://doi.org/10.7449/2005/Superalloys_2005_135_154).
- [60] Y.Q. Chen, E. Francis, J. Robson, M. Preuss, S.J. Haigh, Compositional variations for small-scale gamma prime ( $\gamma'$ ) precipitates formed at different cooling rates in an advanced Ni-based superalloy, *Acta Mater.* 85 (2015) 199–206.
- [61] K. Wakashima, B.H. Choi, T. Mori, Plastic incompatibility and its accommodation by diffusional flow: Modelling of steady state creep of a metal matrix composite, *Mater. Sci. Eng. A.* 127 (1990) 57–64. [https://doi.org/10.1016/0921-5093\(90\)90189-A](https://doi.org/10.1016/0921-5093(90)90189-A).
- [62] H.J. McQueen, B. Baudalet, *Comparison and Contrast of Mechanisms, Microstructures, Ductilities in Superplasticity and Dynamic Recovery and Recrystallization*, Pergamon Press Ltd, n.d. <https://doi.org/10.1016/B978-1-4832-8412-5.50061-8>.
- [63] M. Sundararaman, P. Mukhopadhyay, S. Banerjee, Carbide Precipitation in Nickel Base Superalloys 718 and 625 and Their Effect on Mechanical Properties, *Superalloys 718, 625, 706 Var. Deriv.* (1997) 367–378. [https://doi.org/10.7449/1997/Superalloys\\_1997\\_367\\_378](https://doi.org/10.7449/1997/Superalloys_1997_367_378).
- [64] A.W. Dix, W.F. Savage, Factors influencing strain-age cracking in Inconel X-750, *Weld J.* 50 (1971) 247.
- [65] S. Floreen, G.E. Fuchs, W.J. Yang, The Metallurgy of Alloy 625, *Superalloys 718, 625, 706 Var. Deriv.* (1994) 13–37. [https://doi.org/10.7449/1994/Superalloys\\_1994\\_13\\_37](https://doi.org/10.7449/1994/Superalloys_1994_13_37).

- [66] R. Lawitzki, S. Hassan, L. Karge, J. Wagner, D. Wang, J. von Kobylinski, C. Krempaszky, M. Hofmann, R. Gilles, G. Schmitz, Differentiation of  $\gamma'$ - and  $\gamma''$ - precipitates in Inconel 718 by a complementary study with small-angle neutron scattering and analytical microscopy, *Acta Mater.* 163 (2019) 28–39. <https://doi.org/10.1016/j.actamat.2018.10.014>.
- [67] G. Lemos, M.C. Fredel, F. Pyczak, U. Tetzlaff, Influence of Distinct Manufacturing Processes on the Microstructure of Ni-Based Metal Matrix Composites Submitted to Long Thermal Exposure, *Key Eng. Mater.* 809 (2019) 79–86. <https://doi.org/10.4028/www.scientific.net/KEM.809.79>.
- [68] P.R. Bhowal, E.F. Wright, E.L. Raymond, Effects of cooling rate and  $\gamma'$  morphology on creep and stress-rupture properties of a powder metallurgy superalloy, *Metall. Trans. A.* 21 (1990) 1709–1717. <https://doi.org/10.1007/BF02672587>.
- [69] D. Furrer, H. Fecht, Ni-based superalloys for turbine discs, *Jom.* 51 (1999) 14–17. <https://doi.org/10.1007/s11837-999-0005-y>.
- [70] F. Campbell, *Manufacturing Technology for Aerospace Structural Materials*, Elsevier, 2006. <https://doi.org/10.1016/B978-1-85617-495-4.X5000-8>.
- [71] V. Mamedov, Spark plasma sintering as advanced PM sintering method, *Powder Metall.* 45 (2002) 322–328. <https://doi.org/10.1179/003258902225007041>.
- [72] W. Yucheng, F. Zhengyi, Study of temperature field in spark plasma sintering, *Mater. Sci. Eng. B Solid-State Mater. Adv. Technol.* 90 (2002) 34–37. [https://doi.org/10.1016/S0921-5107\(01\)00780-2](https://doi.org/10.1016/S0921-5107(01)00780-2).
- [73] M. Tokita, *Spark Plasma Sintering (SPS) Method, Systems, and Applications*, Second Edi, Elsevier Inc., 2013. <https://doi.org/10.1016/B978-0-12-385469-8.00060-5>.
- [74] D. Levasseur, M. Brochu, Interparticle liquid film formation during Spark Plasma Sintering of Inconel 718 superalloy, *Adv. Mater. Res.* 409 (2012) 763–768. <https://doi.org/10.4028/www.scientific.net/AMR.409.763>.
- [75] O.F. Ogunbiyi, T. Jamiru, E.R. Sadiku, L.W. Beneke, O.T. Adesina, T.A. Adegbola, Microstructural characteristics and thermophysical properties of spark plasma sintered Inconel 738LC, *Int. J. Adv. Manuf. Technol.* 104 (2019) 1425–1436. <https://doi.org/10.1007/s00170-019-03983-w>.
- [76] S. Pasebani, A.K. Dutt, J. Burns, I. Charit, R.S. Mishra, Oxide dispersion strengthened nickel based alloys via spark plasma sintering, *Mater. Sci. Eng. A.* 630 (2015) 155–169. <https://doi.org/10.1016/j.msea.2015.01.066>.
- [77] B.A. Obadele, O.O. Ige, P.A. Olubambi, Fabrication and characterization of titanium-nickel-zirconia matrix composites prepared by spark plasma sintering, *J. Alloys Compd.* 710 (2017) 825–830. <https://doi.org/10.1016/j.jallcom.2017.03.340>.
- [78] D. Miracle, Metal matrix composites – From science to technological significance, *Compos. Sci. Technol.* 65 (2005) 2526–2540. <https://doi.org/10.1016/j.compscitech.2005.05.027>.
- [79] A.J. Cyriac, *Metal Matrix Composites: History, Status, Factors and Future*, Oklahoma

State University, 2011.

- [80] K. Chawla, *Metal matrix composites*, Springer, 2006.
- [81] I. Ibrahim, F. Mohamed, E.J. Lavernia, Particulate reinforced metal matrix composites - a review, *J. Mater. Sci.* 26 (1991) 1137–1156. <https://doi.org/10.1007/BF00544448>.
- [82] H.L. Cox, The elasticity and strength of paper and other fibrous materials, *Br. J. Appl. Phys.* 3 (1952) 72–79. <https://doi.org/10.1088/0508-3443/3/3/302>.
- [83] H.J. Ryu, S.I. Cha, S.H. Hong, Generalized shear-lag model for load transfer in SiC/Al metal-matrix composites, *J. Mater. Res.* 18 (2003) 2851–2858.
- [84] K. Park, F.A. Mohamed, Creep Strengthening in a Discontinuous SiC-Al Composite, *Metall. Mater. Trans. A.* 26 (1995) 3119–3129.
- [85] C.S. Meyer, Crack-Inclusion Interaction: A Review, 2018. <https://doi.org/10.13140/RG.2.2.13028.07041>.
- [86] A. Evans, C.S. Marchi, A. Mortensen, *Metal Matrix Composites in Industry: an Introduction and a Survey*, 1st ed., Springer Science, New York, 2003. <https://doi.org/10.1007/978-1-4615-0405-4>.
- [87] R. Arsenault, S. Fishman, M. Taya, Deformation and fracture behavior of metal-ceramic matrix composite materials, *Prog. Mater. Sci.* 38 (1994) 1–157. [https://doi.org/10.1016/0079-6425\(94\)90002-7](https://doi.org/10.1016/0079-6425(94)90002-7).
- [88] M. Finot, Y.L. Shen, a. Needleman, S. Suresh, Micromechanical modeling of reinforcement fracture in particle-reinforced metal-matrix composites, *Metall. Mater. Trans. A.* 25 (1994) 2403–2420. <https://doi.org/10.1007/BF02648860>.
- [89] S. Pal, K.K. Ray, R. Mitra, Room temperature mechanical properties and tensile creep behavior of powder metallurgy processed and hot rolled Al and Al-SiCp composites, *Mater. Sci. Eng. A.* 527 (2010) 6831–6837. <https://doi.org/10.1016/j.msea.2010.07.075>.
- [90] A.C. Reddy, Influence of Volume Fraction, Size, Cracking, Clustering of Particulates and Porosity on the Strength and Stiffness of 6063/ SiCp Metal Matrix Composites, *Int. J. Res. Eng. Technol.* 4 (2015) 434–442.
- [91] A.F. Whitehouse, H.M.A. Winand, Tensile creep response of Al-SiC particulate and whisker composites, *Scr. Mater.* 41 (1999) 817–822. [https://doi.org/10.1016/S1359-6462\(99\)00230-4](https://doi.org/10.1016/S1359-6462(99)00230-4).
- [92] M. Manoharan, C. Liu, J.J. Lewandowski, Microstructure and particle size effects on fracture in aluminum metal matrix composites, *Icf7.* (1989) 2977–2985.
- [93] U. Tetzlaff, A. Gerber, R. Amelang, G. Lemos, Investigation of the creep resistance of a spray-compacted Si-particle reinforced Al-based MMC (DISPal® S270), *Key Eng. Mater.* 809 (2019) 87–93. <https://doi.org/10.4028/www.scientific.net/KEM.809.87>.
- [94] S. Madeira, G. Miranda, V.H. Carneiro, D. Soares, F.S. Silva, O. Carvalho, The effect of SiCp size on high temperature damping capacity and dynamic Young's modulus of hot-pressed AlSi-SiCp MMCs, *Mater. Des.* 93 (2016) 409–417.

- <https://doi.org/10.1016/j.matdes.2015.12.147>.
- [95] R.J. Arsenault, N. Shi, Dislocation generation due to differences between the coefficients of thermal expansion, *Mater. Sci. Eng.* 81 (1986) 175–187. [https://doi.org/10.1016/0025-5416\(86\)90261-2](https://doi.org/10.1016/0025-5416(86)90261-2).
- [96] D.J. Lloyd, Aspects of fracture in particulate reinforced metal matrix composites, *Acta Met. Mater.* 39 (1991) 59–71.
- [97] W.H. Hunt, J.R. Brockenbrough, P.E. Magnusen, Al-Si-Mg Composite model system: microstructural effects on deformation and damage evolution, *Scr. Metall. Mater.* 25 (1990) 15–20.
- [98] D.J. Lloyd, Particle reinforced aluminium and magnesium matrix composites, *Int. Mater. Rev.* 39 (1994) 1–23. <https://doi.org/10.1179/095066094790150982>.
- [99] R.J. Arsenault, N. Shi, C.R. Feng, L. Wang, Localized deformation of SiC/Al composites, *Mater. Sci. Eng. A.* 131 (1991) 55–68. [https://doi.org/10.1016/0921-5093\(91\)90344-M](https://doi.org/10.1016/0921-5093(91)90344-M).
- [100] A. Rutecka, Z.L. Kowalewski, K. Pietrzak, L. Dietrich, K. Makowska, J. Woźniak, M. Kostecki, W. Bochniak, A. Olszyna, Damage development of Al/SiC metal matrix composite under fatigue, creep and monotonic loading conditions, *Procedia Eng.* 10 (2011) 1420–1425. <https://doi.org/10.1016/j.proeng.2011.04.236>.
- [101] X.D. Hui, Y.S. Yang, Z.F. Wang, G.Q. Yuan, X.C. Chen, High temperature creep behavior of in-situ TiC particulate reinforced Fe-Cr-Ni matrix composite, *Mater. Sci. Eng. A.* 282 (2000) 187–192.
- [102] H.T. Tsang, C.G. Chao, Tensile and Creep Properties of in-Situ TiB/Ti MMC, *Acta Metall.* 37 (1997) 1359–1365.
- [103] L.C. Sun, L.L. Shaw, Processing and creep resistance of nickel/yttria composites, *J. Mater. Sci.* 33 (1998) 4893–4903. <https://doi.org/10.1023/A:1004405512619>.
- [104] L.C. Davis, J.E. Allison, Micromechanics effects in creep of metal-matrix composites, *Metall. Mater. Trans. A.* 26 (1995) 3081–3089. <https://doi.org/10.1007/BF02669438>.
- [105] A.F. Whitehouse, Creep of Metal Matrix Composites, in: A. Kelly, C. Zweben (Eds.), *Compr. Compos. Mater.*, Elsevier, 2000: p. 6000. <https://doi.org/10.1016/B0-08-042993-9/00014-0>.
- [106] V.I. Babitsky, J. Wittenburg, K. Naumenko, H. Altenbach, Constitutive models of creep, *Found. Eng. Mech.* (2007) 17–84. [https://doi.org/10.1007/978-3-540-70839-1\\_2](https://doi.org/10.1007/978-3-540-70839-1_2).
- [107] N. Ohno, M. Kawabata, J. Naganuma, Aging effects on monotonic, stress-paused, and alternating creep of type 304 stainless steel, *Int. J. Plast.* 6 (1990) 315–327.
- [108] D.R.H. Jones, M.F. Ashby, Mechanisms of Creep, and Creep-Resistant Materials, in: *Eng. Mater.* 1, Elsevier, 2019: pp. 381–394. <https://doi.org/10.1016/b978-0-08-102051-7.00022-1>.
- [109] T. Balakrishna Bhat, V.S. Arunachalam, Strengthening mechanisms in alloys, *Proc. Indian Acad. Sci. Sect. C Eng. Sci.* 3 (1980) 275–296. <https://doi.org/10.1007/BF02842915>.



- [110] F.R.N. Nabarro, Creep at very low rates, *Metall. Mater. Trans. A Phys. Metall. Mater. Sci.* 33 (2002) 213–218. <https://doi.org/10.1007/s11661-002-0083-8>.
- [111] F.R.N. Nabarro, H.L. Villiers, *The Physics of Creep*, 1995. [https://doi.org/10.1016/0966-9795\(96\)00037-4](https://doi.org/10.1016/0966-9795(96)00037-4).
- [112] P.K. Venkiteswaran, D.M.R. Taplin, *The Creep Fracture of Inconel X-750 at 700 °C*, 8 (1974). <https://doi.org/10.1179/msc.1974.8.1.97>.
- [113] D.P. Pope, S.S. Ezz, Mechanical properties of Ni3Al and nickel-base alloys with high volume fraction of  $\gamma'$ , *Int. Mater. Rev.* 29 (1984).
- [114] W.D. Nix, B. Ilshner, *Mechanisms Controlling Creep of Single Phase Metals and Alloys*, Pergamon Press Ltd, n.d. <https://doi.org/10.1016/B978-1-4832-8412-5.50243-5>.
- [115] F.H. Norton, *The creep of steel at high temperatures*, Library (Lond). (1929) 90.
- [116] O. Golan, A. Arbel, D. Eliezer, D. Moreno, The applicability of Norton's creep power law and its modified version to a single-crystal superalloy type CMSX-2, *Mater. Sci. Eng. A.* 216 (1996) 125–130. [https://doi.org/10.1016/0921-5093\(96\)10400-7](https://doi.org/10.1016/0921-5093(96)10400-7).
- [117] H.J. Frost, M.F. Ashby, *Deformation-Mechanism Maps (The Plasticity and Creep of Metals and Ceramics)*, Pergamon Press Ltd, Oxford, 1982.
- [118] Y. Li, T.G. Langdon, An examination of a substructure-invariant model for the creep of metal matrix composites, *Mater. Sci. Eng. A.* 265 (1999) 276–284. [https://doi.org/10.1016/S0921-5093\(98\)01131-9](https://doi.org/10.1016/S0921-5093(98)01131-9).
- [119] O.D. Sherby, R.H. Klundt, A.K. Miller, Flow Stress, Subgrain Size, and Subgrain Stability at Elevated Temperature, *Metall. Trans. A.* 8 (1977) 843–850.
- [120] S.L. Robinson, O.D. Sherby, Mechanical behavior of polycrystalline tungsten at elevated temperature, *Acta Metall.* 17 (1969) 109–125. [https://doi.org/10.1016/0001-6160\(69\)90132-1](https://doi.org/10.1016/0001-6160(69)90132-1).
- [121] J. Rösler, E. Arzt, A new model-based creep equation for dispersion strengthened materials, *Acta Metall. Mater.* 38 (1990) 671–683. [https://doi.org/10.1016/0956-7151\(90\)90223-4](https://doi.org/10.1016/0956-7151(90)90223-4).
- [122] E. Arzt, *Creep of Dispersion Strengthened Materials : A Critical Assessment*, *Res Mech.* 31 (1991) 399–453.
- [123] R.C. Reed, T. Tao, N. Warnken, Alloys-By-Design: Application to nickel-based single crystal superalloys, *Acta Mater.* 57 (2009) 5898–5913. <https://doi.org/10.1016/j.actamat.2009.08.018>.
- [124] C.M.F. Rae, R.C. Reed, Primary creep in single crystal superalloys: Origins, mechanisms and effects, *Acta Mater.* 55 (2007) 1067–1081. <https://doi.org/10.1016/j.actamat.2006.09.026>.
- [125] Z. Zhu, H. Basoalto, N. Warnken, R.C. Reed, A model for the creep deformation behaviour of nickel-based single crystal superalloys, *Acta Mater.* 60 (2012) 4888–4900. <https://doi.org/10.1016/j.actamat.2012.05.023>.

- [126] A. Drexler, A. Fischerswörning-Bunk, B. Oberwinkler, W. Ecker, H. Gänsler, A microstructural based creep model applied to alloy 718, *Int. J. Plast.* 105 (2018) 62–73. <https://doi.org/10.1016/j.ijplas.2017.11.003>.
- [127] T. Link, M. Feller-Kniepmeier, Shear Mechanisms of the  $\gamma'$  Phase in Single-Crystal Superalloys and Their Relation to Creep, *Metall. Trans. A.* 23 (1992) 99–105.
- [128] G. Eggeler, A. Dlouhý,  $\gamma'$ -Phase Cutting during High Temperature Shear Creep Deformation of CMSX6 Superalloy Single Crystals, *Phys. Status Solidi.* 149 (1995) 349–353.
- [129] D.R. Lesuer, C.K. Syn, O.D. Sherby, An Evaluation of Power Law Breakdown in Metals, Alloys, Dispersion Hardened Materials and Compounds, *Met. Soc. Honor. Symp.* (2000).
- [130] A. Nowotnik, P. Pędrak, J. Sieniawski, M. Góral, Mechanical properties of hot deformed Inconel 718 and X750, 50 (2012) 74–80.
- [131] R.A. Stevens, P.E.J. Flewitt, The dependence of creep rate on microstructure in a gamma prime strengthened superalloy, *Acta Metall.* 29 (1981) 867–882. [https://doi.org/10.1016/0001-6160\(81\)90129-2](https://doi.org/10.1016/0001-6160(81)90129-2).
- [132] P. Rodriguez, Serrated plastic flow, *Bull. Mater. Sci.* 6 (1984) 653–663. <https://doi.org/10.1007/BF02743993>.
- [133] C. Zener, J.H. Hollomon, Effect of strain rate upon plastic flow of steel, *J. Appl. Phys.* 15 (1944) 22–32. <https://doi.org/10.1063/1.1707363>.
- [134] Y. Estrin, L.P. Kubin, Plastic instabilities: phenomenology and theory, *Mater. Sci. Eng. A.* 137 (1991) 125–134. [https://doi.org/10.1016/0921-5093\(91\)90326-1](https://doi.org/10.1016/0921-5093(91)90326-1).
- [135] S.K. Sondhi, B.F. Dyson, M. McLean, Tension-compression creep asymmetry in a turbine disc superalloy: Roles of internal stress and thermal ageing, *Acta Mater.* 52 (2004) 1761–1772. <https://doi.org/10.1016/j.actamat.2003.12.017>.
- [136] F. Louchet, A model of negative creep in nickel-based superalloys, *Scr. Metall. Mater.* 33 (1995) 913–918. [https://doi.org/10.1016/0956-716X\(95\)00299-B](https://doi.org/10.1016/0956-716X(95)00299-B).
- [137] R.C. Picu, A mechanism for the negative strain-rate sensitivity of dilute solid solutions, *Acta Mater.* 52 (2004) 3447–3458. <https://doi.org/10.1016/j.actamat.2004.03.042>.
- [138] R. Timmins, G.W. Greenwood, D.F. Dyson, Negative creep in a nickel-base superalloy, *Scr. Metall.* 20 (1986) 67–70. [https://doi.org/10.1016/0036-9748\(86\)90214-0](https://doi.org/10.1016/0036-9748(86)90214-0).
- [139] R.A. Stevens, P.E.J. Flewitt, The effects of gamma prime precipitate coarsening during isothermal aging and creep of the nickel-base superalloy IN-738, *Mater. Sci. Eng.* 37 (1979) 237–247. [https://doi.org/10.1016/0025-5416\(79\)90157-5](https://doi.org/10.1016/0025-5416(79)90157-5).
- [140] F.A. Mohamed, M.M.I. Ahmed, T.G. Langdon, Factors influencing ductility in the superplastic Zn-22 Pct Al eutectoid, *Metall. Trans. A.* 8 (1977) 933–938. <https://doi.org/10.1007/BF02661575>.
- [141] E. Lang, V. Lupinc, A. Marucco, Effect of thermomechanical treatments on short-range ordering and secondary-phase precipitation in NiCr-based alloys, *Mater. Sci. Eng. A.* 114 (1989) 147–157. [https://doi.org/10.1016/0921-5093\(89\)90853-8](https://doi.org/10.1016/0921-5093(89)90853-8).

- [142] H.A. Kuhn, H. Biermann, T. Ungár, H. Mughrabi, An X-ray study of creep-deformation induced changes of the lattice mismatch in the  $\gamma'$ -hardened monocrystalline nickel-base superalloy SRR 99, *Acta Metall. Mater.* 39 (1991) 2783–2794. [https://doi.org/10.1016/0956-7151\(91\)90095-l](https://doi.org/10.1016/0956-7151(91)90095-l).
- [143] D. Caillard, A. Couret, Dislocation Cores and Yield Stress Anomalies, in: *Dislocations in Solids*, Toulouse, 1996: pp. 69–134. [https://doi.org/10.1016/S1572-4859\(96\)80005-2](https://doi.org/10.1016/S1572-4859(96)80005-2).
- [144] P.B. Hirsch, Kear-Wilsdorf locks, jogs and the formation of antiphase-boundary tubes in Ni3Al, *Philos. Mag. A.* 74 (2006) 1019–1040. <https://doi.org/10.1080/01418619608242174>.
- [145] S. Keshavarz, Z. Molaeinia, A.C.E. Reid, S.A. Langer, Morphology dependent flow stress in nickel-based superalloys in the multi-scale crystal plasticity framework, *Crystals*. 7 (2017) 1–22. <https://doi.org/10.3390/cryst7110334>.
- [146] B.H.K. R. Ramesh, B. Pathiraj, Crystal Structure Changes in Ni3Al and Its Anomalous Temperature Dependence, *J. Mater. Process. Technol.* 56 (1996) 78–87.
- [147] M.C. Pandey, A.K. Mukherjee, D.M.R. Taplin, Prior deformation effects on creep and fracture in inconel alloy X-750, *Metall. Trans. A.* 15 (1984) 1437–1441. <https://doi.org/10.1007/BF02648573>.
- [148] T.-F. Chen, G.P. Tiwari, Y. Iijima, K. Yamauchi, Volume and Grain Boundary Diffusion of Chromium in Ni-Base Ni-Cr-Fe Alloys., *Mater. Trans.* 44 (2003) 40–46. <https://doi.org/10.2320/matertrans.44.40>.
- [149] J. Coakley, D. Dye, H. Basoalto, Creep and creep modelling of a multimodal nickel-base superalloy, *Acta Mater.* 59 (2011) 854–863. <https://doi.org/10.1016/j.actamat.2010.08.035>.
- [150] Z. Zhu, H. Basoalto, N. Warnken, R.C. Reed, A model for the creep deformation behaviour of nickel-based single crystal superalloys, *Acta Mater.* (2012). <https://doi.org/10.1016/j.actamat.2012.05.023>.
- [151] J.-S. Zhang, Creep of Second Phase Particles Strengthened Materials, in: *High Temp. Deform. Fract. Mater.*, Elsevier, 2010: pp. 83–101. <https://doi.org/10.1533/9780857090805.1.83>.
- [152] Y. Han, M.C. Chaturvedi, A Study of Back Stress During Creep Deformation of a Superalloy Inconel 718, 85 (1987) 59–65.
- [153] O.. Sherby, Factors affecting the high temperature strength of polycrystalline solids, *Acta Metall.* 10 (1962) 135–147. [https://doi.org/10.1016/0001-6160\(62\)90058-5](https://doi.org/10.1016/0001-6160(62)90058-5).
- [154] C.P. Cutler, S.W.K. Shaw, The Interrelationship of  $\gamma'$  Size, Grain Size and Mechanical Properties in IN-939, a Cast Nickel-base Superalloy, *Strength Met. Alloy.* 2 (1979) 1357–1362. <https://doi.org/10.1016/B978-1-4832-8412-5.50224-1>.
- [155] T.A. Khalifa, T.S. Mahmoud, A.M. Korsunsky, Tensile and Creep Behavior of Extruded AA6063/SiC[sub p] Al MMCs, 101 (2010) 101–113. <https://doi.org/10.1063/1.3366502>.
- [156] A.G. Fallis, Affordable Metal-Matrix Composites for High Performance Applications,

2013. <https://doi.org/10.1017/CBO9781107415324.004>.
- [157] S. Spigarelli, M. Cabibbo, E. Evangelista, T.G. Langdon, Creep properties of an Al-2024 composite reinforced with SiC particulates, *Mater. Sci. Eng. A.* 328 (2002) 39–47. [https://doi.org/10.1016/S0921-5093\(01\)01698-7](https://doi.org/10.1016/S0921-5093(01)01698-7).
- [158] J. Lin, O.D. Sherby, Creep of oxide dispersion strengthened materials (with special reference to TD Nichrome), *Res Mech.* 2 (1978) 63. [http://ntrs.nasa.gov/search.jsp?R=19780021274%5Cnhttp://ntrs.nasa.gov/archive/nasa/casi.ntrs.nasa.gov/19780021274\\_1978021274.pdf%5Cnhttp://hdl.handle.net/2060/19780021274](http://ntrs.nasa.gov/search.jsp?R=19780021274%5Cnhttp://ntrs.nasa.gov/archive/nasa/casi.ntrs.nasa.gov/19780021274_1978021274.pdf%5Cnhttp://hdl.handle.net/2060/19780021274).
- [159] M. Taya, R.J. Arsenault, *Metal Matrix Composites - Thermomechanical Behavior*, 1989. [https://doi.org/10.1016/S1874-5679\(13\)60001-X](https://doi.org/10.1016/S1874-5679(13)60001-X).
- [160] A.H. Clauer, B.A. Wilcox, Steady-State Creep of Dispersion-Strengthened Nickel, *Met. Sci. J.* 1 (1967) 86–90. <https://doi.org/10.1179/msc.1967.1.1.86>.
- [161] K.T. Park, E.J. Lavernia, F.A. Mohamed, High temperature creep of silicon carbide particulate reinforced aluminum, *Acta Metall. Mater.* 38 (1990) 2149–2159. [https://doi.org/10.1016/0956-7151\(90\)90082-R](https://doi.org/10.1016/0956-7151(90)90082-R).
- [162] Z. Lin, F.A. Mohamed, Creep and microstructure in powder metallurgy 15 vol.% SiCp-2009 Al composite, *J. Mater. Sci.* 47 (2012) 2975–2984. <https://doi.org/10.1007/s10853-011-6131-2>.
- [163] Y. Li, T.G. Langdon, A Comparison of the Creep Properties of an Al-6092 Composite and the Unreinforced Matrix Alloy, 29 (1998) 2523–2531.
- [164] Y. Li, T.G. Langdon, A simple procedure for estimating threshold stresses in the creep of metal matrix composites, *Scr. Mater.* 36 (1997) 1457–1460. [https://doi.org/10.1016/S1359-6462\(97\)00041-9](https://doi.org/10.1016/S1359-6462(97)00041-9).
- [165] J. Čadek, V. Šustek, M. Pahutová, Is creep in discontinuous metal matrix composites lattice diffusion controlled?, *Mater. Sci. Eng. A.* 174 (1994) 141–147.
- [166] S.C. Tjong, Z.Y. Ma, Steady state creep deformation behaviour of SiC particle reinforced 2618 aluminium alloy based composites, *Mater. Sci. Technol.* 15 (1999) 429–436.
- [167] J.S. Benjamin, Mechanical alloying — A perspective, *Met. Powder Rep.* 45 (1990) 122–127. [https://doi.org/10.1016/S0026-0657\(10\)80124-9](https://doi.org/10.1016/S0026-0657(10)80124-9).
- [168] D.B. Williams, C.B. Carter, *Transmission Electron Microscopy: A Textbook for Materials Science*, Springer, Boston, 2009. <https://doi.org/10.1007/978-0-387-76501-3>.
- [169] L.B. McCusker, R.B. Von Dreele, D.E. Cox, D. Louër, P. Scardi, Rietveld refinement guidelines, *J. Appl. Crystallogr.* 32 (1999) 36–50. <https://doi.org/10.1107/S0021889898009856>.
- [170] B.H. Toby, R factors in Rietveld analysis: How good is good enough?, *Powder Diffr.* 21 (2006) 67–70. <https://doi.org/10.1154/1.2179804>.
- [171] J.C. Taylor, I. Hinczak, *Rietveld made easy*, Sietronics Pty Limited, 2006.

- [172] A. Mendelson, E. Roberts Jr., S.S. Manson, Optimization of time-temperature parameters for creep and stress rupture, with application to data from German cooperative long-time creep program, Cleveland, 1965.
- [173] K. Fisher, Grain Boundary Characterization in an X750 Alloy MRS Fall meeting, (2012).
- [174] G.P. Sabol, R. Stickler, Microstructure of Nickel-Based Superalloys, *Phys. Status Solidi*. 35 (1969) 11–52. <https://doi.org/10.1002/pssb.19690350102>.
- [175] H. Kitaguchi, Microstructure-Property Relationship in Advanced Ni-Based Superalloys, *Metall. - Adv. Mater. Process.* (2012) 20–41. <https://doi.org/10.5772/52011>.
- [176] A. International, ASM Specialty Handbook: Nickel, Cobalt, and Their Alloys, 2000.
- [177] R. Brunetaud, D. Coutsouradis, T.T. Gibbons, Y. Lindblom, D.B. Meadowcroft, R. Stickler, High temperature Alloys for Gas Turbines, D. Reidel, 1982.
- [178] S.A. Speakman, Basics of Rietveld Refinement, (2007) 1–25.
- [179] S.S. Manson, A. Mendelson, Optimization of Parametric Constants for Creep Rupture Data by Means of Least Squares, 1959. <https://doi.org/10.1007/BF01867395>.
- [180] J. Wang, H. Sehitoglu, Intermetallics Dislocation slip and twinning in Ni-based L1 2 type alloys, *Intermetallics*. 52 (2014) 20–31. <https://doi.org/10.1016/j.intermet.2014.03.009>.
- [181] A.K. Sinha, Growth of MC particles on stacking faults and dislocations, *Metallography*. 20 (1987) 37–45. [https://doi.org/10.1016/0026-0800\(87\)90063-2](https://doi.org/10.1016/0026-0800(87)90063-2).
- [182] B. Alabbad, L. Li, S. Tin, Controlling the grain boundary morphology and secondary g0 precipitate size distribution in Ni-base superalloys, *J. Alloys Compd.* (2019) 931–941.
- [183] P. Kontis, E. Alabort, D. Barba, D.M. Collins, A.J. Wilkinson, R.C. Reed, On the role of boron on improving ductility in a new polycrystalline superalloy, *Acta Mater.* 124 (2017) 489–500. <https://doi.org/10.1016/j.actamat.2016.11.009>.
- [184] H.L. Danflou, M. Marty, A. Walder, Formation of Serrated Grain Boundaries and Their Effect on the Mechanical Properties in a P/M Nickel Base Superalloy, *Superalloys 1992 (Seventh Int. Symp.* (2012) 63–72. [https://doi.org/10.7449/1992/superalloys\\_1992\\_63\\_72](https://doi.org/10.7449/1992/superalloys_1992_63_72).
- [185] R.J. Mitchell, H.Y. Li, Z.W. Huang, On the formation of serrated grain boundaries and fan type structures in an advanced polycrystalline nickel-base superalloy, *J. Mater. Process. Technol.* 209 (2009) 1011–1017. <https://doi.org/10.1016/j.jmatprotec.2008.03.008>.
- [186] A.K. Koul, G.H. Gessinger, On the mechanism of serrated grain boundary formation in Ni-based superalloys, *Acta Metall.* 31 (1983) 1061–1069. [https://doi.org/10.1016/0001-6160\(83\)90202-X](https://doi.org/10.1016/0001-6160(83)90202-X).
- [187] W. Wei, H. Wang, Z. Gao, Z. Wei, Microstructure evolution of as-cast Nb-Ti-C alloys, *Trans. Nonferrous Met. Soc. China*. 19 (2009) 440–443.
- [188] N. Durlu, Titanium carbide based composites for high temperature applications, *J. Eur.*

- Ceram. Soc. 19 (1999) 2415–2419. [https://doi.org/10.1016/S0955-2219\(99\)00101-6](https://doi.org/10.1016/S0955-2219(99)00101-6).
- [189] M. Li, J. Coakley, D. Isheim, G. Tian, B. Shollock, Influence of the initial cooling rate from gamma prime supersolvus temperatures on microstructure and phase compositions in a nickel superalloy, *J. Alloys Compd.* 732 (2018) 765–776.
- [190] U. Tetzlaff, H. Mughrabi, Enhancement of the High-Temperature Tensile Creep Strength of Monocrystalline Nickel-Base Superalloys by Pre-Rafting in Compression, *Superalloys*. 1 (2000) 273–282.
- [191] J.A. Del Valle, A.C. Picasso, I. Alvarez, R. Romero, Age-hardening behavior of Inconel X-750 superalloy, *Scr. Mater.* 41 (1999) 237–243. [https://doi.org/10.1016/S1359-6462\(99\)00151-7](https://doi.org/10.1016/S1359-6462(99)00151-7).
- [192] A.P. Mouritz, Fracture processes of aerospace materials, in: *Introd. to Aerosp. Mater.*, Woodhead Publishing Limited, 2012: pp. 428–453. <https://doi.org/10.1533/9780857095152.428>.
- [193] S.A. Sajjadi, S.M. Zebarjad, Study of fracture mechanisms of a Ni-Base superalloy at different temperatures, *J. Achiev. Mater. Manuf. Eng.* 18 (2006) 227–230.
- [194] S. Floreen, F. Mechanics, Metallurgical Factors Affecting the Crack Growth Resistance of a Superalloy, *Metall. Trans. A.* 8A (1977) 51–55.
- [195] E. Balikci, R.A. Mirshams, A. Raman, Fracture behavior of superalloy IN738LC with various precipitate microstructures, *Mater. Sci. Eng. A.* 265 (1999) 50–62.
- [196] F.R.N. Nabarro, Rafting in Superalloys, *Metall. Mater. Trans. A.* 27 (1996) 513–530.
- [197] T. M. Pollock, A. S. Argon, Directional coarsening in nickel-base single crystals with high volume fractions of coherent precipitates, *Acta Metall. Mater.* 42 (1994) 1859–1874.
- [198] T. Sugui, Z. Jinghua, Z. Huihua, Y. Hongcai, X. Yongbo, Aspects of primary creep of a single crystal nickel-base superalloy, *Mater. Sci. Eng. A.* 262 (1999) 271–278.
- [199] A. Epishin, T. Link, Mechanisms of high-temperature creep of nickel-based superalloys under low applied stresses, *Philos. Mag.* 84 (2007) 1979–2000. <https://doi.org/10.1080/14786430410001663240>.
- [200] T. Tinga, W.A.M. Brekelmans, M.G.D. Geers, Directional coarsening in nickel-base superalloys and its effect on the mechanical properties, *Comput. Mater. Sci.* 47 (2009) 471–481. <https://doi.org/10.1016/j.commatsci.2009.09.013>.
- [201] S. Li, J. Tao, T. Sugui, H. Zhuangqi, Influence of precipitate morphology on tensile creep of a single crystal nickel-base superalloy, *Mater. Sci. Eng. A.* 455 (2007) 461–466. <https://doi.org/10.1016/j.msea.2006.11.136>.
- [202] A. Altincekic, E. Balikci, Precipitate Rafting in a Polycrystalline Superalloy During Compression Creep, *Metall. Mater. Trans. A Phys. Metall. Mater. Sci.* 45 (2014) 5923–5936. <https://doi.org/10.1007/s11661-014-2558-9>.
- [203] Z. Yu, X. Wang, F. Yang, Z. Yue, J.C.M. Li, Review of  $\gamma'$  Rafting Behavior in Nickel-Based Superalloys: Crystal Plasticity and Phase-Field Simulation, *Crystals*. 10 (2020) 1095. <https://doi.org/10.3390/cryst10121095>.

- [204] W.J. Mills, The Deformation and Fracture Characteristics of Inconel X-750 at Room Temperature and Elevated Temperatures, (1980).
- [205] M.P. Singh, G.M. Lucas, Blade Design and Analysis for Steam Turbines, McGraw-Hill, 2011.
- [206] J.P. Poirier, Reply to Diffusion-controlled dislocation creep: A defense, *Acta Metall.* 27 (1979) 401–403. [https://doi.org/10.1016/0001-6160\(79\)90032-4](https://doi.org/10.1016/0001-6160(79)90032-4).
- [207] M.G. Mckimpson, T.E. Scott, Processing and Properties of Metal Matrix Composites Containing Discontinuous Reinforcement, *Mater. Sci. Eng.* 107 (1989) 93–106.
- [208] R.R. Unocic, G.B. Viswanathan, P.M. Sarosi, S. Karthikeyan, J. Li, M.J. Mills, Mechanisms of creep deformation in polycrystalline Ni-base disk superalloys, 484 (2008) 25–32. <https://doi.org/10.1016/j.msea.2006.08.148>.
- [209] R. Lagneborg, Bypassing of dislocations past particles by a climb mechanism, *Scr. Metall.* 7 (1973) 605–613.
- [210] T. Murakumo, T. Kobayashi, Y. Koizumi, H. Harada, Creep behaviour of Ni-base single-crystal superalloys with various  $\gamma'$  volume fraction, *Acta Mater.* 52 (2004) 3737–3744.
- [211] L.D. Landau, E.M. Lifshitz, J.B. Sykes, W.H.R.H. Dill, Theory of Elasticity, *Phys. Today.* 7 (1960) 1–4. <https://doi.org/10.1063/1.3057037>.
- [212] D. Raynor, J.M. Silcock, Strengthening Mechanisms in  $\gamma'$  Precipitating Alloys, *Met. Sci. J.* 4 (1970) 121–130.
- [213] E. Arzt, J. Rösler, The kinetics of dislocation climb over hard particles-II. Effects of an attractive particle-dislocation interaction, *Acta Metall.* 36 (1988) 1053–1060. [https://doi.org/10.1016/0001-6160\(88\)90159-9](https://doi.org/10.1016/0001-6160(88)90159-9).
- [214] T.M. Pollock, A.S. Argon, Creep resistance of CMSX-3 nickel base superalloy single crystals, *Acta Metall. Mater.* 40 (1992) 1–30. [https://doi.org/10.1016/0956-7151\(92\)90195-K](https://doi.org/10.1016/0956-7151(92)90195-K).
- [215] T.P. Gabb, S.L. Draper, D.R. Hull, R.A. Mackay, M. V. Nathal, The role of interfacial dislocation networks in high temperature creep of superalloys, *Mater. Sci. Eng. A.* 118 (1989) 59–69. [https://doi.org/10.1016/0921-5093\(89\)90058-0](https://doi.org/10.1016/0921-5093(89)90058-0).
- [216] J. Douin, P. Veyssi re, P. Beauchamp, Dislocation line stability in Ni<sub>3</sub>Al, *Philos. Mag. A Phys. Condens. Matter, Struct. Defects Mech. Prop.* 54 (1986) 375–393. <https://doi.org/10.1080/01418618608240722>.
- [217] J.K. Tien, B.H. Kear, G.R. Leverant, On the High Activation Energy for Steady State Creep of Particle Strengthened Systems, *Scr. Metall.* 6 (1972) 135–140.
- [218] K. Mayer, H. Mehrer, E. Lessmann, W. Sch ule, Self-diffusion of Nickel at Low Temperatures, *Phys. Status Solidi.* 689 (1976) 689–698.